Pre-clinical Evaluation of Therapeutic Microbubbles for the Treatment of Colorectal Cancer

Laura Elizabeth McVeigh

The University of Leeds

Leeds Institute of Biomedical and Clinical Sciences

School of Medicine

March 2018

Submitted in accordance with the requirements for the degree of

Doctor of Philosophy

The candidate confirms that the work submitted is her own and that appropriate credit has been given where reference has been made to the work of others.

Acknowledgements

I would like to thank EPSRC for sponsoring my studentship, Leeds Microbubble Consortium for useful discussions and advice, and staff at the SBS mouse facility for all their behind the scenes work. I would also like to thank Paul Loadman, Antonia Wierzbicki, Jade Spencer and Amanda Race from the Institute of Cancer Therapeutics, University of Bradford, for all their knowledge and help with the LC-MS/MS. Special thanks to James McLaughlan for advice with US experiments and to Radwa Abou-Saleh for producing the liposomes, without you none of this would have been possible.

My supervisor Louise, your energy and enthusiasm was contagious. I will be forever grateful for your laissez-faire supervision, you were there when I needed you but let me have the freedom and independence to stand on my own two feet. It was a privilege to work with you. Thank you to my secondary supervisors Steve Evens, Alex Markham and Pam Jones for their guidance and discussions. And Nikki, thank you for taking me under your wing all those years ago, for your unrelenting patience and support, assistance with MB experiments, thesis proof reading and of course your friendship.

The Molecular Gastroenterology research group, Milene Volpato, Sarah Perry, Gemma Marston and Mark Hull, thank you for sitting through my weekly lab presentations and for your advice and discussions throughout my PhD.

Antonia, my dear friend and lab partner, despite working together in close proximity for 4-years, we have always worked as a team and supported each other. Your ability to do your PhD on decaf coffee alone will always impress me!

Anastasia, Imeshi, Nick and Spiros, my office comrades, thank you for the coffee time, discussions and laughs. I shall miss you all.

Alex, you have always believed in me and given me confidence when I've needed it. Thank you for the late night trips to the lab, for helping me label tubes and of course your unconditional love, especially during the final writing stage.

Finally, I would like to thank my mum, dad and my brother Andy for their unrelenting encouragement, love and support for which I will be eternally grateful.

Abstract

Colorectal cancer (CRC) is the third most common cancer worldwide. Despite improvements in the overall 5-year survival rate, success has not been reflected in those over 75-years of age or those diagnosed with advanced stages of the disease. It has been proposed that a targeted, triggered drug-delivery system would optimise drug delivery to tumours, a fundamental yet difficult requirement for the effective treatment of cancer.

Microbubbles (MBs), 2 μm in diameter and consisting of a lipid stabilised gas core, were engineered to carry a low dose payload of the chemotherapy prodrug irinotecan and subsequently its active metabolite SN38. These drug-loaded MBs were termed therapeutic MBs (thMBs) and were specifically targeted to tumour vasculature using the pro-angiogenic receptor expressed by endothelial cells, vascular endothelial growth factor receptor-2 (VEGFR2). Once injected (intravenously), a short, low-frequency pulse of ultrasound (US) was deployed externally to the tumour and used as a 'trigger' to destroy the thMBs, releasing the drug at the target site and increasing intracellular drug delivery to the tumour tissue.

A liquid chromatography tandem mass spectrometry method was developed and validated to determine concentrations of irinotecan and/or SN38 and their metabolites from murine CRC xenograft tumours, tissues and blood. Pharmacokinetic studies were performed to compare biodistribution after multiple doses of thMBs to normal delivery methods. Irinotecan thMBs enhanced tumour drug accumulation and/or retention and increased efficacy compared to free drug. The more potent SN38 was then investigated *in vitro*, and thMB drug delivery was developed for the more efficient treatment of CRC *in vivo*. SN38 thMBs resulted in 93% tumour growth inhibition compared to the control and drug was detected in tumour tissues 72-hours post final treatment, with significant tumour pharmacodynamic response determined.

Finally, an orthotopic murine model of human CRC liver metastases was established using US guided injection to offer a novel, minimally-invasive model of advanced disease for more translatable pre-clinical testing of anti-cancer agents.

Table of Contents

List of Figures

List of Tables

Abbreviations

%AR	Percentage Analyte Recovery
%CV	Percentage Coefficient of Variation
αvβ3	Integrin Alpha 5 and Integrin Beta 3
2D	2-Dimentional
3D	3-Dimentional
5-FU	Fluorouracil
ADME-Tox	Absorption, Distribution, Metabolism, Excretion and Toxicity
AJCC	American Joint Committee on Cancer
ALT	Alanine Transaminase
APC	7-ethyl-10-[4-N-(5-aminopentanoic acid)-1-piperidino]carbonyloxycamptothecin
APC	Adenomatous Polyposis Coli
AST	Aspartate Transaminase
ATCC	American Type Culture Collection
AUC	Area Under the Curve
BBB	Blood Brain Barrier
CA	California
CA4	Combretastatin A4
CA4P	Combretastatin A4 Phosphate
CAPOX	Capecitabine and Oxaliplatin
CARPA	Complement Activation-Related Pseudoallergy
CE	Carboxylesterase
CIN	Chromosomal Instability
C_{max}	Maximum Concentration
CRC	Colorectal Cancer
CT	Computed Tomography
CTNNB1	Catenin-β1
CYP	Cytochrome
d10	Ten Deuterium atoms
DAB	3,3'-Diaminobenzidine
DHPE	1,2-Dihexadecanoyl-sn-Glycero-3-Phosphoethanolamine, Triethylammonium Salt
DLS	Dynamic Light Scattering
DMEM	Dulbecco's Modified Eagle Medium
DMSO	Dimethyl sulfoxide
DNA	Deoxyribonucleic Acid
DOX	Doxorubicin
DPPC	1,2-dipalmitoyl-sn-glycero-3-phosphocholine
DSPC	1,2-distearoyl-sn-glycero-3-phosphocholine
DSPE	1,2-distearoyl-sn-glycero-3-phosphoethanolamine
DSPE-biotin-PEG_{2000}	1,2-distearoyl-sn-glycero-3-phosphoethanolamine-N-[biotinyl(polyethylene glycol)-2000]
ED_{50}	Effective Dose for 50% of patients
EGFR	Epidermal Growth Factor Receptor
EPR	Enhanced Permeability and Retention

ERUS	Endorectal Ultrasound
F/T	Freeze/Thaw
FAM123B	Family with Sequence Similarity 123B (also known as AMER1)
FAP	Familial Adenomatous Polyposis
FCS	Foetal Calf Serum
FDA	Food and Drug Administration
FDG	18-Fluor-Labeled Fluorodeoxyglucose
FOLFIRI	Fluorouracil, Leucovorin, and Irinotecan
FOLFOX	Folinic Acid, Fluorouracil and Oxaliplatin
FZD10	Frizzled Class Receptor 10
g	Times Gravity
Gd-EOB-DTPA	Gadolinium-ethoxybenzyl-diethylenetriamine penta-acetic Acid
GEMM	Genetically Engineered Mouse Models
GI_{50}	50% Growth Inhibition
H&E	Haematoxylin and Eosin
HNPCC	Hereditary Nonpolyposis Colorectal Cancer
HPLC	High Pressure Liquid Chromatography
i.v.	Intravenous
IC_{50}	Half Maximal Inhibitory Concentration
IVCs	Individually Ventilated Cages
KRAS	Kirsten Ras
LC-MS/MS	Liquid Chromatography Tandem Mass Spectrometry
LOD	Limit of Detection
LONDs	Lipid-Stabilised Oil Nanodroplets
LOQ	Limit of Quantification
LRP5	Low-Density Lipoprotein Receptor-Related Protein 5
Ltd	Limited
m/z	Mass-to-Charge Ratio
M3-PALS	Mixed Measurement Model Phase Analysis
MA	Massachusetts
MAPK	Mitogen-Activated Protein Kinase
MB(s)	Microbubble(s)
MHz	Mega-Hertz
MI	Mechanical Index
min	Multiple Intestinal Neoplasia
MLC	Mary Lyon Centre
MRC	Medical Research Council
MRI	Magnetic Resonance Imaging
MRM	Multiple Reaction Monitoring
mRNA	Messenger Riboneucleic Acid
Msh2-/-	MutS Homologue 2
MSI	Microsatellite Instability
MTT	3-[4,5-Dimethylthiazol-2-yl]-2,5-diphenyl-tetrazolium bromide
mV	Millivolts

NICE	National Institute for Health and Care Excellence
NPC	7-ethyl-10-(4-amino-1-piperidino) carbonyloxycamptothecin
OC	Optical colonoscopy
PA(s)	Peak area(s)
PBS	Phosphate Buffered Saline
PD	Pharmacodynamic
PEG	Poly(ethyleneglycol)
PET	Positron Emission Tomography
PFA	Paraformaldehyde
PGF	Placental Growth Factor
pH2AX	Phosphorylated Histone H2AX
PI3K	Phosphatidylinositol 3-Kinase
PI3KCA	Phosphatidylinositol-4,5-Bisphosphate 3-Kinase Catalytic Subunit-α
PK	Pharmacokinetic
PRF	Pulse Repetition Frequency
PTEN	Phosphatase and Tensin Homologue
ROS	Reactive Oxygen Species
RPMI	Roswell Park Memorial Institute
RT	Room Temperature
RT(s)	Retention Time(s)
SD	Standard Deviation
SFRP	Secreted Frizzled-Related Protein
SHERPAs	SHockwavE-Ruptured nanoPayload cArriers
siRNA	Small Interfering Ribonucleic Acid
SMAD4	SMAD Family Member 4
SN38	7-ethyl-10-hydroxycamptothecin
SN38-G	7-ethyl-10-hydroxycamptothecin-glucuronide
SPIOs	Superparamagnetic Iron Oxide Nanoparticles
STR	Short Random Repeat
Sutcut	Subcutaneous
TD_{50}	Toxic Dose for 50% of Patients
TGFBR2	TGFβ Receptor 2
TGFβ	Transforming Growth Factor-β
thMB(s)	Therapeutic Microbubble(s)
TI	Therapeutic Index
TNM	Tumour Node Metastasis
UARP	Ultrasound Array Research Platform
UGT1A1	UDP-glucuronosyltransferase 1A-1
UK	United Kingdom
UPLC	Ultra-High Pressure Liquid Chromatography
US	Ultrasound
US-trigger	Ultrasound-Trigger
USA	United States of America
UV-Vis	Ultraviolet-Visible Spectrophotometry

v/v	Volume/Volume
VEGF	Vascular Endothelial Growth Factor
VEGFA	Vascular Endothelial Growth Factor-A
VEGFR2	Vascular Endothelial Growth Factor Receptor-2
w/v	Weight/Volume
β-Glu	Beta-Glucuronidase

Chapter 1

Introduction

1 Introduction

1.1 Colorectal cancer

Colorectal cancer (CRC) is the fourth most commonly diagnosed cancer within the UK, accounting for 12% of all new cancers cases (Cancer Research UK, cancerresearchuk.org, accessed March 2018). Survival rates have more than doubled in the last 40 years but five-year survival is still less than 60% and it is the second most common cause of cancer-related death in the UK (Cancer Research UK, cancerresearchuk.org, accessed March 2018). Worldwide, over a million people are diagnosed each year with rates highest in the more developed countries. Occurrence is strongly associated with age with 83% of cases diagnosed in those over 60 (Arnold *et al.,* 2017). Treatment in the elderly is especially challenging; surgery is high risk and chemotherapy has increased risk of toxic side effects, often complicated by other chronic health conditions (Balducci and Extermann, 2000; Marosi and Köller, 2016). Despite improvements in the overall 5-year survival rate, success has not been reflected in those over 75-years of age (Cancer Research UK, cancerresearchuk.org, accessed March 2018) and with an increasingly aging population, rates of CRC are set to rise.

Liver metastasis is the leading cause of death for patients diagnosed with CRC. Early diagnosis of CRC (Stage I) has a 5-year survival rate of 98%, in comparison to late stage (Stage IV) where this falls to just 8% (Cancer Research UK, cancerresearchuk.org, accessed March 2018). More than 50% of those diagnosed with CRC will go on to develop liver metastases during their lifetime. Surgical resection of metastases are recommended (if feasible), however 70% will go on to experience recurrence (Tomlinson *et al.,* 2007).

This chapter will review the development of CRC, current treatments and challenges. The role of nanomedicine and drug delivery systems as novel therapies will be introduced and the use of *in vivo* imaging, specifically ultrasound (US) which can be used theranostically with thMBs to enhance drug delivery. Finally, the need for superior models of CRC will be highlighted, in order to improve and accelerate the pre-clinical phase of novel drug development for more rapid translation to the clinic.

1.2 CRC development and disease progression

1.2.1 Risk factors and prevention

Age is strongly related to CRC risk with 94% of cases diagnosed in those over 50-years of age in the UK (Cancer Research UK, cancerresearchuk.org, accessed March 2018). 5-10% of

those are thought to have been due to hereditary conditions (Jackson-Thompson *et al.,* 2006). Familial adenomatous polyposis (FAP) is caused by mutations in the tumour suppressor gene adenomatous polyposis coli (APC) which accounts for 1% of all cases (Eshghifar *et al.,* 2017; Aoki and Taketo, 2007). Hereditary nonpolyposis colorectal cancer (HNPCC) is caused by mutations in the DNA repair MLH1 and MLH2 genes, and accounts for 2-6% of cases (Järvinen *et al.,* 2000; Lynch and Lynch, 2000).

Environmental risk factor such as diets high in fat and animal protein and low in fibre, obesity, reduced physical exercise, smoking and high alcohol intake are all associated with increased CRC risk (Boyle and Langman, 2000; De Jong *et al.,* 2005; Zisman *et al.,* 2006; Ratna and Mandrekar, 2017).

The vast majority of CRC cases are preventable by dietary changes, regular physical exercise and maintaining a healthy body weight, all of which combined with early screening programmes could pick up CRC in the early stages where successful outcomes are high (Haggar and Boushey, 2009; Marley and Nan, 2016).

1.2.2 Tumorigenesis

CRC develops via a multistep process, involving morphological and genetic changes which have been estimated to accumulate over 5-10 years (Kozuka *et al.,* 1975)(**Figures 1.1 and 1.2**). These changes occur in adenomas, benign, precancerous growths protruding into the intestinal lumen. Adenomas are precursor lesions and can form anywhere along the colon and rectum, but only a small fraction will go on to acquire malignancy, therefore early detection and resection are vital to the prevention of CRC development.

Fearon and Vogelstein were the first to define the multistep genetic hypothesis, from the early adenoma to carcinoma and finally metastasis (Fearon and Vogelstein, 1990). As the adenoma increases in size, genetic and epigenetic changes may occur and accumulate. The cancer cells may then proceed to invade nearby tissue and/or the wall of the colon/rectum, with metastasis the final stage of the multistep process (**Figure 1.2**).

It has been discovered that CRC arises from single or multiple genetic or epigenetic events, chromosomal instability, CpG island methylator phenotype and microsatellite instability (Tariq and Ghias, 2016; Pancione *et al.,* 2012). The most common mutations in CRC include those in APC, catenin-β1, KRAS, BRAF, SMAD4, transforming growth factor-β receptor 2, TP53, phosphatidylinositol-4,5-bisphosphate 3-kinase catalytic subunit-α, AT-rich interactive domain 1A, SRY (sex- determining region Y) box 9 (SOX9), family with sequence similarity 123B and ERBB2 (**Figure 1.1**). Mutations in these genes instigate tumorigenesis

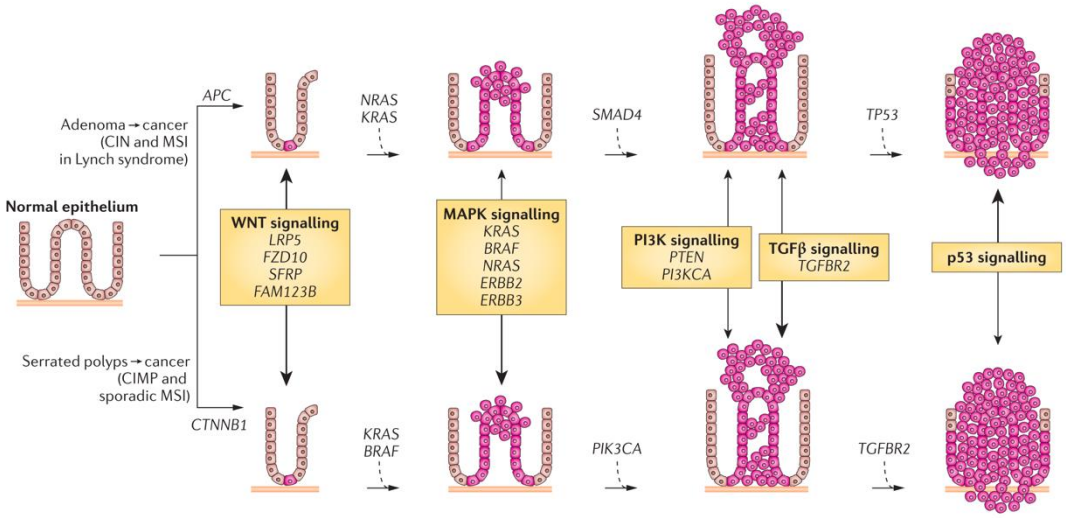

Figure 1.1 The sequence of events promoting adenoma to carcinoma.

A schematic showing the multistep carcinogenic progression from adenoma to carcinoma (primary tumour). The signalling pathways altered during the sequence are shown in bold with the genes responsible given for each. APC, adenomatous polyposis coli; CIN, chromosomal instability; CTNNB1, catenin-β1; FAM123B, family with sequence similarity 123B (also known as AMER1); FZD10, frizzled class receptor 10; LRP5, low-density lipoprotein receptor-related protein 5; MAPK, mitogen-activated protein kinase; MSI, microsatellite instability; PI3K, phosphatidylinositol 3-kinase; PI3KCA, phosphatidylinositol-4,5-bisphosphate 3-kinase catalytic subunit-α; PTEN, phosphatase and tensin homologue; SFRP, secreted frizzled-related protein; SMAD4, SMAD family member 4; TGFβ, transforming growth factor-β; TGFBR2, TGFβ receptor 2. Taken from (Kuipers *et al.,* 2015).

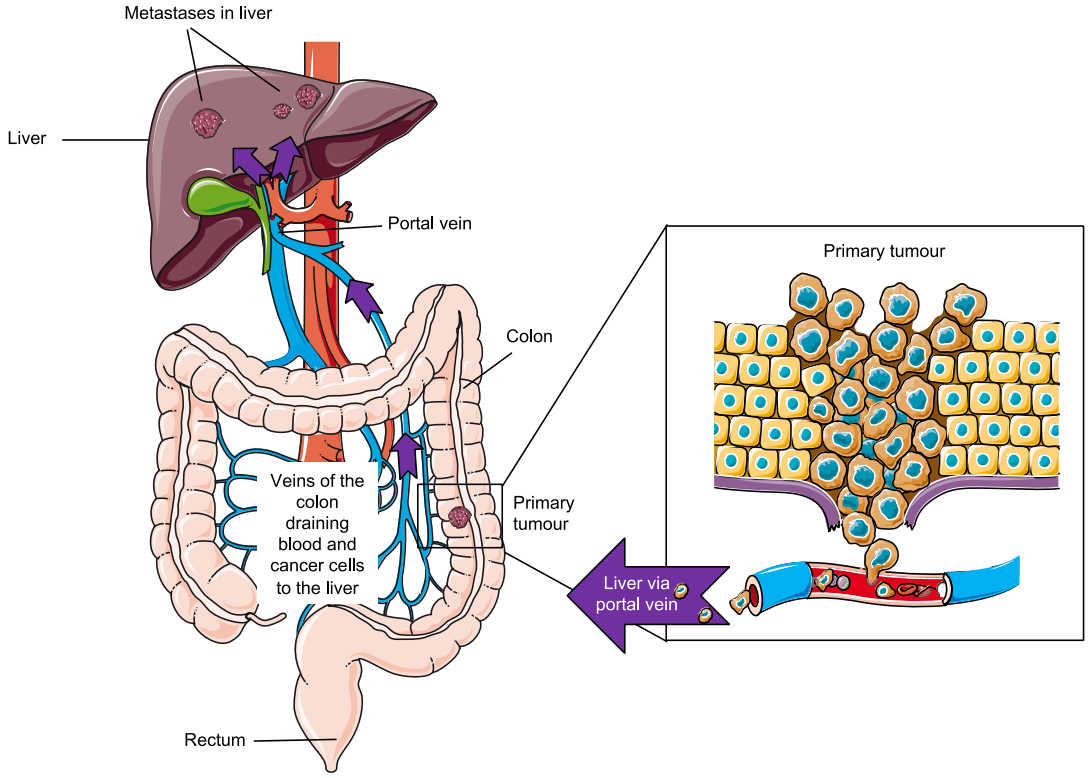

Figure 1.2 Progression of CRC carcinoma to liver metastases.

A schematic showing the progression from carcinoma (primary tumour) to formation of liver metastases. Cancer cells from the primary tumour of the colon or rectum invade, intravasate, survive the circulatory system, extravasate and colonise at a distant site. Drainage of the intestinal mesentery veins into the hepatic portal vein, allows cancer cells from the primary tumour to be transported to secondary sites in the liver, the most common site of secondary metastasis. Less than 0.01% of circulating cancer cells will manage to form metastases. Created using Smart Servier Medical Art (https://smart.servier.com/).

by altering important signalling pathways (WNT–β-catenin, epidermal growth factor–mitogen-activated protein kinase, phosphatidylinositol 3-kinase and TGFβ), or by modifying genes which control DNA repair and cell proliferation (Kuipers *et al.,* 2015; Tariq and Ghias, 2016). More recently, CRC has been subtyped according to the mutations present and this classification system may be used to target therapy and predict treatment outcomes (Dienstmann *et al.,* 2017; Guinney *et al.,* 2015). For example, anti-epidermal growth factor receptor (EGFR) therapy is inefficient in CRCs with mutations in codon 12 and 13 of KRAS (Knickelbein and Zhang, 2015).

1.2.3 Tumour angiogenesis

Tumours can reach a volume of 1-2 mm^3 before they must recruit blood vessels to sustain further growth (Folkman, 1971; Muthukkaruppan *et al.,* 1982). This process is known as the angiogenic switch and is a critical hallmark of tumour development (Hanahan and Weinberg, 2000). Hypoxia is a key driver of tumour angiogenesis, with oxygen deprived cancer cells releasing vascular endothelial growth factor-A (VEGFA) which binds to vascular endothelial growth factor receptor-2 (VEGFR2) expressed on the surface of endothelial cells in close proximity to the tumour. This stimulates vascular sprouting and the formation of a vascular network to deliver oxygen and nutrients to the cancer cells for further growth and progression. However, tumour vasculature is abnormal, tortuous and leaky, resulting in high interstitial pressure and ultimately limits tumour drug uptake (Heldin *et al.,* 2004). Anti-angiogenic drugs targeting VEGF/VEGFR2 have been proven effective for metastatic CRC, however long term use can result in more aggressive metastatic cancers (Battaglin *et al.,* 2018)

1.2.4 Invasion-metastatic cascade

For metastasis to take place, a sequence of events known as the invasion-metastatic cascade must occur. This is a multistep process and the mechanisms which drive metastasis are not fully understood. Cancer cells invade, intravasate, survive the circulatory system, extravasate and colonise at a distant site (Mina and Sledge, 2011). Less than 0.01% of circulating cancer cells will manage to successfully colonise a foreign microenvironment, and is considered the most difficult of the five steps (Fidler, 1970; Chambers *et al.,* 1995). Many cancer cells will remain dormant in their new environment or cannot instigate the angiogenic switch need for tumour development (Barken *et al.,* 2010; Naumov *et al.,* 2006).

For those patients that present with CRC metastases, 70% are found in the liver, followed by the thorax (32-47%)(Riihimaki *et al.,* 2016). This may be due to the drainage of the intestinal mesentery into the hepatic portal venous system, allowing cancer cells from the primary tumour to be transported via hematogenous dissemination to secondary sites in the liver. Blood from the liver is then pumped to the lungs via the heart and hence the second most common site of metastasis is the thorax (Riihimaki *et al.,* 2016; van der Geest *et al.,* 2015).

Sites of metastases are not random, Paget's Seed and Soil Hypothesis (1889) first proposed cancer cells (seeds) had a preference for particular microenvironments or organs (soil) they metastasise to (Paget, 1889). Metastases would not form by chance, only when the 'seed' found its optimal 'soil'. Others disputed this, the Anatomical – Mechanical Hypothesis, that vascular and lymphatic drainage from the primary tumour site was responsible for metastases formation in the first organ it passes (Ewing, 1928). It is generally accepted that either mechanism (or both) plays a role depending on the placement of the primary tumour (Langley and Fidler, 2011; Fidler, 2003).

1.2.5 Progression of liver metastasis

Once a single cancer cell manages to intravasate and escape the primary tumour, negotiate the circulatory system, and lodge itself in a hepatic sinusoid, the process of liver metastasis has begun (Mook *et al.,* 2008).

The liver sinusoid consists of sinusoidal endothelial cells, Kupffer cells, hepatic stellate cells and pit cells, all of which play a role in CRC liver metastases development (Paschos *et al.,* 2014). A single layer of sinusoidal endothelial cells line the sinusoids, separated from the hepatocytes by the Space of Disse (De Leeuw *et al.,* 1990). Sinusoidal endothelial cells have demonstrated both a preventative and a metastatic aiding role. They are able to rapidly remove and degrade autotaxin from the circulation, an enzyme which promotes the invasive properties of cancer cells (Jansen *et al.,* 2009).

Cancer cells must attach to the sinusoidal endothelial cells via selectins and later form stronger integrin mediated tumour cell adhesions in order to resist the flow of blood and keep in position (Mook *et al.,* 2008). Under the influence of cytokines, sinusoid endothelial cells may express E-selectin, an adhesion molecule which encourages cancer cell adhesion and extravasation (Khatib *et al.,* 1999).

The first line of defence are the immune cells in the form of Kupffer cells (macrophages) and pit cells (liver-associated natural killer cells), which work together to remove cancer

cells (Timmers *et al.,* 2004; Langers *et al.,* 2012). However, they can become saturated with increasing numbers of malignant cells arriving in the sinusoids (Bayón *et al.,* 1996). If cancer cells evade the immune system and form a strong adherence to a sinusoidal endothelial cell, they are very quickly able to migrate through endothelial pores into the Space of Disse and within 48-hours they reach the hepatocytes and begin developing into a micrometastases (Shimizu *et al.,* 2000). The progression from micro to macrometastases takes weeks to months, or potentially they may lie in a dormant state for a long period of time (Panis *et al.,* 1992; Gao *et al.,* 2017). As described for CRC development, the angiogenic switch must occur for growth and progression of the tumour of which VEGFA and VEGFR2 play a major role (Paschos *et al.,* 2014).

1.3 Current treatments for CRC

CRC treatment regimens are based on the stage of disease at diagnosis. The earlier the disease is diagnosed, the more likely the patient will survive (**Figure 1.3**). Staging of disease is undertaken using various imaging modalities (**Section 1.6**), and only then is the most appropriate course of action determined. The tumour node metastasis or TNM staging system from the American Joint Committee on Cancer (AJCC) stages disease from I-IV (Weisenberg, 2018). TNM classifies tumour progression by the size and extension of the primary tumour, its level of lymph node involvement and whether or not metastasis has occurred (**Table 1.1**). The higher the stage, the more advanced the disease and the worse the prognosis (**Figure 1.3**). This staging system is important not only from a treatment and prognosis perspective, but also to gauge efficacy of the treatment and for data sharing of clinical trial outcomes and international statistics.

Five-year survival in the UK has doubled in the last 40 years (Cancer Research UK, cancerresearchuk.org, accessed March 2018). These improvements have resulted from improved adjuvant chemotherapy and surgical advancements, especially for Stage III CRC (Bujanda *et al.,* 2010). New therapies such as bevacizumab, a monoclonal antibody directed against the vascular endothelial growth factor (VEGF) and improvements in imaging of metastases have also shown modest improvements in late stage CRC (Siegel *et al.,* 2017). The focus should now be on improving prognosis for Stage IV disease where five-year survival is just 7-8% and where an increasingly aging population requires a tumour targeted approach with less toxic side effects.

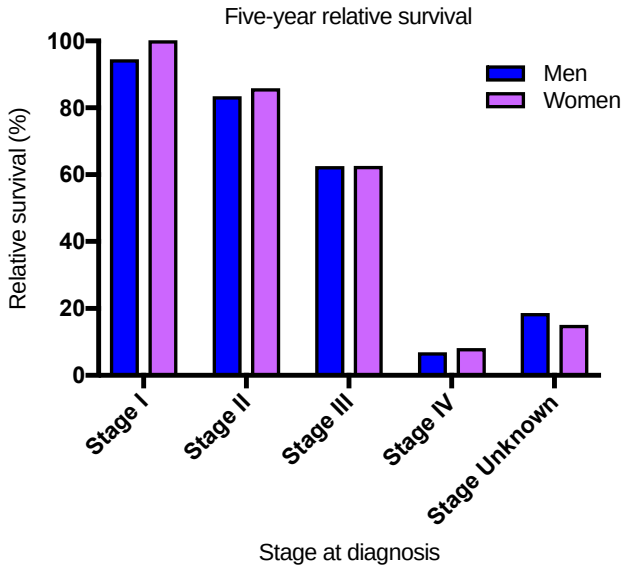

Figure 1.3 CRC five-year relative survival (%), by stage at diagnosis.

Survival is strongly dependent on the stage of disease at diagnosis. Five-year survival is 95-100% for those diagnosed with Stage I, whereas only 7-8% with Stage IV. Data from adults aged 15-99 (2002-2006). There were no significant differences between men or women at any stage (Taken from Cancer Research UK, cancerresearchuk.org, accessed March 2018).

Table 1.1 The Tumour Node Metastasis (TNM) staging system.

CRCs are Staged I-IV depending on their TNM score which is based on the level of invasiveness and lymph node involvement of the primary tumour. TNM staging is from the American Joint Committee on Cancer (AJCC, 8th Edition). Key is shown below, the higher the stage, the more advanced the disease and the worse the prognosis. Taken from (Weisenberg, 2018).

	T	N	M
Stage 0	Tis	N0	M0
Stage I	T1-T2	N0	M0
Stage IIA	T3	N0	M0
Stage IIB	T4a	N0	M0
Stage IIC	T4b	N0	M0
Stage IIIA	T1-T2	N1/N1c	M0
	T1	N2a	M0
Stage IIIB	T3-T4	N1/N1c	M0
	T2-T3	N2a	M0
	T1-T2	N2b	M0
Stage IIIC	T4a	N2a	M0
	T3-T4a	N2b	M0
	T4b	N1-N2	M0
Stage IVA	Any T	Any N	M1a
Stage IVB	Any T	Any N	M1b
Stage IVC	Any T	Any N	M1c

Primary tumour (T)	Regional lymph nodes (N)	Distant metastasis (M)
Tis: Carcinoma in situ, intramucosal carcinoma	**N0**: No regional lymph node metastasis	**M0**: No distant metastasis by imaging; no evidence of tumor in other sites or organs
T1: Tumour invades the submucosa	**N1**: Metastasis in 1-3 lymph nodes	**M1**: Distant metastasis
T2: Tumour invades the muscularia propria	**N1a**: Metastasis in 1 regional lymph node	**M1a**: Metastasis confined to 1 organ or site without peritoneal metastasis
T3: Tumour invades through the muscularis propria into the pericolorectal tissues	**N1b**: Metastasis in 2 - 3 regional lymph nodes	**M1b**: Metastasis to 2 or more sites or organs is identified without peritoneal metastasis
T4a: Tumour invades through the visceral peritoneum	**N1c**: No regional lymph nodes are positive but there are tumor deposits in the subserosa, mesentery or nonperitonealized pericolic or perirectal/mesorectal tissues	**M1c**: Metastasis to the peritoneal surface is identified alone or with other site or organ metastases
T4b: Tumour directly invades or adheres to other adjacent organs or	**N2**: Metastasis in 4 or more regional lymph nodes	
	N2a: Metastasis in 4 - 6 regional lymph nodes	
	N2b: Metastasis in 7 or more regional lymph nodes	

1.3.1 Surgical resection

Surgical resection is the mainstay of CRC treatment, where the section of diseased colon is removed along with nearby affected lymph nodes (Stage II/III) (West *et al.,* 2010). The only curative treatment option for patients with CRC liver metastases is surgical resection of isolated liver metastases, however, currently only 20% of these patients are eligible for this surgery (Jones and Poston, 2017). The majority are not amenable due to size, location or number of tumours (Jones and Poston, 2017). Surgery is followed by adjuvant chemotherapy as standard, although for Stage I where an adenoma has been removed with subsequent clean margins, additional treatment may not be necessary (Carrato, 2008).

1.3.2 Radiotherapy

External-beam radiation treatment is not uncommon for CRC and can be given pre or post-operatively, with benefits seen in decreasing yearly risk of recurrence (Colorectal Cancer Collaborative Group, 2001). It can be used to shrink tumours which are too large or difficult to resect, reduce risk of local recurrence or palliatively for those with advanced metastatic cancer or those not fit enough for surgery (Jones *et al.,* 2014). It can also be used in combination with chemotherapy (chemoradiotherapy), such as 5-FU or capecitabine, which has been shown to sensitise cancer cells to the radiation (Ojima *et al.,* 2006; Byfield, 1989).

Side effects are dependent on the radiation dose and irradiated volume but commonly include nausea, diarrhoea, delayed wound healing, bladder irritation, rectal bleeding, incontinence and impotence in men (Morris and Haboubi, 2015).

1.3.3 Monoclonal antibodies

The development of targeted therapies aimed at inhibiting specific cell signalling pathways has improved overall survival of metastatic CRC to 20-24 months, compared to current chemotherapy regimens which give 18 months (Moriarity *et al.,* 2016). Cetuximab (Erbitux®) and panitumumab (Vectibix®) are anti-EGFR antibodies approved for use in 2006 and 2007, respectively, for the treatment of metastatic CRC, but only in patients with wild-type KRAS (Markman *et al.,* 2010). Binding to EGFR inhibits angiogenesis, tumour invasiveness and metastatic spread (Toffoli *et al.,* 2007). Side effects of both include severe dermatological toxicities (Balagula *et al.,* 2011).

In 2004, the FDA approved bevacizumab (Avastin), a humanised anti-vascular endothelial growth factor-A (VEGFA) monoclonal antibody and the first anti-angiogenic therapy for the treatment of metastatic CRC in combination with chemotherapy (Folkman, 2006). Further clinical trials using antiangiogenic therapy with chemotherapy for metastatic CRC have had much success in terms of survival and quality of life for patients (Wagner *et al.,* 2009). In 2012, the FDA approved aflibercept (Zaltrap), a fully humanised monoclonal antibody which inhibits VEGF-A, -B and placental growth factor (PGF), used in combination with folinic acid, 5-FU and irinotecan (FOLFIRI) for the treatment of metastatic CRC. In 2015, the FDA approved ramucirumab (Cyramza), a fully humanised anti-VEGFR2 monoclonal antibody for the treatment of advanced gastric cancer, metastatic non-small cell lung cancer and metastatic CRC in combination with chemotherapy (Singh and Parmar, 2015). Clinical trials of monoclonal antibodies targeting tumour angiogenesis are increasing, in particular those targeting VEGFR2.

1.3.4 Chemotherapy

Chemotherapy can be given pre or post-operatively depending on the stage of disease. Adjuvant chemotherapy given post-operatively may be used to eradicate micro-metastases and reduce risk of future recurrence. Neoadjuvant chemotherapy is given pre-operatively, to eradicate micro-metastases and significantly down stage the tumour to allow for resection (Zhou *et al.,* 2013). Palliative chemotherapy may be used to prolong survival and minimise symptoms for terminal cancer patients with metastatic CRC.

Chemotherapy is associated with toxic side effects, greatly affecting the general quality of life of cancer patients. Side effects depend on the drugs administered, the dosage and number of treatments but commonly include alopecia, mouth ulcers, nausea and vomiting, diarrhoea and myelosuppression (C.S. Lee *et al.,* 2014; Sargent *et al.,* 2011). Identifying patients at risk of adverse or severe side effects from chemotherapy drugs is recommended where possible. For example, patients with the UGT1A1 gene polymorphism associated with irinotecan toxicity or the thymidylate synthase gene polymorphism associated with 5-FU or capecitabine toxicity (Takano and Sugiyama, 2017; Lecomte *et al.,* 2004).

With improved long term survival, the long term side effects of chemotherapy such as fatigue, insomnia, depression, sensory neuropathy and gastrointestinal problems are impacting on the quality of life of survivors (Denlinger and Barsevick, 2009; Beijers *et al.,* 2016).

1.3.4.1 Combination chemotherapy

High dose, single agent chemotherapy can have dose limited toxicities and combinations of lower doses have been found to be just as effective with less toxic side effects. Standard first line treatment for unresectable metastatic CRC is FOLFOX, a combination of folinic acid, fluorouracil (5-FU) and oxaliplatin or FOLFIRI a combination folinic acid, 5-FU and irinotecan. CAPOX (capecitabine and oxaliplatin) is also an effective first line treatment for metastatic CRC.

1.3.4.2 Fluorouracil (5-FU) and capecitabine (Xeloda®)

5-FU has been in medical use since 1962 and was the only drug used for CRC treatment up until the late 1990s when irinotecan and oxaliplatin were approved. Inhibition of the thymidylate synthase enzyme prevents thymidine formation needed for DNA replication and proliferation. Capecitabine is an orally administered 5-FU prodrug, which has comparable efficacy and safety profile to i.v. 5-FU. Patient preference for oral therapies due to improvements in quality of life make capecitabine a viable alternative to 5-FU (Aguado *et al.,* 2014).

Common side effects include thrombocytopenia (low platelet count), neutropenia (low neutrophil count), mucositis (inflammation and ulceration of the gastrointestinal tract), diarrhoea, hand-foot syndrome (blistering and painful hand and feet) and cardiotoxicity (damage to heart muscle) (Matsusaka and Lenz, 2015; Diasio and Harris, 1989).

1.3.4.3 Oxaliplatin (Eloxatin®)

Oxaliplatin is administered intravenously to treat CRC that has metastasised. It is a platinum based antineoplastic which forms platinum-DNA adducts, inhibiting DNA replication. It has been in medical use since 1996 but tends to be used in combination chemotherapies such as FOLFOX rather than as a single agent (Kweekel *et al.,* 2005).

Oxaliplatin-induced neuropathy (acute and chronic symptoms) can occur in a high percentage of patients receiving FOLFOX, with 89% reporting at least one symptom (Pachman *et al.,* 2015). Ototoxicity (ear damage) are less than 1% and renal toxicity less than 3% (Kweekel *et al.,* 2005).

1.3.4.4 Irinotecan (Campto®)

Irinotecan is a successful chemotherapy drug used for primary and secondary line treatment of CRC (FDA approval given in 1998)(Shimada *et al.,* 1993). It is a semi-synthetic derivative of the cytotoxic quinolone alkaloid ‘camptothecin’, extracted from the Chinese

tree *Campotheca acuminate* or 'Happy Tree' and used for centuries in Traditional Chinese Medicine as an anti-cancer agent. Its chemical isolation and structure was determined in 1966 (Wall *et al.,* 1996).

Irinotecan itself has limited activity and exerts its anticancer effect once converted to its active metabolite SN38 (7-ethyl-10-hydroxy-camptothecin)(**Figure 1.4**). Despite the success of SN38 *in vitro* as an anti-cancer agent, it is extremely hydrophobic and thus far cannot be dissolved in any pharmaceutically acceptable solvent. For these reasons it is not currently in clinical use (Bala *et al.,* 2013).

SN38 is thought to have cytotoxic effects on cells in S phase. The mechanism of action involves the inhibition of topoisomerase I, an enzyme vital to DNA replication and transcription (Robert and Rivory, 1998). The role of topoisomerase I is to bind to supercoiled DNA and induce reversible single-strand breaks, reducing torsional strain. However, when SN38 inhibits the bound enzyme, the replication fork of the unwinding DNA collides with the bound complex, inducing irreversible double-strand breaks (Hsiang *et al.,* 1989; Rivory, 2002; Hsiang *et al.,* 1985). These double strand breaks will ultimately lead to cell death in proliferating cells.

Despite irinotecan's success, dose limiting side effects include severe diarrhoea and myelosuppression (**Figure 1.4**)(Shafi and Bresalier, 2010). It has been estimated that 36% of patients experience severe toxicity from irinotecan therapy (Marsh and Hoskins, 2011). Other side effects include nausea, vomiting, alopecia and fatigue; all common toxicities exhibited by patients during high dose chemotherapy. Early onset and delayed severe diarrhoea (Stage 3-4) is the most serious side effect, the former due to cholinergic syndrome and the latter being more serious following 24-hours post irinotecan treatment. Irinotecan's enterohepatic recirculation phenomenon gives a prolonged elimination half-life of SN38, altered pharmacokinetic (PK) profiles and is responsible for the delayed, severe diarrhoea. β-glucuronidase enzymes found within the colon convert SN38 from SN38-G, increasing the risk of delayed and severe diarrhoea (Takakura *et al.,* 2012). The exact mechanisms of irinotecan induced diarrhoea are not known, but may be related to levels of β-glucuronidase enzymes increasing luminal SN38 concentrations and direct mucosal damage (Stein *et al.,* 2010).

The UGT1A1 gene polymorphism is used as a predictor of irinotecan-associated toxicity and treatment efficacy (Schulz *et al.,* 2009). The polymorphism results in high and sustained plasma concentrations of SN38 as the UGT1A1 enzyme used to metabolise SN38

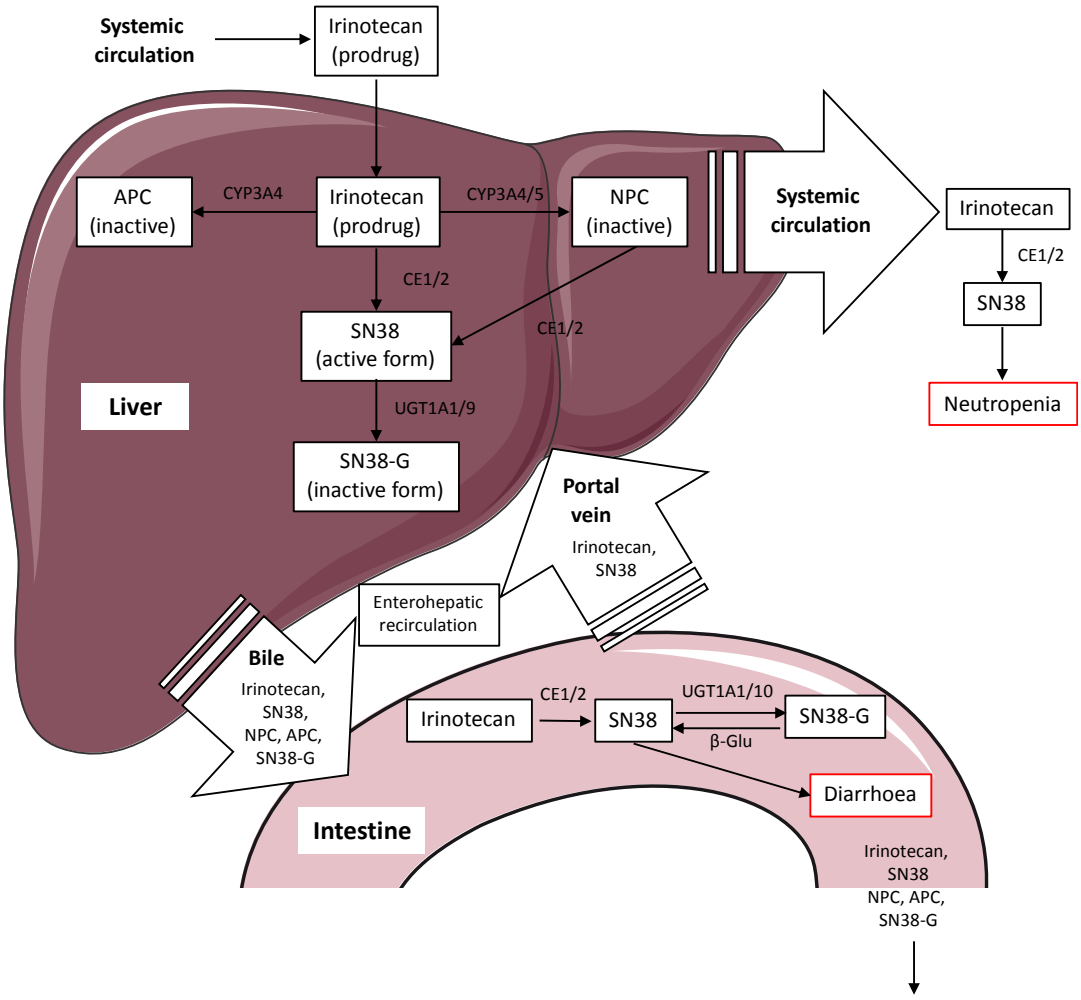

Figure 1.4 Schematic of irinotecan metabolism.

Carboxylesterase 1 and 2 (CE1/2) mediated formation of the active metabolite SN38 occurs primarily in the liver. Cytochrome 3A4 and 5 (CYP3A4/5) mediated metabolism of irinotecan forms other known inactive metabolites APC and NPC. NPC can be further hydrolysed by CE1/2 to form SN38. SN38 is subsequently glucuronated to SN38-G via UDP glucuronosyltransferase 1A-1 and -9 (UGT1A1/9) in the liver. Biliary excretion of irinotecan and metabolites into the small intestine allows further metabolism of irinotecan to SN38. Enterohepatic recirculation of irinotecan and SN38 is via the portal vein whereby it re-enters systemic circulation. SN38-G in the intestinal tract is reconverted into SN38 by bacterial β-glucuronidase (β-Glu) and re- glucuronidation via UGT1A1/10. Excretion of metabolites is primarily via the faeces. Neutropenia and diarrhoea are dose related toxicities from SN38 formation in plasma and gastrointestinal tract, respectively.

has reduced/limited activity. Identifying patients carrying the homozygous genotype UGT1A1*28 is important to minimise adverse drug reactions and severe side effects in patients receiving high doses of irinotecan (Takano and Sugiyama, 2017). However, irinotecan metabolism is complex and many other polymorphisms exist not limited to UGT1A1, which may play a role in abnormal metabolism and severe side effects. Further studies into genotype-based therapy, are necessary for chemotherapeutic efficacy and in terms of dose limiting side effects for patients receiving irinotecan treatment.

Neutropenia is defined as abnormally low levels of circulating neutrophils (type of white blood cell) and it reduces the body's ability to fight infections. Neutropenia is directly related to concentrations of SN38 in patient plasma and SN38-G/SN38 plasma ratios can be used to predict irinotecan related neutropenia (Hirose *et al.,* 2012).

1.4 The challenges in drug treatment of CRC

The challenges in drug treatment of CRC are to develop therapeutics which are more effective; to provide curative treatment and palliative care with less toxic side effects. These challenges are the same for all cancers, not limited to CRC.

1.4.1 Chemotherapy: Dose limiting side effects and drug resistance

Clinically, anti-cancer drugs are administered in cycles at or near the maximum tolerated dose with long drug-free periods to allow recovery from the toxic side effects. High doses are used in order for cytotoxic concentrations to reach the tumour. It has been suggested that the increased incidence of side effects is associated with improved survival in CRC patients (Twelves *et al.,* 2012; Stintzing *et al.,* 2011; Hofheinz *et al.,* 2012). In reality, the debilitating toxic side effects experienced by some patients compromises their quality of life and essentially limits the effectiveness of the treatment (**Section 1.3.4**).

Multidrug resistance to chemotherapy occurs in 90% of patients with late stage disease and is thought to be the main factor relating to treatment failure (Longley and Johnston, 2005). Mechanisms of drug resistance are associated with increased efflux or reduced uptake of drug into the cancer cells or an increased rate of drug metabolism, all of which reduce efficacy of the treatment (Longley and Johnston, 2005; Hammond *et al.,* 2016). Long drug-free periods between cycles of chemotherapy have also been associated with drug resistance (De Souza *et al.,* 2011). Metronomic dosing has been suggested as an alternative approach (Maiti, 2014). Metronomic dosing uses frequent, low doses with no

drug-free periods and aims to sustain a low drug concentration in the blood without the side effects associated with high doses (Bahl and Bakhshi, 2012).

Chemotherapeutics are typically limited by poor aqueous solubility, insufficient tumour accumulation or drug uptake, poor efficacy and toxicity (Liu *et al.,* 2013). It has been proposed that a tumour-targeted, drug delivery method would reduce side effects by decreasing the required dose needed for anti-cancer effect by improving concentrations delivered to the tumour tissue and overcoming drug resistance (Misra *et al.,* 2010; Bertrand *et al.,* 2014; Shi *et al.,* 2016; Huang *et al.,* 2016).

1.5 Nanomedicine and drug delivery systems

It has been estimated that over 90% of anti-cancer drugs are limited by their bioavailability and PK profiles (Iwamoto, 2013). Drug delivery vehicles at the nano or micrometre scale can be used to increase the aqueous solubility of a drug allowing it to be delivered in a controlled manner over time, avoiding high systemic concentrations associated with toxicity and overcoming drug resistance (Misra *et al.,* 2010; Bertrand *et al.,* 2014; Shi *et al.,* 2016).

The therapeutic index of a drug is the ratio between its toxic and therapeutic dose (**Figure 1.5**). Therefore, improving the therapeutic index using a drug delivery system may increase tumour drug concentrations and simultaneously reduce toxic side effects, improving patient quality of life. Optimising drug delivery to tumour tissue whilst limiting off-site toxicity is a fundamental yet difficult requirement for the effective treatment of cancers. Tumours typically consist of poorly organised vasculature, have an irregular blood flow and high interstitial pressure within the tumour tissue. It is for these reasons that systemic drug delivery and distribution throughout the tumour is inefficient and therefore limits the response of the tumour to treatment (Minchinton and Tannock, 2006).

In an effort to overcome these problems, various drug delivery vehicles have been developed to improve bioavailability, protect non-target tissues from off-site toxicity and associated side effects and improve PK profiles in terms of absorption, distribution, metabolism, excretion and toxicity (ADME-Tox) (**Figure 1.6**). In particular, allowing drugs which have demonstrated anti-cancer efficacy *in vitro*, but *in vivo* exhibited short half-lives, rapid metabolism and clearance or off-target toxicity, to be delivered.

Drug delivery vehicles such as polymer-drug conjugates, dendrimers, lipid-stabilised oil nanodroplets, micelles and liposomes (see **Section 1.5.1**) have demonstrated enormous potential over the last two decades for tumour targeted drug delivery

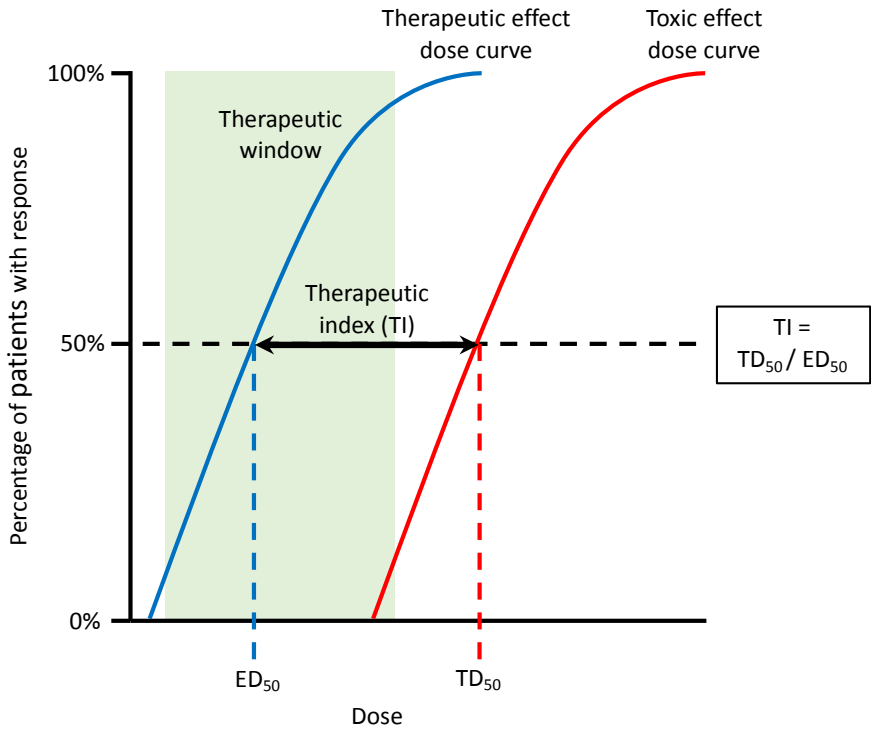

Figure 1.5 A dose-response curve demonstrating the concept of therapeutic index.

The therapeutic index (TI) is used as a measure of drug safety. It is the ratio of the toxic dose (TD) to the effective dose (ED). ED_{50} = The dose where 50% of the patients receive the desired therapeutic effect. TD_{50} = The dose where 50% of the patients experience toxic side effects. The therapeutic window (green box) is shown as the range of therapeutically effective concentrations which includes most of the therapeutic effect dose curve and less than 10% of the toxic effect dose curve.

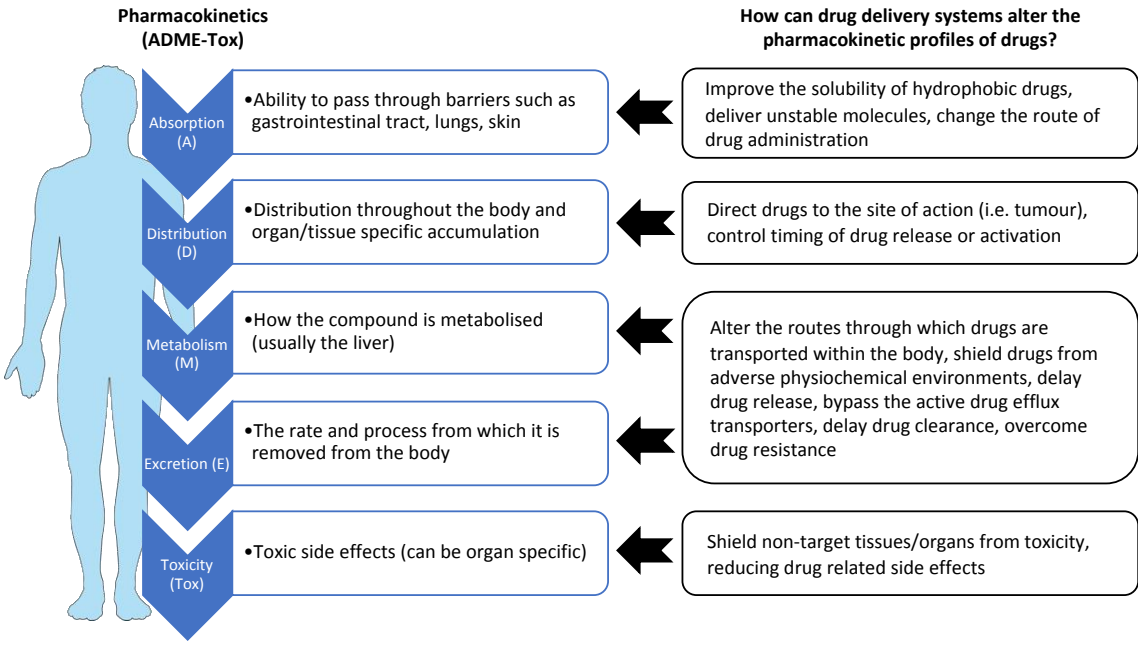

Figure 1.6 PK profiles of drugs can be altered by drug delivery systems.

PK is the study of absorption, distribution, metabolism, excretion and toxicity (ADME-Tox) of therapeutics. These parameters can be altered in different ways by the use of drug delivery systems resulting in more efficient drug delivery and/or reduced side effects (Sun *et al.,* 2017).

(Sercombe *et al.,* 2015; Allen and Cullis, 2013; Minchinton and Tannock, 2006; Shi *et al.,* 2016; Mico *et al.,* 2017). The size, shape and charge of the vehicle or nanoparticle individually effect its biodistribution (**Figure 1.7**) and are important factors to take into consideration when designing a drug delivery system (Blanco *et al.,* 2015). Also, the balance between stability and drug release of the vehicle is vital to ensuring delivery to the tumour site for pharmacological effect, with premature systemic release associated with toxicity and poor safety profiles. The incorporation of targeting moieties may increase accumulation of drug at the target site or the use of external energetic triggers or intrinsic tumour triggers can be combined to enhance tumour-specific drug delivery (Sun *et al.,* 2017).

Unfortunately, further translation into clinical practice has not transpired due to failings in biodistribution and the heterogeneity of human disease requiring more relevant animal models for pre-clinical testing and more reliable translation (Anselmo and Mitragotri, 2016). There is also a lack of PK data investigating metabolic fate as it is difficult for multicomponent systems to be compared to small molecule drugs. Furthermore, reproducible synthesis and scale-up methods need to be addressed in the pre-clinical phase of development for drug product quality requirements and regulations (Crommelin and Florence, 2013; Anselmo and Mitragotri, 2016)

1.5.1 Examples of drug delivery systems

1.5.1.1 PEG-drug conjugates

Poly(ethyleneglycol) or PEG, is a clinically established biocompatible polymer (Jevševar *et al.,* 2010). It is one of the most widely investigated water-soluble linear polymers for drug delivery and many functional PEGs are available commercially (Joralemon *et al.,* 2010). PEGylation can protect against protein enzymatic degradation and increase circulation lifetimes by evading immune capture and clearance via the macrophage-monocyte system, important for pharmaceutical applications (Yona and Gordon, 2015; Jokerst *et al.,* 2011). PEGylation of nanoparticles may inadvertently increase targeting efficiency of attached ligands as increased circulation lifetimes increases the opportunity to bind to the target, all important for therapeutic delivery systems (Jokerst *et al.,* 2011; Jevševar *et al.,* 2010).

EZN-2208 is a multiarm PEG conjugate of the topoisomerase I inhibitor SN38, which increased water solubility by 1000 fold (Sapra *et al.,* 2008). Currently Phase II clinical trials have shown prolonged half-life, good tolerability and antitumor activity with advanced

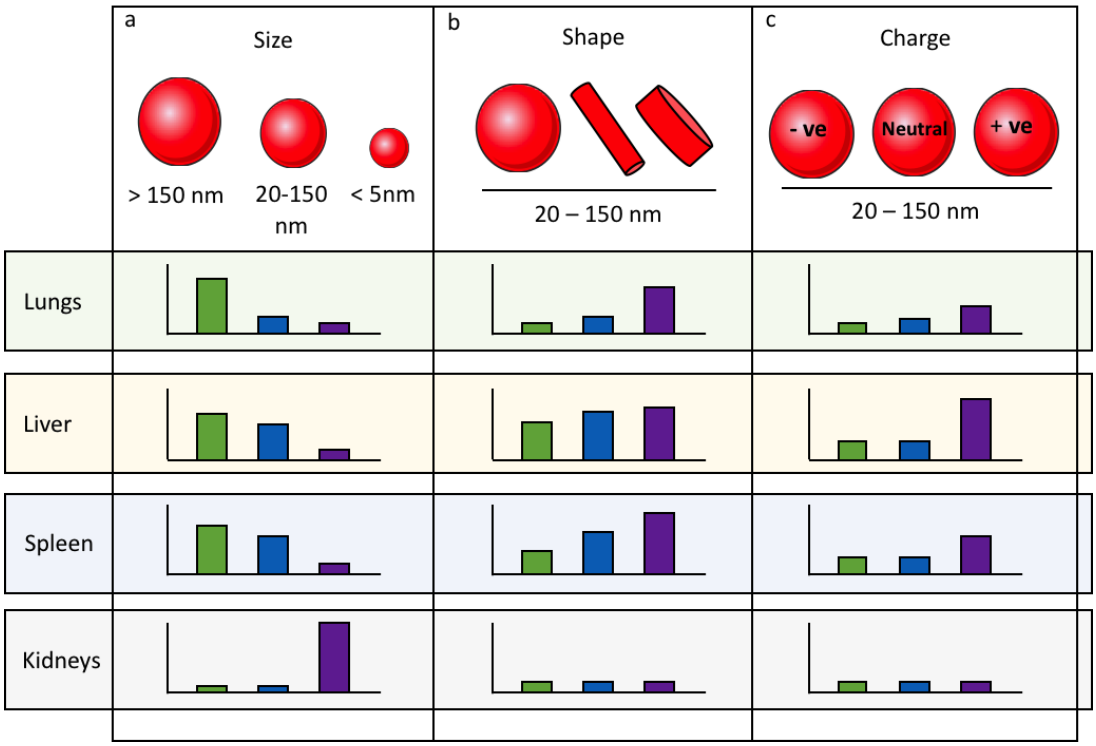

Figure 1.7 Nanoparticle size, shape and charge alter biodistribution within major organs.
The distribution of nanoparticles within the body is dependent on (a) size, (b) shape and (c) charge. Distribution profiles for lung, liver, spleen and kidney are shown. For example, nanoparticles less than 5 nm are preferentially excreted via the kidneys, whereas particles more than 150 nm preferentially accumulate in the lungs, liver and spleen (Blanco *et al.,* 2015). When designing a drug delivery system, it is important to take into account how each parameter may play a role in the biodistribution of the carrier and encapsulated drug. Taken from (Blanco *et al.,* 2015).

solid tumours (Garrett *et al.,* 2013; Norris *et al.,* 2014; Patnaik *et al.,* 2013; Kurzrock *et al.,* 2012) (**Table 1.2**). Etirinotecan pegol (NKTR-102), has a large-chain PEG core to which 4 molecules of irinotecan are attached (**Figure 1.8 a**). Phase II and III studies of etirinotecan pegol for non-small cell lung carcinoma and metastatic breast cancer respectively, have shown promising results (Aggarwal *et al.,* 2018; Twelves *et al.,* 2017).

1.5.1.2 Polymeric dendrimers

Dendrimers are nano-sized, star shaped macromolecules which consist of symmetric branching around a central core (**Figure 1.8 b**). They can be highly functionalised and drugs can be physically entrapped or conjugated to the surface, ideal for biological interactions (Abbasi *et al.,* 2014). A recent drugless design has had anticancer effect depleting bioavailable copper from breast, lung and colon xenograft tumours (Lyu and Peng, 2017). However, much focus has been on improving the biocompatibility and toxicity profiles mainly due to surface charge and modifications (Cheng *et al.,* 2011; Ziemba *et al.,* 2011; Madaan *et al.,* 2014). Dendrimer synthesis is time consuming and expensive, factors which need to be addressed before commercialisation. Recently, a Phase I study of dendrimer-docetaxel (DEP® docetaxel) has been completed in patients with advanced cancer, but the majority of studies remain in the pre-clinical phases.

1.5.1.3 Polymeric micelles

Micelles are amphiphilic molecules arranged as a spherical monolayer in aqueous solutions (**Figure 1.8 c**). They contain a hydrophobic core which is stabilised by a hydrophilic outer layer or shell, with a diameter of between 5-100 nm (J. Wang *et al.,* 2015). Micelles are easy to produce and functionalise, they can be self-assembling and hydrophobic drugs can be loaded into the hydrophobic core for drug delivery (Matsumura, 2008). They are rapidly cleared from circulation but the incorporation of PEG into the shell addresses this (Husseini and Pitt, 2008).

NK012 is micelle formulated SN38 that has shown promise against a range of cancers in pre-clinical trials alone (Koizumi *et al.,* 2006; Takahashi *et al.,* 2010) and in combination with other drugs such as cisplatin and bevacizumab (Nagano *et al.,* 2009; Nagano *et al.,* 2010; Kenmotsu *et al.,* 2010). Phase I and II clinical trials are on-going for advanced solid tumours and relapsed small cell lung cancer (Hamaguchi *et al.,* 2010; Burris *et al.,* 2016; Raefsky *et al.,* 2011) (**Table 1.2**). Micelle formulations of paclitaxel (NK105), doxorubicin (SP1049C) and cisplatin (NC-6004) are also under clinical investigation (Oerlemans *et al.,* 2010), with Phase II results pending.

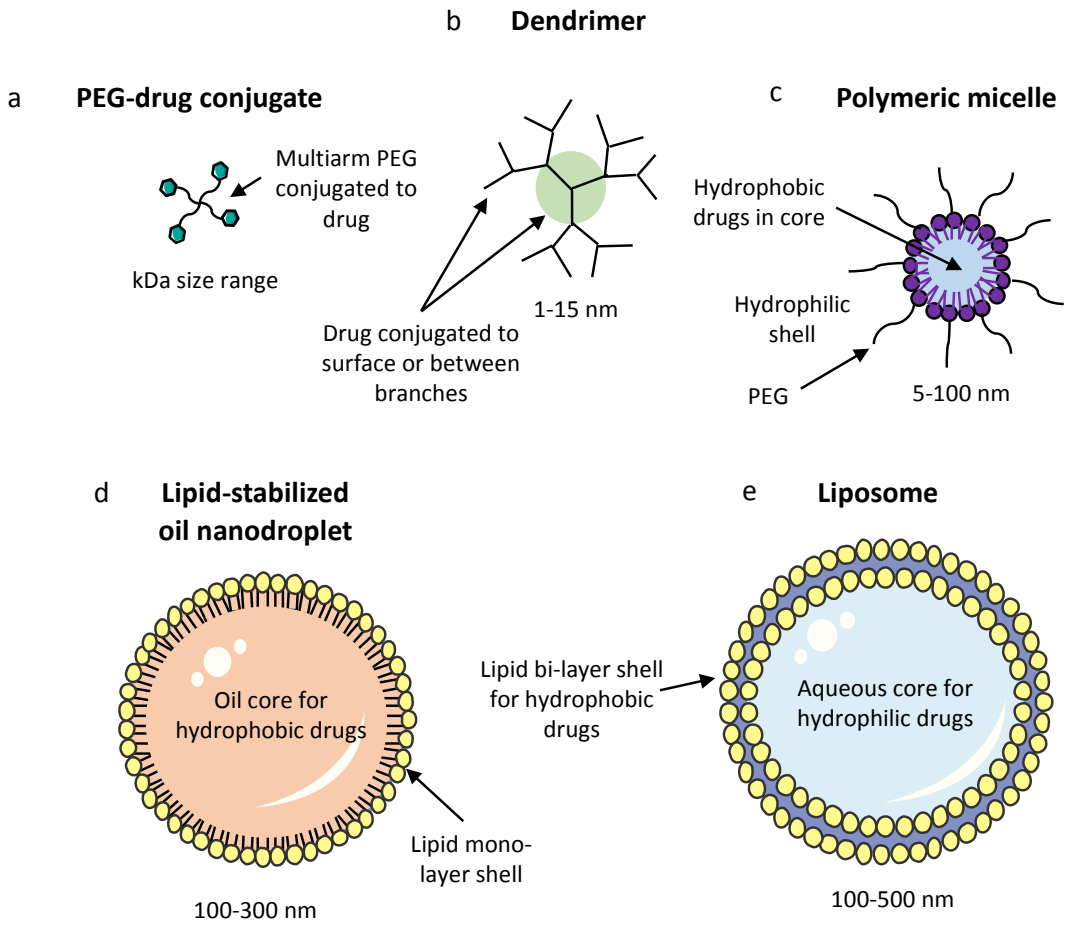

Figure 1.8 Schematic of drug-carrier systems for nanomedicine approach.

Examples of drug-carrier systems for drug delivery (a) PEG-drug conjugate, (b) dendrimer, (c) polymeric micelle, (d) lipid-stabilised oil nanodroplet and (e) liposome. All can be functionalised with ligands and PEGylated to increase *in vivo* circulation times. Not to scale.

Table 1.2 SN38 formulations which have passed into clinical trials.

Currently none have been approved for clinical use. Table compiled using ClinicalTrials.gov (database of privately and publicly funded clinical studies conducted around the world). References not available (N/A) or results not published.

Year	Formulation	Phase	Disease	Identifier / Stage	Success or failure?	References
2010	NK012 (SN38 Micelles) and Carboplatin	Phase I	Triple negative breast cancer	NCT01238952/ Completed	Ongoing	N/A
2010	NK012 (SN38 Micelles) and 5-FU/LV	Phase I	Advanced solid tumours/metastatic colorectal cancer	NCT01238939/ Completed	Further exploration warranted	N/A
2010	EZN-2208 (PEG-SN38) and in combination with bevacizumab	Phase I	Refractory solid tumours	NCT01251926/ Completed	Well tolerated but no survival advantages	(Jeong *et al.,* 2014)
2010	EZN-2208 (PEG-SN38)	Phase I /II	Paediatric patients with solid tumours	NCT01295697/ Unknown	Unknown	(Norris *et al.,* 2014)
2009	EZN-2208 (PEG-SN38)	Phase II	Metastatic breast cancer	NCT01036113/ Unknown	Further exploration warranted	(Osborne *et al.,* 2012)
2009	EZN-2208 (PEG-SN38) (With or without cetuximab)	Phase II	Patients with metastatic colorectal carcinoma	NCT00931840/ Unknown	Well tolerated but no survival advantages - discontinued	(Garrett *et al.,* 2013)
2009	NK012 (SN38 Micelles)	Phase II	Patients with relapsed small cell lung cancer	NCT00951613/ Completed	Positive efficacy and manageable toxicity	(Raefsky *et al.,* 2011)
2009	NK012 (SN38 Micelles)	Phase II	Patients with advanced, metastatic triple negative breast cancer	NCT00951054/ Completed	Unknown	N/A
2007	NK012 (SN38 Micelles)	Phase I	Patients with refractory solid tumours	NCT00542958/ Completed	Well tolerated and further exploration warranted	(Hamaguchi *et al.,* 2010; Burris *et al.,* 2008)
2007	EZN-2208 (PEG-SN38)	Phase I	Advanced solid tumours or lymphoma	NCT00520637/ Completed	Well tolerated and further exploration warranted	(Kurzrock *et al.,* 2012)
2007	EZN-2208 (PEG-SN38)	Phase I	Advanced solid tumours or lymphoma	NCT00520390/ Completed	Well tolerated and further exploration warranted	(Patnaik *et al.,* 2013)
2006	Liposomal SN38	Phase II	Metastatic colorectal cancer	NCT00311610/ Completed	Discontinued – no survival benefit	(Ocean *et al.,* 2008)

2005	Liposomal SN38	Phase II	Small cell lung cancer	NCT00104754/ Withdrawn prior to enrolment	Unknown	N/A
2002	Liposomal SN38	Phase I	Advanced cancer	NCT00046540/ Completed	Well tolerated and further exploration warranted	(Kraut *et al.,* 2004) (Kraut *et al.,* 2017)

1.5.1.4 Lipid-stabilised oil nanodroplets

Lipid-stabilised oil nanodroplets (LONDs) are nanoemulsions for hydrophobic drug delivery (**Figure 1.8 d**) and are currently in the preliminary stages of development (Mico *et al.,* 2017). They work by encapsulation of a drug within the oil core of a phospholipid coated nanodroplet and are typically between 100-300 nm, stable for up to 6 weeks and easily functionalised (Mico *et al.,* 2017). LONDs encapsulating the vascular disrupting agent combretastatin A4 (CA4) have recently been tested in combination with irinotecan in an *in vivo* model of CRC with promising tumour growth inhibition in comparison to irinotecan alone (Antonia Charalambous, personal communication).

1.5.1.5 Liposomes

Liposomes are well-established drug carriers and have been extensively studied and proven to alter drug distribution patterns, prolong circulation time, improve efficacy and reduce toxicity (Gabizon and Papahadjopoulos, 1988). They can encapsulate hydrophilic drugs in their aqueous core, and hydrophobic drugs in their lipophilic bilayer shell (Bozzuto and Molinari, 2015) (**Figure 1.8 e**). Circulation times can be increased further by the incorporation of PEG into the lipid membranes (Alexis *et al.,* 2008).

SN38 liposomes have reached Phase I and II clinical trials for advanced cancer, small cell lung cancer and metastatic CRC, demonstrating a safe toxicity profile but did not improve response rate compared to irinotecan (Kraut *et al.,* 2017; Kraut *et al.,* 2004; Ocean *et al.,* 2008)(**Table 1.2**). PEGylated liposomal doxorubicin (Doxil®) was approved by the FDA in 1995, the first nano formulation for clinical use in ovarian, breast cancer and Kaposi's sarcoma (Barenholz, 2012). PEGylated irinotecan liposomes (Onivyde™) were approved in 2015 by the FDA for combination therapy with 5-FU and folinic acid for metastatic pancreatic cancer (Passero *et al.,* 2016; Zhang, 2016). However, NICE has not given approval due to the high cost, despite improving survival by two-months (metastatic pancreatic cancer survival on average just 2-6 months) (Fleeman *et al.,* 2017).

1.5.2 Enhanced permeability and retention (EPR) effect

The EPR effect is a phenomenon whereby nanoparticles or macromolecules accumulate preferentially in solid tumours (Greish, 2012). Due to the rapid angiogenesis which occurs during tumour growth, vasculature is abnormal, leaky and impaired with fenestrations between endothelial cells allowing molecules of a certain size to extravasate tumour tissue more effectively than 'normal' tissues (Greish, 2012; Sun *et al.,* 2017). This, coupled with

poor lymphatic drainage associated with tumours, increases the retention effect further. Many drug delivery vehicles have been designed specifically in order to take advantage of this phenomenon (Sun *et al.,* 2017; Allen and Cullis, 2013; Blanco *et al.,* 2015). However, the EPR effect remains a controversial concept, with significant debate over its role in human cancers due to nanoparticles generally failing to increase efficacy and make a significant clinical impact, despite promising preclinical results using mouse models (Bae and Park, 2011; Greish, 2012).

It has been suggested that stimuli responsive systems may actively increase tumour drug delivery and may provide the required improvement in cancer outcomes with existing or future agents, given the unreliability of the EPR effect thus far.

1.5.3 Stimuli responsive systems

Stimuli responsive systems are able to control the timing and location of tumour drug release by responding to local or external stimulation. The use of external energetic triggers (US, heat, light, magnets) or intrinsic tumour triggers (pH, redox) have grown in popularity and can be combined to enhance tumour-specific drug delivery (Vladimir, 2009).

Sonodynamic therapy combines externally applied low intensity US with sonosensitisers which are co-administered with chemotherapy drugs and can be focused deep inside the body (Costley *et al.,* 2015). Acoustic cavitation, produces reactive oxygen species (ROS) and heat, and can have synergistic effects when combined with a chemotherapy agent (Wan *et al.,* 2016).

Localised hyperthermia may be used to shrink tumours or sensitise them to chemotherapy and radiotherapy. Localised microwave, radiofrequency and US can be used to raise the tumour temperature to 42°C, inducing cell death (Jha *et al.,* 2016). Hyperthermia can also reach hypoxic tumour regions where radiotherapy and chemotherapy are less effective (Oei *et al.,* 2017).

Magnetic fields can enhance tumour accumulation of superparamagnetic iron oxide nanoparticles (SPIOs) containing chemotherapeutic agents (Quinto *et al.,* 2015). In addition, when exposed to an alternating magnetic field, heat is generated for hyperthermic effects (Quinto *et al.,* 2015). Magnetic microbubbles (see **Section 1.7**) combine magnetic field with US for enhanced drug accumulation in tumours (Chertok and Langer, 2018; Owen *et al.,* 2015; Sheng *et al.,* 2017)

pH sensitive liposomes and micelles can take advantage of the slightly more acidic conditions created by hypoxia in the tumour microenvironment as a stimulus for drug release and also as an internal stimulus in acidic conditions in intracellular endosomes and lysosomes (Liu *et al.,* 2013; Lv *et al.,* 2016).

1.5.4 Theranostics

The combination of therapeutic and diagnostic agents has been termed 'theranostics' (Lammers *et al.,* 2011). Theranostics are imaging modalities combined with contrast agents or nanoparticles which have been surface functionalised and/or drug-loaded (Janib *et al.,* 2010). Their multifunctional formulations are highly relevant in the era of personalised medicine, with the ability to simultaneously image drug delivery and determine tumour response (Lammers *et al.,* 2011).

For example, the use of drug-loaded nanocarriers attached to microbubbles (see **Section 1.7**) may be termed theranostic agents, enabling imaging of the tumour via US imaging and simultaneously having therapeutic effect. The drug can then be visualised via the MBs in 'real-time' within the body and targeted for local release once it reaches the tumour vasculature. MBs are clinically approved for contrast-enhanced US imaging and therefore allow for potential theranostic applications combining imaging with targeted, triggered drug delivery (Qin, Caskey et al. 2009).

1.6 *In vivo* imaging modalities for CRC

Non-invasive imaging techniques are important tools for diagnostic medical imaging as accurate staging of CRC is essential for prognosis, treatment planning and also for assessing drug efficacy and response (Kekelidze *et al.,* 2013). Each widely used modality has its own advantages and disadvantages; magnetic resonance imaging (MRI), positron emission tomography (PET), computed tomography (CT), optical and US have been summarised in **Table 1.3**. These imaging modalities are all available for small animal research and facilitate pre-clinical investigation and clinical translation (O'Farrell *et al.,* 2013).

1.6.1 Magnetic resonance imaging (MRI)

MRI is the recommended imaging modality for initial staging of CRC (Kekelidze *et al.,* 2013). It uses a strong magnetic field and a radiofrequency source to acquire images exhibiting high special resolution and good soft tissue contrast, however acquisition time is long and the machinery is expensive (O'Farrell *et al.,* 2013; Berger, 2002).

Table 1.3 Advantages and disadvantages of imaging modalities for CRC.

Contrast agents listed for each modality or not applicable (N/A). Taken and adapted from (O'Farrell *et al.,* 2013).

Modality	Contrast agent	Advantages	Disadvantages
Molecular Resonance Imaging (MRI)	• Gadolinium-based	• High spatial resolution • Good soft tissue contrast • Provides both anatomical and functional information	• Low sensitivity • Relatively long acquisition time • Requires expensive equipment • Gadolinium cannot be used in patients with kidney disease
Positron Emission Tomography (PET)	• Radio-labelled tracers	• Provides biochemical information • High sensitivity • 3D imaging • Tumour metabolism and drug biodistribution	• Limited anatomical information • Required specialised equipment • Requires radio-nucleotide facilities • Requires expensive equipment • Ionising radiation
Computed Tomography (CT)	• Iodine • barium	• High sensitivity anatomical imaging • Provides 3D image	• Lower resolution • Limited functional information • Poor soft tissue contrast • Requires expensive equipment • Ionising radiation • Iodine and barium can have adverse effects
Optical colonoscopy	• N/A	• High resolution • Visualisation of entire colon and rectum • Biopsy and polypectomy can be performed	• Invasive • Requires full oral bowel cleansing prior to examination • May require sedation
Optical (Luminescence and fluorescence)	• Luciferase • Fluorescent proteins or dyes or Quantum dots	• Wide applicability • Simultaneously monitor several molecular events • Relatively inexpensive • Amenable to smaller research laboratories	• Pre-clinical only • Requires genetic manipulation of investigated cells • Provides limited anatomical information • Reduced sensitivity with increased imaging depth • Background due to auto-fluorescence
Ultrasound (US)	• Microbubbles	• Good resolution • Real-time • Provides both anatomical and functional information • Fast and portable technique • Relatively inexpensive • Amenable to smaller research laboratories • Microbubbles have and excellent safety profile	• Inability to image through bone or lung • More difficult in obese patients

Gadolinium-based contrast agents have been used clinically for three-decades for MRI contrast-enhanced imaging, gadolinium-ethoxybenzyl-diethylenetriamine penta-acetic acid (Gd-EOB-DTPA) is especially useful for imaging liver metastases (Lee *et al.,* 2009). Gadolinium must be used with caution in patients with renal failure as it is associated with nephrogenic system failure, and it has also been shown to accumulate in brain, with unknown consequences thus far (Pullicino and Das, 2017).

1.6.2 Positron emission tomography and computed tomography (PET-CT)

Positron emission tomography (PET) is a technique used to create 3D images and measure blood flow, oxygen and glucose metabolism. Radio-labelled tracers such as 18-fluor-labeled fluorodeoxyglucose (FDG) an analogue of glucose, are used to enhance imaging of brain, liver and tumours (Chowdhury *et al.,* 2010).

Computed tomography (CT) uses x-ray scanning to produce 3D images much more quickly than MRI, but with poor soft tissue contrast (Subhawong *et al.,* 2010). Iodine and barium are radio contrast agents, the latter being used to enhance imaging of the gastrointestinal tract and relatively non-toxic due to its insolubility reducing bioavailability (Hrvoje and Greenstaff, 2014).

PET-CT scan combines PET with CT to form a superimposed image and is more accurate than the two scans preformed individually, however exposure to harmful ionising radiation can be substantial. PET-CT is rarely used for the initial staging of CRC but is useful in detecting local recurrence and metastases and can also be used to predict tumour response to chemoradiotherapy and to plan therapy (O'Connor *et al.,* 2011).

1.6.3 Optical imaging

Optical colonoscopy (OC) is the first modality used to investigate and detect the early stages of CRC, with the ability to take biopsies and remove adenomas (Zauber *et al.,* 2012). The procedure involves an invasive endoscopic examination where a flexible fibreoptic endoscope is passed into the anus to examine the colon by high definition images of the lumen. It is stressful to the patient and requires prior fasting and a full colon cleanse using oral laxatives and carries the added risk of perforation (Liang and Richards, 2010).

Optical imaging using bioluminescence and fluorescence reveals molecular and biological processes and is used pre-clinically in small animals only (Cool, Breyne, *et al.,* 2013).

1.6.4 Ultrasound (US)

Sound frequencies of around 1 MHz and higher are used for medical imaging (Ihnatsenka and Boezaart, 2010). The human audible range is much lower, between 20 and 20,000 Hertz (Smagowska and Pawlaczyk-Łuszczyńska, 2013). It is for this reason that the medical use of such high frequencies is termed 'ultra' sound. The maximum depth of imaging depends on the frequency of US used, lower frequencies can penetrate deeper but with a loss of image resolution. A clinical frequency of 10 MHz, can image to a depth of approximately 4 cm or more depending on the tissue (Ihnatsenka and Boezaart, 2010). US has many uses, diagnostically and with the use of microbubbles (MBs) for contrast-enhanced imaging, therapeutically using high intensity focused US or for triggered drug delivery (Wood and Sehgal, 2015; Seo and Kim, 2017).

Endorectal ultrasound (ERUS) is the most accurate modality for the staging of Stage I CRC tumours, although MRI is more accurate for later stages (Kekelidze *et al.,* 2013). Intraoperative US is used for detecting additional liver lesions not observed with preoperative imaging techniques and also for imaging tumours which are located close to major blood vessels during resection (Sahani *et al.,* 2004). Doppler US is useful for determining the presence of liver metastases. It measures hepatic arterial blood flow relative to portal venous flow and this ratio has been shown to increase in those with tumours in the liver (Leen *et al.,* 1995).

MBs have been in use clinically for three decades as contrast agents for enhanced US imaging (Stride and Saffari, 2003). MBs are micron sized, between 1-8 μm in diameter, consisting of a shell stabilised gas core (Wilson and Burns, 2010). They are injected directly into the vasculature, greatly enhancing echogenicity (ability to reflect US waves). This phenomenon was discovered incidentally when saline containing air-bubbles was intravenously injected and noted as a 'cloud of echoes' when imaging the aortic root (Gramiak and Shah, 1968). The commercial development of first-generation MBs as contrast agents began in the 1980's, with large air-filled, short lived MBs. It was not until the use of high-molecular weight gases that second-generation MBs were used to enhance grey scale and Doppler imaging (Cosgrove, 1996).

Commercially available MBs differ in their shell and gas core composition. The shell material is important for MB elasticity in response to US and also influences *in vivo* circulation times (Ignee *et al.,* 2016). Potential shell materials are phospholipids lipids and lipid/surfactants ('soft-shelled'), or albumin, galactose and polymers ('hard

shelled')(Paefgen *et al.,* 2015). The gas core influences the MBs acoustic properties and their solubility (Ignee *et al.,* 2016). Often an inert, high molecular weight gases such as perfluorocarbons and sulphur hexafluoride with low diffusion coefficients and low solubility in water are used to increase *in vivo* lifetimes (Lindner, 2004). **Table 1.4** lists the different compositions of clinical approved MBs for use as contrast agents.

The clinical use of contrast-enhanced imaging has increased over the last decade, assessing focal lesions of the liver (Ferraioli and Meloni, 2018; Jang *et al.,* 2009), lesions and cysts of the kidney (Tenant and Gutteridge, 2016), as well as the detection and assessment of atherosclerosis (Schinkel *et al.,* 2016) and tumour perfusion (Saini and Hoyt, 2014). MBs are blood pool agents limited to the vasculature and show a similar pattern of uptake to that of CT or MRI vascular contrast agents without contrast leakage into tumour interstitium as with CT or MRI (Jang *et al.,* 2009). MBs are metabolised after a few minutes and the gas within the core is exhaled via the lungs and the phospholipid shell is metabolised via the endogenous phospholipid metabolic pathway in the liver (Correas *et al.,* 2001). MBs can therefore be used in patients with renal failure where contrast-enhanced MRI or CT would not be applicable (Piscaglia *et al.,* 2006). Due to the high safety profile and success of MBs in the clinical environment, their potential use as drug delivery vehicles has been popularised.

1.7 Therapeutic drug delivery using MBs

MBs have recently been harnessed as vehicles for drug delivery (Ting *et al.,* 2012; Fan *et al.,* 2013; Graham *et al.,* 2014) as they combine US-triggered release with enhanced intracellular drug uptake presumably via sonoporation effects (Taylor *et al.,* 2007; O'Neill *et al.,* 2009; Lin *et al.,* 2010; Arvanitis *et al.,* 2011; Ting *et al.,* 2012).

MBs engineered as drug delivery vehicles have demonstrated potential therapeutic capabilities and offer many advantages over standard drug therapy (Sennoga *et al.,* 2017; Cochran *et al.,* 2011; Cavalieri *et al.,* 2010). Delivering chemotherapy drugs to tumours in this way has the potential to improve the therapeutic index of a drug; increasing the delivered dose without increasing the harmful side effects associated with it. MBs can be co-administered with drug or they can be engineered to carry a payload of drug, in a variety of different ways (**Figure 1.9**). Drugs can be dissolved in an oil layer inside the shell termed 'lipospheres' (Unger, McCreery, Sweitzer, Robert, *et al.,* 1998), incorporated into the MB shell itself (Unger, McCreery, Sweitzer, Vielhauer, *et al.,* 1998) or attached electrostatically to the outside in the case of gene therapy (Lentacker *et al.,* 2006). MBs

Table 1.4 Clinically approved MBs for contrast enhanced US imaging.

A list of examples and compositions of commercially available MB contrast agents. Taken and adapted from (Lindner, 2004; Paefgen *et al.,* 2015; Ignee *et al.,* 2016).

Name	Manufacturer	Shell	Gas	Mean size (μm)
Albunex	MolecularBiosystems	Albumin	Air	4.3
Optison	Mallinckrodt/ Amersham	Albumin	Octafluoropropane	2 - 4.5
Definity/ Luminity	Bristol-Myers Squibb Medical Imaging	Lipid/surfactant	Octafluoropropane	1.1 - 3.3
Imagent	Imcor	Lipid/surfactant	N_2/perfluorohexane vapor	6
Sonovue/ Lumason	Bracco Diagnostics	Lipid	Sulphur hexafluoride	2 - 3
Sonazoid	Nycomed/Amersham	Lipid	Perfluorobutane	3

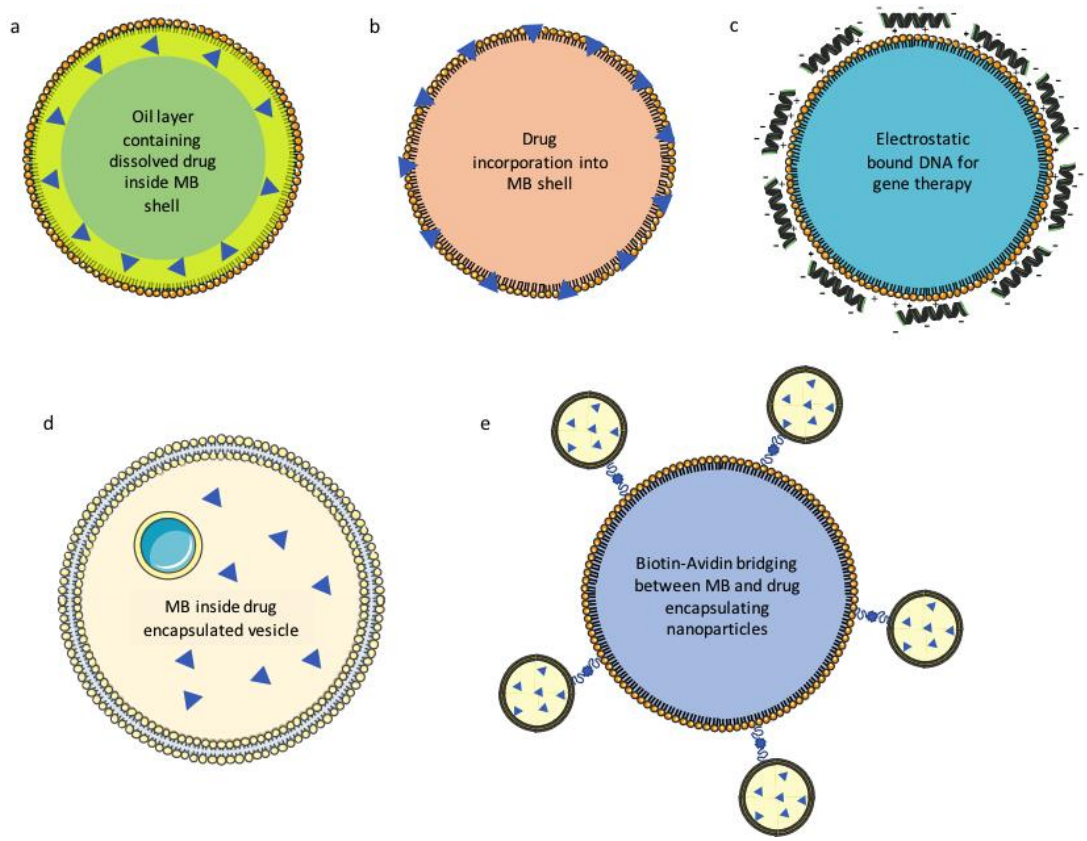

Figure 1.9 Schematic representation of MB architectures in respect to drug loading.

(a) Drugs can be dissolved in an oil layer inside the MB shell (Unger, McCreery, Sweitzer, Robert, *et al.,* 1998), or (b) incorporated into the MB shell itself (Unger, McCreery, Sweitzer, Vielhauer, *et al.,* 1998). (c) DNA can be electrostatically bound to the outside of the MB, in the case of gene therapy (Lentacker *et al.,* 2006). (d) MBs can also be encapsulated within a drug-loaded liposome (Ibsen *et al.,* 2011), or (e) drug encapsulated nanoparticles can be attached via biotin-avidin bridging (Kheirolomoom *et al.,* 2007). Not to scale.

can be encapsulated within a drug-loaded liposome coined SHockwavE-Ruptured nanoPayload cArriers (SHERPAs)(Ibsen *et al.,* 2011). Drugencapsulating nanoparticles such as liposomes, micelles or LONDs can also be attached via avidin- biotin linkages (Kheirolomoom *et al.,* 2007; Mico *et al.,* 2017).

Co-administration or co-delivery of MBs and drug has had proven success (Escoffre *et al.,* 2013a; Yu *et al.,* 2016; Kotopoulis *et al.,* 2013) however it relies on drug being in close proximity to MBs when the US in applied, which requires high circulating doses and therefore the toxic side effects which are associated.

Another option is to attach drug encapsulated nanocarriers to the outer shell of MBs for increased loading capacity. Due to the drug encapsulation, there is also scope for delivering hydrophobic drugs or those that have previously proven too toxic for normal delivery methods. Due to the proven efficacy of SN38 as an anti-cancer agent, but with failings due to toxicity and insolubility issues, it has been proposed as a promising compound for encapsulation and delivery via MBs (Lei *et al.,* 2004). It has been reasoned that using more potent drugs such as SN38, limits the dose needed for therapeutic efficacy (Li *et al.,* 2012).

Evidence of increased drug delivery using liposomes attached to MBs has been demonstrated by increasing locally released drug (De Cock *et al.,* 2016; Cool, Geers, *et al.,* 2013; Burke *et al.,* 2011). Liposomes themselves are not acoustically active (lack a gaseous core), but when combined with the mechanical properties of MBs, drug delivery is increased. It is thought that microstreaming, shock waves and microjetting play a role in destroying the membranes of the carriers resulting in improved local release of the drug and simultaneously drug uptake (Cool, Geers, *et al.,* 2013). Due to the close proximity of the drug to the MB during US application, it is more likely to benefit from the biophysical effects of cavitation. The specificity of the technique allows for a much-reduced dose of drug, and in turn reducing harmful side effects.

US and MBs work together in two ways, delivering and destroying drug-loaded MBs in the target area, and aiding drug uptake at a cellular level. Its high safety profile and ability to non-invasively focus energy deep inside the body makes it ideal for combining with drug-loaded MBs for an US mediated delivery modality (Pitt *et al.,* 2004). Drug-loaded MBs are injected intravenously and arrive at the tumour site, US is focused on the tumour region and the MB are destroyed as they pass through the US beam. Destruction at the target site locally delivers a payload of chemotherapy drug directly to the tumour. The exact way in which MB and US enhance drug delivery at a cellular level is not entirely understood, but it

has been suggested there are various biophysical mechanisms that play a role (Fan *et al.,* 2014). MBs and US-driven mechanisms of intracellular delivery

Sonoporation caused by shockwaves and microjetting has been proposed as the main mechanisms of intracellular drug delivery using MBs (**Figure 1.10**). Scanning electron microscope images have shown micron-sized perforations within the cell membranes of endothelial cells adjacent to MBs after a short exposure to US. Using fluorescent microscopy, these perforations appeared to 'reseal' themselves very quickly and it was suggested that calcium ion-independent and calcium ion-triggered mechanisms were involved (Tachibana *et al.,* 1999; Kudo *et al.,* 2009). Also, it has been shown that supposed cell-impermeable molecules enter cells when combined with US. A study by (Meijering *et al.,* 2009), found that in addition to membrane perforations, US also enhanced endocytosis mechanisms, which may be responsible for the increased uptake of macromolecules. However, there is conflicting evidence of whether endocytosis plays a role in the uptake of drug molecules and this may be down to the large variation of US frequencies, duration of exposure or number of pulses used in these experiments. One group used varying acoustic pressures and investigated the uptake of different sized molecules to determine which uptake mechanism was playing a role (De Cock *et al.,* 2015). They found that lower acoustic pressures shifted uptake to endocytosis routes whereas with higher acoustic pressures the uptake was mainly via the formation of pores (De Cock *et al.,* 2015). This discovery highlights the importance of selecting the correct acoustic pressure to optimise drug delivery, and also the need for more MB behaviour-based drug delivery experiments.

MBs in combination with US for delivery of genes or drugs to target tissues has been previously demonstrated (Mayer *et al.,* 2008; Cool, Geers, *et al.,* 2013; P. Huang *et al.,* 2013). When MBs are subjected to US frequencies a phenomenon occurs, known as cavitation. Cavitation is divided into two types, stable (non-inertial) and inertial (**Figure 1.10**). Stable cavitation occurs when a bubble in fluid is forced to oscillate (compress and expand), whereas inertial cavitation occurs when a bubble rapidly expands and collapses producing a shockwave (Leighton, 2007). When these effects take place in the vasculature of a targeted tissue, they enhance the efficiency of the drug by increasing uptake at a cellular level (Chen and Hwang, 2013).

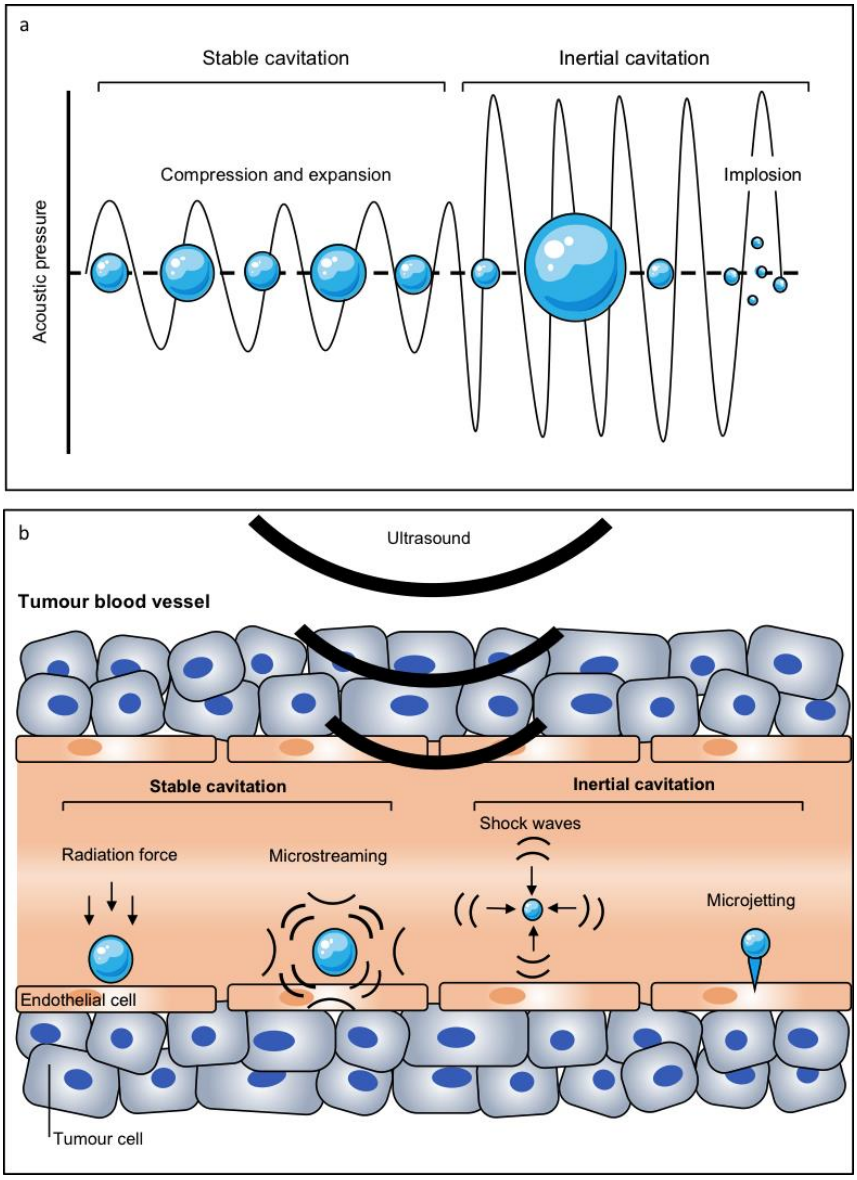

Figure 1.10 The behaviour of MBs with varying acoustic pressure and resulting mechanical effects. (a) A schematic demonstrating the behaviour of MBs with varying acoustic pressures. Stable cavitation involves the stable compression and expansion of the MBs. Inertial cavitation results in an implosion causing destruction and/or fragmentation of the MB. (b) A schematic demonstrating the mechanical effects of US on MBs when in contact with endothelial cells lining the tumour vasculature. Stable cavitation of MBs can induce radiation forces, pushing MBs towards vessel walls and bring them into closer contact with endothelial cells. MB expansion and contraction causes microstreaming of the surrounding fluid which may cause pores to form in cell membranes. Inertial cavitation can cause shock waves and microjetting. Shockwaves are caused by MB collapse, which can in turn disrupt the cell membrane. If a MB collapses close to a cell membrane, the implosion is asymmetrical, and a jet of fluid is forced towards the surface of the cell and pores are created. These mechanical effects can be taken advantage of in order to enhance drug delivery at a cellular level.

1.7.1. Active targeting of MBs

MBs are solely vascular blood pool agents and therefore luminal endothelial cell receptors associated with tumour angiogenesis may be most suitable for targeting tumours. Molecular targets of angiogenesis such as vascular endothelial growth factor receptor 2 (VEGFR2), integrins ($\alpha v\beta 3$), endoglin, P-selectin and Neuropilin-1, have been previously demonstrated for a range of solid tumours using target MBs and US (**Table 1.5**).

VEGFR2 is upregulated in tumour blood vessels and thought to play a major role in tumour angiogenesis. In the last decade, pre-clinical studies have shown VEGFR2 to be a valid molecular marker for MBs in xenograft models of CRC (Ellis *et al.,* 2000; Bruns *et al.,* 2000; Peyman *et al.,* 2012). The anti-angiogenic drug ramucirumab which targets VEGFR2 has recently been approved for the treatment of metastatic CRC in combination with FOLFIRI (RAISE trial) which increased overall survival and progression free survival compared to FOLFIRI alone (Tabernero *et al.,* 2015). VEGFR2 MBs which have been dual (VEGFR2, $\alpha v\beta 3$) and triple targeted (VEGFR2, $\alpha v\beta 3$, P-selectin) have also been described to enhance MB accumulation in models of cancer and a similar strategy might prove useful in CRC (Warram *et al.,* 2011; Willmann, Lutz, *et al.,* 2008).

Although not essential for MB drug delivery, ligands can be attached and are used to enhance MB accumulation at specific molecular sites, i.e. tumours (Fan *et al.,* 2013; Hernot and Klibanov, 2008). The adhesion of MBs to the microvessel wall keeps the MBs in position long enough for US triggered destruction and improves the probability that the drug is taken up by the cancer cells (Hernot and Klibanov, 2008). Targeted MB binding to endothelial cell receptors occurs under flow conditions, with very little time for receptor-ligand bond formation. These bonds then have to resist the shear forces of flowing blood long enough to allow sufficient accumulation. Careful selection of the target and the binding affinity and specificity of the ligand is vital under these conditions, and the MB architecture must be optimised accordingly.

1.7.2. MB production methods

Commercially available MB contrast agents approved for use clinical use in the UK are Optison® and Sonovue® (Ignee *et al.,* 2016). These come in powder form and are reconstituted with saline and shaken by hand for 20-seconds prior to i.v. administration. Conventionally, MBs are produced by either sonication or mechanical agitation of the MB lipids and can be functionalised easily for pre-clinical investigations (Qin *et al.,* 2009). However, these methods produce polydisperse MBs with bubbles as large as 10 mm in

Table 1.5 Pre-clinical molecular targets of angiogenesis using MBs.

Taken and adapted from (Wang *et al.,* 2018)

Tumour	Animal model	Molecular target	References
Colorectal	Mouse	VEGFR2	(Pysz *et al.,* 2012; Anderson *et al.,* 2010; H. Wang *et al.,* 2015; Pysz *et al.,* 2010)
Breast	Mouse	$\alpha_v\beta_3$	(Anderson *et al.,* 2011)
	Mouse	VEGFR2	(Lee *et al.,* 2008; Bachawal *et al.,* 2013; Bzyl *et al.,* 2011)
	Mouse	VEGFR2, $\alpha_v\beta_3$, P-selectin	(Warram *et al.,* 2011)
	Mouse	Neuropilin-1	(Zhang *et al.,* 2015)
	Rat	VEGFR2	(Pochon *et al.,* 2010)
Pancreatic	Mouse	VEGFR2	(Pysz *et al.,* 2015)
	Mouse	VEGFR2, VEGF, CD105	(Korpanty *et al.,* 2007)
	Mouse	Thy1/CD90	(Foygel *et al.*, 2013)
	Rat	VEGFR2	(Tardy *et al.,* 2010; Frinking *et al.,* 2012)
Glioma	Rat	$\alpha_v\beta_3$	(Ellegala *et al.,* 2003)
Ovarian	Hen	$\alpha_v\beta_3$	(Barua *et al.,* 2014)
	Mouse	$\alpha_v\beta_3$	(Willmann *et al.,* 2010)
Fibrosarcoma	Mouse	$\alpha_v\beta_3$	(Jun *et al.,* 2010)
Other	Mouse	VEGFR2	(Willmann, Paulmurugan, *et al.,* 2008; Wei *et al.,* 2014)
	Mouse	VEGFR2, $\alpha_v\beta_3$	(Willmann, Lutz, *et al.,* 2008)
	Mouse	VEGFR2, $\alpha_v\beta_3$, endoglin	(Deshpande *et al.,* 2011; Leguerney *et al.,* 2015)
	Mouse	VEGFR2, $\alpha_v\beta_3$, P-selectin	(Sorace *et al.,* 2012)
	Mouse	$\alpha_v\beta_3$	(Leong-Poi *et al.,* 2003)

diameter which are inappropriate for *in vivo* use (Peyman *et al.,* 2012). For that reason, a microfluidic platform has been created for the single-step, rapid production of polydisperse MBs (**Figure 1.11**) and demonstrated for reliable, liposome loaded, functionalised MBs of a known size (mean diameter 1-2 μm) and concentration (1 x 10^9 MBs/ml) (Peyman *et al.,* 2012). On-chip production of nanobubbles and lipid stabilised oil-shelled MBs are also possible (Peyman *et al.,* 2016; Churchman *et al.,* 2018). Monodispersed MB populations are also produced in this way however, currently concentrations produced are too low to be used clinically (Peyman *et al.,* 2012).

1.7.3. Clinical trials of functionalised MBs for imaging and drug delivery

The first Phase I clinical trial using functionalised BR55 MBs which contained a VEGFR2 lipopeptide in the MB shell for contrast imaging of VEGFR2 in ovarian and breast lesions had the ability to differentiate between benign and malignant lesions (Willmann *et al.,* 2017).

The first clinical trial using MBs to enhance drug delivery has been undertaken in patients with inoperable pancreatic cancer, using MBs co-delivered with gemcitabine and showed significantly improved survival, with 4 out of 10 patients removed from the study to undergo surgical resection (Dimcevski *et al.,* 2016).

A dose escalation clinical trial investigating blood brain barrier (BBB) opening with MBs and US, has been demonstrated safe with carboplatin in patients with recurrent glioblastoma and is currently ongoing (Carpentier *et al.,* 2016). More preclinical trials using functionalised MB are necessary to demonstrate feasibility, safety and efficacy using targeting ligand and/or cytotoxic drugs.

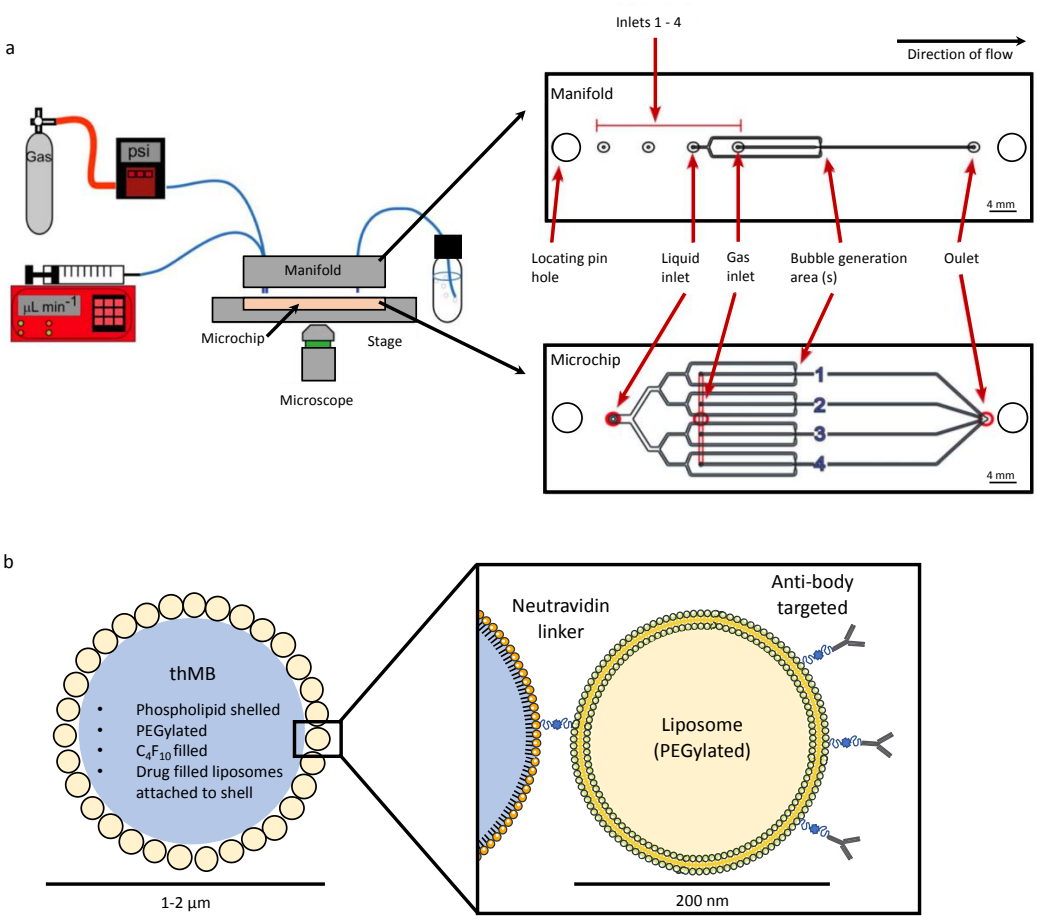

Figure 1.11 Single step formation of polydispersed microbubbles (MBs) using a microfluidic chip. (a) Schematic of the set up showing the gas flow controller, syringe pump and stage. The manifold and microchip are shown in more detail, producing drug-loaded MBs in a single step and collected in a glass vial for immediate use (Peyman *et al.,* 2012). (b) Schematic of the therapeutic microbubbles (thMBs) produced by this method. Gas core is C_4F_{10} pulsed with C_6F_{14} for increased stability (Abou-Saleh *et al.,* 2016). Drug-loaded liposomes are attached to the phospholipid shell via neutravidin-biotin linkages and targeted using an anti-VEGFR2 antibody. Not to scale.

1.8 Pre-clinical, murine models of CRC

Mouse models of human diseases are an essential part of the translational pipeline. Pre-clinical studies using mouse models can provide both mechanistic data on drug targets as well as drug targeting and efficacy *in vivo*. However, no single model of CRC is capable of reproducing all stages of human CRC. The use of several models or the generation of complex genetically engineered mouse models (GEMM) are necessary to reproduce disease progression in order for accurate and reliable pre-clinical testing of novel therapeutics.

Models recapitulating CRC are either genetically modified or transplantable (**Figure 1.12**). GEMM generally take a long time to establish, whereas transplantable models are much quicker but involve implantation of cancer cells or tissues (Young *et al.,* 2013). The strengths and weaknesses of each will be discussed (**Table 1.6**).

Models of late stage disease are lacking and are an urgent requirement, as metastatic disease is the leading cause of death in CRC cancer patients. *In vivo* models are necessary for drug discovery and screening novel therapies in this area (Oh *et al.,* 2017). Models that are rapid, non-invasive, reproducible for large cohorts and can be monitored quickly, easily and cheaply for quicker more relevant translation of such research into the clinic.

1.8.1. Genetically engineered mouse models (GEMMs) of CRC

The first model of the hereditary CRC syndrome familial adenomatous polyposis (FAP) was developed in 1990 and referred to as the APC $^{min/+}$ (multiple intestinal neoplasia) mouse model (Moser *et al.,* 1990). These mice form hundreds of tumours in the small and large intestine which do not form metastases and have a have an average life span of just 119 days. They are useful for studying genetic events driving early disease. Variations of this model in terms of the location of the APC mutation and genotype/phenotype correlation have been developed (Fodde *et al.,* 1994; Oshima *et al.,* 1995; Colnot *et al.,* 2004).

A GEMM which combines activation of KRAS with APC inactivation ($KRAS^{V12G}/APC^{+/1638N}$) developed an average of 30 tumours per mouse and after 6-months 20% of mice developed liver micrometastases (Janssen *et al.,* 2006). Cre-lox technology can allow control of location and timing of APC deletions giving rise to tissue-specific mutations (El Marjou *et al.,* 2004).

$Msh2^{-/-}$ (MutS homologue 2) is a paralog for HNPCC or Lynch syndrome (Edelmann *et al.,* 1999). These mice have a short life expectancy of between 6-12 months, with

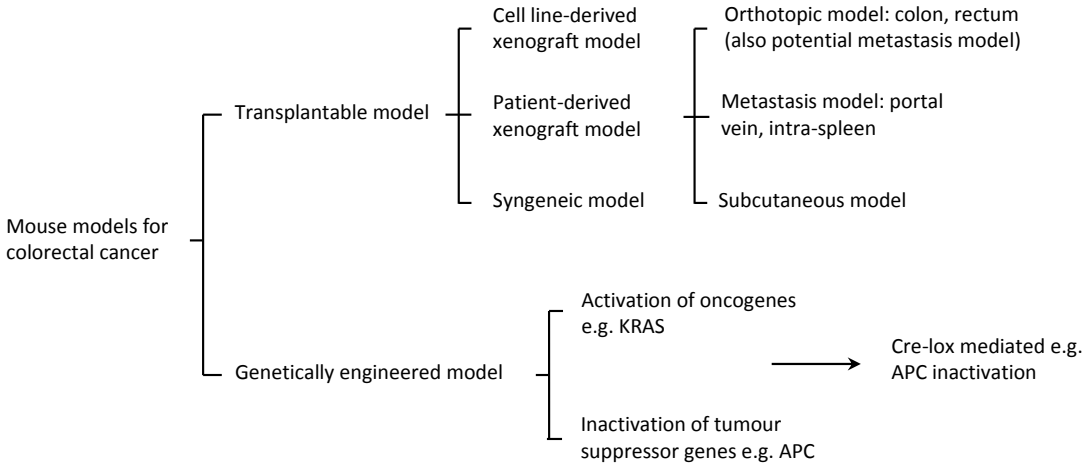

Figure 1.12 Murine models of CRC.

Mouse models can be divided into transplantable or genetically engineered models. In general, transplantable models are much quicker to establish, cheaper and accessible to a majority of research laboratories. Taken and adapted from (Oh *et al.,* 2017).

Table 1.6 Murine models of CRC: strengths and weaknesses.

Strengths and weaknesses of each murine model of CRC are given. Taken and adapted from (Mcintyre *et al.,* 2015)

Colorectal cancer model	Strengths	Weaknesses
Genetically modified	• More accurately representation of tumour development than transplantable models • Provide useful information about the effects of specific genetic mutations during carcinogenesis • Host has intact immune system • No species mismatch between tumour and stromal cells	• Expensive (labour intensive and time consuming) • Rarely metastasise
Subcutaneous xenograft: human cancer cells injected into immune deficient mouse	• Low cost • Rapid tumour growth • Well characterised cell lines • Easy to genetically manipulate prior to transplantation • Model accessible to majority of research labs • Rapid and easy subcutaneous injection to implant	• Not representative of advanced disease • Have undergone significant clonal selection • Microenvironment differences • Species mismatch in tumour (human) and stromal (mouse) cell may limit cross-talk • Immune deficient host • Rarely metastasise
Orthotopic xenografts of CRC cell lines: injection of cells into intestinal serosa of immune deficient mouse	• As above • More natural microenvironment for CRC cells • Some metastasise to liver	• As above (except for 'rarely metastasise') • May require surgery to implant cells
Patient-derived xenografts: Suturing of 1-2 mm fragments of CRC to intestine of immune deficient mouse	• Reproducible liver metastasis • Avoid selection of dominant clones during long-term cell culture • Temporary preservation of species-specific tumour-stromal cross talk • More natural microenvironment for CRC cells	• Not readily scalable • Host (mouse) stromal cells replace human stromal cells within a few weeks (species mismatch) • Immune deficient host • Limited availability of surgical specimens • Expensive (labour intensive and time consuming)
Syngraft/Isograft: Suturing 1-2 mm mouse tumour fragments or mouse tumour cells to genetically inbred, immune competent mouse	• No species mismatch between tumour and stromal cells • Host has intact immune system that enables testing of immunomodulatory anti-cancer agents	• Expensive (labour intensive and time consuming surgery for tumour fragment transplantation) • The model is not human

gastrointestinal adenocarcinomas forming in 80% of mice that survive 8-10 months (Reitmair *et al.,* 1996).

CRC development and metastasis is the result of complex genetic alterations over time and currently GEMM are limited by only having a few mutant alleles and mostly for studying early stages of disease as opposed to metastasis (Johnson and Fleet, 2013; Clark and Starr, 2016).

1.8.2. Transplantable mouse models of CRC

Transplantable models involve the implantation of cultured cancer cells into a host, these can be syngeneic (mouse cell lines) or xenograft (human cell lines) models. Syngeneic uses cells from the same species in which they originated and can therefore be grown in immune competent mice. There is no mismatch between tumour and stromal cells and an intact immune system enables testing of immunomodulatory anti-cancer agents. Xenograft models use human derived cell lines or patient-derived cells and are injected into immune deficient hosts, with mismatch between tumour and stromal cells. Surgery may be required to implant cells or tumour tissue fragments when creating an orthotopic model. In general, transplant models are less expensive and quicker to develop than genetically modified versions, and they can use well characterised cell lines which are easy to genetically manipulate prior to transplantation (Mcintyre *et al.,* 2015).

1.8.2.1 Subcutaneous models

The most common transplantable method is via subcutaneous implantation, resulting in palpable tumours where size can be monitored easily by calliper measurements (Tomayko and Reynolds, 1989). It has been found that tumour volumes measured using pre-clinical high frequency US (HFUS) are more accurate and require up to 30% less mice for statistically significant studies compared with calliper measurements (Ingram *et al.,* 2013; Ayers *et al.,* 2010).

Subcutaneous xenograft models have been used in some respect for almost every anti-cancer therapy used today, and have shown some predictive value in terms of clinical translatability (Johnson *et al.,* 2001; Voskoglou-Nomikos *et al.,* 2003). However, only 5% of compounds that have shown promise will eventually be approved for clinical use (Sharpless and DePinho, 2006). Subcutaneous and orthotopic models have shown differences in drug sensitivities suggesting that the tumour microenvironment must play a role (Zhao *et al.,* 2017; Manzotti *et al.,* 1993). Tumours grown subcutaneously do not accurately represent the clinical tumour microenvironment which contains fibroblasts,

immune cells and an extracellular matrix which have all been shown to be influencing factors for tumour establishment and growth (Wang *et al.,* 2017). Therefore, orthotopic models which mimic the clinical tumour environment may allow for more reliable and quicker translation of therapeutics to the clinic.

1.8.2.2 Orthotopic models

Transplantable orthotopic CRC liver metastases models are typically established either by serosal injection of cells or implantation of tissue to the colon, intrasplenic injection or i.v. injection of cells into the portal vein (W.Y. Lee *et al.,* 2014; Oh *et al.,* 2017).

Orthotopic models of primary CRC involve the surgical implantation of CRC cells into the serosa of the intestine, and over time liver metastases can form. When injecting cells into the colon, the metastatic potential is dependent on the cell line used and resulting metastasis is unpredictable, unreliable and time dependent. These models accurately represent metastasis from primary site to the liver but are rarely used as they are technically challenging and time-consuming procedures. Refinements to this technique have involved the microinjection of cells between the mucosa and the muscularis externa layers of the caecal wall (Céspedes *et al.,* 2007) and a non-surgical trans-anal rectal injection (Donigan *et al.,* 2009).

Intrasplenic injection of cancer cells reliably and rapidly produces liver metastases (Lavilla-Alonso *et al.,* 2011; Hawcroft *et al.,* 2012; Shimizu *et al.,* 2000; Magistri *et al.,* 2017). It also represents metastasis in terms of extravasation but not from the normal primary site, and the spleen is often surgically removed after injection which is a vital organ of the immune system.

There are many risk factors associated with surgery, requiring longer times under general anaesthetic, higher risk of infection, inflammation and healing time, loss of body mass, stress to the animal and higher risk of mortally (Balcombe *et al.,* 2004). Small animal surgery is labour intensive, time consuming to produce large cohorts and requires highly skilled personnel.

A number of studies have been conducted to investigate the factors which may influence metastasis of xenograft models, such as the cell line (Flatmark *et al.,* 2004), injection site and mouse age and strain (Hackl *et al.,* 2013; Lavilla-Alonso *et al.,* 2011). However, there is still a requirement for a better representative model of CRC and liver metastases that also fulfil the aims of the National Centre for the 3Rs (replacement, refinement and reduction) (Prescott and Lidster, 2017).

1.9 Aims and objectives

The aim of this research was to investigate the potential of targeted, triggered drug delivery using thMBs and US for the treatment of CRC.

Objectives to achieving this aim were:

I. To develop and establish a protocol for detecting concentrations of irinotecan and its metabolites in murine tissues using LC-MS/MS
II. PK analysis and biodistribution of irinotecan after targeted, triggered drug delivery using an *in vivo* model of CRC
III. To further develop targeted, triggered drug delivery using SN38 for the treatment of CRC
IV. To establish an orthotopic model of CRC liver metastases

Chapter 2

Materials & Methods

2. Materials and Methods

2.1. Liquid chromatography-triple quad tandem mass spectrometry (LC-MS/MS) analysis of murine tissues for irinotecan and its metabolites

2.1.1. Preparation of stock solutions and standards

Master stock solutions of irinotecan hydrochloride, SN38 (both Sigma-Aldrich) and SN38-Glucuronide (Santa-Cruz, USA) were prepared individually in dimethyl sulfoxide (DMSO, Sigma-Aldrich, UK) at a 1 mg/ml concentration and stored as recommended. From the master stock solution, a working stock solution was prepared in methanol (HPLC grade, Fisher Scientific, UK) to a 10 µg/ml concentration, aliquoted and stored at -80°C. Working stock solutions were prepared on a monthly basis.

A fresh standard curve was prepared from working stocks and run each day of analysis. Five-point standard curves were prepared by serial dilution (1:1) using methanol, including a blank containing methanol only. Tubes were vortex mixed and transferred to vials for analysis. Peak areas (PAs) from the standard curves were plotted against the known concentration and the slope of the curve was used to calculate drug concentration.

2.1.2. Preparation of samples

Tissue, serum and plasma samples were kept at 4°C while weighed and methanol was added to make a 1:4 homogenate using an ULTRA-TURRAX® homogeniser (IKA, Oxford UK). Serum/plasma samples did not require homogenisation. Liposome and thMB samples were diluted in methanol to a concentration within the standard curve. The resulting homogenate/methanol solution was immediately vortexed then centrifuged at 10,000 g for 5-minutes (4°C), to separate out the solid protein precipitate. The supernatant was then transferred into vials to be analysed by LC-MS/MS.

2.1.3. Preparation and use of internal standards

An internal standard was used to control for extraction, injection and ionization variability and therefore improving precision and accuracy of the method of detection. The appropriate internal standard was added at the same concentration to samples and standards. Each internal standard was chosen to give a reliable LC-MS/MS signal and similar retention time to that of the compound of interest. It was important to spike

samples in a range that was above the limit of quantitation but within the concentration range of the samples so as to not suppress the ionization of the analytes.

For the irinotecan PK study (**Chapter 3**), an internal standard was used. A master stock of the internal standard, irinotecan-d10 hydrochloride (Santa-Cruz, USA) was prepared in methanol at a concentration of 1 mg/ml and stored at -80°C. From the master stock, a working stock was prepared by dilution to 10 µg/ml in methanol. From this, 2 µl was transferred to 'spike' each 20 µl sample so that the final concentration was 1 µg/ml. Standard curves were also spiked in this way.

An internal standard was used for all SN38 *in vivo* experiments (**Chapters 4** and **5**). A master stock of the internal standard tolbutamide (Sigma-Aldrich, UK) was prepared in methanol at a concentration of 1 mg/ml and stored at -80°C. From the master stock, a working stock of a suitable concentration was prepared in methanol. This methanol was then used to make the initial 1:4 homogenates. Standard curve serial dilutions were also diluted 1:4 with internal standard.

2.1.4. Equipment

Analyses were performed on an Acquity Ultra-High Pressure Liquid Chromatography (UPLC) system (Waters Corporation, Milford, MA, USA) for the liquid chromatography separation of the compounds of interest. Chromatographic separation was obtained using an Acquity UPLC BEH C18 column (1.7 µM, 2.1×100 mm, Waters Corporation, Milford, MA, USA) with a column temperature of 40°C. A triple quadrupole Quattro Premier Mass Spectrometer (MS/MS) (Waters Corporation, Milford, MA, USA) was used with an ESI (Electrospray Ionisation) source operating in positive ionisation mode. Compounds were detected using the multiple reaction monitoring (MRM) settings detailed in **Table 2.1**.

Samples were eluted using a stepwise gradient at a flow rate of 0.3 ml/min for a total run time of 26-minutes. The flow conditions on the column are further detailed in **Table 2.2.** The C18 column and mobile phases were chosen and loosely based on a previously published method using the same compounds and UPLC (Chen *et al.,* 2012). The gradient was optimised using in house HPLC (**Section 2.2.3**) before developing the LC-MS/MS method. Mobile Phase A was 90% dH_2O, 10% methanol and 0.1% formic acid and Mobile Phase B was 90% (v/v) methanol, 10% (v/v) dH_2O and 0.1% (v/v) formic acid.

Instrument control and data acquisition were performed using MassLynx^{TM} version 4.0 software (Waters Corporation, Milford, MA, USA). The individual chromatograms

Table 2.1 Multiple reaction monitoring (MRM) settings used for detection of each compound using LC-MS/MS.

Compounds of interest (irinotecan, SN38, SN38-G and NPC) and internal standards (Tolbutamide and irinotecan-d10) are shown. Mass to charge ratio (m/z).

Compound	Precursor/Product Ion (m/z)	Dwell (sec)	Cone Voltage	Collision Energy (volts)
Irinotecan	587.3 > 124.00	0.15	25	45
Irinotecan	587.3 > 166.97	0.15	25	45
SN38	393.2 > 264.17	0.15	35	30
SN38	393.2 > 293.04	0.15	35	30
SN38	393.2 > 349.13	0.15	35	30
SN38-G	569.8 > 349.89	0.20	35	30
SN38-G	569.8 > 393.75	0.20	35	30
NPC	519.4 > 127.08	0.20	45	25
NPC	519.4 > 349.06	0.20	45	25
NPC	519.4 > 392.85	0.20	45	25
Tolbutamide	271.2 > 154.96	0.20	20	15
Tolbutamide	271.2 > 171.96	0.20	20	15
Irinotecan-d10	597.3 > 133.10	0.15	25	45
Irinotecan-d10	597.3 > 177.07	0.15	25	45

Table 2.2 Flow conditions on the LC-MS/MS column.

Gradient of Mobile Phase A (%A) and Mobile Phase B (%B) are shown as a percentage. Mobile Phase A was 90% dH2O, 10% methanol and 0.1% formic acid and Mobile Phase B was 90% (v/v) methanol, 10% (v/v) dH2O and 0.1% (v/v) formic acid. Total run time was 25-minutes.

Stage	Time (min)	Flow (mL/min)	%A	%B
1	Initial	0.3	80	20
2	15	0.3	20	80
3	16	0.3	0	100
4	20	0.3	0	100
5	21	0.3	80	20
6	25	0.3	80	20

(identified from specific mass-to-charge ratios) were selected for analysis. In brief, each individual chromatogram had an x-axis (retention time, minutes) and a y-axis (% signal intensity) and a calculated PA for the drug of interest (**Figure 2.1**).

2.1.5. Concentrating of samples to improve detection by LC-MS/MS

Due to the low concentrations of SN38 delivered, additional steps were added to improve the detection of very low concentrations of SN38 and SN38-G. The internal standard tolbutamide (Sigma-Aldrich, UK) was used to improve precision and accuracy due to the additional sample preparation steps and variation in volumetric recovery between steps (evaporation and reconstitution).

2.1.6. Sample preparation of LC-MS/MS analysis

For LC-MS/MS analysis, tissues were weighed and homogenised in 1:4 methanol (spiked with internal standard tolbutamide (Sigma-Aldrich, UK)) for 45 seconds at a speed of 6.45 m/s (2 cycles), using Bead Ruptor 24 Bead Mill Homogenizer (OMNI International, USA) with 2.8 mm zirconium ceramic oxide beads. A clear supernatant was obtained by centrifugation, dried at 37°C using GeneVac EZ-2 centrifugal evaporator (Genevac Ltd, UK), re-suspended in 25 µl of methanol, and analysed by LC-MS/MS (as before, **Section 2**).

2.1.7. Extrapolation using the standard curve

A standard curve was plotted of PA against concentration, and the gradient used to determine concentration of drug detected. This was further multiplied by the dilution factor to determine final drug concentration (per gram of tissue or per ml of serum/plasma).

When an internal standard was used, the ratios of PA to internal standard PAs were determined for samples and standards. These ratios were then plotted against known concentrations of the standards to produce a standard curve. The slope of the curve was used to calculate the concentration of drug per gram of tissue (or per ml of serum/plasma).

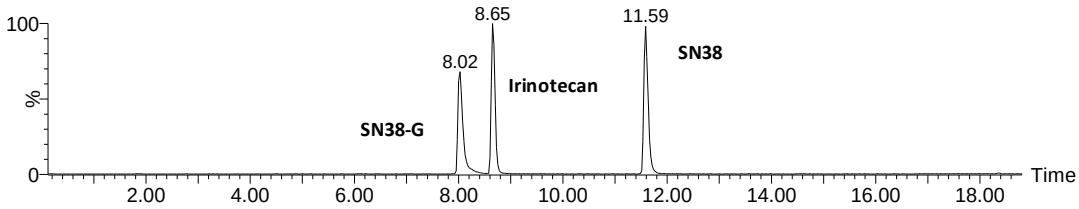

Figure 2.1 An example chromatogram of compounds of interest.

SN38-G, irinotecan and SN38 gave retention times of 8.02, 8.65 and 11.59 minutes, respectively (MassLynx™ version 4.0 software, Waters, UK). Y-axis = extracted ion intensity (%) and x-axis = time in minutes.

2.2. High performance liquid chromatography (HPLC) to quantify irinotecan concentrations in liposomes and thMBs

2.2.1. Preparation of standards

Irinotecan master stock (previously described **Section 2.1.1**) was diluted to make 2 mg/ml using methanol to make a working stock. Standards were created from this working stock by diluting 1:1 using methanol to make a 5-point standard curve with the highest concentration of 1 mg/ml.

2.2.2. Preparation of samples

Previously injected irinotecan thMB samples were kept at 4°C prior to analysis. A total of 5 thMB samples were prepared for HPLC analysis by the addition of methanol (1:10), vortex mixed and microcentrifuged at 10,000 g for 5-minutes. Liposome samples were also prepared by the addition of methanol (1:100) followed by vortex and centrifuge as for thMBs.

2.2.3. Equipment

Samples and standards were analysed using a Waters Alliance 2695 HPLC (Waters Corporation, Milford, MA, USA) linked to a Waters 2996 Photodiode Array Detector. 10 µl of sample was eluted using a stepwise gradient at a flow rate of 1 ml/min on a Hichrom RPB column (3.5 µm, 25 cm x 2.1 mm) (Hichrom Limited, UK)(**Table 2.3**). Mobile Phase A and B were the same as for LC-MS/MS described in **Section 2.1.4**.

The 'Empower2' software (Waters Corporation, Milford, MA, USA) was used to determine PAs of the chromatograms, extracted at a wavelength of 373.0 nm (example chromatogram shown in **Figure 2.2**), and a table reading retention time (minutes) and PA was created. The PA from chromatograms of the standards were used to plot a standard curve for known concentrations of irinotecan. From this, the slope of the curve was calculated and used to determine the concentration of irinotecan using the PAs from the chromatograms of the thMB and liposome samples.

Table 2.3 Flow conditions on the column.

Flow condition are shown for HPLC analysis of irinotecan concentrations detected in thMB and liposome samples. Mobile phase A (%A) and mobile phase B (%B) are shown as a percentage. Mobile Phase A was 90% dH2O, 10% methanol and 0.1% formic acid and Mobile Phase B was 90% (v/v) methanol, 10% (v/v) dH2O and 0.1% (v/v) formic acid. Total run time was 15-minutes.

Stage	Time (min)	Flow (mL/min)	%A	%B
1	Initial	1.0	90	10
2	7	1.0	10	90
3	9	1.0	10	90
4	10	1.0	90	10
5	15	1.0	90	10

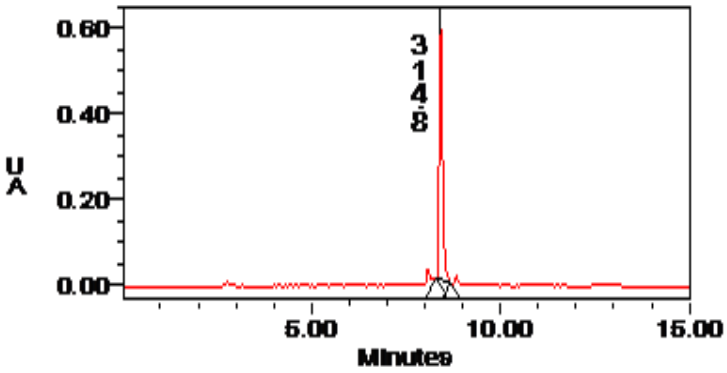

Figure 2.2 Example of an irinotecan HPLC chromatogram.

Chromatogram was extracted at wavelength 373.0 nm and gives a single peak at 8.413 minutes with a peak area of 3712018, equivalent to 226.4 µg/ml of irinotecan (Empower 2 software (Waters Corporation, Milford, MA, USA)). Total run time of 15-minutes. AU = Absorbance units.

2.3. Tissue culture

2.3.1. Cell lines

The human colorectal adenocarcinoma cell line SW480, the metastatic-derived (lymph node) SW620 were isolated from the same patient and contain a mutant APC gene (Leibovitz *et al.,* 1976; Hewitt *et al.,* 2000; Ilyas *et al.,* 1997). The human colorectal carcinoma cell line HCT116 contained wild type APC but mutant KRAS (Brattain *et al.,* 1981; Ilyas *et al.,* 1997). The mouse endothelial cell line SVR was isolated from pancreatic islets of C57BL/6 adult mice (Arbiser *et al.,* 1997). All were obtained from the American Type Culture Collection (ATCC).

MC38 luc11A mouse syngeneic CRC cells expressing luciferase were a kind gift from Professor D. Beauchamp, University of Virginia. MC38 luc11A originated from the parent cell line MC38, which was isolated after repeated treatments of the carcinogen 1,2-dimethylhydrazine dihydrochloride and was found to be KRAS mutant (Corbett *et al.,* 1975).

All cell lines were regularly screened for mycoplasma and all human cell lines were short random repeat (STR) DNA profile authenticated. All cell lines were screened for mouse-specific viruses prior to culturing for xenograft implantation.

2.3.2. Tissue culture conditions

Cells were maintained in vented T75 tissue culture flasks (Corning Life Sciences, UK) using Roswell Park Memorial Institute medium 1640 (RPMI Medium 1640, Gibco™) supplemented with 10% (v/v) foetal calf serum (FCS) (Invitrogen, UK) (specifically cell lines: HCT116, SW620, SW480 and MC38luc11A) at 37°C in a 5% CO_2 atmosphere. The SVR cells were maintained under the same conditions but using Dulbecco's Modified Eagle Medium (DMEM, Gibco™) supplemented with 5% (v/v) FCS (Invitrogen, UK). Cells were passaged at 70-80% confluence, by washing with sterile phosphate buffered saline pH 7.4 (PBS, Invitrogen, UK) before being harvested by trypsinisation. Culture medium was added back into the flask to block the action of trypsin before the cells were collected and centrifuged at 400 g for 5-minutes in Eppendorf™ 5810R centrifuge (Eppendorf™ Hamburg, Germany). The supernatant was discarded, and the cells re-suspended in medium and split 1 in 5 (SW480, SW620) or 1 in 10 (HTC116, MC38luc11A and SVR) into a fresh T75 tissue culture flask containing fresh medium.

2.3.3. Preparation of cells for xenografts

SW480 cells were cultured according to the protocol outlined in **Section 2.3.2**. Cells were re-suspended in PBS after being centrifuged at 400 g, the total cell count was obtained manually using a Neubauer haemocytometer, and the concentration was adjusted to $1x10^7$ cells/ml. Cells were mixed thoroughly and 100 µl was injected subcutaneously into the right hind flank of female CD1 or BALB/c nude mice.

2.4. Chemosensitivity assay

The MTT assay was used to determine cell viability. This test measures the ability of the cells to convert the water-soluble, yellow tetrazolium salt, MTT (3-[4,5-Dimethylthiazol-2-yl]-2,5-diphenyl-tetrazolium bromide, Sigma-Aldrich, UK), into water insoluble, purple, formazan crystals, via mitochondrial enzymes (Mosmann, 1983). Crystals are dissolved in DMSO (Sigma-Aldrich, UK) and the optical density was measured using spectrophotometer, as described below.

Cells were seeded at 4000 cells per well of a 96-well plate across 11 lanes out of 12. One lane was used as a blank (no cells, 100 µl medium), and another lane was used as a vehicle control (cells, 0.1% DMSO). Cells were incubated under previously described conditions, for 24 hours (**Section 2.3.2**).

For SN38 cytotoxicity assays, the highest SN38 concentration was sonicated for 20-minutes and vortex mixed repeatedly to solubilise in the media, and dilutions were made from this stock. Medium from the cells was then carefully removed and replaced with fresh media containing a range of SN38 (Sigma-Aldrich, UK) concentrations. Cells were exposed to SN38 for either 72-hours or 24-hours with media carefully removed, washed with fresh media and finally replaced with fresh media, being left to recover for a further 48-hours. Cell viability was determined using the MTT assay. 10 µl of MTT (5 mg/ml) was added to each well and incubated under normal tissue culture conditions for 4 hours. The medium was removed and 150 µl of DMSO was added to dissolve the crystals. The absorbance was measured at 620 nm using a Mithras LB 940 multimode microplate reader (Berthold Technologies, Bad, Wildbad, Germany). The mean absorbance was calculated from 4 measurements per dilution (8 measurements for the controls) and the absorbance of the blank was subtracted from each value. The adjusted absorbance values were used to calculate the percentage of cell survival using control values as 100% cell survival, see equation below:

$$\% \boldsymbol{viability} = (\boldsymbol{absorbance\ of\ treated\ cells} \div \boldsymbol{absorbance\ of\ control\ cells}) \times \mathbf{100}$$

Cytotoxicity curves were plotted as percentage viability against drug concentration (Log_{10}), transformed and fitted using a non-linear fit, log(inhibitor) vs. response – Variable slope (four parameters). Biphasic curves were fitted with a non-linear fit – biphasic. IC_{50} values were expressed as a mean (Graphpad – Prism version 7, La Jolla, CA, USA).

2.5. Topoisomerase I enzyme-linked immunosorbent assay (ELISA)

2.5.1. Preparation of samples

Cell lysates were prepared by detaching cells as previously described (**Section 2.3.2**) and collected by centrifugation. Cells were washed three times in ice-cold PBS and re-suspended in the same. Resulting suspensions were frozen at -80°C and thawed (repeated three times). Centrifuged at 1500 g for 10-minutes at 4°C and the supernatants stored at -80°C until needed.

Tissue homogenates were prepared by weighing, then rinsing in ice-cold PBS. Tissues were minced using fine scissors and homogenised in 5 ml of PBS with a Micro Tissue Grinder (Pellet Pestles – Cordless Motor, Kimble® Kontes, Sigma-Aldrich) with Kimble® Kontes 1.5 ml Disposable Pellet Pestles (blue polypropylene, autoclavable, Sigma-Aldrich, UK). Resulting suspensions were frozen at -80°C and thawed (repeated twice), followed by centrifugation at 5000 g for 5-minutes at 4°C. The supernatants were then stored at -80°C until needed.

2.5.2. Protein assay

A standard curve was prepared at a suitable concentration range using a stock concentration of BSA (Sigma-Aldrich, UK) at 10 mg/ml. 10 µl of each standard was added to wells of a 96-well plate (in duplicate) with blanks. Then 10 µl of each sample was added (in triplicate) to the wells of the 96-well plate. Using the Bio-Rad DC Protein Assay Kit (Biorad, Life Science, UK) 25 µl reagent A was added to each well, then 200 µl of reagent B to each well. Plate was incubated (shaking) at room temperature (RT) for 15-minutes and the absorbance was measured at 570 nm (Mithras LB 940 multimode microplate reader, Berthold Technologies, Bad, Wildbad, Germany). The mean absorbance was calculated per dilution and the absorbance of the blank was subtracted from each value. A standard curve was plotted, and the protein concentration of the samples calculated using the gradient of the trend line (linear).

2.5.3. Topoisomerase I ELISA

An ELISA for topoisomerase I (human or mouse) (Cloud-Clone Corp., Houston, TX, USA) was used as per manufacturer's instructions. A standard curve was prepared at a suitable concentration range. Absorbance was measured at 450 nm (Mithras LB 940 multimode microplate reader, Berthold Technologies, Bad, Wildbad, Germany). The mean absorbance was calculated per dilution and the absorbance of the blank was subtracted from each value. A standard curve was plotted (Log/Log) and the protein concentration of the samples calculated using the gradient of the trend line (linear).

2.6. UGT1A1 enzyme-linked immunosorbent assay (ELISA)

2.6.1. Preparation of samples

Cell lysates were prepared by detaching cells as previously described (**Section 2.3.2**) and collected by centrifugation. Cells were washed three times in ice-cold PBS and re-suspended in the same. The resulting suspension was sonicated twice using a tip sonicator (Branson Sonifier 250, Danbury, CT, USA) in an ice bath for 15-seconds at 50% duty cycle and an output control of 3. The suspension was then centrifuged at 1500 g for 10-minutes at 4°C and supernatants stored at -80°C until needed.

Tissue homogenates were prepared by weighing, then rinsing in ice-cold PBS. Tissues were suspended in 5 ml of PBS and minced using fine scissors. The resulting suspension was twice sonicated for 30-seconds at 50% duty cycle and an output control of 3. The suspension was then centrifuged at 5000 g for 5-minutes at 4°C and supernatants stored at -80°C until needed.

2.6.2. UGT1A1 enzyme-linked immunosorbent assay (ELISA)

The protein concentration of each sample was determined as previously described, (**Section 2.5.2**). An ELISA for UGT1A1 (human or mouse) from EIAab®, Wuhan, China, was used as per manufacturer's instructions. A standard curve was prepared at a suitable concentration range. Absorbance was measured at 450 nm (Mithras LB 940 multimode microplate reader, Berthold Technologies, Bad, Wildbad, Germany). The mean absorbance was calculated per dilution and the absorbance of the blank was subtracted from each value. A standard curve was plotted (Log/Log) and the protein concentration of the samples calculated using the gradient of the trend line (linear).

2.7. Irinotecan liposomes

2.7.1. Generation of irinotecan liposomes

The method of liposomal encapsulation is described in brief and was kindly performed by Dr Radwa Abou-Saleh (Department of Physics and Astronomy, University of Leeds, UK). The lipid shell was composed of 63:32:5:0.1 mole % DSPC:Cholesterol:DSPE-Biotin-PEG2000:Texas Red® DHPE. Irinotecan encapsulation was performed using the manganese sulphate pH gradient method (Messerer *et al.,* 2004). Briefly, the dried lipid film was hydrated with 300 mM manganese sulphate buffer (pH 3.4) to a total lipid concentration of 24 mg/ml. Liposomes were filtered using a 200 nm pore diameter polycarbonate membranes in a mini-extruder at 60-70°C. The external buffer was exchanged using a column equilibrated with pH 7.4 SHE buffer (300 mM sucrose, 20 mM HEPES and 15 mM EDTA). Ionophore was added to liposomes at 0.5 µg/mg lipids and incubated at 60°C for 10-minutes. Irinotecan was then added to the lipids at a 0.6:1 w/w ratio and incubated for 2-hours at 60°C, in a light-free environment. A Sephadex G25 column, equilibrated with pH 7.4 SH buffer (300 mM sucrose, 20 mM HEPES) was used to removed unencapsulated irinotecan. Drug concentration was quantified by HPLC (see **Section 2.2**).

Irinotecan thMB production and *in vivo* experiments were performed by Dr Nicola Ingram (Leeds Institute of Biomedical and Clinical Sciences, University of Leeds, UK). Murine tissues from *in vivo* experiments were kindly provided for LC-MS/MS analysis and the thMB samples used for HPLC analysis, both performed by Laura McVeigh using facilities at the Institute of Cancer Therapeutics, University of Bradford, UK.

2.8. SN38 liposomes: Generation and characterisation

2.8.1. Generation of SN38 liposomes

The method of liposomal encapsulation is described in brief and was kindly performed by Dr R Abou-Saleh (School of Physics and Astronomy, University of Leeds, UK). The lipid shell of the liposomes comprised 57:39:4:0.1 molar % of DSPC:Cholesterol:DSPE-Biotin-PEG_{2000}:Texas Red-DHPE. In addition, negatively charged cardiolipin was added to the lipid mixture at 11% of the total mass in order to bind and entrap SN38 within the liposome. Lipids were mixed and dried under a stream of nitrogen, then under a vacuum overnight to remove any traces of chloroform or methanol. SN38 was dissolved in 0.1 M ammonium hydroxide buffer to 2 mg/ml and the encapsulation procedure was carried out as previously described (Ahmad and Zhang, 2005). Briefly, the dried lipid film was hydrated

with 2 mg/ml SN38 in 0.1M ammonium hydroxide and 10% sucrose, pH 11 to a total lipid concentration of 42 mg/ml. This suspension was then extruded with a mini-extruder (Avanti Polar Lipids, Alabaster, USA) through polycarbonate membrane filters at 60-70 ˚C and reduction in the vesicle diameter was obtained by passing the liposomes through 400 nm and 200 nm pore sizes, respectively.

The liposomes were then divided to aliquots, frozen in liquid nitrogen and dehydrated by freeze-drying over-night using a VerTis BenchTop Pro (SP Scientific) at 60mT and 104.6°C. Aliquots were stored at -20°C until needed. Liposomes were rehydrated overnight with 10 mM acetate buffer (pH 2) at 4°C then passed through a 200 nm pore syringe filter before use.

2.8.2. Liposome sterility

20 µl of liposome sample was co-incubated with tissue culture medium and incubated for 72 h at 37°C. Medium was inspected daily under 100× objective with 1.5× internal magnification using an Olympus CK641 (Hamburg, Germany) for colour change or indication of infection.

2.8.3. Liposome size, zeta potential and concentration

qNano (iZON, Oxford, UK) was used to determine diameter and concentration of liposomes (performed by Dr R Abou-Saleh). The concentration was measured using a 200 nm nanopore. A 1:1000 dilution of carboxylated polystyrene calibration particles were used as reference. Liposome samples were diluted 1:1000 using PBS before analysing.

A Zetasizer (Malvern Instruments Ltd, UK) was used to determine the hydrodynamic diameter of freshly rehydrated liposomes by dynamic light scattering (DLS). This was also used to measure the zeta-potential, by passing a voltage through the sample and mixed measurement model phase analysis (M3-PALS) technology determined the mean reading in mV.

A Nanosight N300 (Malvern Instruments Ltd, UK) was used to determine liposome concentration. Liposome samples were diluted, and Nanoparticle Tracking Analysis software established the modal value of liposomes per ml.

2.8.4. Liposome chemosensitivity assays

The concentration of SN38 within the liposome batches was determined by LC-MS/MS, see **Section 2.1.2**. The known concentration was used to prepare serial dilutions of the liposomes in tissue culture medium to apply to SW480 cells (same concentrations and MTT

method used previously (**Section 2.4**). Cells were treated for 24 or 72-hours and compared to free SN38.

2.9. On-chip generation of MBs and *in vivo* administration

Irinotecan or SN38 liposomes were loaded onto VEGFR2-targeted MBs which were generated using a microfluidic chip (**Figure 2.3**) following the method described in (Peyman *et al.,* 2012). MBs were produced quickly, 1 ml of MBs could be produced within 10-minutes. Liposome loading was estimated using the average size (1.6 μm) and concentration (1 x 10^8 MB/ml) of the MB population. Approximately 400 liposomes of 200 nm diameter would fit around a single MB.

2.9.1. Preparation of MB lipids

4 mg (95% DPPC, 5% DSPE biotin PEG_{2000}) of lipids were vortex mixed in a glass vial and dried under nitrogen for 1-hour or until a dried lipid film could be visualised. Vials were stored at -20°C and used within 2-3 weeks. The lipid film was then resuspended in sterile PBS to a concentration of 2 mg/ml. 10 μl of 41.7 μM neutravidin (Thermo Fisher Scientific, MA USA) stock was incubated for 20-minutes with 8 x 10^{11} liposomes. Neutravidin concentrations were optimised in earlier experiments by Dr R Abou-Saleh, School of Physics and Astronomy, University of Leeds, data not shown). The neutravidin/liposome mixture was then incubated with the resuspended MB lipids for 20-minutes at 4°C. After incubation, 10 μl/ml C_6F_{14} (Sigma-Aldrich, USA) was added and vortex mixed. This MB solution was fed into the microfluidic system at 60 μl/ min with a gas pressure of 20 psi. thMBs were produced with a C_4F_{10} gas core.

2.9.2. Concentration and size of MBs

The concentration and size of MBs were measured post production. A counting chamber was constructed using a coverslip placed on a glass microscope slide. 50 μm thick polyethylene terephthalate as spacers were used to ensure the bubbles were not flattened under the weight of the coverslip. MBs were diluted 1:10 and a volume of 30 μl was placed under the coverslip by capillary action. **Figure 2.4** shows a bright field image of the MBs in the counting chamber. Images were taken using the 40× objective with 1.5× internal lens (Nikon Eclipse Ti-U, Tokyo, Japan) over 10 regions of the slide and an in-house macro was used with ImageJ software (Maryland, USA) the mean bubble diameter and bubble concentration. Bubbles less than ~0.75 μm were not counted due to the optical resolution of the microscope.

2.9.3. Targeting MBs to VEGFR2

MBs were targeted to VEGFR2 post production by the addition of 0.1 µg of anti-mouse biotinylated VEGFR2 antibody (eBiosciences, CA, USA) per 10^7 thMBs. thMBs were incubated with the antibody for 20-minutes at RT. VEGFR2 antibody concentrations were optimised previously within the group by Dr N Ingram (Leeds Institute of Biomedical and Clinical Sciences, University of Leeds, UK).

2.10. Animals

The mice were 5-7-week-old female CD-1 nude mice or BALB/c nude mice (originally obtained from Charles River Laboratories, Kent) and maintained in house. All mice were maintained under high health status conditions and are specific pathogen free (SPF) status. Animals are housed in individually ventilated cages (IVCs) with access to food and water *ad libitum*. All procedures were approved by the UK Home Office and carried out according to the Animals (Scientific Procedures) Act 1986 and under personal licence authority to Laura McVeigh.

2.10.1. Administration of thMBs (*in vivo*)

CD1® nude mice were inoculated subcutaneously with 1×10^7 SW480 CRC cells (see **Section 2.3.3** and **2.10**). Tumour volumes were measured by calliper and using high frequency US. When tumour volumes reached 100-150 mm^3 (~8-10 days post inoculation), mice were randomly assigned to treatment cohorts. Treatments were administered intravenously (i.v.) via tail vein. See individual figure legends for further details such as injection volume. If the animal required an US-trigger, it was administered 4-minutes post i.v. injection.

2.10.2. Ultrasound-trigger (US-trigger)

The US-trigger was produced using a purpose built single element US system termed Ultrasound Array Research Platform (UARP)(McLaughlan *et al.,* 2013; Freear *et al.,* 2014). The frequency and acoustic pressures were predetermined using the polydisperse MB populations produced using the on-chip method so that the resonate size corresponded to the US frequencies used (McLaughlan *et al.,* 2016). With the mouse supine, the transducer was brought into position, perpendicular to the tumour region with the use of adequate coupling gel (EcoGel 100™; Eco-Med Pharmaceuticals Inc., Mississauga, Canada). A 5-second 'tone burst' was produced by a 2.2 MHz unfocused transducer (V323, Olympus NDR, UK), generating a 10 µs US pulse with a peak negative pressure of 260 kPa with a

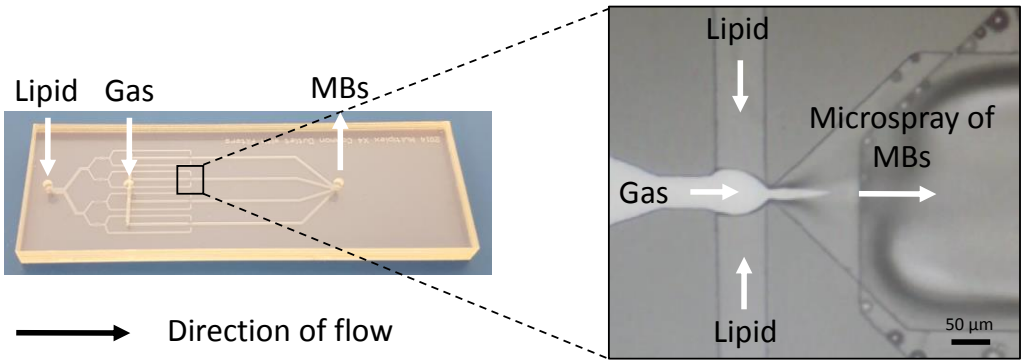

Figure 2.3 On-chip MB production.

The chip (Epigem, RedCar, UK) consists of separate lipid and gas inlets that feed into 4 flow focusing modules (black box outlines a single flow focusing module). The MBs are formed by a microspray regime and collected from a single outlet port. The microfluidic chip was designed by Dr Sally A Peyman (Peyman *et al.,* 2012).

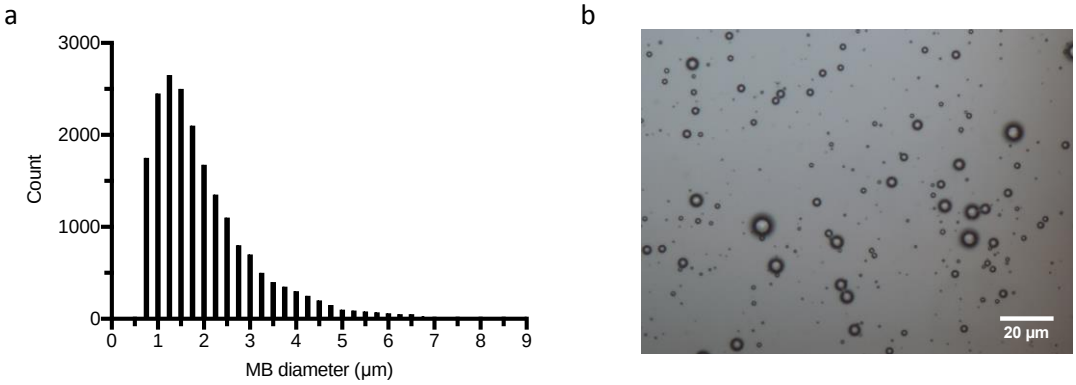

Figure 2.4 On-chip MB production of polydispersed populations.

(a) Histogram showing MB population from microfluidic on-chip micro-spray regime. Mean diameter was 2 µm with a dispersity index of 50%. None of the MBs produced using this regime were greater than 8 µm in diameter. Taken from (Peyman *et al.,* 2012). (b) SN38 liposomes attached to MBs. Taken by bright field microscopy using a 40× objective with 1.5× internal magnification (Nikon Eclipse Ti-U, Tokyo, Japan). An in-house macro was used with ImageJ to determine size and concentration of the MBs per image.

1 kHz pulse repetition frequency (PRF). This US-trigger was used for *in vivo* work in **Chapters 3-4**.

In **Chapter 5** additional US-triggers were used. The tone burst was extended from 5-seconds to a total sonication time of 120-seconds. The 120-second chirp US-trigger with a -6 dB bandwidth of 80% with a frequency between 3-7 MHz was produced by a 5.0 MHz unfocused transducer (V310, Olympus NDT, UK), generating a pulse with a peak negative pressure of 110 kPa with a 1 kHz PRF. See **Figure 2.5** for image of the UARP and example depictions of the described US sequences.

2.10.3. *In vivo* measurements of tumour volume: Calliper

Mechanical calliper measurements were taken twice per week to determine tumour volume. The following equation was used to determine the tumour volume:

$$\boldsymbol{Tumour\ volume} = \boldsymbol{length}\ (mm)\ \times\ \boldsymbol{height}\ (mm)\ \times\ (\boldsymbol{\pi} \div \boldsymbol{6})$$

2.10.4. *In vivo* measurements of tumour volume: High-Frequency Ultrasound (HFUS)

HFUS was preformed weekly to measure tumour volume. Using a Vevo 770 high-frequency US system (Fujifilm VisualSonics, Inc, Ontario, Canada), a 40 MHz (RM-704) or 25 MHz (RM-710B) transducer (both from VisualSonics, Inc, Ontario, Canada), was held above the animal as described (Abdelrahman *et al.,* 2012), and imaged in B mode. Vevo 770 version 3 software (Fujifilm VisualSonics, Inc, Ontario, Canada) was used for post-acquisition 3D reconstructions and used to calculate tumour volumes, as described in (Ingram *et al.,* 2013). A more detailed description can be found in **Section 6.2.2 and Figure 6.3**.

a.

b. i. ii.

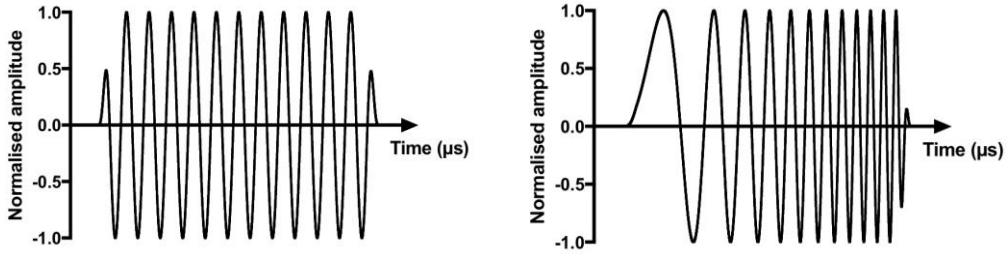

Figure 2.5 The ultrasound-trigger (US-trigger).

(a) The US-trigger was generated by the Ultrasound Array Research Platform (UARP) (b. i) Representative tone burst (2.25 MHz transducer) and (b. ii) chirp (5.0 MHz transducer with frequency range of 3 to 7 MHz) US sequences (McLaughlan *et al.,* 2013; Freear *et al.,* 2014).

2.10.5. Body mass

Body mass was a useful indicator of animal health. Animals were weighed using digital scales prior to the start of an experiment. During an experiment, animals would be weighed twice per week, and monitored for weight loss. A loss of 10% body mass would indicate poor health and the animal would be closely monitored. Weight loss of more than 20% would indicate severe pain or illness and require immediate sacrifice.

2.10.6. Tissue collection

Organs were extracted immediately post-sacrifice (by cervical dislocation) and halved. First half was transferred to cryovials and flash frozen using liquid nitrogen (then stored at -80°C). The other half was placed in 4% (w/v) paraformaldehyde (PFA) for 24-hours and transferred to 70% (v/v) ethanol to be processed for paraffin wax embedding (**Section 2.13**).

2.11. Blood collection, processing and analysis

Blood was collected post-sacrifice from the heart for either plasma or serum. Plasma was extracted from blood collected in 1.3 ml paediatric blood tubes K3 EDTA (Greiner Bio-One Limited, Gloucester, United Kingdom) and kept on ice. Tubes were centrifuged for 15-minutes at 1300 g (4°C) and supernatant transferred to cryovials and stored at -80°C until required. Serum was obtained by clotting whole blood at RT and centrifuging for 15-minutes at 1300 g (4°C). The clear serum supernatant was then transferred to Eppendorf tubes and stored at -80°C until required

2.11.1. Haematology analysis

Fresh blood was collected in 1.3 ml paediatric blood tube K3 EDTA (Greiner Bio-One Limited, Gloucester, United Kingdom) and analysed using a Scil Vet ABC ™Haematology Analyser (Scil Animal Care Company, Gurnee, IL, USA). The analyser was calibrated using mouse blood controls with normal and low levels blood cells (QC Pack ABX Minotrol 16, Horiba ABX SAS, Horiba Medical). Each sample was analysed 3 times and the mean value taken.

2.11.2. Alanine aminotransferase (ALT) liver enzyme analysis

Plasma samples were sent on dry ice for external analysis by The Mary Lyon Centre (MLC) Pathology, Medical Research Council (MRC) Harwell, Oxfordshire, UK. A Beckman Coulter

AU680 clinical chemistry analyser (Beckman Coulter, Inc., CA, USA) was used to determine ALT concentrations.

2.12. Whole organ *ex vivo* metabolism study using murine liver and human CRC xenograft tumours

Immediately after sacrifice, xenograft tumours (SW480) and livers were collected and washed in ice cold PBS. Tissues were halved, weighed and placed in separate tubes. PBS (37°C) spiked with irinotecan (10 µg/ml) was added 1:4, before immediately homogenising using a hand blender. Homogenates were placed in a water bath at 37°C and thoroughly vortex mixed before sampling at set time points. The samples were processed for LC-MS/MS analysis as described in **Section 2.1**.

2.13. Tissue processing for immunohistochemistry

All antibody concentrations were based on previously optimised studies performed by Dr Nicola Ingram and Dr Gemma Marston (Leeds Institute of Biomedical and Clinical Sciences, University of Leeds, UK).

2.13.1. Fixation of tissue

Immediately after sacrifice, tissues were fixed by immersion in 4% (w/v) PFA overnight at RT. The tissue was then washed in PBS and submerged and stored in 70% (v/v) ethanol prior to processing. The processing and embedding of fixed tissues was carried out by Mr Michael Shires (Senior Laboratory Technician, Leeds Institute of Cancer and Pathology).

2.13.2. Sectioning paraffin wax embedded tissue

After storing at 4°C overnight, paraffin-embedded tissue was transferred to ice water prior to loading into a Leica Biocut 2030 microtome (Leica Biosystems, Wetzlar, Germany). Serial sections were cut at 5 µm, mounted onto Superfrost™ slides (Thermo Fisher Scientific, MA, USA), left to dry at 37°C overnight and stored at RT.

2.13.3. Haematoxylin and Eosin (H&E)

Sections were cleared of paraffin wax by 3 × 5-minutes incubations in Histo-Clear (a xylene substitute, National Diagnostics, UK) followed by rehydration through 3 × 1-minute incubations in 100% ethanol. Sections were then incubated in haematoxylin (Sigma, UK) for 1-minute followed by 3 × 1-minute sequential rinses in tap water, Scott's tap water and tap water. Sections were incubated in 1% (v/v) Eosin (Sigma, UK) for 1-minute followed by a 1-minute rinse in tap water. Sections were then dehydrated through 3 × 100% ethanol

washes before 3 × final rinses in Histo-Clear. Coverslips were then mounted on top of the sections with DePex (Sigma, UK) before being left to dry overnight in a well-ventilated space.

2.13.4. Mitotic body count

H&E stained tumour slides were scanned using an Aperio slide scanner (Leica Biosystems, Wetzlar, Germany) at 20× magnification and anonymised. ImageScope (Leica Biosystems, Wetzlar, Germany) was used to view the slides and calculate tumour area. Mitotic bodies were manually counted and the number of mitoses per mm^2 calculated.

2.13.5. Necrosis

H&E stained tumour slides were scanned using an Aperio slide scanner (Leica Biosystems, Wetzlar, Germany) at 20× magnification and anonymised. ImageScope (Leica Biosystems, Wetzlar, Germany) was used to view the slides and calculate tumour area by drawing around the tumour manually. Total area of necrosis (calculated by manually drawing around the necrotic regions) and total tumour area were determined to give percentage necrosis per tumour area.

2.13.6. Vessel density (CD31)

CD31 was used as an pan-endothelial cell marker and positive blood vessels were stained and quantified to determine microvessel density of xenograft tumour sections. Tumour sections were deparaffinised, heat-mediated antigen retrieval was carried out in citrate buffer (pH 6) and endogenous avidin and biotin were blocked (Vectorlabs, Burlingame, USA). After blocking, sections were incubated with the antibody at a 1:20 dilution (0.01 mg/ml) for one hour (rat anti-mouse CD31, clone SZ31, Dianova GmbH, Germany). After washing, a biotinylated rabbit anti-rat secondary antibody was applied at a 1:200 dilution (6.5 mg/ml) for 30-minutes (Dako, United Kingdom). ABC/HRP solutions were then applied (Vectorlabs, Burlingame, USA) and the vessels were visualised with 3,3'-Diaminobenzidine (DAB, Dako, UK). The slides were scanned using an Aperio slide scanner (Leica Biosystems, Wetzlar, Germany) at 20× magnification. Ten 0.25 mm^2 boxes were placed randomly throughout the tumour section using RandomSpot software version 6.02 (Wright *et al.,* 2015) and the number of CD31-positive vessels was counted manually. Vessel density was calculated as number of CD31 positive vessels per 0.25 mm^2.

2.13.7. Vessel density (VEGFR2)

VEGFR2 was used as a marker of angiogenesis and positive blood vessels were stained and quantified to determine microvessel density of xenograft tumour sections. Sections were deparaffinised and heat-mediated antigen retrieval was carried out using pH 9.0 Tris/EDTA/Tween-20 (10mM/1mM/0.05%) buffer. Endogenous peroxidases and casein were also blocked and sections incubated with rabbit anti-mouse VEGFR2 primary antibody (55B11, Cell Signaling Technology®, MA, USA) applied at 1:100 for 1-hour at RT. After washing, a rabbit Envision-HRP polymer and DAB were used for visualisation (Dako, United Kingdom). The slides were scanned using an Aperio slide scanner (Leica Biosystems, Wetzlar, Germany) at 20× magnification. Ten 0.25 mm^2 boxes were placed randomly throughout the tumour section using RandomSpot software version 6.02 (Wright *et al.,* 2015) and the number of VEGFR2-positive vessels was counted manually. Vessel density was calculated as number of VEGFR2 positive vessels per 0.25 mm^2.

2.13.8. Apoptosis (Cleaved Caspase-3)

Cleaved Caspase-3 staining of the tumours was used as a biomarker of apoptosis. Staining was carried out as previously described for CD31 (**Section 2.13.6**), except that slides were incubated overnight at 4°C with the primary antibody at a 1:250 dilution (Cleaved Caspase-3 (Asp175) Antibody #9661, Cell Signaling Technology®, MA, USA). Seven images were taken at 40× magnification and an in-house macro was used in ImageJ to determine percentage brown (DAB positive) to blue (haematoxylin positive) staining.

2.13.9. Double strand breaks (phosphorylated histone H2AX)

Phosphorylated histone H2AX (pH2AX) was used as a marker for SN38 efficacy as its mode of action forms single strand DNA breaks that are subsequently converted to double strand breaks (Matthaios *et al.,* 2012). pH2AX staining of the tumours was carried out as described for CD31 (**Section 2.13.6**), except that the antibody was applied at a 1:400 dilution (Phospho-Histone H2A.X (Ser139) (20E3) Rabbit mAb #9718, Cell Signaling Technology®, MA, USA). Images were taken and scored as described for Apoptosis, **Section 2.13.8**.

2.13.10. Quantification of perivascular inflammation in liver

Perivascular inflammation (PVI) was defined as the accumulation of lymphocytes, and possibly histiocytes and eosinophils, in a dense mass around a vessel, indicating inflammation. PVI was scored in the livers of treated and untreated animals. H&E stained

liver sections (as described, **Section 2.13.3**), were digitally scanned at 20× magnification and anonymised. The area of inflammation (μm^2) per tissue section was determined using ImageScope. The percentage inflammation was determined using the following equation:

$$\boldsymbol{Inflammation}\ (\%)$$
$$= \left(\boldsymbol{inflammation\ area}\ (\mu m^2) \div \boldsymbol{liver\ section\ area}\ (\mu m^2)\right) \times \mathbf{100}$$

2.14. Statistical analyses

All statistical analyses were performed using GraphPad Prism 7 (©2017 GraphPad Software, Inc., CA, USA). See figure legends for type of analysis used in each experiment and significance.

Chapter 3

Irinotecan thMBs:

PK Studies using a Murine

Model of CRC

Introduction

One of the fundamental requirements of cancer therapeutics is to improve drug delivery to tumours. Mass spectrometry is a powerful analytical tool, offering accurate and precise measurement of drug concentrations, allowing invaluable insight into PK; biodistribution and intratumoral drug deposition and metabolism (McLafferty, 1981; Petrovic and Barceló, 2013).

Irinotecan is a prodrug, requiring carboxylesterases to transform it to the active metabolite SN38 (**Section 1.3.4.4**). This conversion is vital for efficacy of the drug and availability of carboxylesterases is a limiting factor of its use. Similarly, the rate of deglucuronidation of SN38 to the inactive SN38-G by UGT1A enzymes is a fine balance between drug efficacy and dose limiting side effects. The incorporation of mass spectrometry into pre-clinical trials is essential for future drug delivery and development using thMBs.

The first aim of this study was to develop a sensitive LC-MS/MS method to quantify irinotecan and its metabolites in murine serum/plasma and tissue homogenates. The precision, short-term stability, extraction efficiency and effects of freeze-thaw cycles were also studied to ensure method validity. The method was then used to quantify irinotecan and metabolites from murine blood and tissue samples to support PK and biodistribution studies using irinotecan and future studies using SN38.

3. Results

3.1. Optimisation and validation of LC-MS/MS for the detection of irinotecan and metabolites

3.1.1. Optimisation of LC-MS/MS channels

Irinotecan and its metabolites SN38, SN38-G, NPC and two internal standards irinotecan-d10 and tolbutamide (internal standards for irinotecan and SN38, respectively), were individually optimised by firstly preforming multiple reaction monitoring (MRM) scans to find the retention time (RT) of the compound and optimal settings for detection. Using a previous method by Chen *et al*., (2012) as a reference, a daughter scan was run with varying collision energies in order to determine optimal precursor (daughter) ions for each compound in order to increase detection sensitivity (Chen *et al.,* 2012). The structures and molecular weights for each analyte, along with the daughters are displayed in **Figure 3.1** and **Figure 3.2** and also listed in **Table 2.1**.

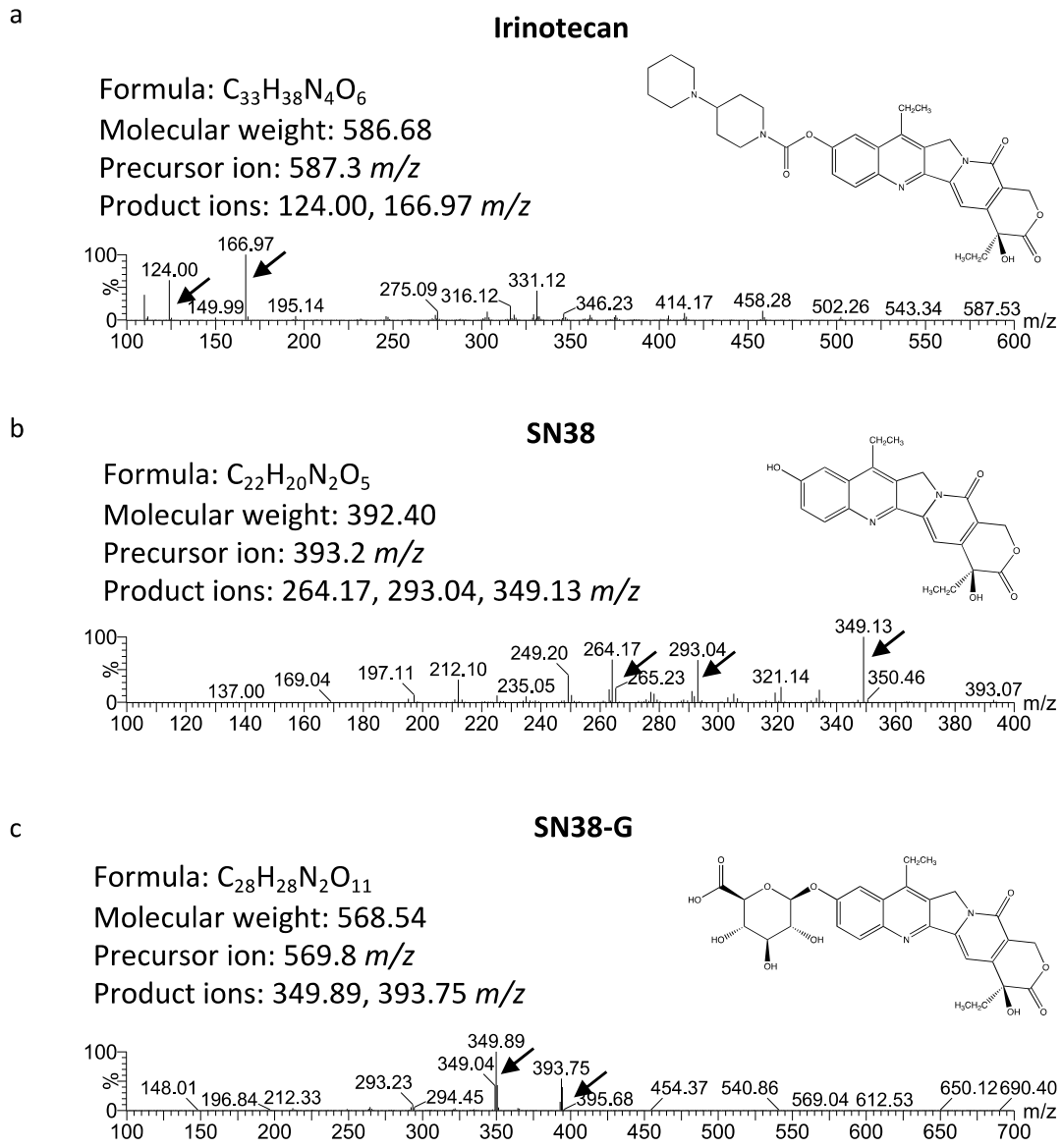

Figure 3.1 Mass spectra of product ions (daughters) for irinotecan, SN38 and SN38-G.

The chemical structures, molecular weights, precursor and product ions (indicated by black arrows and in detailed in **Table 2.1**) are given for (a) irinotecan, (b) SN38 and (c) SN38-G. (a-c) Y-axis shows extracted ion intensity (%) and x-axis shows mass-to-charge ratio (m/z).

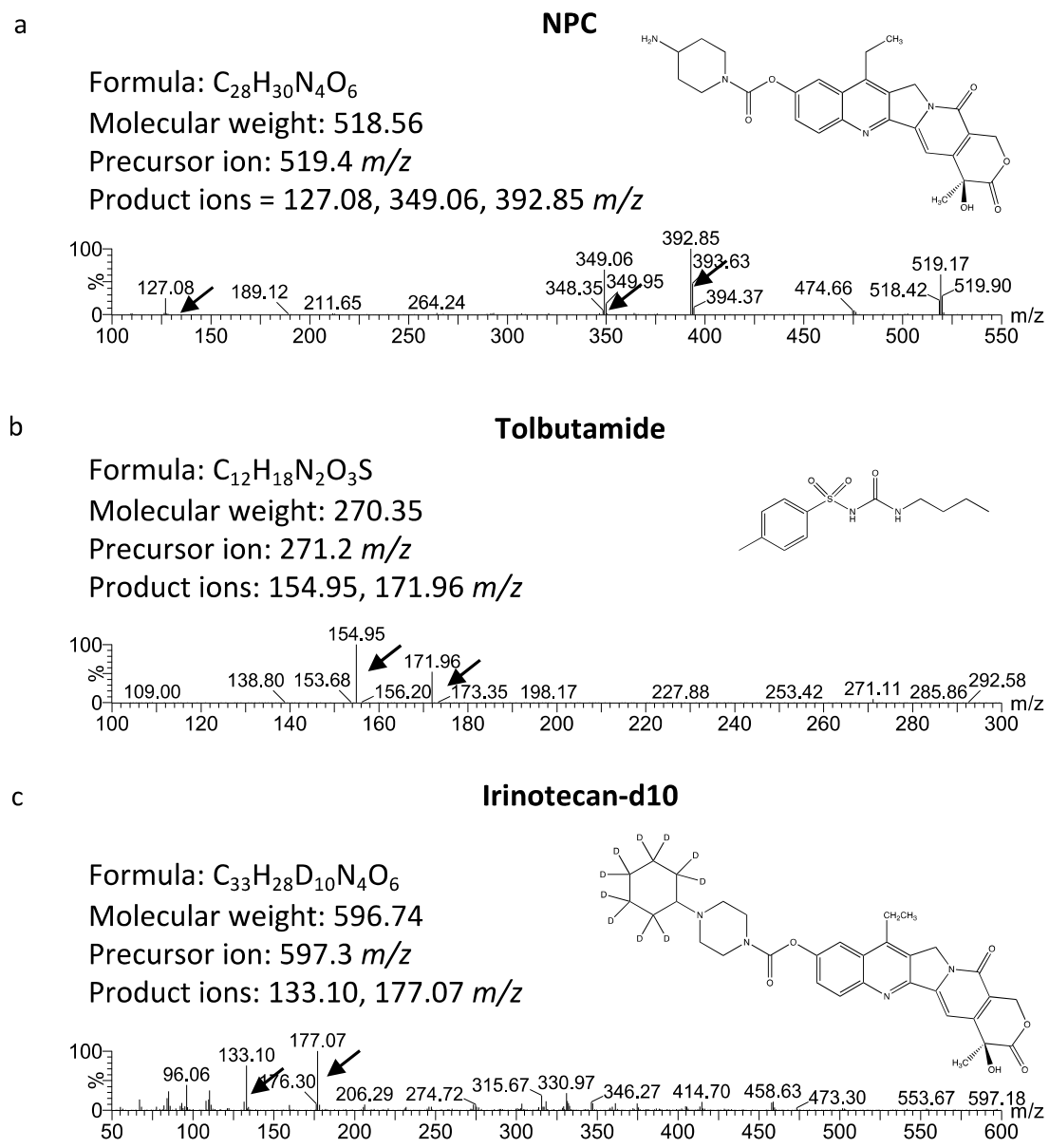

Figure 3.2 Mass spectra of product ions (daughters) for NPC, tolbutamide and irinotecan-d10.
The chemical structures, molecular weights, precursor and product ions (indicated by black arrows and in detailed in **Table 2.1**) are given for (a) NPC and internals standards (b) tolbutamide and (c) irinotecan-d10. Tolbutamide and irinotecan-d10 and were used as internal standards for SN38 and irinotecan, respectively. (a-c) Y-axis shows extracted ion intensity (%) and x-axis shows mass-to-charge ratio (m/z).

3.1.2. Retention times using the optimised channels

Representative chromatograms of drug standards are shown in **Figure 3.3** showing irinotecan, SN38, SN38-G, NPC, and internal standards irinotecan-d10 and tolbutamide. No endogenous interfering peaks were visible at the RT of each compound of interest. The RT for irinotecan was approximately 6.8 minutes, SN38 was 9.8 minutes, SN38-G was 6.1 minutes, NPC was 6.5 minutes, tolbutamide was 10.5 minutes and irinotecan-d10 was 6.6 minutes.

3.1.3. Standard curves

Typical standard curves for the compounds of interest are shown in **Figure 3.4**. High or low concentration standard curves were made up fresh from master stock and diluted 1:1 to produce a 6-point curve, and run each day by LC-MS/MS. The standard curves were linear and working range was either 'high' 1000-16 ng/ml or 'low' 100-1.5 ng/ml.

3.1.4. Limit of detection

The limit of detection (LOD) is the lowest concentration of analyte to be detected above background noise (FDA, 2001). The developed method was shown to be highly sensitive for all of the analytes tested. Example chromatograms of SN38 are shown (**Figure 3.5**), where decreasing amounts of a 10 ng/ml solution of SN38 in methanol were examined by LC-MS/MS. A concentration of 0.1 ng/ml could be detected, more than 3 times above background noise. The LODs for each analyte are shown in **Table 3.1**. Irinotecan and SN38-G both had a LOD of 0.5 ng/ml. The percentage coefficient of variation (%CV) was high for all analytes at the lower limit of detection. However, the LOD only accounts for the most likely, reliably detectable, lower-limit and may not therefore be an accurate, quantifiable value.

3.1.5. Limit of quantification

Limit of quantification (LOQ) is the lowest concentration at which the analyte can be reliably detected and quantified. Each analyte must be at least 3 times the peak area (PA) of background noise with a %CV of less than 20% (FDA, 2001). The LOQ for irinotecan was 1 ng/ml and 0.5 ng/ml for SN38 and SN38-G. LOQ was slightly higher than the LOD presumably due to the increased background created by endogenous proteins in the supernatant after centrifugation as opposed to the cleaner methanol standard (without protein) used for LOD analysis.

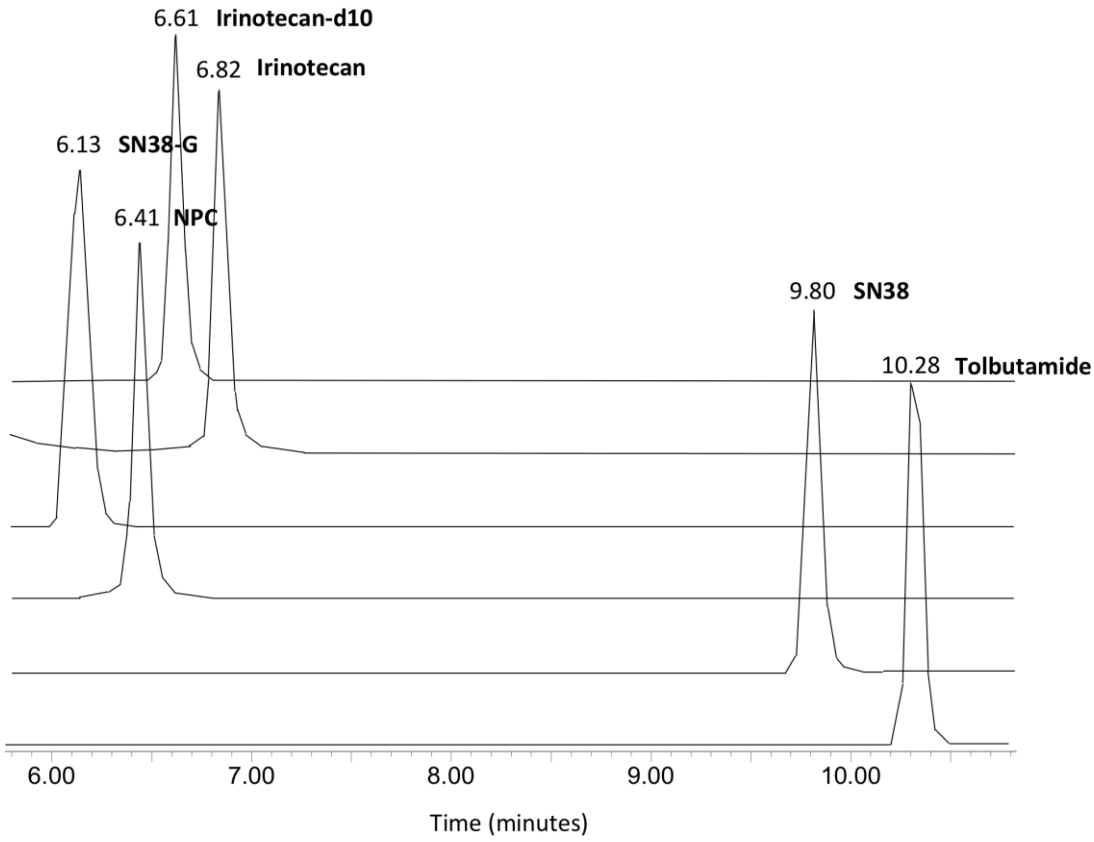

Figure 3.3 A merged chromatogram displaying the retention times for each compound of interest. Retention times were as follows, irinotecan (6.82 minutes), SN38 (9.80 minutes), SN38-G (6.13 minutes), NPC (6.41 minutes), tolbutamide (10.28 minutes) and irinotecan-d10 (6.61 minutes). Irinotecan-d10 and tolbutamide were used as internal standards for irinotecan and SN38, respectively.

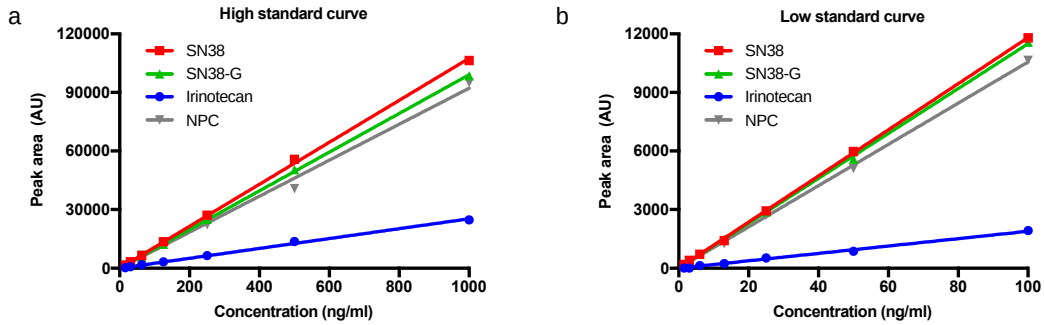

Figure 3.4 Example standard curves for each compound of interest.

Standard curves were made fresh from master stocks of irinotecan, SN38, SN38-G and NPC and run on the LC-MS/MS each day. (a) Example of a typical 'high' concentration standard curve starting at 1000 ng/ml and diluted 1:1. (b) Example of a typical 'low' concentration standard curve starting at 100 ng/ml and diluted 1:1.

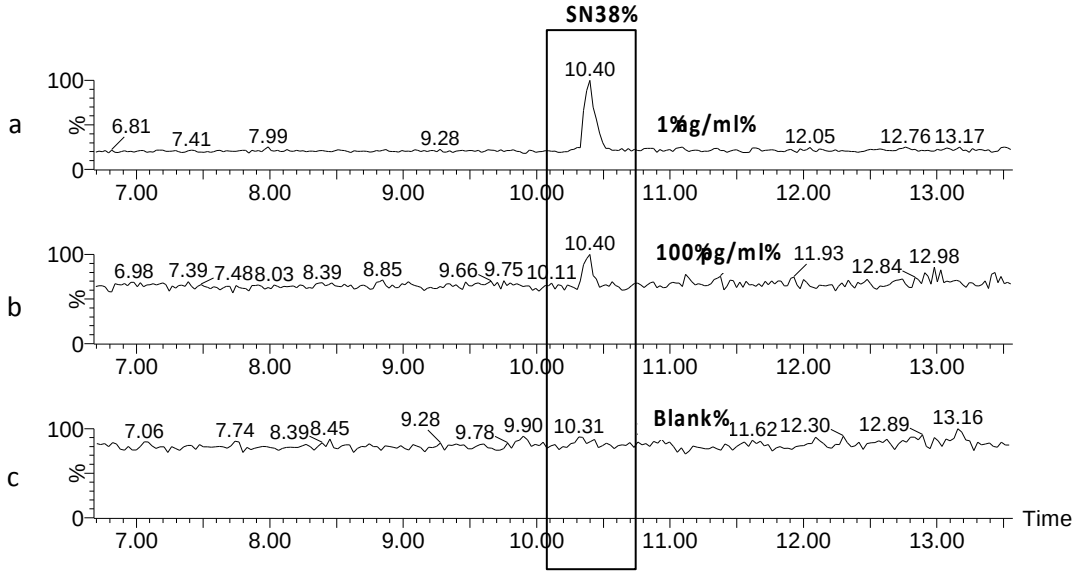

Figure 3.5 Chromatograms depicting the limit of detection (LOD) for SN38.

To determine the LOD, decreasing amounts of SN38 in methanol were examined by LC-MS/MS. (a-b) The black rectangle highlights the SN38 peak at 10.40 minutes for both concentrations (a = 1 ng/mg and b = 0.1 ng/ml). (c) No peak was detected in the blank methanol sample. LOD for SN38 is 100 pg/ml as shown in (b). (a-c) Y-axis shows extracted ion intensity (%) and x-axis shows time in minutes.

Table 3.1 Limit of detection (LOD) for irinotecan, SN38 and SN38-G.

To determine the LOD, decreasing amounts of a 10 ng/ml solution of SN38 in methanol were examined by LC-MS/MS. LOD for irinotecan and SN38-G was 0.5 ng/ml and 0.1 ng/ml for SN38. The level of agreement between standards and actual concentrations were determined as the level of concordance (%) and calculated from the mean of 5 samples. Standard deviation (SD), coefficient of variation (CV).

Analyte	Concentration (ng/ml)	Concordance (%)	SD (%)	CV (%)
Irinotecan	10	100	0.0	0.0
	1	100	62	62
	0.5	74	104	141
SN38	10	100	0.0	0.0
	1	95	33	35
	0.1	148	85	58
SN38-G	10	100	0.0	0.0
	1	97	31	32
	0.5	111	37	33

Table 3.2 Limit of quantification (LOQ) for irinotecan, SN38 and SN38-G.

To determine the LOQ, decreasing amounts of a 10 ng/ml solution of all three compounds in drug-free murine plasma were examined by LC-MS/MS. LOQ was 1 ng/ml for irinotecan and 0.5 ng/ml for SN38 and SN38-G. The level of agreement between standards and actual concentrations were determined as the level of concordance (%) and calculated from single samples.

Analyte	Concentration (ng/ml)	Concordance (%)
Irinotecan	10	100
	1	87
	0.5	-
SN38	10	100
	1	109
	0.5	124
SN38-G	10	100
	1	100
	0.5	102

3.1.6. Stability of compounds over 18-hours

The stability of the compounds of interest were investigated over time to ensure the average run times at 8°C were not having a deleterious effect. Standards were kept in the sample chamber at 8°C and analysed by LC-MS/MS every 2-hours over an 18-hour period to imitate the approximate run time overnight (**Figure 3.6**). The %CV for human clinical trial analysis is cut off at 15%, however for pre-clinical PK study below 20% was acceptable (FDA, 2001). Both irinotecan and SN38 had a %CV below 15%, within the acceptable range. However, SN38-G had a %CV of 16.5%, indicating it was less stable than the other two compounds, but within the limits for pre-clinical studies.

3.1.7. Sample carry-over

The carry-over between samples in LC-MS/MS should ideally be less than 1% to ensure that there is no cross-contamination of samples (FDA, 2001). No detectable carry-over of any analyte was found when analysing the blank vials run in-between samples. Examples of clear chromatograms are shown in **Figure 3.7**, and this suggests that samples were not cross-contaminated during the run process. At higher drug concentrations, carry-over may have occurred but concentrations were kept below 1 μg/ml as the LC-MS/MS was highly sensitive and the *in vivo* doses administered were very low and from a late time-point. Standards were always run from lowest to highest concentration to minimise any possibility of cross-contamination.

3.1.8. Stability of compounds after repeated cycles of freeze-thaw

Murine tissue samples were stored at -80°C following collection and the extraction process was performed on ice at 4°C where possible. Once processed, samples were analysed by LC-MS/MS. However, in instances of machine failure which occurred several times, samples had to be re-frozen and run at a later time. To ensure freeze-thaw did not affect sample analysis, drug standards (1 μg/ml) were frozen on dry ice (-80°C), followed by rapid thawing to 37°C. This process was repeated for a total of 5 cycles. Control standards were kept at 4°C and did not undergo freeze thaw, serving as a reference. Freeze-thawed samples had a %CV of less than 0.2% for SN38 and 1.2% for SN38-G, but irinotecan gave 8.2% and may be susceptible to degradation through multiple freeze/thaw cycles which should therefore be avoided (**Table 3.3**).

3.1.9. Extraction efficiency of the LC-MS/MS method

Extraction efficiency is the percentage recovery of an analyte spiked and extracted from a biological matrix in comparison to the analyte spiked and extracted from the extraction solvent (methanol) (FDA, 2001). It is determined to ensure the method of extraction is producing a reliable percentage recovery of the compounds of interest.

A hand-held Turrex blender was used to homogenise tissues and extract the compounds in methanol at 1:4 tissue:methanol (w/v) followed by centrifugation to obtain a clear supernatant which was analysed by LC-MS/MS. Accuracy was determined as the agreement between the compound spiked into methanol compared to the same concentration spiked into tissues and reported as percentage analyte recovery (%AR) and should be 100% ± 20% (FDA, 2001). **Table 3.4** displays the %AR for each compound of interest. Samples resulting in more that 100% AR were due to the reduced volume after proteins were pelleted from the homogenate and indicated none was bound to the protein fraction. The hand-held blender gave high extraction efficiency for each compound from each tissue. Tumour, liver, kidney and colon were all within the acceptable range, however, only one sample was analysed per tissue. Serum did not require homogenisation and therefore the %AR is simply methanol extraction and centrifugation and shows none is bound to the protein fraction. This homogenisation method was time consuming, as it required cleaning between each sample (potential cross-contamination) and also produced heat (potentially degrade compounds of interest), despite this it gave a good %AR for each tissue investigated.

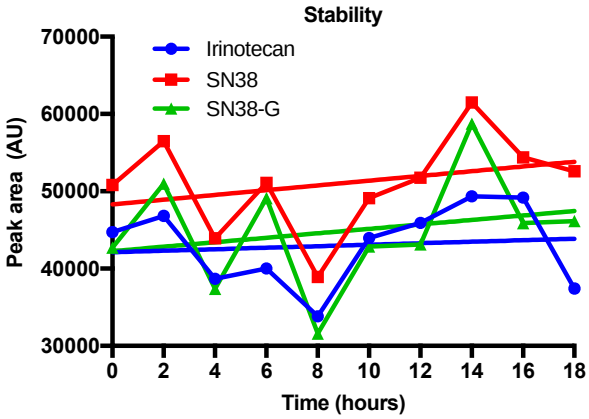

	Irinotecan	SN38	SN38-G
Average (PA)	42987	51062	44850
SD	5251	6273	7415
%CV	12.2	12.3	16.5

Figure 3.6 Stability of irinotecan and its metabolites.

A concentration of 1 µg/ml was injected from the same sample every 2-hours for each compound. Stability of compounds over 18-hours at 8°C (temperature of the sample chamber), indicated acceptable %CV for each. All compounds exhibited acceptable stability within this time period. Average peak area (PA) is given for each injection, standard deviation (SD), percentage coefficient of variation (%CV). A linear regression trend line is shown for each compound.

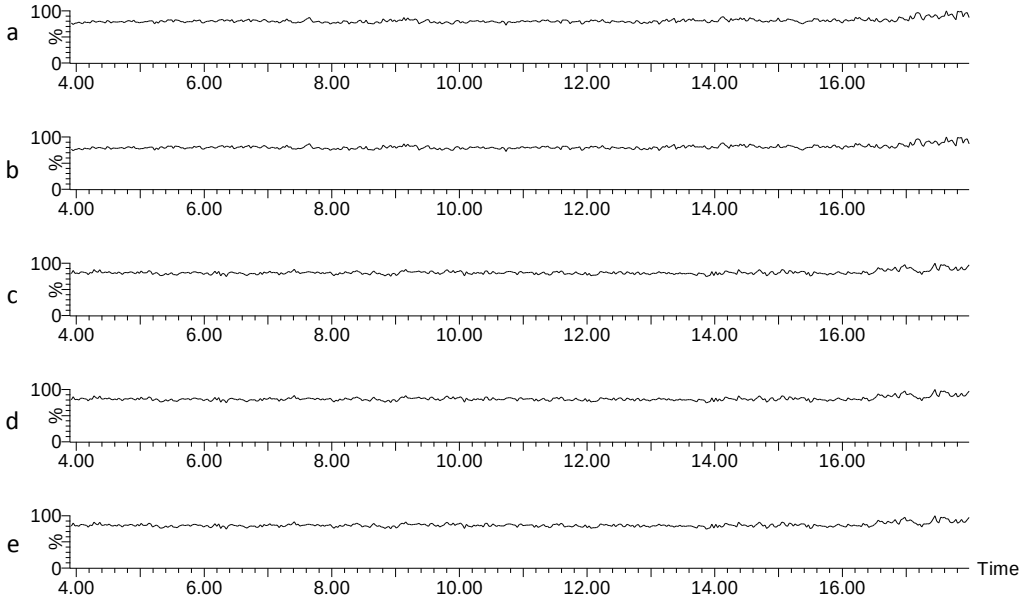

Figure 3.7 Example chromatograms for analysis of sample carry-over (cross-contamination). Chromatograms from methanol blanks run between 1 µg/ml concentrations of irinotecan, SN38, SN38-G and NPC to detect potential carry-over (a-e). No peaks were detected within the RT range of the analytes (6-11 minutes), indicating no carry-over at these concentrations. (a-e) Y-axis shows extracted ion intensity (%) and x-axis shows time in minutes .

Table 3.3 Freeze-thaw (F/T) cycles on stability of compounds.

Drug standards of 1 µg/ml underwent a total of 5 cycles of freezing (-80°C) and thawing (37°C). Samples that did not undergo freeze-thaw cycles served as references (standard). Irinotecan may be susceptible to degradation through multiple F/T cycles and should be avoided. Peak area (PA) is given for each compound (n=1), standard deviation (SD), percentage coefficient of variation (%CV).

	Irinotecan (PA)	SN38 (PA)	SN38-G (PA)
Freeze/thaw	42929	50854	95843
Standard	38220	50689	94291
Mean	40575	50772	95067
SD	3330	117	1097
%CV	8.2	0.2	1.2

Table 3.4 Extraction efficiency of irinotecan, SN38 and SN38-G in murine tissues (by LC-MS/MS).

Tissue homogenates were spiked with 1 µg/ml of irinotecan, SN38 and SN38-G and compared to 100% methanol spiked with the same to give percentage analyte recovery (%AR) shown. More than 100% AR was due to the reduced volume after proteins were pelleted from the homogenate and shows none was bound to this protein fraction. %AR values are single samples. *Serum did not require homogenisation.

Tissue	Irinotecan AR (%)	SN38 AR (%)	SN38-G AR (%)
Tumour	86.8	106.9	108.1
Liver	112.0	115.0	119.2
Kidney	97.4	113.9	119.8
Colon	104.6	120.7	134.3
Serum*	103.0	114.1	124.4

3.2. Whole organ *ex vivo* metabolism of irinotecan

3.2.1. *Ex vivo* metabolism of irinotecan using LC-MS/MS

The validated LC-MS/MS method was first applied to an *ex vivo* metabolism study using fresh whole murine liver and human CRC xenograft tissue. Whole organ, *ex vivo* drug metabolism experiments are useful for correlating *in vitro* and *in vivo* drug dosing by providing insight into carboxylesterase enzyme kinetics. Irinotecan is converted to SN38 *in vivo* by carboxylesterases 1 and 2 predominantly located in the liver (Guichard *et al.,* 1999). It was therefore important to assess whether the liver and tumour tissue used in the *in vivo* model of CRC contained the required enzymes to convert irinotecan to its active form and at what rate this could be achieved. To investigate *ex vivo* PK of irinotecan, fresh liver and human SW480 CRC xenografts were harvested from female CD1 nude mice and used to create crude *ex vivo* metabolism models. Irinotecan was spiked into homogenised tissues at concentrations of 10 µg/ml, sampled overtime at 37°C and analysed by LC-MS/MS. Rates of irinotecan and SN38 metabolism were determined for each tissue over a 3-hour time period.

The formation of SN38 was linear for both liver (R^2 = 0.98) and tumour (R^2 = 0.86) over the sampling period of 185-minutes (**Figure 3.8**). The liver produced four times more SN38 than tumour tissue, with a SN38 percentage change increase of 344%, whereas tumour produced just 44%. The rate of conversion to SN38 in the liver was 12-times the rate of production in the tumour tissue, 33.9 compared to 2.8 ng/min, respectively. These data show that livers of CD1 nude mice can metabolise irinotecan to SN38. SW480 tumours also metabolised irinotecan at a lesser extent but produced SN38 concentrations within the IC_{50} found *in vitro* for SW480 cells (**Section 4.1**). The LC-MS/MS method developed successfully extracted and detected concentrations of irinotecan and SN38 from mouse tissues.

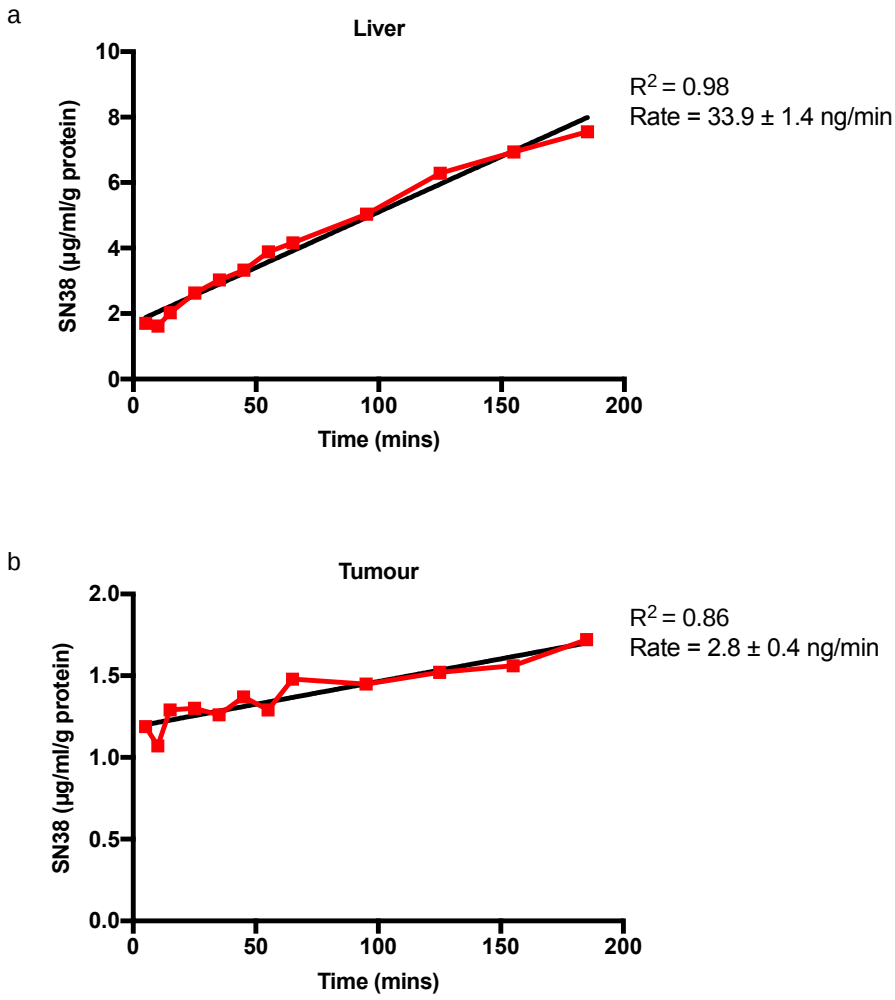

Figure 3.8 *Ex vivo* metabolism study of irinotecan in murine liver and xenograft tumour.

Ex vivo metabolism of irinotecan to SN38 by (a) murine liver and (b) human SW480 CRC xenograft tissue from a CD1 nude mouse. Tissues were homogenised in PBS, spiked with irinotecan and incubated at 37°C for the duration. Samples were analysed by LC-MS/MS to give concentrations per gram of protein (n=1 for each time point). Liver produced 4-times more SN38 than tumour within a total time period of 3-hours. SN38-G was not detected in any of the samples analysed, presumably the low concentrations of SN38 meant SN38-G would be below the limit of detection. Red line = SN38 concentration over time, black line = linear regression (rate = slope ± standard error), each time point is n=1.

3.3. PK study of free irinotecan in a murine model of CRC

An *in vivo* PK study of irinotecan in CD1 nude mice was performed to investigate the impact of dose on PK including biodistribution, metabolic profiles and clearance times in human CRC xenografts, major organs and blood. This study was performed to facilitate direct comparison to the concentrations detected in murine tissues following thMB drug delivery of irinotecan.

3.3.1. LC-MS/MS analysis of mouse tissues and serum for the detection of irinotecan and its metabolites

The newly validated LC-MS/MS method was successfully applied to determine the tissue and serum concentration-time profiles of irinotecan and its metabolites following systemic delivery. **Figure 3.9** and **Figure 3.10** show the PK profiles of two doses (50 mg/kg and 2.4 mg/kg) of single administration of i.v. irinotecan over 1-72 or 1-24 hour time periods, respectively. After 1-hour, low dose irinotecan at 2.4 mg/kg showed rapid diffusion into tissues and after 24-hours a near total clearance was observed. High dose irinotecan at 50 mg/kg gave the highest concentrations of irinotecan in tissues and serum. After 24-hours concentrations detected were within the pharmaceutically active range and by 72-hours the drug had been cleared. Both doses of irinotecan gave initial maximum concentrations in liver > spleen > kidney. The highest concentrations of SN38 were found in liver > kidney > serum, and for SN38-G, liver > kidney > colon. It was difficult to directly compare high and low doses, additional timepoints would have given greater insight into whether the profiles of metabolism and excretion were dose dependant. However, these doses were useful for comparison of metabolism and retention to irinotecan delivered using thMBs (**Section 3.4**).

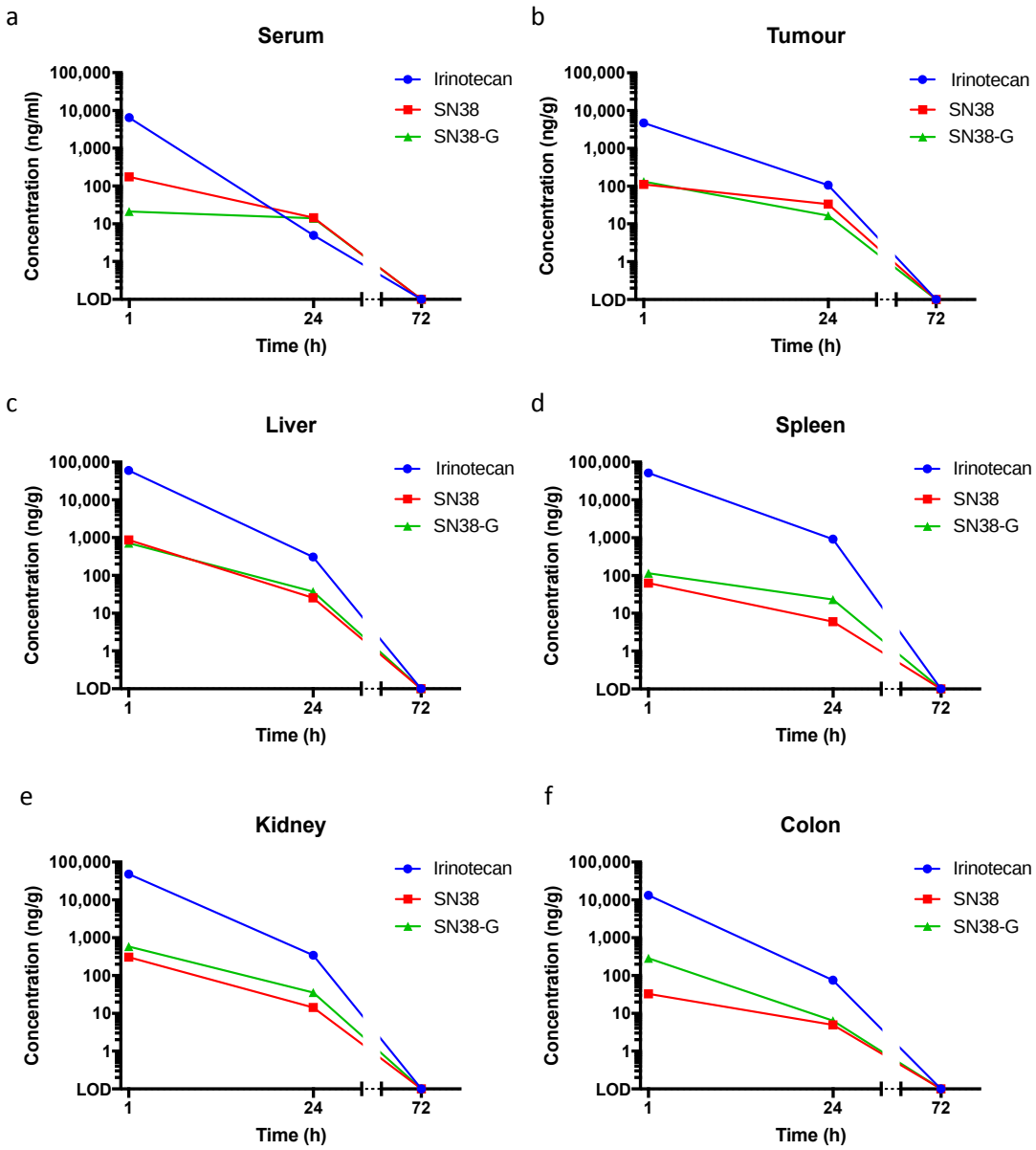

Figure 3.9 *In vivo* pharmacokinetic (PK) study of high-dose irinotecan.

A single i.v. bolus of 50 mg/kg irinotecan was administered to CD1 nude mice bearing human SW480 CRC xenografts. Tissues and serum were analysed by LC-MS/MS. Irinotecan, SN38 and SN38-G concentrations depreciated in a time dependent manner, with none detected after 72-hours. Each time point is a single mouse. LOD indicates none detected or less than the limit of detection.

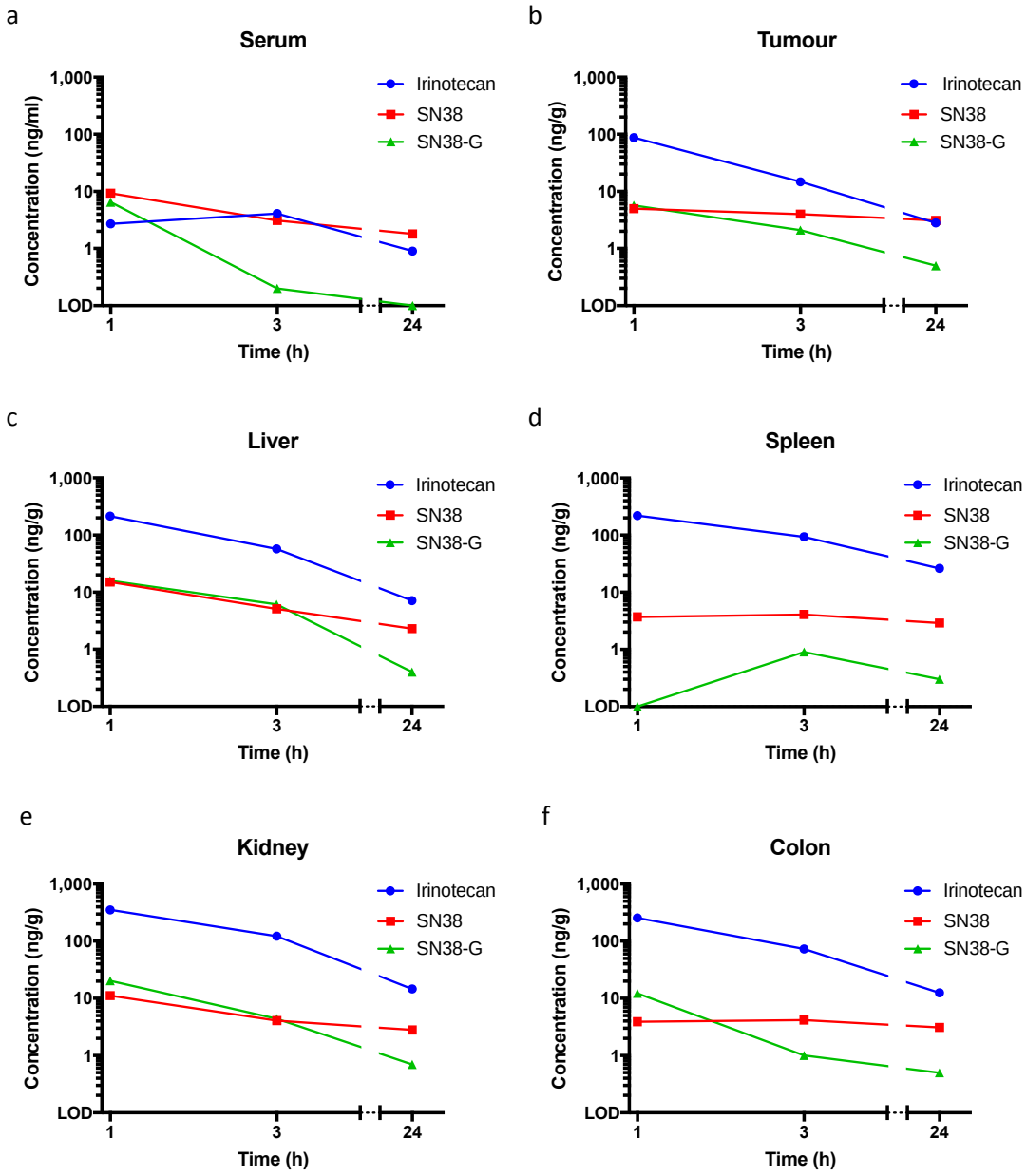

Figure 3.10 *In vivo* pharmacokinetic (PK) study of low-dose irinotecan.

A single i.v. bolus of 2.4 mg/kg irinotecan was administered to CD1 nude mice bearing human SW480 CRC xenografts. Tissues and serum were analysed by LC-MS/MS. Irinotecan, SN38 and SN38-G concentrations depreciated in a time dependent manner and were detectable after 24-hours (with the exception of serum). Each time point is a single mouse. LOD indicates none detected or less than the limit of detection.

3.4. Targeted, triggered drug delivery using irinotecan thMBs

LC-MS/MS was used to determine tissue concentrations of irinotecan and its metabolites from an *in vivo* study which used thMBs to deliver liposomally encapsulated irinotecan (~2.4 mg/kg) in combination with an US-trigger (x5 doses every 2-3 days). 72-hours post final treatment, tissues were collected for analysis. Dr N Ingram (Postdoctoral Researcher within the group), performed the experiment and kindly gifted tissues for analysis by Laura McVeigh using facilities at the Institute of Cancer Therapeutics, University of Bradford (UK).

3.4.1. Irinotecan thMBs: Quantification of drug loading by HPLC

For targeted US-triggered delivery of irinotecan, liposomes were attached to MBs to produce thMBs (**Figure 1.11**). Initial drug concentrations of irinotecan liposomes preparations were estimated using UV-Vis (as determined by Dr R Abou-Saleh, School of Physics and Astronomy, University of Leeds, data not shown). These estimates were used to load thMBs at a dose of 60 µg per mouse (2.4 mg/kg) per treatment. Based on these estimated doses, a control of free drug was administered at the same dose (2.4 mg/kg).

HPLC was used to determine the irinotecan concentration of thMBs at the end of the *in vivo* experiment. Due to the limited lifetime of the thMBs, it was not possible to predetermine their drug concentration prior to injection, therefore a portion of each sample was kept for analysis by HPLC at a later date. Two samples of irinotecan encapsulated liposomes (samples 1 and 2) gave concentrations of 22.1 mg/ml and 13.1 mg/ml, respectively (**Table 3.5**). The variation in drug loading between samples was high, with the second sample containing just over half the concentration of irinotecan as the first. In order to compensate for the lower drug concentration, liposome numbers were adjusted so that the irinotecan dose remained the same throughout the treatment schedule. However, this may have affected the number of liposomes bound to the MBs and/or free liposome may have been present in the dose delivered. Liposomes were prepared weekly and used to drug load thMBs made on each day of treatment. The average dose administered was 67.5 ± 8.3 µg equivalent to 2.7 ± 0.3 mg/kg see **Table 3.6**.

Table 3.5 Quantification of irinotecan in liposome preparations.

Irinotecan concentrations were quantified using HPLC. Mean irinotecan concentration was 17.6 ± 6.3 mg/ml. Liposome preparations (samples 1 and 2) were used to drug load MB preparations, shown in **Table 3.6**. Liposome sample 1 was used to produce the thMB samples 1-3, and 2 was used to produce thMB samples 4-5. Irinotecan was measured at a wavelength of 373 nm. Standard deviation (SD).

Liposome sample	Irinotecan (mg/ml)
1	22.1
2	13.1
Mean	17.6
SD	6.3

Table 3.6 Quantification of irinotecan thMB preparations.

Irinotecan concentrations were quantified using HPLC. Irinotecan was measured at a wavelength of 373 nm. Mean dosage was 2.7 ± 0.3 mg/kg. Dosage was calculated using the average weight of the CD1 female mouse cohort (0.025 kg). Five thMB samples were analysed (a total of 5-treatments) and the mean shown ± standard deviation (SD).

thMB sample	Irinotecan (µg/ml)	Dose per 150 µl injection (µg)	Dosage (mg/kg)
1	392.8	58.6	2.3
2	488.3	72.9	2.9
3	489.6	73.1	2.9
4	499.4	74.5	3.0
5	390.0	58.2	2.3
Mean	452.0	67.5	2.7
SD	55.5	8.3	0.3

3.4.2. Irinotecan thMBs: Biodistribution using LC-MS/MS

LC-MS/MS was also used to determine tissue concentrations of irinotecan, SN38 and SN38-G, from the longitudinal *in vivo* experiment that used targeted, triggered thMB drug delivery of liposomally encapsulated irinotecan (**Figure 3.11**). A dosing schedule of 5-treatments over a 2-week period was carried out using a xenograft mouse model of human CRC (SW480). 72-hours post final treatment, tissues were harvested for analysis.

Irinotecan thMBs + US statistically significantly inhibited tumour growth compared with equivalent low dose free irinotecan and vehicle control after 5-treatments, $p < 0.05$ and $p < 0.001$, respectively (**Figure 3.12**). thMBs + US resulted in 41% tumour growth inhibition compared to the vehicle control at end-point. There was no significant reduction in tumour growth in the thMBs - US group suggesting that an US-trigger was required for effective drug release, penetration and/or retention in tumour.

Of the three groups that received irinotecan, the only tumours to contain detectable concentrations of irinotecan and SN38 were those that had received targeted, triggered thMB delivery (thMB + US) (**Figure 3.13**). The two other groups thMB - US or Free, had no detectable levels of any analyte in tumour tissue.

Tissue biodistribution for all groups are shown in **Figure 3.14**. Irinotecan and SN38 were not detected in any other tissue apart from the thMBs - US and Free cohorts, with the exception of colon. The US-trigger appears to be responsible for the drug retention observed in tumour as well as other, off-target tissues (liver, kidney, spleen, colon). In the thMB + US group tissues, the highest concentrations of irinotecan were found in the liver and spleen, followed by kidney, tumour and colon. The highest concentrations of the active metabolite SN38, were found in colon, tumour and liver. Spleen and kidney had only 1/8 samples with SN38 detected at very low concentrations (7/8 samples were below the limit of detection). SN38-G was below the limit of detection in all the samples analysed.

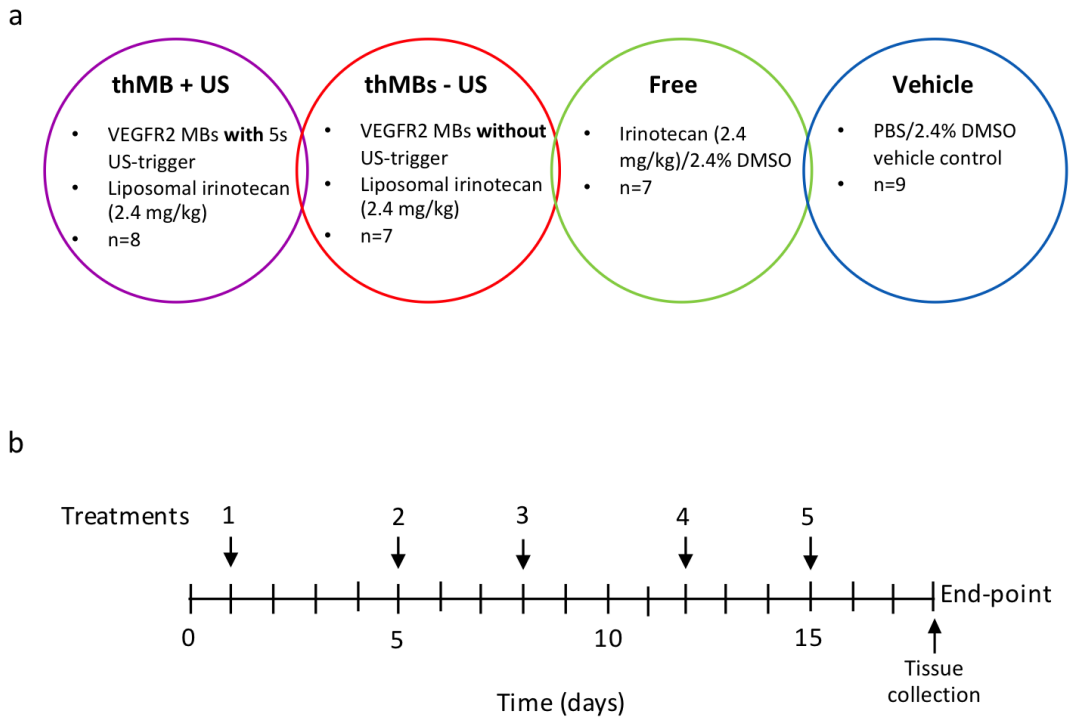

Figure 3.11 Irinotecan thMB cohorts and treatment schedule.

Tumour PK response was investigated. (a) Abbreviated nomenclature and treatment groups are shown with (n = number of mice per group). (b) Treatment schedule depicted. Treatments were initiated one-week post subcutaneous inoculation with SW480 CRC cell line (Day 1). Five doses of 2.4 mg/kg irinotecan (thMBs or Free) or a control (Vehicle) without drug were administered via i.v. injection over a 2-week period. End-point and tissue collection was 72-hours post final treatment. ThMBs were targeted to VEGFR2 and the US-trigger was a tumour localised 5-second 'tone burst' administered 4-minutes post bolus injection. Irinotecan thMB production and *in vivo* experiments were performed by Dr Nicola Ingram (Leeds Institute of Biomedical and Clinical Sciences, University of Leeds, UK).

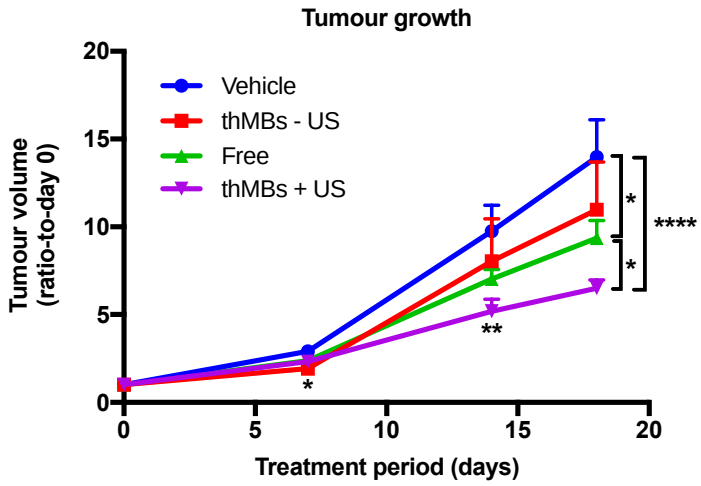

Figure 3.12 Low dose irinotecan delivery using US-triggered thMBs inhibits tumour growth. Effect of thMBs on tumour volume measured by HFUS imaging (mean (± SEM) ratio-to-day 0. A total of 5-treatments of irinotecan (~2.4 mg/kg) were given over a 2-week period, for treatment schedule and cohorts see **Figure 3.11**. Irinotecan thMB + US significantly inhibited tumour growth compared to control groups. Day 7 thMBs + US significantly different to Vehicle *p = 0.033, day 14 thMBs + US significantly different to Vehicle **p = 0.002, day 18 thMBs + US significantly different to Vehicle ****p = < 0.0001, thMBs – US *p = 0.036, and Free is also significantly different to Vehicle *p = 0.049. All statistics using Mann Whitney (two-tailed). ThMBs were targeted to VEGFR2 and the US-trigger was a tumour localised 5-second 'tone burst' administered 4-minutes post bolus injection. Irinotecan thMB production and *in vivo* experiments were performed by Dr Nicola Ingram (Leeds Institute of Biomedical and Clinical Sciences, University of Leeds, UK).

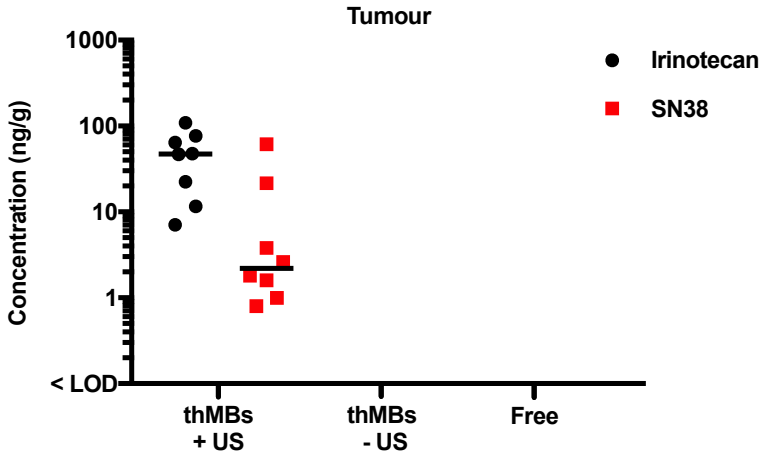

Figure 3.13 Tumour concentrations of irinotecan and its metabolite SN38 after irinotecan thMBs treatments.

Therapeutic microbubbles (thMBs) with or without US-trigger (+ US or - US) were compared to the equivalent free irinotecan dose. A total of 5-treatments of irinotecan (~2.4 mg/kg) were given over a 2-week period (**Figure 3.11**). Samples were collected for LC-MS/MS analysis 72-hours post final treatment. thMBs + US was the only cohort with detectable drug concentrations in tumour tissues. SN38-G was not detected in any of the samples analysed. Cohort number: thMBs + US (n = 8), thMBs - US (n = 8), Free (n = 7). Median value denoted by the bar. No data points indicate none detected (or less than the LOD). ThMBs were targeted to VEGFR2 and the US-trigger was a tumour localised 5-second 'tone burst' administered 4-minutes post bolus injection.

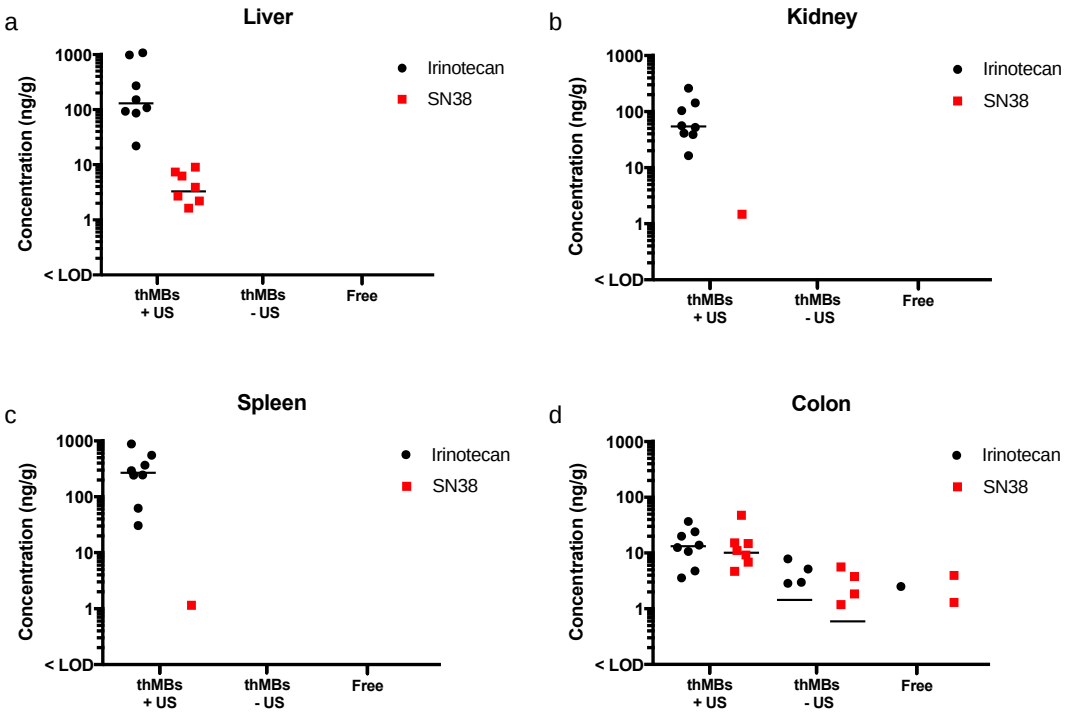

Figure 3.14 Tissue biodistribution of irinotecan and its metabolite SN38 after irinotecan thMBs treatments.

Therapeutic microbubbles (thMBs) with or without US-trigger (+ US or - US) were compared to the equivalent free irinotecan dose. A total of 5-treatments of irinotecan (~2.4 mg/kg) were given over a 2-week period (**Figure 3.11**). Samples were collected for LC-MS/MS analysis 72-hours post final treatment. (a-d) thMBs + US gave detectable drug concentrations in all tissues. (d) Colon was the only tissue to contain detectable drug concentrations in the other cohorts (thMBs - US and Free). SN38-G was not detected in any of the samples analysed. Group sizes: thMBs + US (n = 8), thMBs - US (n = 8), Free (n = 7). Median value denoted by the bar. No data points indicate none detected (or less than the LOD). ThMBs were targeted to VEGFR2 and the US-trigger was a tumour localised 5-second 'tone burst' administered 4-minutes post bolus injection.

3.4.3. Irinotecan thMBs: Relative percentages of irinotecan and its metabolites in comparison to free irinotecan

The LC-MS/MS method developed here was not able to distinguish encapsulated from free drug. Therefore, it was unable to inform as to whether the irinotecan detected in tissues was liposomally encapsulated and protected from metabolism, or 'free' drug that had been released and available for metabolism. Plotting the data from **Figures 3.10, 3.13 and 3.14** as relative percentages allows the comparison of the proportions of the parent drug with its metabolites, independent of concentration (**Figure 3.15**). Comparing thMBs + US (72-hours post final treatment) with 2.4 mg/kg free drug delivery at 1, 3 and 24-hours, can give insight into the mechanism of drug release when using thMBs for drug delivery.

The conversion of irinotecan to SN38 is dependent on the levels of carboxylesterase enzymes present in each tissue or blood. Liposomes typically release drug slowly and the presence of SN38 was evidence of drug release. The highest percentages of SN38 from the thMBs + US group (**Figure 3.15 a**) were detected in the colon, and tumour had the second highest. Liver, spleen and kidney all had ~100% irinotecan suggesting the irinotecan detected in these tissues was encapsulated or perhaps retained within the macrophage-monocyte system i.e. unavailable for metabolism.

For 2.4 mg/kg free drug (**Figure 3.15 b**), tumour, liver, kidney, spleen and colon all had a similar metabolism profile, with the relative percentage of irinotecan falling over time with increasing SN38 and low percentages of SN38-G. The highest relative percentages of SN38 were found in serum, followed by tumour, liver, kidney/colon and spleen. In serum, after 1-hour equal percentages of SN38 and SN38-G were found with low circulating irinotecan. After 3-hours SN38-G was lower leaving equal irinotecan and SN38 until 24-hours where SN38-G was completely cleared leaving less irinotecan than SN38.

As no drug or metabolites were detected after 72-hours (2.4 mg/kg x5 doses or 50 mg/kg free irinotecan), it suggests that it is this drug accumulation and retention in tumours that has improved the therapeutic window of irinotecan. The metabolic profiles of free drug indicated a fall in total irinotecan over time with increasing SN38, and completely eliminated by 72-hours. The thMB tissues had high percentages of irinotecan with SN38 mostly found in tumour and colon. This suggests that thMBs have increased the therapeutic window of irinotecan allowing not only drug retention but more importantly higher percentages of the active metabolite within tumour tissues after 72-hours.

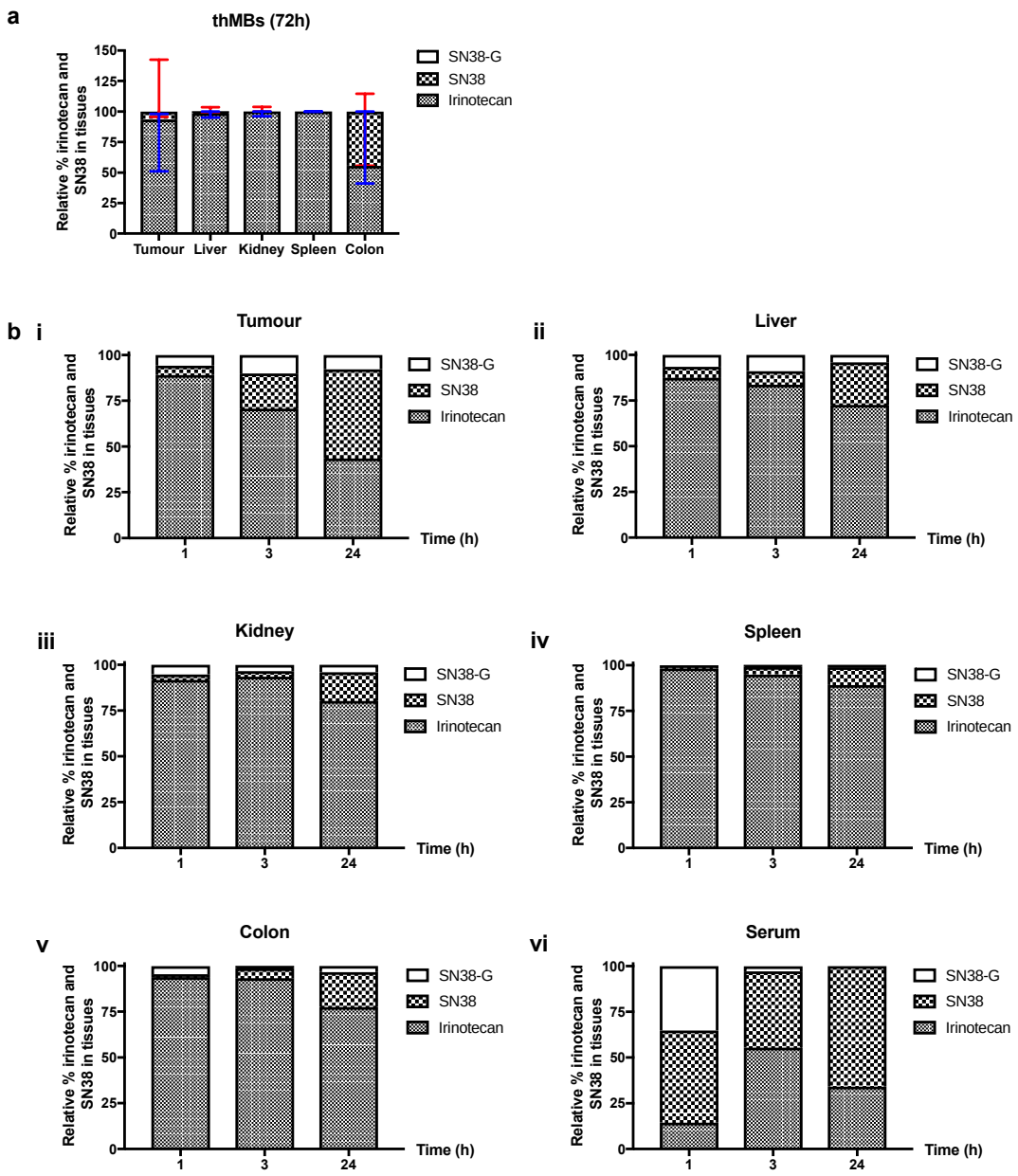

Figure 3.15 Relative percentages of irinotecan and its metabolites SN38 and SN38-G.

Relative percentages of irinotecan and metabolites after (a) Irinotecan thMBs (+ US) 2.4 mg/kg x5, collected 72-hours post final treatment (n=8). Each bar represents median (± 95% CI) percentage. Plotted from data presented in **Figure 3.13** and **Figure 3.14**. (b) Free irinotecan 2.4 mg/kg single dose over time (1, 3 and 24-hours). Each bar represents data from a single mouse. Plotted from data presented in **Figure 3.10**. High relative percentages of irinotecan (a) suggests the drug has remained encapsulated and protected from metabolism when compared to free drug (b).

3.4.4. Irinotecan thMBs: Irinotecan and metabolites detected in murine colon

The only other tissue with detectable concentrations of analytes from thMBs - US and Free cohorts was colon. ThMBs + US had the highest levels of irinotecan and SN38 detected in 8/8 and 7/8 respectively followed by thMBs - US which had 4/8 colons with irinotecan and SN38 detected, lastly free irinotecan had 2/7 colons with irinotecan and just one colon had detectable levels of SN38 (**Figure 3.16**).

Further metabolism of irinotecan to SN38 by carboxylesterases in the gut, combined with intrahepatic recycling of SN38-G to SN38, may explain the higher percentage ratio of SN38 to irinotecan found in the colons of all groups. Linear regression curves are shown for each group (**Figure 3.16 a**) and combined (**Figure 3.16 b**) (p = <0.005 and 0.0001 respectively). However, the free group has just one value and it falls outside of the 95% probability lines.

Despite detection of irinotecan and SN38 in the colons from all groups, these concentrations of SN38 would be considered very low. None of the mice experienced diarrhoea, a dose-limiting side effect of irinotecan in humans, suggesting that there was no adverse effect at these concentrations.

a

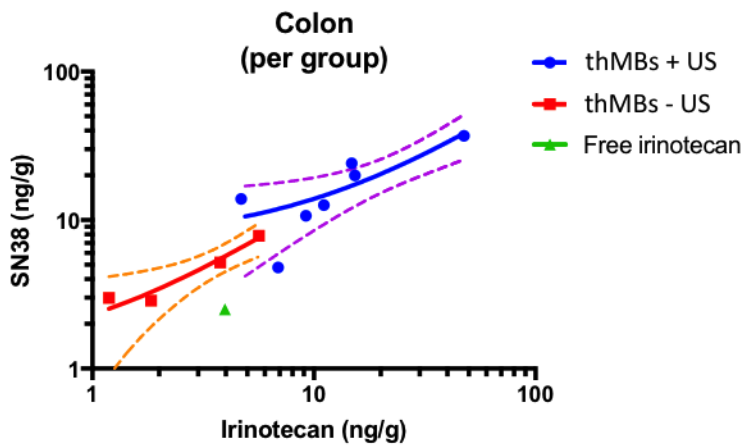

	thMBs + US	thMBs - US
Goodness of fit		
R squared	0.8042	0.9682
Is slope significantly non-zero?		
P value	0.0062	0.016
Deviation from zero	Significant	Significant

b

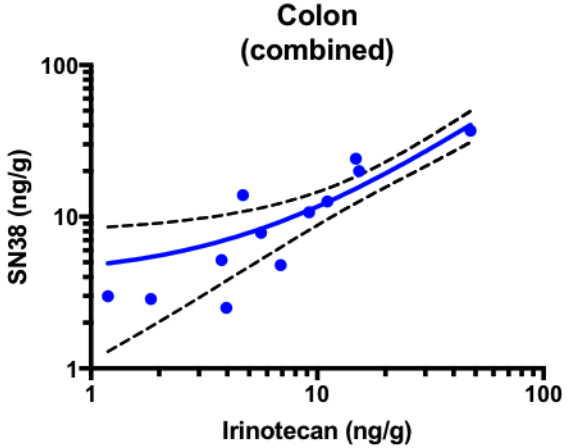

Goodness of fit	
R squared	0.8346
Is slope significantly non-zero?	
P value	<0.0001
Deviation from zero	Significant

Figure 3.16 Irinotecan and its metabolite SN38 detected in the colon of all treatment groups (LC-MS/MS).

A total of 5-treatments of irinotecan (~2.4 mg/kg) were given over a 2-week period (**Figure 3.11**). Samples were collected for LC-MS/MS analysis 72-hours post final treatment. A linear conversion relationship between irinotecan and SN38 was found in colons for therapeutic microbubbles (thMBs) with or without US-trigger (+ US or - US) and for all groups (thMBs + US, thMBs - US and Free) combined. ThMBs were targeted to VEGFR2 and the US-trigger was a tumour localised 5-second 'tone burst' administered 4-minutes post bolus injection. R squared, and P value displayed in tables below each graph. Dotted line indicates 95% confidence level.

3.5. Discussion

This chapter presents a newly developed and validated LC-MS/MS method to quantify concentrations of irinotecan and its metabolites in murine xenograft tumours, tissues and blood samples. The method was successfully applied to study *ex vivo* metabolism and PKs of free irinotecan and finally was used to determine whether targeted, triggered thMBs could successfully deliver irinotecan to tumours using an *in vivo* model of human CRC.

Irinotecan is a prodrug whereby hydrolysis by carboxylesterases transforms it into its active form SN38, a highly toxic topoisomerase I poison (Mathijssen *et al.,* 2001; Chabot, 1997). However, a low percentage of total irinotecan is actually metabolised to the active SN38 in humans (Senter *et al.,* 2001; Zamboni *et al.,* 1998). SN38 formation within tumour is an important aspect of its anticancer effect (Xu *et al.,* 2002). SN38 is then further deactivated by glucuronidation to SN38-G and it is the rate of glucuronidation which impacts its efficacy (Tobin *et al.,* 2006).

3.5.1. Optimisation and Validation of LC MS/MS: Detection of Irinotecan, SN38 and SN38-G

A validated and optimised method using LC-MS/MS was successfully applied to determine concentrations of irinotecan and metabolites from murine xenograft tumours, tissues and blood samples (**Section 3.1**). This has been performed previously in pre-clinical plasma and tumour samples from rabbit, porcine and human (Khan *et al.,* 2005; Goldwirt *et al.,* 2012; Park *et al.,* 2014; Chen *et al.,* 2012). However, the LC-MS/MS method presented here required optimisation, determination of limits of detection and the extraction method validated using our own drug standards, in order to provide the sensitivity and accurate drug and metabolite quantification required to access thMB delivery *in vivo*. This LC-MS/MS method represents the first quantitative determination of irinotecan and SN38 after *in vivo* delivery of targeted, US-triggered thMBs.

The LOD for irinotecan and SN38-G was 0.5 ng/ml and for SN38 was 0.1 ng/ml. In plasma, the LOQ was 0.5 ng/ml for both SN38 and SN38-G and for irinotecan was 1 ng/ml. The differences seen between LOD and LOQ were to be expected, with more background signal created by endogenous proteins from the plasma and typical of tissue homogenate supernatants (FDA, 2001). Analyte standards were stable over average run times with no detectable carry-over observed between samples. Freeze-thawing should be avoided for irinotecan but SN38 and SN38-G showed little variation over 5-cycles. Analytical recovery was high using the extraction method described with all compounds and tissues within the

100 ± 20% efficacy range, despite being time-consuming. This could be improved in future with the use of a bead homogeniser which rapidly processes samples in bulk with no risk of sample cross-contamination.

In addition, this method required only 20 µl of sample supernatant for analyte quantification, useful for small tumour samples or low volumes of blood. Taken as a whole, the LC-MS/MS method described is sensitive, precise and accurate and allows rapid simultaneous quantification of irinotecan and metabolites from murine blood and tissue samples. This method was used to analyse irinotecan metabolism, PK and biodistribution studies using murine models of human CRC and further studies using SN38 thMB throughout this thesis.

3.5.2. *Ex vivo* drug metabolism study using irinotecan

Spiking liver and tumour *ex vivo* provided an insight into the metabolism of irinotecan and whether the metabolites produced would be at detectable levels (**Section 3.2**). Irinotecan at 10 µg/ml was used to emulate concentrations delivered with *in vivo* dosing using thMBs and was a way of observing metabolite formation over time and whether these concentrations would be detectable at low doses. Irinotecan spiking produced detectable levels of SN38 but other metabolites SN38-G and NPC were not detected (or below the LOD). Therefore, detection of SN38-G or NPC from low levels of irinotecan was deemed unlikely.

A blender homogeniser was used creating a tissue homogenate containing tissue pieces, whole cells and lysed cells. Potentially this homogenisation method was not efficient enough to lyse all cells and release the necessary enzymes in sufficient concentrations to produce detectable concentrations of metabolites.

Ex vivo spiking is uncommon, microsomal assays using pooled liver samples with various centrifugation, dialysation and protein quantification steps are normally used to collect enzymes for metabolism studies (Senter *et al.,* 2001; Iyer *et al.,* 1998; Lu *et al.,* 2015). Murine liver microsomes were available commercially but not for the strain of mouse or the human CRC tumour used for the *in vivo* study. However, *ex vivo* spiking was a rapid and easy way to determine the presence of the required enzymes for irinotecan conversion and ability to produce SN38 at therapeutic concentrations (Guichard *et al.,* 1999). Although it was limited and potentially an inaccurate way of assessing drug metabolism of irinotecan, it determined SN38 could be formed in both liver and SW480 xenograft tumours from CD1 nude mice, vital for its anti-tumour effect. This study also validated that

irinotecan and SN38 could be extracted from murine tissues using the newly developed LC-MS/MS method.

3.5.3. PK study of free irinotecan

A PK study (**Section 3.3**) was used to quantify irinotecan and its metabolites in mouse tissues and serum after i.v. injection of free irinotecan at 50 mg/kg (equivalent to clinical dosage) and 2.4 mg/kg (approximate amount delivered by thMBs). This study enabled the determination of irinotecan and metabolite clearance times to allow direct comparison to thMB delivery using the same model. After 24-hours, the 2.4 mg/kg dose showed near total clearance of SN38, and the 50 mg/kg dose was totally cleared by 72-hours. A similar study by Kalra *et al*. (2014) used 40 mg/kg free irinotecan and resulted rapid clearance from the plasma of NOD/SCID mice within 8-hours, with 90% of irinotecan cleared from the xenograft tumour within 24-hours and less than 48-hours for SN38 (Kalra *et al.,* 2014).

The half-lives of irinotecan and SN38 in murine plasma are approximately 0.6 and 7.4-hours respectively (Bissery *et al.,* 1996). The half-lives for SN38-G and NPC have not been defined in the literature for mice. However, with such few data points in this study, it is difficult to compare to other PK studies. Increasing the number of mice per time point would greatly improve confidence of each data point, and facilitate determination of PK parameters such as AUC, C_{max} and half-life of free drug in this model of human CRC. This would also allow precise clearance times and therefore determine how much longer thMB delivery extends the therapeutic window of irinotecan delivered in this way. Most PK studies only establish plasma profiles however, this study included major organs and tumours, all important to understanding potential side effects and tumour efficacy. Tumour PK analysis is not easy in humans, but has been shown has many benefits, such as predicting efficacy via drug concentrations reaching the tumour tissues and its rate of degradation and also in assessing potential drug resistance (Susan, 2015; Cummings *et al.,* 2003).

Comparing the 2.4 mg/kg PK to the *ex vivo* metabolism study over 3-hours, SN38-G was detected at similar levels to SN38 in all tissues after 1 and 3-hours. This indicates that homogenisation of the tissues before spiking with irinotecan was potentially inefficient (as previously discussed) and needs further optimising. However, like the *ex vivo* study, liver had much higher concentrations of SN38 than tumour (but more irinotecan found in the liver than tumour). Comparing the relative percentage of irinotecan and SN38, tumour had a higher percentage of SN38 than liver after 3-hours, but similar levels after 1-hour. This

may be explained by the differences between *ex vivo* and *in vivo* metabolism studies. *Ex vivo* metabolism takes place in a closed experimental system whereas *in vivo* is much more complex, with the rates of excretion changing the PK profiles. A high proportion of irinotecan is rapidly excreted unmetabolised via the hepatobiliary route, which may explain the differences between liver and tumour tissues *in vivo,* in this study.

This study enabled the determination of irinotecan and metabolite clearance times and metabolism profiles to allow direct comparison to thMB delivery using the same model of human CRC.

3.5.4. Irinotecan thMBs: HPLC quantification of drug loading

HPLC was successfully used to determine concentrations of irinotecan encapsulated in the liposomal formulations used for each of the x5 treatments over 2-weeks (**Section 3.4.1**). The dose loaded onto thMBs was thought to be the same as the free-drug (low dose) control, predetermined by UV-Vis to calculate irinotecan concentration upon liposome manufacture. The mean irinotecan dose per thMB treatment was 67.5 ± 8.3 µg (2.7 ± 0.3 mg/kg), the free irinotecan dose was 60 µg (2.4 mg/kg, diluted from fresh stock, concentration not determined). The inability to accurately pre-determine drug concentration prior to delivery was a problem which needed to be overcome. The use of HPLC or LC-MS/MS to quantify drug concentrations in liposomes before thMB production would have ensured more accurate drug loading. Quantities of liposomes required for whole experiments could be produced, aliquoted and freeze dried for storage to ensure treatment doses were reproducible throughout. These changes will be introduced to ensure the accuracy and reproducibility of drug doses in future pre-clinical studies.

3.5.5. Irinotecan thMBs: Biodistribution of irinotecan and SN38

The first known targeted, triggered thMB drug delivery of irinotecan has been demonstrated here and may have extended the therapeutic window of low dose irinotecan in a model of human CRC. End-point tumour growth inhibition was statistically significantly different to free irinotecan, and the vehicle control with no observable toxic effects. A previous study had shown that irinotecan (free drug) in combination with MBs and US increased doubling times of human glioblastoma xenograft tumours compared to irinotecan alone, but did not investigate biodistribution as in this study (Escoffre *et al.,* 2013b).

The validated LC-MS/MS method was then used to quantify irinotecan, SN38 and SN38-G in murine CRC xenograft tumours and tissues from this study where US was used to deliver

irinotecan in VEGFR2-targeted liposomes attached to MBs (thMBs). The tissues were harvested 72-hours after the last dose of irinotecan had been delivered. The results showed that only the mouse cohort given thMB + US had detectable irinotecan and SN38 in their tissues (with the exception of colon). This thMB delivery method has seemingly extended the 'therapeutic window' of irinotecan, a low dose was given yet using this modality, both irinotecan and SN38 were detected after 72-hours, but no SN38-G. Presumably the detection of SN38-G would be unlikely at such low SN38 concentrations and likely well below limit of detection.

The overall findings of the irinotecan thMB delivery study found tumour concentrations of SN38 were on average 6.7 times higher than those of liver, however not statistically significant. It is presumed that the addition of the US-trigger aided in the delivery of irinotecan to the tumour tissues via mechanisms of sonoporation and/or increased endocytosis (Lentacker *et al.,* 2014; McLaughlan *et al.,* 2013; Ferrara, 2008). The concentrations of SN38 found were in the low ng/ml range, comparable to the SW480 IC_{50} value found *in vitro* of for 72-hour SN38 treatment (**Section 4.1**), and therefore in the range for therapeutic effect. The tumour volumes for the experiment showed a 41% tumour growth inhibition compared to the vehicle control (**Figure 3.12**). Taken in combination with the tumour drug retention shown by LC-MS/MS, it appears that thMB + US improve the therapeutic index of irinotecan delivered in this way.

Interspecies differences in carboxylesterase enzyme levels and substrate kinetics are important factors to consider (Lian *et al.,* 2018). In rodents, metabolism of irinotecan to SN38 is up to 50%, whereas in humans it is less than 8% (Senter *et al.,* 2001; Zamboni *et al.,* 1998). This suggests humans may require much higher doses of irinotecan to have similar SN38 concentrations and the associated anti-cancer efficacy. Delivery of SN38 directly could improve tumour responses in man as carboxylesterase concentrations are a limiting factor for irinotecan efficacy (Iyer *et al.,* 2015) and in turn reduce interpatient variability. Due to its hydrophobic nature and pH-dependent activity, liposomal encapsulation has been a popular delivery option (Lei *et al.,* 2004; Pal *et al.,* 2005; Ahmad and Zhang, 2005) and ideal for loading onto the MB shell, an important factor for MB drug delivery (De Cock *et al.,* 2016).

Using a higher dose of irinotecan is limited by its liposomal encapsulation efficacy, with batch to batch variation high (**Table 3.5**). Irinotecan thMBs given in combination with vascular disrupting agent combretastatin A4 phosphate (CA4P), anti-angiogenic monoclonal antibody bevacizumab or EGFR-targeted monoclonal antibody cetuximab

(Wildiers *et al.,* 2004; Kuroda *et al.,* 2010; Wilke *et al.,* 2008) may improve tumour growth inhibition. However, combinations must be carefully considered to avoid adverse PK interactions such as the case of inhibition of glucuronidation or reduced clearance times (Gupta *et al.,* 1996; Gupta *et al.,* 1997).

The extended therapeutic window of irinotecan may be due in part to the liposomal formulation of the drug before attachment and delivery via MBs (Cool, Geers, *et al.,* 2013). A study by Sadzuka *et al.,* (1998) demonstrated that liposomes gave a protective effect in normal tissue, in addition to improving the tissue distribution profile but conversion to SN38 was not improved (Sadzuka *et al.,* 1998). It is possible that this protective effect allowed the accumulation and slow release of irinotecan from the liposomes once it had been delivered to tissues and why after 72-hours both it and SN38 remained at detectable levels.

It is well known that liposomalisation of chemotherapy drugs can improve anti-cancer effect and reduce dose limiting side effects (Gill *et al.,* 1995; Sadzuka *et al.,* 1997). A previous study by Sadzuka *et al.,*(1998) found liposomalisation of irinotecan reduced intestinal side effects, which may explain why the mice in this study did not experience diarrhoea, a major side effect of irinotecan (Sadzuka *et al.,* 1998). A study by Kalra *et al.,* (2014) found that using a nanoliposomal formulation of irinotecan (5-times lower than free drug) compared to the same dose of free irinotecan used in this PK study (50 mg/kg), had detectable concentrations of irinotecan and SN38 more than 168-hours post injection (Kalra *et al.,* 2014). As in this study, 90% of the free irinotecan had been cleared from circulation after 24-hours. This thMB study used a 25-times lower dose and was detectable 72-hours later. Exactly how long irinotecan is retained for remains unknown thus far.

3.5.6. Effect of the US-trigger

Liposomalisation of irinotecan alone does not explain why the control group thMB - US did not extent the therapeutic window, containing the same dose of loaded liposomes but without US-trigger. The US-trigger was an unfocused narrow beam with a mechanical index (MI) of 0.21 by Church approximation (Church, 2005) and a duty cycle of 1%, which was deployed over the xenograft tumour for a total of 5-seconds. The beam would presumably destroy thMBs flowing through and attached to the tumour vasculature. The US may have had the power to pass a bit beyond the tumour (especially the smaller tumours), deeper into the abdomen of the mouse. However, the beam would quickly lose its power and would no longer have the acoustic pressure to destroy MBs. The beam was narrow with an

estimated the angle of divergence of 4° (personal communication Dr J McLaughlan). The possibility of the US-trigger destroying thMBs in other organs unlikely. It is more likely that the increased drug retention seen in other organs and tissues after 72-hours in the thMBs + US group is due to the US-trigger releasing liposomes from the thMBs within the tumour region to be taken up by cancer cells via endocytosis or via sonoporation effects. Those liposomes not rapidly taken up then circulate and tumour uptake may be increased further via EPR effect or retained in other tissues (Maeda, 2015; Fang *et al.,* 2018). The thMBs - US group would have circulating intact thMBs which are too large to escape the vasculature, MBs in the literature are quickly taken up by the cells of the macrophage-monocyte system and cleared relatively quickly. Those left in circulation, are prone to shrinkage as gas leaks out of the MB, forming MB lipid/liposomes clumps, this increased size compared to a single circulating liposome would have an increased clearance times. The larger the particle, the quicker the clearance (Alexis *et al.,* 2008).

3.5.7. Side effects of irinotecan thMBs

The murine colon tissues were the only tissues to have detectable levels of irinotecan and SN38 in all three cohorts of experimental animals following irinotecan delivery. This may have been due to the well documented 'enterohepatic recirculation' of irinotecan and SN38. It is this phenomenon that often leads to delayed, stage 3-4 diarrhoea experienced by patients receiving irinotecan chemotherapy treatment. No diarrhoea side effects were observed in any of the experimental cohorts used, not even with the highest dose of free-irinotecan used. Presumably, higher doses are needed to induce this side effect in mice. Other side effects to monitor in future experiments would be blood parameters for neutropenia, colon crypt deformation, fatty or inflamed liver and liver enzyme levels such as ALT and AST.

3.6. Summary

This chapter has presented a newly developed and validated LC-MS/MS method to quantify concentrations of irinotecan and its metabolites in murine xenografts, tissues and serum samples. The method was successfully applied to study *ex vivo* metabolism and PKs of free irinotecan and finally was used to determine that thMBs could successfully deliver low dose irinotecan to tumours with significant tumour growth inhibition using an *in vivo* model of human CRC. Increased accumulation and/or retention of irinotecan and SN38 in tumours (although not preferentially) may have increase the therapeutic index of drug delivered in this way. Further optimisation of the liposome drug loading is necessary to

ensure that treatments are uniform throughout the experiments and also for further clinical translation.

Chapter 4

SN38 thMBs:

In Vitro to *In Vivo* PK and PD Studies of Very Low Dose SN38

Introduction

Irinotecan is a prodrug, requiring carboxylesterases to transform it to the more active metabolite SN38 (Mathijssen *et al.,* 2001; Humerickhouse *et al.,* 2000). This conversion is vital for efficacy of the drug but human liver is inefficient with only 2-5% of irinotecan converted to SN38 (Senter *et al.,* 2001). Local conversion by tumour carboxylesterases is thought to play a role and may explain the variable response of solid tumours to irinotecan chemotherapy (Xu *et al.,* 2002). SN38 delivered directly would eliminate this rate limiting dependence on carboxylesterase presence. However, SN38 is severely hydrophobic and can therefore not be administered at therapeutic doses in any pharmaceutically suitable solvent. One solution to this would be to formulate SN38 into a protective nanostructure such as a liposome, micelle or polymersome (Sepehri *et al.,* 2014; Zhang *et al.,* 2013; Iyer *et al.,* 2015; Pal *et al.,* 2005). The advantages of encapsulation are many, not only making SN38 'deliverable', but keeping it in its pH-dependent active form and protecting the payload until it has reached its target, thereby reducing off-site toxicity. In addition, targeting ligands can be attached to the outside of the nanoparticle to target or enhance delivery to cancer cells as shown in *in vitro* studies (Geers *et al.,* 2013; McLaughlan *et al.,* 2013).

The aim of this chapter was to determine IC_{50} values for SN38 *in vitro* and compare these with liposomal formulations produced and optimised by Dr R Abou-Saleh, School of Physics and Astronomy, University of Leeds. These liposomes were then used *in vivo* to investigate tumour and tissue SN38 and metabolite profiles over time by comparing thMBs + US drug delivery with that of free drug. A longitudinal study was used to determine the tolerability, tumour inhibition and drug deposition after multiple treatments of very low dose SN38 thMBs. A further investigation on the effect of the US-trigger alone on tumour pharmacodynamics (PD) was also undertaken.

4. Results

4.1. SN38 cytotoxicity *in vitro*

Cytotoxicity assays were performed on human and mouse CRC cell lines and a mouse endothelial cell line to determine IC_{50} values. IC_{50} is the half maximal inhibitory concentration; the concentration of a drug required for 50% growth inhibition (Sebaugh, 2011). The lower the IC_{50} value, the greater potency.

The SN38 IC_{50} values for human CRC cell lines SW480, SW620, HCT116 and mouse CRC and endothelial cell lines MC38 luc11a and SVR, respectively, were measured by MTT cell proliferation assays with a broad range of SN38 concentrations. Due to the hydrophobic nature of SN38, sonication of the drug in tissue culture medium prior to cell application was necessary to ensure solubilisation. To confirm that the sonication step was not having an effect on the drug prior to application, LC-MS/MS was used to compare SN38 before and after 20-minutes sonication. No statistical differences were observed between the samples and SN38 was therefore assumed to be unaffected by the process (**Table 4.1**).

The dose-response curves at 24 and 72-hours for each cell line tested are shown in **Figure 4.1**, each fitting a typical sigmoidal profile with the exception of the HCT116 cell line which was biphasic (**Figure 4.1 a iii.**). SN38 was found to be highly cytotoxic, being most sensitive with HCT116, SW480 and SW620 cell lines, followed by the MC38 luc11A cell line (**Table 4.2**). The endothelial cells (SVR) were most resistant to SN38. All the mean IC_{50} values reported were determined from three independent experiments and were in the low ng/ml range. These values were 100-2000 times lower than those determined using irinotecan (Dr N Ingram, personal communication). No statistical differences were found between SW480 and SW620 IC_{50} values, presumably as they were derived from the primary and secondary tumours from the same patient (Leibovitz *et al.,* 1976). IC_{50} values between treatment times of 24 and 72-hours showed little variation, apart from the HCT116 and MC38luc11A cell lines. The 72-hour exposure in HCT116s showed a slight fall in cell viability compared to 24-hours in both IC_{50} values $p = 0.003$ and 0.01 for highest and lowest values (unpaired t-test (two-tailed)). Whereas in the MC38 luc11A the opposite was evident, 72-hour exposure showed an increase in cell viability compared to 24-hour IC_{50} values $p = 0.011$ (unpaired t-test (two-tailed)).

4.2. Topoisomerase I: Protein concentrations in human CRC cell lines

Topoisomerase I concentrations play an important role in DNA replication and transcription, and tumour levels may be a biomarker of chemotherapeutic efficacy of topoisomerase I inhibitors such as SN38 (Pfister *et al.,* 2009; Burgess *et al.,* 2008). An ELISA was used to determine topoisomerase I protein concentrations within the human CRC cell lines previously described (**Section 4.1**, **Figure 4.2**). No statistical differences were found between SW480 and SW620 cell lines in terms of IC_{50} values (with the exception of the biphasic HCT116), or topoisomerase I protein concentrations, suggesting that

Table 4.1 Sonication of SN38 prior to chemosensitivity assays does not have detrimental effect on the drug.

Due to the hydrophobic nature of SN38, sonication of the drug in tissue culture medium prior to chemosensitivity assay application (**Figure 4.1** and **Table 4.2**) was necessary to ensure solubilisation. Peak areas (PA) were compared between sonicated and non-sonicated samples (n=3). No differences were found between groups, suggesting sonication did not have a detrimental effect on the compound. Standard deviation (SD), percentage coefficient of variation (%CV).

Sample	Sonicated (PA)	Not sonicated (PA)
1	99907	102827
2	100859	100089
3	95153	94152
Mean	98640	99023
SD	3057	4435
%CV	3.1	4.5

Table 4.2 Table of IC_{50} values from SN38 chemosensitivity assay.

Human and mouse CRC (SW480, SW620, HCT116, MC38 luc11A) and mouse endothelial (SVR) cell lines, were treated with SN38 for 24 or 72-hours, followed by MTT assay. SN38 was highly toxic to all cell lines evaluated, with IC_{50} values in the nano molar (nM) concentration range. HCT116 had a biphasic response and therefore two values have been given.

		IC_{50} (nM)	
Species	Cell line	24 h	72 h
Human	SW480	7.2	6.4
	SW620	3.3	4.4
	HCT116	3.0	2.4
		0.6	0.4
Mouse	MC38 luc11A	19.0	28.5
	SVR	196.4	157.2

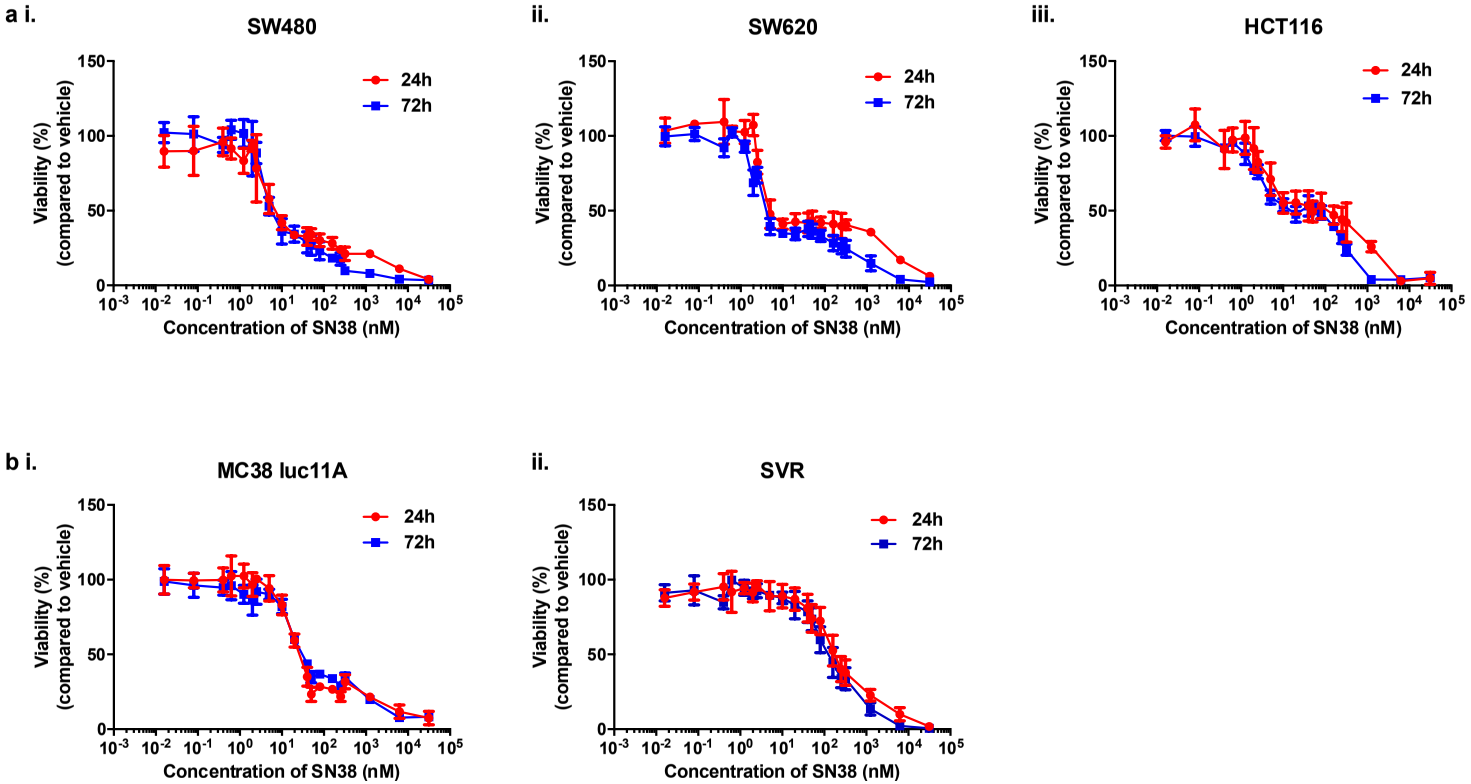

Figure 4.1 SN38 chemosensitivity assays.

(a) Human colorectal cancer cell lines (b) Mouse cell lines, i) colorectal and ii) endothelial cell lines. SN38 was high cytotoxic in all cell lines evaluated. The dose-response curves for each cell line were fitted to a sigmoidal profile, with the exception of (a iii) HCT116 cell line which was biphasic. Each data point is a mean of three experiments run in quadruplet. Percentage viability was calculated by using a vehicle control of 100% viability. IC_{50} values determined are shown in **Table 4.2**. Red = 24-hour treatment, blue = 72-hour treatment.

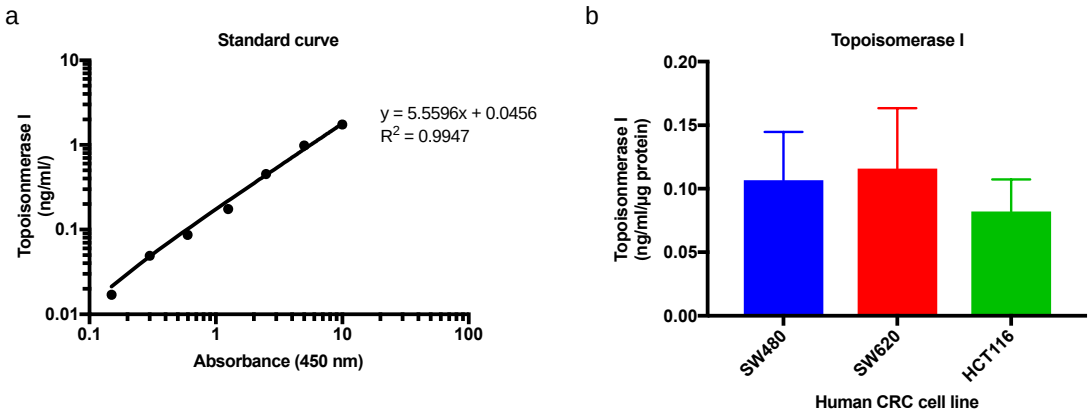

Figure 4.2 Concentrations of topoisomerase I detected in human CRC cell lines.

An ELISA was used to quantify topoisomerase I protein concentrations which were normalised to µg of total protein. a) The standard curve used to quantify topoisomerase I protein concentrations from b) human CRC cell lines (SW480, SW620 and HCT116). No statistical differences between cell lines were found. Mean (± standard deviation) are shown, three samples per cell line and each run in duplicate on a single ELISA plate.

topoisomerase I may indeed be a biomarker of SN38 response in this cohort of CRC cell lines.

4.3. SN38 liposome characterisation

Liposomes encapsulating SN38 were produced and optimised by Dr R Abou-Saleh, following the patented method for the lipid based formulation of SN38 (Ahmad and Zhang, 2005). The liposomes were fully characterised prior to their use in production of SN38 thMBs. Liposomes were aliquoted, freeze-dried and stored at -20°C until needed. Sterility of the liposomes was established prior to characterisation. Liposome characterisation was carried out to determine the size, concentration, drug concentration, structure, stability over time and cytotoxicity *in vitro*.

4.3.1. Sterility

For *in vitro* and *in vivo* studies, it was important to determine sterility of the samples prior to use. Liposomes were rehydrated using sterile 10 mM acetate buffer (pH 2) at 4°C and sterility was confirmed for each preparation by co-incubation of liposomes and tissue culture medium for 72-hours at 37°C. No contamination was found by inspection using x100 magnification or medium colour change suggesting both liposomes and acetate buffer were sterile. As an extra precaution, liposomes were also filtered aseptically through a 200 nm pore directly prior to use.

4.3.2. Size and concentration

Liposome size needed to be within an optimal range (50-450 nm) for medical use (Bozzuto and Molinari, 2015) and of a suitable concentration for the optimal and reproducible loading of thMBs. The size and concentration were measured using the qNano (iZON), a tunable resistive pulse sensing technique (200 nm pore size). The mean diameter of particles within this preparation was 242 ± 65 nm with a concentration of 4×10^{12} liposomes per ml (**Figure 4.3**).

4.3.3. Stability

UV-Vis was used to investigate stability of SN38 concentration within the liposome batch by sampling each week over a three-week period (performed by Dr R Abou-Salah) (**Figure 4.4**). Drug concentration appeared to be stable over this period and in the following experiments liposomes once reconstituted, were used within this time frame.

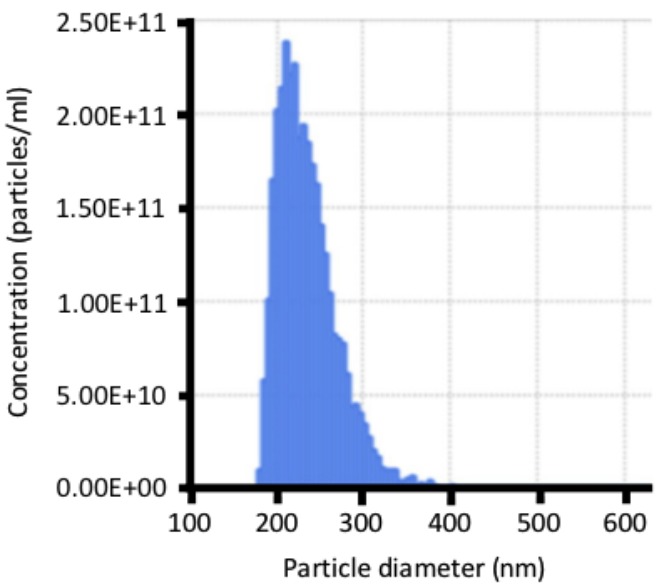

Figure 4.3 SN38 liposome size and concentration (qNano).

The qNano was used to determine the mean diameter of 242 ± 65 nm. Concentration was determined as 4 x 10^{12} liposomes/ml (diluted 1:20 prior to reading).

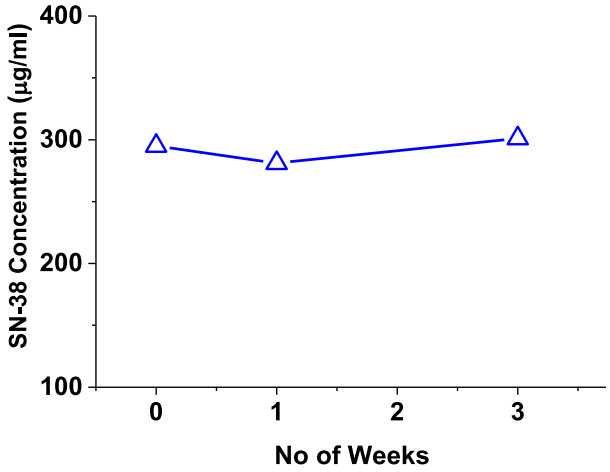

Figure 4.4 SN38 liposomes: Drug stability over time

UV-Vis was used to investigate SN38 concentration by sampling liposomes (n=1) over a three-week time period. Drug concentration appeared stable during this time.

4.3.4. SN38 concentration in liposomes

LC-MS/MS was used to determine the concentration of SN38 within the liposome preparation. Five aliquots were sampled from the original preparation and analysed by LC-MS/MS on the same day. The mean concentration of SN38 was 233.6 ± 45.9 µg/ml (**Table 4.3**). Variability between aliquots was high with a range of 179.3-299.5 µg/ml, despite being from the same preparation.

4.3.5. Cytotoxicity assays

The liposomal IC_{50} values of SN38 were determined by MTT cell proliferation assays using the SW480 CRC cell line (**Figure 4.5**). The cytotoxicity curves of SN38 liposomes were compared to free drug controls. Both liposomes and free drug were highly cytotoxic with IC_{50} values in the low nano-molar range and exhibited very similar cytotoxicity curves. SW480s were slightly more resistant to liposomal SN38 giving IC_{50} of 8.2 and 10.5 nM compared to free drug IC_{50} of 2.8 and 2.5 nM after 24 and 72-hour treatments, respectively. The differences in IC_{50}s between liposomal and free were not statistically significant, but variations could be due to the drug being protected in a liposome shell and released more slowly than the direct application of free drug, or the different cell response and cell internalisation pathways between free and liposomal SN38.

4.4. Optimising the LC-MS/MS method for very low dose SN38 detection in murine tissues

4.4.1. Improving sensitivity using an additional drying step

SN38 has been found to be 100-2000 times more potent than irinotecan *in vitro*. Therefore, SN38 was used at much lower doses than irinotecan in the preliminary *in vivo* experiments. In order to improve detection of very low dose SN38 in mouse tissues a more sensitive LC-MS/MS method was developed. To do this, an additional step was added to concentrate the extracted samples and improve the likelihood of detection. SN38 and SN38-G standard curves were compared before and after sample drying to determine any detrimental effect of pressure, heat and light experienced in the drying chamber on the standards. The slope of the standard curves did not differ for dried or undried samples suggesting that drying was an acceptable method to concentrate the samples (**Table 4.4**). Despite this, standard curves were always performed using dried samples and the internal standard tolbutamide was added to both samples and standards to improve reliability of the data with the additional steps and low expected concentrations.

Table 4.3 Concentration of SN38 in first liposome preparation (LC-MS/MS).

LC-MS/MS was used to determine a mean SN38 concentration of 233.6 ± 45.9 µg/ml (mean ± standard deviation (SD) of five samples).

Sample	SN38 (µg/ml)
1	179.3
2	255.5
3	299.5
4	209.5
5	224.2
Mean	233.6
SD	45.9

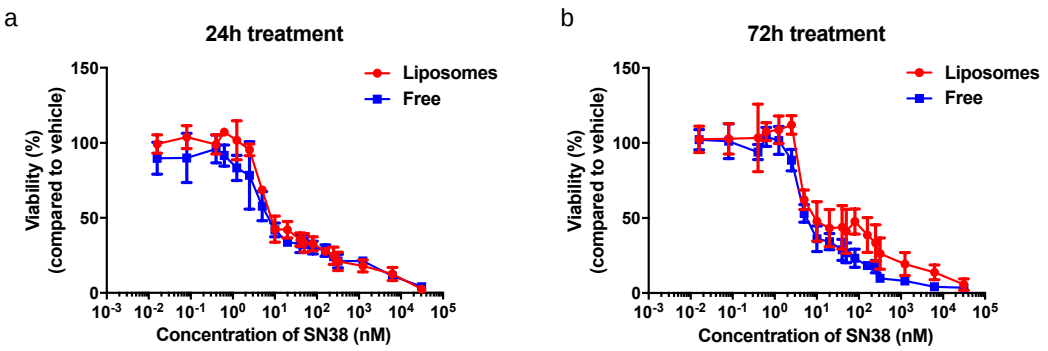

	IC_{50} (nM)	
SN38 treatment	24 h	72 h
Liposomes	8.2	10.5
Free drug	2.8	2.5

Figure 4.5 Chemosensitivity curves and IC_{50} values using SN38 liposomes.

SW480 CRC cells were treated with either SN38 liposomes or equal concentrations of free drug for (a) 24 or (b) 72-hours, IC_{50} values given below. No significant differences were observed between treatments or time points. Each data point is a mean of three MTT assay experiments run in quadruplet. SN38 liposome concentrations were determined via LC-MS/MS prior to use.

Table 4.4 Standard curves for SN38 and SN38-G were unaffected by additional concentration step. A comparison of the slopes from the standard curves for (a) SN38 and (b) SN38-G. The standard curves were unaffected by the additional concentration step to improve detection of very low concentrations of drug and its metabolite from murine tissue samples. Values given are peak areas from LC-MS/MS analysis. Mean ± standard deviation (SD) of three analyses, percentage coefficient of variation (%CV). Each standard curve was prepared fresh from master stock and run on non-consecutive days.

a

	SN38-G	
Slope	Control	Dried
1	86.9	87.0
2	91.5	95.3
3	89.4	88.3
Mean	89.3	90.2
SD	2.3	4.4
%CV	2.6	4.9

b

	SN38	
Slope	Control	Dried
1	353.1	351.7
2	335.6	336.4
3	342.3	340.1
Mean	343.7	342.7
SD	8.8	8.0
%CV	2.6	2.3

4.4.2. Analytical recovery using bead homogeniser

To improve sample processing time and reduce potential cross-contamination prior to LC-MS/MS analysis, a bead homogeniser was used instead of the Turrex blender described in **Section 3.3.9**. The bead homogeniser was capable of processing 24-small volume samples in 90-seconds in a closed vessel (no risk of cross-contamination). Accuracy was determined as the agreement between the compounds spiked into methanol compared to the same concentration spiked into tissues and reported as the percentage analytical recovery. **Table 4.5** displays the percentage analytical recovery for irinotecan, SN38 and SN38-G from homogenised murine tissues. The bead homogeniser gave high extraction efficiency. All compounds of interest were above 83% for all tissues investigated, within the acceptable range 100 ± 20% (FDA, 2001). Samples resulting in more than 100% recovery were due to the reduced volume after the protein had been pelleted from the homogenate and confirmed that none had bound to the protein fraction. The bead homogeniser was rapid, processing 48-samples in 80-seconds, with no risk of cross-contamination, minimal heat production and resulted in high analytical recovery. This method was therefore adopted in all further experiments.

Table 4.5 Bead homogenisation: Analytical recovery of compounds of interest from murine tissues.

Murine tissue homogenates were spiked with 1 µg/ml of irinotecan, SN38 and SN38-G and compared to methanol spiked with the same. Percentage recovery is given and shows good analytical recovery from tissues when compared to methanol at 100%. More than 100% recovery was due to the reduced volume after proteins had been pelleted from the homogenate and shows none was bound to the protein fraction. Mean percentage of three replicates ± standard deviation. *Plasma did not require homogenisation.

Tissue	Irinotecan (%)			SN38 (%)			SN38-G (%)		
Tumour	92.3	±	2.2	93.4	±	1.2	88.3	±	0.5
Liver	102.8	±	9.0	96.1	±	3.2	85.7	±	6.3
Kidney	89.2	±	2.5	91.1	±	3.0	87.1	±	2.2
Colon	88.4	±	3.7	93.3	±	1.6	85.1	±	5.6
Spleen	82.6	±	2.2	90.0	±	3.8	90.2	±	6.3
Lung	90.9	±	6.3	90.3	±	4.3	88.9	±	5.1
Skin	109.1	±	0.5	106.6	±	2.0	99.4	±	2.6
Plasma*	107.9	±	1.4	100.7	±	2.6	85.9	±	1.0

4.5. SN38 thMBs: *In vivo* PK and biodistribution profiles

For targeted US-triggered delivery of SN38, liposomes were attached to MBs to produce thMBs (**Figure 1.11**). In order to determine *in vivo* PK and biodistribution of the SN38 thMBs (0.04 mg/kg), a single dose was administered intravenously into CD1 nude mice bearing CRC xenografts. An US-triggered destruction pulse was administered to the tumour post injection. A control of SN38 free drug was administered in the same way (without US-trigger) and time dependent tissue distribution of SN38 and SN38-G was determined by LC-MS/MS (**Figure 4.6**).

As seen in **Figure 4.6 a. i**, SN38 was detected in all tissues 1-hour post thMB administration, with the exception of brain. Peak levels of SN38 were seen in all tissues after 1-hour between 100 – 0.5 ng/g (liver > spleen > colon > kidney/lung > heart > tumour > ovary > plasma), although colon levels peaked after 3-hours. Highest concentrations were found in liver which was the only tissue to have SN38 at more than 3-hours and up to 48-hours post injection. The inactive metabolite SN38-G followed a similar pattern to SN38 (**Figure 4.6 a. ii**), with peak concentrations after 1-hour ranging from 40 – 0.3 ng/ml (liver > tumour > colon > kidney/ovary/lung > plasma > heart), again colon levels peaked after 3-hours with even higher concentrations than those found in liver tissue. None was detected in spleen or brain. At 3-hours SN38-G was only found in colon, liver and kidney, and none was detectable after this time-point.

The free SN38 control (see **Figure 4.6 b. i**), again gave peak tissues concentrations after 1-hour post i.v. SN38. Concentrations ranged between 20 – 0.8 ng/ml (liver > lung/spleen > heart > colon), with none detected in tumour, kidney, plasma, ovary or brain tissue. SN38 concentrations were approximately ten-times lower than those found after thMB delivery when detected in the same tissues, although lung tissues did not follow this pattern, having similar concentrations by both doses. The only tissues which had detectable SN38 after 3-hours were liver and heart, with liver the only tissue to have detectable levels of SN38 at 24-hours. No SN38-G was detected in any tissues, with the exception of liver having very low levels (2.5 ng/g) at 1-hour (**Figure 4.6 b. ii**).

Taken as a whole, this data has demonstrated that the LC-MS/MS method was able to determine tissue concentrations of SN38 and its metabolite after very low doses of SN38 were administered. It also shows that SN38 thMB delivery has increased circulation times/reduced elimination of the drug when compared to the same dose of free.

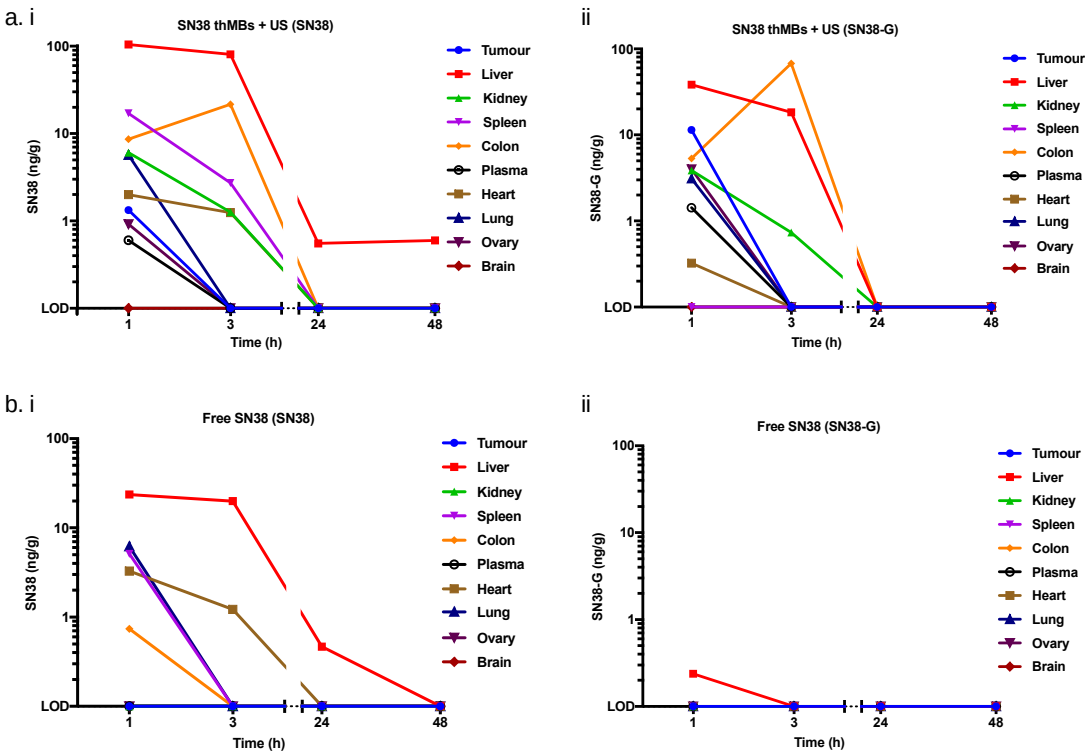

Figure 4.6 ThMB pharmacokinetic (PK) profiles of SN38 and its metabolite SN38-G.

Single dose (0.04 mg/kg) SN38 was used to compare thMBs with free drug *in vivo*. (a) SN38 thMBs PK profiles for (i) SN38 and (ii) SN38-G. ThMBs were targeted to VEGFR2 and the US-trigger was a tumour localised 5-second 'tone burst' administered 4-minutes post bolus injection. (b) SN38 free drug PK profiles for (i) SN38 and (ii) SN38-G. SN38 thMBs extended the PK profile for both tumour and other tissues whereas free drug was rapidly metabolised and excreted. Concentrations were detected by LC-MS/MS and each data point was a mean of two or a single animal. LOD = limit of detection.

This was particularly obvious in tumour tissue where SN38 and SN38-G were detectable 1-hour after thMB drug delivery but absent after free drug.

4.6. SN38 thMBs: Longitudinal study investigating tumour PD responses and end-point biodistribution

To investigate the effect of very low dose SN38 thMBs on growth of human CRC xenografts, the same treatment protocol was used as shown previously for irinotecan thMBs (**Figure 3.11**). Very low doses of SN38 were used to determine tolerability at this dosing schedule, effect on tumour growth inhibition and end-point drug biodistribution.

4.6.1. Quantification of SN38 in thMB preparations

The SN38 dose delivered by thMBs was confirmed by LC-MS/MS once the longitudinal experiment had ended. The amount of SN38 delivered was 0.04 ± 0.004 mg/kg or 1.1 ± 0.1 µg per dose, giving a total dose of 6.0 µg over 2 weeks (**Table 4.6**).

4.6.2. Very low dose SN38 delivery using thMBs inhibits tumour growth

A total of five treatments over a 2-week period were given, see **Figure 4.7** for cohort description and treatment schedule. After two thMB treatments there was significant inhibition of tumour growth compared with control group at day 14 ($p < 0.05$) (**Figure 4.8 a**). Tumour growth was also inhibited compared with control at day 21 and day 25 after four and five treatments respectively, but did not reach statistical significance. However, two tumours in the thMBs + T regressed after treatment with SN38 thMBs pointing towards a tumour growth inhibition effect. Tumour doubling time, an indicator of tumour growth rate was not significantly different between thMBs and control (**Figure 4.8 b**) although 2/8 tumours exhibited growth regression. The median value of the control was higher than the thMB group at 6-days and 4-days doubling time, respectively. Notably, one tumour from the control group had a rapid doubling time of more than ten times the doubling time of the rest of the group. Final day tumour mass (**Figure 4.8 c**) was not significantly different between thMBs and control. However, the median tumour mass of the control was higher than the thMB group, 0.41 g and 0.28 g respectively.

Body mass was used as an indicator of animal health and well-being, with weight-loss normally associated with poor health. The percentage change in body mass between the start and end-point was determined and was not significantly different between groups (**Figure 4.8 d**). The mean (± SD) percentage body mass change of the thMB group was -0.4 ± 2.7% compared to the control 1.7 ± 4.5%, suggesting the treatments were well tolerated.

Table 4.6 Quantification of SN38 thMB preparations.

SN38 concentrations in the five thMB treatments were quantified using LC-MS/MS. Mean (± standard deviation (SD)) dosage was 0.04 ± 0.004 mg/kg SN38. Dosage was calculated using the mean mass of the thMB cohort of CD1 female mice (0.027 kg).

thMB sample	SN38 (µg/ml)	SN38 dose per 100 µl injection (µg)	Dosage (mg/kg)
1	11.5	1.2	0.043
2	11.7	1.2	0.043
3	13.6	1.4	0.051
4	10.6	1.1	0.039
5	10.8	1.1	0.040
Mean	11.6	1.2	0.043
SD	1.2	0.1	0.004

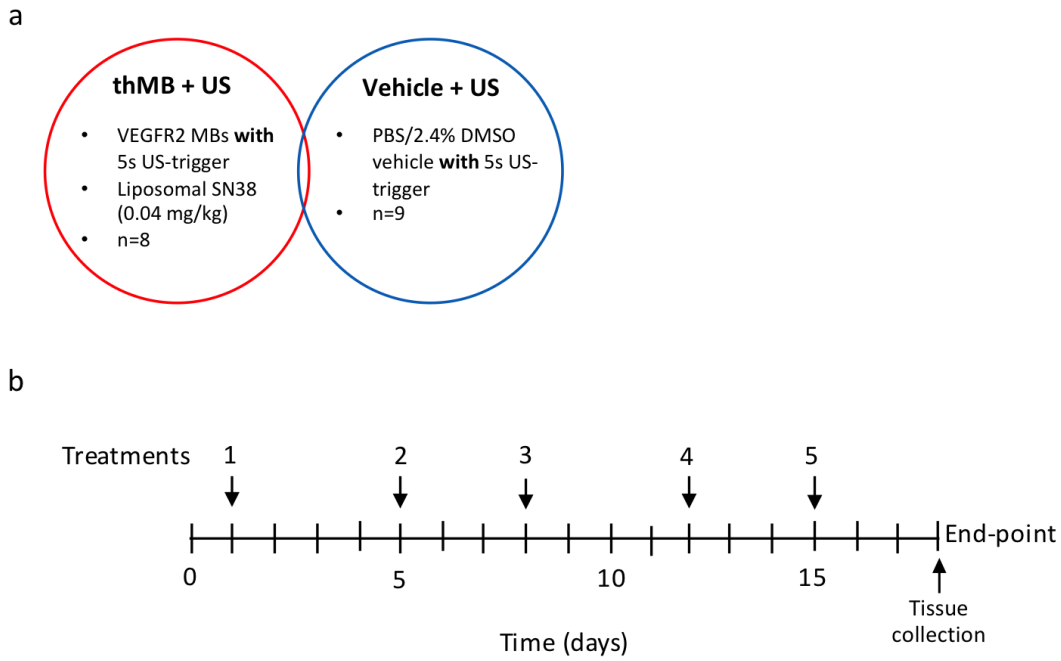

Figure 4.7 SN38 thMB cohorts and treatment schedule.

(a) Abbreviated nomenclature and treatment groups are shown with (n = number of mice per group). (b) Treatment schedule depicted, treatments were initiated one-week post subcutaneous inoculation with SW480 CRC cell line (Day 1). Five doses of 0.04 mg/kg SN38 thMBs or a vehicle control without drug were administered via i.v. injection over a 2-week period. ThMBs were targeted to VEGFR2 and the US-trigger was a tumour localised 5-second 'tone burst' administered 4-minutes post bolus injection. End-point and tissue collection was 72-hours post final treatment.

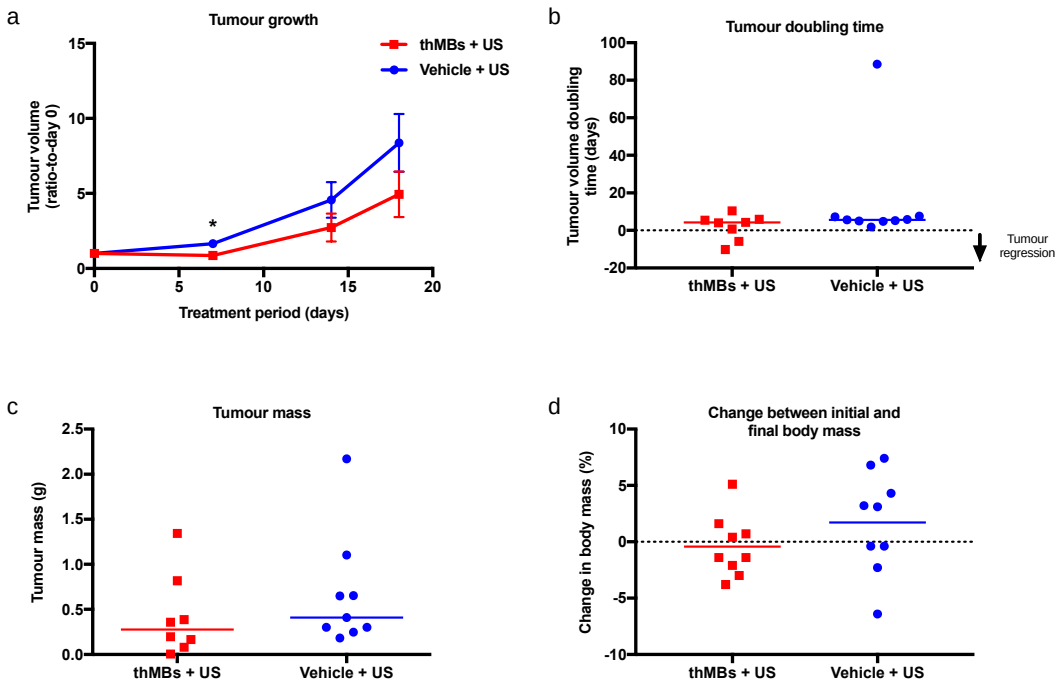

Figure 4.8 Very low dose SN38 delivery using US-triggered thMBs inhibits tumour growth. Tumour pharmacodynamic (PD) response was investigated. (a) Effect of thMBs on tumour volume measured by HFUS imaging (mean (± SEM) ratio-to-day 0). * p = 0.0188 Mann Whitney (two-tailed). (b) Tumour volume doubling time in days (bars represent median value). (c) End-point tumour mass (bars represent median value). (d) A comparison of initial and end-point body mass for each group (bars represent mean value). Tumours and measurements were collected for analysis 72-hours post-final treatment. ThMBs were targeted to VEGFR2 and the US-trigger was a tumour localised 5-second 'tone burst' administered 4-minutes post bolus injection. Red = 5x 0.04 mg/kg SN38 thMBs + US-trigger (n = 8), Blue = 5x Vehicle (PBS + 2.4% DMSO) + US-trigger (n=9).

4.6.3. PD analysis of tumour response after very low dose SN38 delivery using US-triggered thMBs

To investigate mechanisms by which SN38 thMBs inhibited tumour growth, we assessed tumour PD responses consistent with the known mechanisms of action of SN38 (**Figure 4.9**).

Mitotic bodies were used as a marker of proliferation. Tumour histology showed the number of mitotic bodies were not significantly different between the control and thMBs treated tumours, median values were 7 and 10 mitotic bodies/0.25 mm^2, respectively (**Figure 4.9 a**). However, the thMB group contained two tumours where no mitotic bodies were found. Double stranded DNA breaks was used as a marker of SN38 efficacy, however no significant differences were found between control and treated tumours (**Figure 4.9 b**). Median values were 1.3 and 1.5% positive pH2AX staining per mm^2 of tumour tissue, respectively. Apoptosis was used as a marker of controlled cell death, a potential effect of SN38 treatment. There were no significant differences between the control and thMB group, median values were 1.3 and 1.4 % positive cleaved caspase-3 staining per mm^2 of tumour tissue, respectively (**Figure 4.9 c**). Over all the data indicate that SN38 thMB had not had significant effect of tumour PD at these very low doses.

Vessel density is an important factor for successful thMB delivery, as MBs are vascular agents and targeting to endothelial cells was used. Again, no significant differences were found between groups (**Figure 4.9 d**). Median values were 14 and 11 CD1 positively stained vessels per 0.25 mm^2 of tumour tissue for control and treated groups, respectively. This suggested that SN38 delivered in this way did not have an effect on vessel density or that the vessels reformed within 72-hours post-treatment.

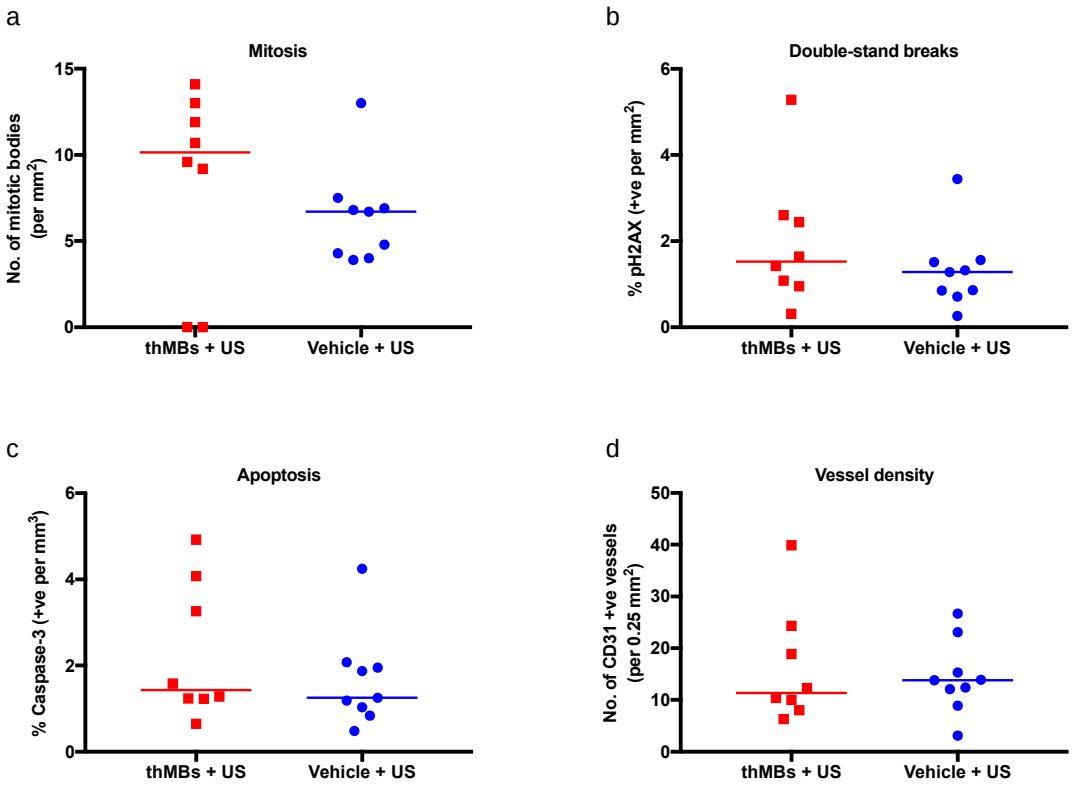

Figure 4.9 Pharmacodynamic (PD) analysis of very low dose SN38 delivery using US-triggered thMBs.

Five treatments of SN38 thMBs or vehicle, both followed by an US-trigger. (a) Number of mitoses per mm^2 of tumour tissue. (b) Double-stranded DNA breaks and (c) apoptosis per mm^2 of tumour. (d) Number of vessels per 0.25 mm^2 of tumour. No significant differences were found between treatment groups, suggesting SN38 thMBs were ineffective at these very low doses. The median value for each group is denoted by a bar (a - d). Tumours were collected for analysis 72-hours post-final treatment. ThMBs were targeted to VEGFR2 and the US-trigger was a tumour localised 5-second 'tone burst' administered 4-minutes post bolus injection. Red = 5x 0.04 mg/kg SN38 thMBs + US-trigger (n = 8), Blue = 5x Vehicle (PBS + 2.4% DMSO) + US-trigger (n=9).

4.6.4. Blood parameters associated with SN38 toxicology

Myelosuppression and neutropenia, are known side effects of clinical irinotecan chemotherapy. End-point blood parameters were investigated to determine SN38 thMB treatment on red blood cells, white blood cells and granulocytes (mainly neutrophils) counts. Red blood cells numbers were within the normal range for CD1 female mice for both thMB and control groups, 5.1 and 6.1 $x10^3$/µl of blood (mean values), respectively. White blood cells numbers were also within the normal range for CD1 female mice for both thMB and control groups, 7.6 and 5.7 $x10^3$/µl of blood (mean values), respectively. No statistical differences were found between control and treated groups, suggesting SN38 thMB treatments had not been detrimental to these parameters (**Figure 4.10 a - b**).

Granulocytes are a type of white blood cell, specifically neutrophils, eosinophils, and basophils. The granulocyte counts for both groups were not significantly different, median values were 1.7 and 1.2 $x10^3$/µl of blood for thMBs and control groups, respectively (**Figure 4.10 c**). Over all the data indicate both white blood cells and granulocyte concentrations were unaffected 72-hours post final treatment.

4.6.5. SN38 biodistribution following thMB treatment (72-hours post final treatment)

Tumours were harvested at end-point, along with liver, kidney, spleen, colon and plasma to determine SN38 concentrations by LC-MS/MS. As very low doses (0.04 mg/kg) were delivered *in vivo*, additional steps were added to the extraction protocol to improve detection (**Section 4.4**).

Low levels of SN38 were detected in tumour, liver and kidney tissues, whilst none was detected in spleen, colon or serum (**Figure 4.11**). 7/8 samples had SN38 in the tumour (range 0.01 to 0.57 ng/g) at 72-hours post final treatment. At these very low doses, the drug was deposited and/or retained preferentially in the tumour tissues. In liver 4/8 had detectable levels of drug ranging from 0.02 to 2.7ng/g, and 4/8 kidney samples had detectable levels of SN38 in the range 0.10 to 0.13 ng/g. SN38-G was not detected in any of the samples analysed.

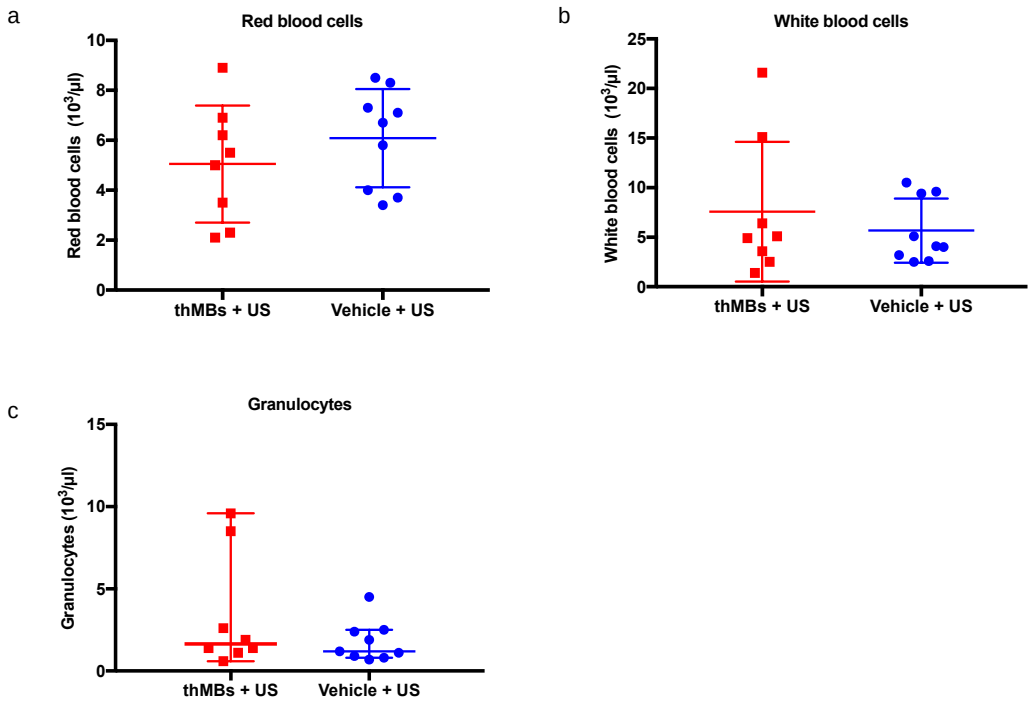

Figure 4.10 Blood parameters associated with clinical toxicity of SN38.

(a) Red blood cells (mean ± SD), (b) White blood cells (mean ± SD) and (c) granulocytes counts (median ± 95% CI) were within the normal range for CD1 nude mice and were not significantly different between groups, suggesting SN38 thMB treatments had not been detrimental to these parameters at this time point. A total of five treatments of SN38 (0.04 mg/kg) were given over a two-week period. Samples were collected for analysis 72-hours post-final treatment. Data presented are n=1. ThMBs were targeted to VEGFR2 and the US-trigger was a tumour localised 5-second 'tone burst' administered 4-minutes post bolus injection. Red = 5x 0.04 mg/kg SN38 thMBs + US-trigger (n = 8), Blue = 5x Vehicle (PBS + 2.4% DMSO) + US-trigger (n=9).

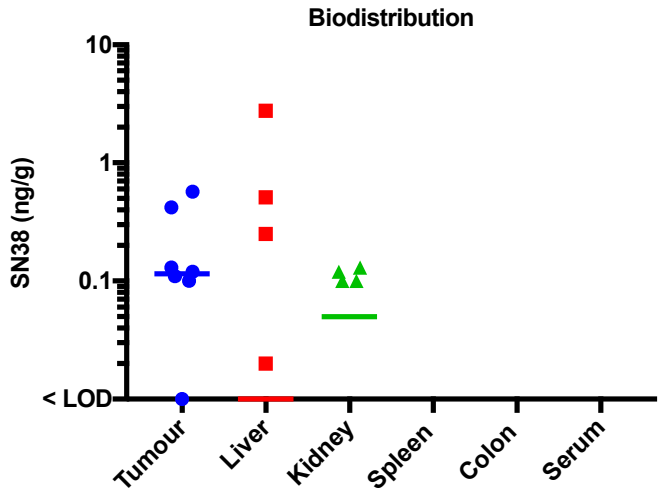

Figure 4.11 SN38 thMBs: Biodistribution of SN38 by LC-MS/MS

SN38 thMBs were targeted to VEGFR2 and the US-trigger was a tumour localised 5-second 'tone burst' administered 4-minutes post bolus injection. A total of five treatments of SN38 (0.04 mg/kg) were given over a two-week period. Samples were collected for analysis 72-hours post-final treatment. SN38 was detected in tumour, liver and kidney samples, with none detected in spleen, colon or serum. A total of 8 samples per tissue group were analysed, absent data point(s) indicates none detected (or less than the LOD). Median value denoted by the bar. SN38-G was not detected in any of the samples analysed at this time point.

4.7. Investigation of US-trigger alone on tumour response

To investigate the effect of the US-trigger alone on human CRC xenografts, the same treatment protocol was used as shown with irinotecan thMBs and SN38 thMBs (**Figure 4.7**) with 2 treatment groups comparing vehicle with an US-trigger (+ US) against a vehicle control without an US-trigger (- US). After five treatments, tumour growth between the groups were similar, with no significant differences found at any time point (**Figure 4.12 a**). Notably, one tumour from the + US group exhibited rapid tumour growth compared to the rest of the group. Tumour doubling time, was not significantly different between groups (**Figure 4.12 b**). The median value of the control was lower than the + US group, 7 days and 8 days doubling time, respectively. Final day tumour mass (**Figure 4.12 c**), was not significantly different between - US and + US groups, 0.7 g and 0.5 g respectively. Data taken as a whole suggested that the US-trigger alone was not having a significant effect on tumour growth inhibition.

The percentage change in body mass between the start and end-point was determined and again not significantly different between groups (**Figure 4.12 d**). The median percentage body mass change was 2% compared to the control -2%, suggesting that treatments were well tolerated.

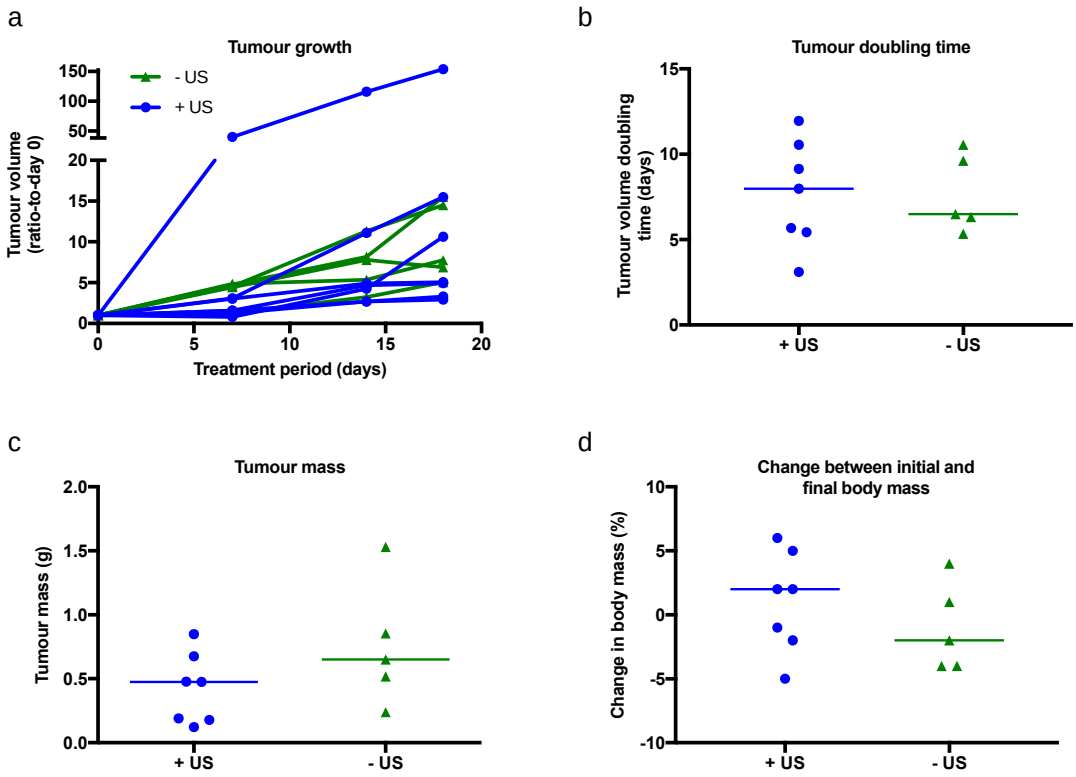

Figure 4.12 US-trigger alone does not inhibit tumour growth.

Five treatments of vehicle (PBS/2.4% DMSO) followed by an 5-second 'tone burst' US-trigger (+ US) or the same without US-trigger (- US). (a) Effect of the US-trigger alone on tumour volume was measured by HFUS imaging (ratio-to-day 0). (b) Tumour volume doubling time in days (bars represent median value). (c) End-point tumour mass (bars represent median value). (d) A comparison of initial and end-point body mass for each group (bars represent median value). No significant differences were found between groups (a-d) suggesting US-trigger alone did not inhibit tumour growth. Blue = Vehicle + US-trigger (n=7), Green = Vehicle without US-trigger (n=5).

4.8. Discussion

This chapter presents the first known demonstration of VEGFR2-targeted, triggered drug delivery of SN38 using thMBs in combination with US. Initial cytotoxicity assays using CRC and endothelial cell lines gave IC_{50} values for SN38 free drug and verified its high potency. Topoisomerase I protein concentrations were determined for the human CRC cell lines and were not significantly different, but a potential biomarker of SN38 efficacy. SN38 was encapsulated in a liposomal formulation and characterised prior to use. An additional step was added to the previously used LC-MS/MS protocol to increase detection of very low concentrations of SN38 and SN38-G used in the SN38 *in vivo* experiments. A PK and biodistribution study was used to demonstrate enhanced tumour-specific drug release after a single thMB dose. This was followed by a longitudinal study involving multiple thMB treatments which confirmed tumour growth inhibition and preferential tumour drug deposition and/or retention over other tissues after 72-hours. SN38 IC_{50} values were used to verify that the concentrations detected in tumour tissues were below the range of those needed for growth inhibition *in vitro*. Further investigation of the US-trigger and its negative effect on tumour growth inhibition (Choijamts *et al.,* 2011; Alamolhoda and Mokhtari-Dizaji, 2015), were unfounded.

4.8.1. SN38 cytotoxicity *in vitro*

The SN38 IC_{50} values for human and mouse CRC cell lines and a mouse endothelial cell line were determined for 24 and 72-hour treatments. A protocol was developed (**Section 4.1**) to ensure the drug solubilised in tissue culture media prior to treatment. Using this optimised method, IC_{50} values were reproducible and all values were in the nano-molar range, 100-2000 times less than the IC_{50} values for irinotecan (micro-molar range) (Dr N Ingram, personal communication). These differences correlate to those determined by other groups (Chabot, 1997; Danks *et al.,* 1999; Kawato *et al.,* 1991) and was not surprising as irinotecan is a prodrug and its toxicity is reliant on its conversion to SN38 which is responsible for its mode of action. The SN38 IC_{50} values were determined *in vitro* in order to assess whether concentrations of SN38 detected in human CRC xenografts were in the range to have an anti-cancer effect.

All the dose-response curves were sigmoidal in shape, apart from the HCT116 cell line which was biphasic. The different response profiles may be explained by the mechanism of action of SN38, particularly the induction of double-stranded DNA breaks (Wu *et al.,* 2002) however, the investigation of the specific mechanisms is beyond the scope of this study.

Comparisons to the literature were limited, most studies have quoted IC_{50} values and when a dose-response curve was shown it was limited to 3-5 concentrations, to few to determine the shape (Liu *et al.,* 2014; Mosallaei *et al.,* 2016; Dinarvand *et al.,* 2015; Sayari *et al.,* 2014). This study used 20 concentrations between 8 Logs, giving a precise demonstration of the dose-response.

All cell lines had IC_{50} values in the nano-molar range. Values found in the literature for comparison were minimal, using different assays, cell lines, controls and treatment times (Sapra *et al.,* 2008; Liu *et al.,* 2014; Dinarvand *et al.,* 2015; Sayari *et al.,* 2014; Mosallaei *et al.,* 2016). The National Cancer Institute (NCI) 'Cancer Screen National data' gave a mean GI_{50} (50% growth inhibition) value of 30 ng/ml for SN38 using six human CRC cell lines (Developmental Therapeutics Program NCI) (Shoemaker, 2006). These values were in keeping with the same nano-molar potency range determined using this method.

IC_{50} values were not statistically different between SW480 and SW620, both were derived from the primary and secondary tumours, from the same patient (Leibovitz *et al.,* 1976). The metastatic line SW620 was isolated from a mesenteric lymph node after recurrence and could have been presumed more resistant (Hammond *et al.,* 2016) but the trend is the opposite. However, chemotherapy was not initiated until after the lymph nodes were resected therefore no possibility of drug induced resistance between the two cell lines (Hewitt *et al.,* 2000).

The potency of SN38 after 24 and 72-hour treatment periods resulted in little difference. Typically, prolonged exposure enhances therapeutic effect. This can be attributed to the cell-cycle specific nature of the drugs used. SN38s mechanism of action takes place during the S-phase of the cell cycle and therefore the longer the exposure the greater the cytotoxicity, as a higher proportion of the cells would have entered in the S-phase (Nakajima *et al.,* 2008). Cell cycle analysis of the treated cells may give more insight into this observed effect. This protocol used single treatments of SN38 for as long as 72-hours, it is possible the drug degraded in that time and daily treatments would have been more appropriate. However, this protocol reflected the treatments for the longitudinal *in vivo* study (**Section 4.6.2**), where a single dose was delivered every 3-4 days and may therefore more accurately reflect the concentrations of SN38 detected in human CRC xenografts and their effect on cell proliferation.

SVR cells displayed marginally less sensitivity to SN38 of all the cell lines tested. Most cytotoxicity studies test only cancer cell lines but the addition of an endothelial cell line as done here is advantageous in terms of assessing SN38 efficacy using thMBs delivered via

the vasculature. SVR cells express VEGFR2, a vascular endothelial cell marker and target for thMB targeting and adhesion to tumour blood vessel walls. As SN38 was shown to be 100-2000 times more toxic than irinotecan, it would be potentially more suited for thMB delivery as currently MB drug-loading is low. In the literature, *in vitro* studies are most commonly performed under 'static' conditions. A group using 'flow' conditions (mimicking venous flow), found sonoporation was reduced under these conditions, an important point to consider with future *in vitro* studies using thMBs and endothelial cell lines (Park *et al.,* 2011).

SW480 cells were subsequently chosen as the cell line for *in vivo* xenograft studies using SN38, due to their high drug sensitivity, high take rate in CD1 nude mice and in order to directly compare to the previous irinotecan thMB *in vivo* experiment (**Section 3.4**), which used SW480 xenografts and the same dosing regimen.

4.8.2. Topoisomerase I: protein concentrations in human CRC cell lines

High topoisomerase I levels in tumours are potential indicators of SN38 sensitivity (Pfister *et al.,* 2012; Pfister *et al.,* 2009). No significant differences were found between human CRC cell lines in this study. However, this was in keeping with the SN38 IC_{50} values presented (**Section 4.1**). One study determined topoisomerase I protein concentrations for HCT116 as more than 70-times the values reported in this study (Jensen *et al.,* 2016). Another study determined topoisomerase I protein concentrations for human CRC cell lines in the region of 3-10 ng/ml/µg protein (Pfister *et al.,* 2009) up to 100 times the mean value of 0.1 ng/ml/µg protein determined in this study. These differences may be accounted for by the different methods used to quantify the protein or alternatively that the freeze/thaw method used for cell lysis was not adequate. Current literature is conflicting as to whether camptothecin efficacy is indeed positively correlated to topoisomerase I protein concentrations. Three studies have found high topoisomerase I protein or mRNA levels to be associated with sensitivity (Burgess *et al.,* 2008; Sugimoto *et al.,* 1990; Kotoh *et al.,* 1994), whereas others have been inconclusive (Jansen *et al.,* 1997; Perego *et al.,* 1994). It has been suggested that other factors such as the rate of proliferation or drug resistance mechanisms may play a role and perhaps drug-induced topoisomerase I cleavable complexes may be a more suitable marker of SN38 efficacy (Goldwasser *et al.,* 1995).

4.8.3. SN38 liposome characterisation

The SN38 liposomes used in the *in vivo* studies in the chapter, were characterised prior to use. Sterility was confirmed before *in vitro* and *in vivo* work commenced, as contamination would have severely compromised experiments. There are many ways to sterilise nanoparticles but they may not be applicable to liposomal formulations, aseptic technique and filtering are recommended (Çağdaş *et al.,* 2014). The mean liposome diameter was determined as 242 nm, slightly larger than nanoparticles used in other *in vivo* tumour studies where less than 200 nm was optimal (Prabhakar *et al.,* 2013; Maeda, 2015). Nanoparticles with a diameter of more than 500 nm are associated with rapid clearance by the macrophage-monocyte system, however particles with a diameter of less than 6 nm are excreted quickly via the kidneys (Longmire *et al.,* 2008; Sun *et al.,* 2017). Liposome sizes in this study may not play such an important role as they were attached to MBs for targeted triggered drug delivery, but it is important to note that larger liposomes, have greater drug loading capacity. However, once thMBs are destroyed, intact circulating liposomes may also act to increase tumour drug delivery. Therefore, liposome size may play a role in increasing circulating times and therefore tumour accumulation via the EPR effect (Maeda *et al.,* 2013; Prabhakar *et al.,* 2013), as discussed previously for irinotecan thMBs.

Future determination of the zeta potential of the SN38 liposomes is needed as surface charge also plays a role in the way liposomes interact with each other and biological systems (Bozzuto and Molinari, 2015).

SN38 concentration of the liposome batch was 233.6 µg/ml, with 20% intra-sample variability despite samples being aliquoted from the same preparation. Preparation variation was also high with irinotecan liposomes (**Section 3.4.1**) and therefore a large batch of SN38 liposomes was produced, aliquoted and freeze-dried, with significant improvements to the final SN38 thMB concentrations (**Section 4.6.1**). SN38 concentration remained stable in the liposomal preparation when investigated over a 3-week period and samples were always used within that time frame. A major challenge in SN38 delivery is the stability of the drug during the shelf-life and physical encapsulation with liposome formulations having most success (Palakurthi, 2015). SN38 liposomes formulated using the same method, were stable up to 6-months with minimal drug release over 120-hours when liposomes where diluted in PBS (in the case of i.v. administration) (Zhang *et al.,* 2004).

Liposomes were slightly less toxic when compared to the same concentrations of free drug *in vitro*, suggesting liposomal formulation was protecting the drug or perhaps the method of internalisation and distribution with cells was different to that of free drug (Przybylo *et al.,* 2016). Previous groups investigating SN38 liposomal cytotoxicity have not used free SN38 controls (Lei *et al.,* 2004; Fang *et al.,* 2016; Zhang *et al.,* 2004). Perhaps the surface charge and incorporation of PEG into the liposome shell (to increase circulation times), has resulted in less toxicity as it has previously been shown to reduce cellular uptake and endosomal escape (Hatakeyama *et al.,* 2007; Li and Huang, 2011). The lack of availability of controls such as none-PEGylated liposomes or empty liposomes (without drug) in order to test this hypothesis, was a limitation of this study.

4.8.4. SN38 thMBs: *In vivo* PK and biodistribution profiles

The efficiency of chemotherapy has relied on high plasma concentrations of drug in order to increase tumour drug concentrations for cancer treatment. Liposomes as drug delivery systems have been advantageous due to increasing circulation time and improving the therapeutic index of drugs, but often fail due to non-specific tissue distribution (Bozzuto and Molinari, 2015).

In this PK study, very low dose SN38 thMBs in combination with an US-trigger showed enhanced tumour-specific drug release and extended time of exposure compared to free drug. Free SN38 was rapidly excreted and none was detected in tumour tissues using these low doses. Comparisons to other literature was limited as SN38 is extremely hydrophobic and delivery is only possible using high concentrations of DMSO. Fang *et al*., 2018 has compared the plasma PK profiles of free and liposomal SN38 (10 mg/kg) over 6-hours and found no significant differences in a non-tumour mouse model. The final biodistribution showed highest concentrations of SN38 in heart, lung > liver, spleen > kidney after free drug (Fang *et al.,* 2018). Other PK and biodistribution studies of SN38 liposomes in mice, found highest concentrations in liver, spleen and lung tissues, however SN38-G concentrations were not determined (Li and Wang, 2016; Pal *et al.,* 2005; Fang *et al.,* 2018). This study found a similar pattern of distribution with both free and thMB delivery, although the thMB group gave similar levels in the colon and kidney as the spleen, indicating different metabolism/excretion mechanisms at play.

Due to the very low doses of SN38 used in this study and therefore relatively rapid excretion, earlier time points would have been more useful for interpreting the differences between free and thMB drug delivery. Higher doses of SN38 with additional time points

may give more insight into the ADME profiles of thMBs. Higher doses of free drug would not be possible as the high concentrations of DMSO necessary would not be ethical. SN38 liposomes would have made a more reliable control (and more clinically relevant) in this comparison, however, due to the limited supply of liposomes this was not possible.

Tumour SN38 concentrations detected after 1-hour were lower than those required to show toxic effect determined *in vitro* (**Section 4.1**). Interestingly, tumour SN38-G in the thMB group was almost 10-times the levels of SN38, more than any other tissue investigated. The enzyme UGT1A1 is responsible for the metabolism of SN38 to the inactive, water-soluble SN38-G for excretion. Low levels of this enzyme in tumours may act as a predictive marker of SN38 efficacy, as the longer the exposure to SN38, the greater the cytotoxic effect. High levels of UGT1A1 have been found in mouse liver and gastrointestinal tract, and in cancers of both of these tissues (Lu *et al.,* 2015; Chen *et al.,* 2013). Determining the UGT1A1 protein concentrations within mouse tissues and human CRC xenografts may give insight into the particularly high SN38-G concentrations observed in this study.

4.8.5. Quantification of SN38 in thMB preparations

LC-MS/MS was successfully used to determine concentrations of SN38 in the very low doses of SN38 thMBs samples, post administration. The mean dose of SN38 per thMB treatment was 0.04 ± 0.004 mg/kg. The standard deviation was low despite findings of 20% variability in the liposomal SN38 concentrations (**Section 4.3.4**). However, having used LC-MS/MS to determine SN38 concentration prior to use appears to have rectified accuracy issues as seen with irinotecan thMBs using UV-Vis for drug quantification (**Section 3.4.1**).

4.8.6. SN38 thMBs: Longitudinal study investigating tumour PD responses and end-point biodistribution

The first known targeted, triggered thMB drug delivery of SN38 has been demonstrated here and shown to reduce tumour volume and extend the therapeutic window of very low dose SN38 in a model of human CRC. Preclinical activity of liposomal SN38 has been shown to be a potent inhibitor of tumour growth (Pal *et al.,* 2005; Lei *et al.,* 2004; Fang *et al.,* 2016). Previous groups have used SN38 nanoparticles in doses as low as 2 mg/kg (Lei *et al.,* 2004; Zhang *et al.,* 2004; Liu *et al.,* 2014; J. Wang *et al.,* 2015), 50-times more per treatment than those used in this study.

Treatments were well tolerated at 0.04 mg/kg with no diarrhoea or significant differences in blood parameters or body mass. Two canine plasma PK studies of liposomal SN38 at a

dose 10-times that used in this study gave peak concentrations after 10-minutes and was well tolerated, however multiple treatments resulted in some blood parameter changes (Li and Wang, 2016; Pal *et al.,* 2005), a known side effect of SN38 treatment. The very low doses used in this study were presumably the reason side effects were not observed and one of the benefits of this type of delivery system.

End-point tumour volumes were not significantly different from the control group, although two tumours from the thMB group did regress. Therefore, unsurprisingly analysis of PD response indicated no significant differences in tumour responses (**Section 4.6.3**). LC-MS/MS analysis of end-point tissues, discovered that not only was drug present but it had preferentially deposited and/or retained in tumour (**Section 4.6.5**). This was surprising as the previous PK and biodistribution study of single dose SN38 thMBs (**Section 4.5**) did not detect SN38 in tumour after more than 1-hour. It is feasible that multiple dosing had an accumulation effect after five-doses every 3-4 days, as low dose irinotecan thMBs were also detected after 72-hours post the final treatment using the same dosing schedule (**Section 3.4**). The EPR effect may have also played a role by allowing SN38 liposomes to accumulate in the tumour over time (Maeda *et al.,* 2013).

Concentrations of SN38 detected in the tumour tissues were much lower than those required to show toxic effect as determined *in vitro* (**Section 4.1**), perhaps the low levels reached between treatments gave tumour cells time to recover and thus PD response was limited. Future experiments using higher doses of SN38 may maintain higher levels within the tumour for increased tumour growth inhibition. Interestingly, tumour volumes were statistically different on Day 7, after 2-treatments had been given. This might suggest that at early time points delivery was so successful that future drug delivery is compromised in terms of VEGFR2 targeting or that drug resistance mechanisms may have developed.

SN38-G was not detected at this late time point and was previously shown to have a higher clearance rate than SN38, even with liver conversion of SN38 to SN38-G up to 40%, the extremely low concentrations of SN38 detected in this study made it unlikely to detect the metabolite (**Section 4.5**).

4.8.7. Investigation of US-trigger alone on tumour response

Sonodynamic therapy is the combination of low-intensity US with sonosensitisers. It has been widely used pre-clinically for its non-invasive tumour growth inhibition effects (Costley *et al.,* 2015; Wood and Sehgal, 2015). US used with sufficient peak negative pressures induces inertial cavitation (the use of sonosensitisers increases this effect). It is

this phenomenon which has been shown to form free radicals, which in turn induces necrosis in cancer cells (Christman *et al.,* 1987; Umemura *et al.,* 1999; Shankar and Pagel, 2011). The previous longitudinal study used very low dose SN38 thMBs + US-trigger (**Section 4.7**) resulting in insignificant differences in end-point tumour volumes when compared to the vehicle + US-trigger control group. Therefore, it was hypothesised the vehicle + US-trigger may have been having an effect on tumour growth and an additional control should have been used. The US-trigger used in this study was a high amplitude, low frequency tone burst (McLaughlan *et al.,* 2016), with a MI of 0.21 (Church, 2005) and a thermal index in soft tissue of 0.09. These parameters were well within the safe range for clinical use (The British Medical Ultrasound Society guidelines) and not enough power to induce hyperthermic effects. Tumour growth was compared between one group receiving a sham i.v. injection, while the other group received sham followed by an US-trigger. No differences in tumour growth rate, end-point tumour mass or tumour doubling time were found, but data indicated a possible trend towards the US-trigger having had a slight tumour growth inhibition effect.

Comparisons of this study with US-mediated drug delivery described in the literature are made difficult by the extreme variability of US conditions used and the inconsistent parameters described for each study. One group using low dose irinotecan in combination with US for the treatment of uterine sarcoma used similar US parameters, a MI of 0.25 but a duty cycle of 50% compared to our 1% (Choijamts *et al.,* 2011). Their US only group displayed reduced tumour volume and prolonged survival *in vivo* compared to the control. Their study was run over a total of 8-weeks with daily US treatments, whereas this study received just five-treatments over 2-weeks. Another group investigating multiple US treatments with hematoporphyrin (an US sensitiser), used a dual frequency system to create inertial cavitation to specifically generate free radicals and successfully reduce tumour volumes compared to controls (Alamolhoda and Mokhtari-Dizaji, 2015). A MI of 0.21 and 0.24, were comparable to this study, but they used a duty cycle of 100%, and treated for 30-minutes, compared to the 5-second US-trigger in this experiment.

Any slight differences between + US and – US groups may have been caused by the induction of free radicals, however compared to other groups' US-parameters, the percentage duty cycle, total sonication time and number of treatments in this study were much less.

4.9. Summary

This chapter has presented the first known demonstration of targeted, triggered drug delivery of SN38 using thMBs in combination with US. Initial cytotoxicity assays verified its high potency, with topoisomerase I protein concentrations a potential biomarker of SN38 efficacy. A PK and biodistribution study was used to demonstrate enhanced tumour-specific drug release after thMBs compared to free, followed by a longitudinal study which confirmed preferential tumour drug deposition over other tissues after 72-hours. However, higher SN38 concentrations maybe needed for tumour growth inhibition and PD effect.

Chapter 5

SN38 thMBs:

PK and PD Studies of Low Dose SN38 in Combination with US-triggers

Introduction

The lowest efficacious dose of nanoformulated SN38 found in murine models to have tumour growth inhibition effects was 2 mg/kg (Lei *et al.,* 2004; Zhang *et al.,* 2004; Liu *et al.,* 2014). Higher doses of SN38 thMBs than those described previously (**Chapter 4**) may further inhibit tumour growth rate, but still be considered 'low dose' in comparison to doses cited in the literature. As MB-mediated drug delivery enhances intratumoral drug concentrations overtime, low doses can be used with equivalent tumour growth inhibition potentially increasing the therapeutic index and reducing off-site toxicity.

The US-trigger used in combination with thMBs may itself be further improved for optimal intratumoral drug delivery. Chirp US sequences have been shown *in vitro* to improve intracellular drug delivery through sonoporation mechanisms (McLaughlan *et al.,* 2013), whereas further optimisation of acoustic pressures has been demonstrated to maximise MB cavitation which in turn increases intracellular drug delivery (De Cock *et al.,* 2015; Kooiman *et al.,* 2014). Targeted MBs have also been described to enhance intracellular delivery when combined with US *in vitro* and *in vivo* (Skachkov *et al.,* 2014; Geers *et al.,* 2013; Warram *et al.,* 2011).

The aim of this chapter was to investigate higher dose SN38 drug delivery using thMBs in combination with an US-trigger using a murine xenograft model of human CRC. PD and biodistribution studies were used to determine tumour growth inhibition effect and drug distribution. Further investigation of the US-trigger in terms of intratumoral drug delivery and mechanisms of drug release and/or uptake using thMBs was evaluated.

5. Results

5.1. SN38 liposome characterisation

Liposomes encapsulating SN38 were produced and optimised by Dr R Abou-Saleh, School of Physics and Astronomy, University of Leeds. These liposomes were aliquoted, freeze-dried and stored at -20°C until needed. Sterility of the liposomes was established prior to characterisation, as before (**Section 4.3.1**). Liposome characterisation was carried out to determine the size, concentration, surface charge and drug concentration.

5.2.1. Size and concentration

For effective drug delivery and reproducibility, liposome size needed to be controlled and within an optimal range. The NanoSight (Malvern Instruments Ltd, UK) was used to

determine size and concentration, with increased accuracy compared with the previously used qNano (Momen-Heravi *et al.,* 2012; Filipe *et al.,* 2010). The NanoSight uses nanoparticle tracking analysis software to track liposomes moving under Brownian motion to calculate hydrodynamic diameters and concentration. Samples were diluted 1:1000 and the size and concentration were measured. The mean hydrodynamic diameter of liposomes within this second preparation was 423.1 ± 10.1 nm with a modal value of 341.7 ± 4.0 nm (**Figure 5.1**). The concentration was $7.68 \times 10^{11} \pm 7.75 \times 10^{10}$ liposomes per ml.

5.2.2. Zeta potential

Nanoparticle surface charge is measured in zeta potential, an important parameter which affects long-term stability of the liposomes. The Zetasizer was used to determine the electrophoretic mobility and calculate the zeta potential for the SN38 liposomes. The zeta potential was determined as -50.2 ± 7.7 mV, suggesting these liposomes would have long term stability with minimal aggregation.

5.2.3. SN38 concentration by LC-MS/MS analysis

LC-MS/MS was used to determine the concentration of SN38 within the liposome preparation. Three aliquots were sampled from the original batch and analysed by LC-MS/MS. The mean concentration of SN38 was 388.7 ± 36.0 µg/ml (**Table 5.1**), nearly twice the concentration of the first liposome preparation (**Section 4.3.4**).

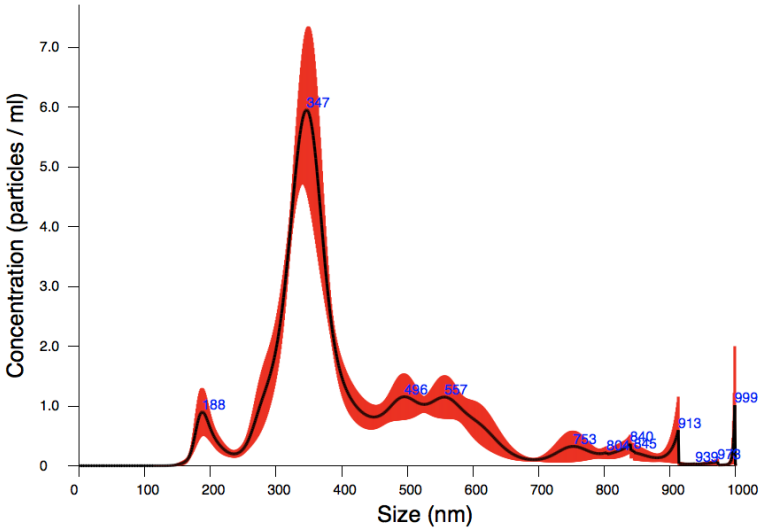

Figure 5.1 SN38 liposome size and concentration.

The NanoSight was used to determine the mean hydrodynamic diameter and liposome concentration. Five readings were taken of diameter and concentration. The mean diameter and concentration (± standard error of the mean) is plotted. The mean diameter was 423.1 ± 10.1 nm and the concentration was $7.68 \times 10^{11} \pm 7.75 \times 10^{10}$ liposomes per ml.

Table 5.1 Concentration of SN38 in the second liposome preparation.

LC-MS/MS was used to determine SN38 concentrations from three separate aliquots of liposome samples from the second preparation of SN38 liposomes. Mean ± standard deviation (SD) of three samples was 388.7 ± 36.0 μg/ml. The SN38 concentration of the second preparation was on average 1.7-times higher than the first (**Table 4.3**).

Sample	SN38 (μg/ml)
1	395.5
2	420.9
3	349.8
Mean	388.7
SD	36.0

5.2. Single dose SN38 liposomes: *In vivo* dose escalation

5.2.1. Dose escalation

Single i.v. doses of 0.1, 0.2 and 0.4 mg/kg were used in an *in vivo* dose escalation study to confirm that a dose ten-times higher than previous used (**Chapter 4**) would be tolerated by female CD1 nude mice with SW480 CRC xenografts. Doses were given in a step wise manner from lowest to highest with a 20-minute interval to monitor immediate behaviour and/or side effects. After 24-hours, behaviour was normal, no loss in body mass or signs of diarrhoea. All doses were well tolerated and therefore for maximum tumour growth inhibition effect the highest dose was used for *in vivo* thMB studies in **Chapter 5**.

5.2.2. Biodistribution profile of SN38 liposomes (0.4 mg/kg)

A single i.v. dose of 0.4 mg/kg SN38 liposomes was used to investigate the biodistribution profile 24-hours post-delivery (**Figure 5.2**). The aim was to compare with SN38 thMB delivery and also to ensure the mice would tolerate the higher dose of drug. The highest dose was calculated from the maximum number of liposomes which could be loaded on $1x10^8$ MBs and later confirmed by LC-MS/MS analysis (**Table 5.2**). Biodistribution indicated rapid clearance, with SN38 below the LOD in kidney, colon and plasma after 24-hours. LC-MS/MS analysis of other tissues revealed highest concentrations of SN38 in lung (5.2 ng/g), nearly twice the concentration detected in liver (2.4 ng/g), followed by spleen (2.1 ng/g), with lowest in the tumour tissue (0.7 ng/g). SN38-G was not detected in any of the tissues analysed.

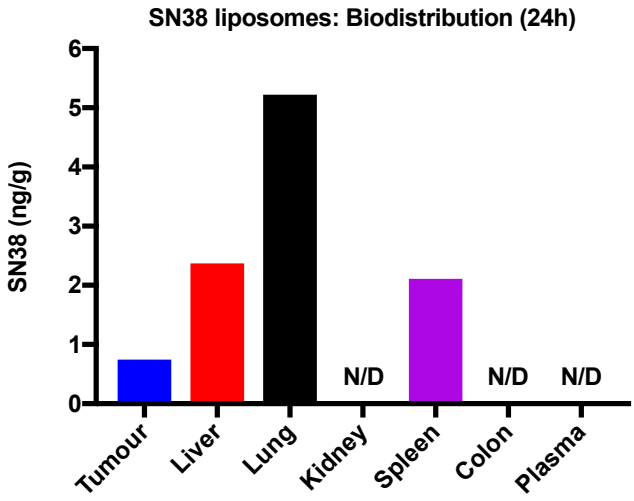

Figure 5.2 Biodistribution of SN38 liposomes.

SN38 concentration in tissue is shown following a single i.v. dose of 0.4 mg/kg SN38 PEGylated liposomes after 24-hours. Data is from a single mouse with a human CRC xenograft (SW480). High concentrations of SN38 were found in lung tissue, followed by liver, spleen and tumour. SN38 was not detected (N/D) or below the limit of detection (< 0.01 ng/ml) in kidney, colon and plasma tissue. SN38-G was not detected in any of the samples analysed.

5.3. Higher dose SN38 thMBs: Longitudinal study investigating tumour PD responses and end-point biodistribution

For targeted US-triggered delivery of SN38, liposomes were attached to MBs to produce thMBs (**Figure 1.11**). A longitudinal study was used to investigate whether a higher dose of SN38 (0.4 mg/kg) would be well tolerated while having a greater effect on tumour growth inhibition as seen in the previous chapter (**Section 4.6**).

5.3.1. Higher dose SN38 delivery using US-triggered thMBs inhibits tumour growth

A total of four treatments over a period of 11-days were given, see cohorts and treatment schedule (**Figure 5.3**). After two thMB treatments there was significant inhibition of tumour growth compared with control group at Day 7 ($p < 0.05$ Mann Whitney (two-tailed)) (**Figure 5.4 a**). Tumour growth was inhibited by 93% compared with control at Day 15 ($p < 0.05$ Mann Whitney (two-tailed)) after four treatments, and three tumours in the thMBs + T cohort regressed.

Tumour doubling time, an indicator of tumour growth rate (**Figure 5.4 b**) confirmed that 3/5 tumours exhibited growth regression while 1/5 had a doubling time of 112 days. The median value of the control was higher than the thMB group at 7 days and -3 days doubling time, respectively. Final day tumour mass (**Figure 5.4 c**) nearly reached statistical significance between the thMB and control groups ($p = 0.08$ Mann Whitney (one-tailed)). Median tumour mass of the treated group was almost 60-times less than that of the control, 0.09 g and 0.52 g, respectively. Taken together, these data point to SN38 thMBs having had significant anti-cancer effect against the growth of SW480 xenograft tumours.

Body mass was used as an indicator of animal health and well-being, with weight-loss being associated with poor health and/or stress. The percentage change in body mass between the start and end-point was determined and was significantly different between groups ($p < 0.05$ Mann Whitney (two-tailed)) (**Figure 5.4 d**). Two mice from the thMB group lost weight (-4.5 and -1.3%), but the body mass of the group did not change over time, compared to the control which gained weight, +3.2% (median values), suggesting the treatments were well tolerated as a whole.

a

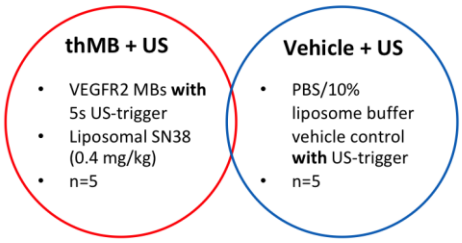

b

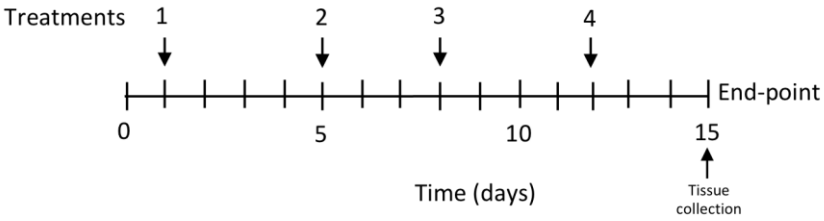

Figure 5.3 SN38 thMB cohorts and treatment schedule

(a) Abbreviated nomenclature and treatment groups are shown with (n = number of mice per group). (b) Treatment schedule depicted, treatments were initiated one-week post subcutaneous inoculation with SW480 CRC cell line (Day 1). Four doses of 0.4 mg/kg SN38 thMBs or a vehicle control without drug were administered via i.v. injection over a 12-day period. ThMBs were targeted to VEGFR2 and the US-trigger was a tumour localised 5-second 'tone burst' administered 4-minutes post bolus injection. End-point and tissue collection was 72-hours post final treatment.

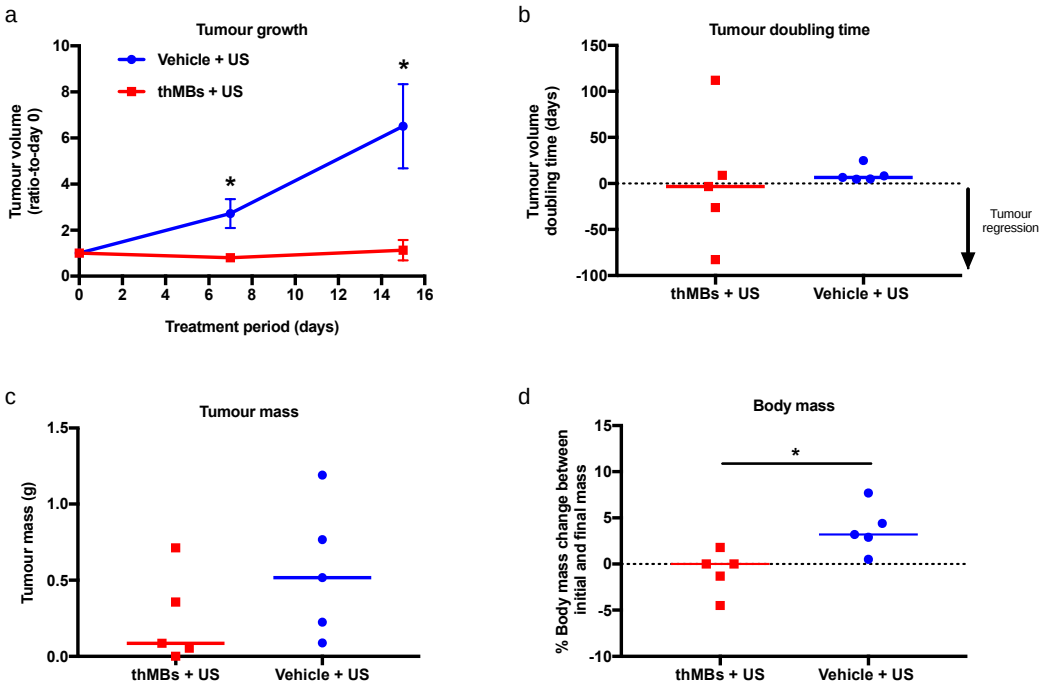

Figure 5.4 SN38 thMBs (0.4 mg/kg) inhibited tumour growth over time.

Tumour pharmacodynamic (PD) response was investigated. (a) Effect of thMBs on tumour volume measured by HFUS imaging (mean (± SEM) ratio-to-day 0), Day 7 * p = 0.048, Day 15 * p = 0.016 Mann Whitney (two-tailed). (b) Tumour volume doubling time in days (bars represent median value). (c) End-point tumour mass (bars represent median value), p = 0.0754 Mann Whitney (one-tailed). (d) A comparison of initial and end-point body mass for each group (bars represent median value). * p = 0.0159 Mann Whitney (two-tailed). ThMBs were targeted to VEGFR2 and the US-trigger was a tumour localised 5-second 'tone burst' administered 4-minutes post bolus injection. ThMBs = 4x 0.4 mg/kg SN38 thMBs + US-trigger (n=5), Vehicle = 4x PBS + 10% liposome buffer + US-trigger (n=5).

5.3.2. PD analysis of tumour response after higher dose SN38 delivery using US-triggered thMBs

To investigate mechanisms by which SN38 thMBs inhibited tumour growth, we assessed tumour PD responses consistent with the known mechanisms of action of SN38 (**Figure 5.5**).

Mitotic bodies were used as a marker of proliferation. Number of mitotic bodies was not significantly different between the control and thMBs treated tumours, median values were 6 and 13 mitotic bodies/mm^2, respectively (**Figure 5.5 a**). However, one tumour from the thMB cohort completely regressed and therefore no mitotic bodies were found.

Double stranded DNA breaks were used as a marker of SN38 efficacy, with significant differences found between control and treated tumours ($p < 0.05$ Mann Whitney (one-tailed)) (**Figure 5.5 b**). Median values were 0.1 and 0.5% positive pH2AX staining per mm^2 of tumour tissue, respectively. ThMBs had five-times more double strand-breaks than the control cohort, a result in keeping with the known mode of action for SN38.

Apoptosis was used as a marker of controlled cell death, a potential effect of SN38 treatment. Significant differences were found between the control and thMB group (*$p < 0.05$ Mann Whitney (two-tailed)), median values were 0.3 and 1.2 % positive cleaved caspase-3 staining per mm^2 of tumour tissue, respectively (**Figure 5.5 c**). ThMB tumours had four-times the percentage apoptosis than the control cohort, a known mode of action of SN38 treatment (Souza *et al.,* 2005).

No significant differences were found between groups in terms of vessel density (**Figure 5.5 d**). Median values were 5.2 and 5.9 CD31 positively stained vessels per 0.25 mm^2 of tumour tissue for control and treated groups, respectively. Indicating thMB treatment was not having an effect on the tumour vasculature at this time point, despite VEGFR2 targeting. However, vessels would regrow in tumours unless complete regression occurred.

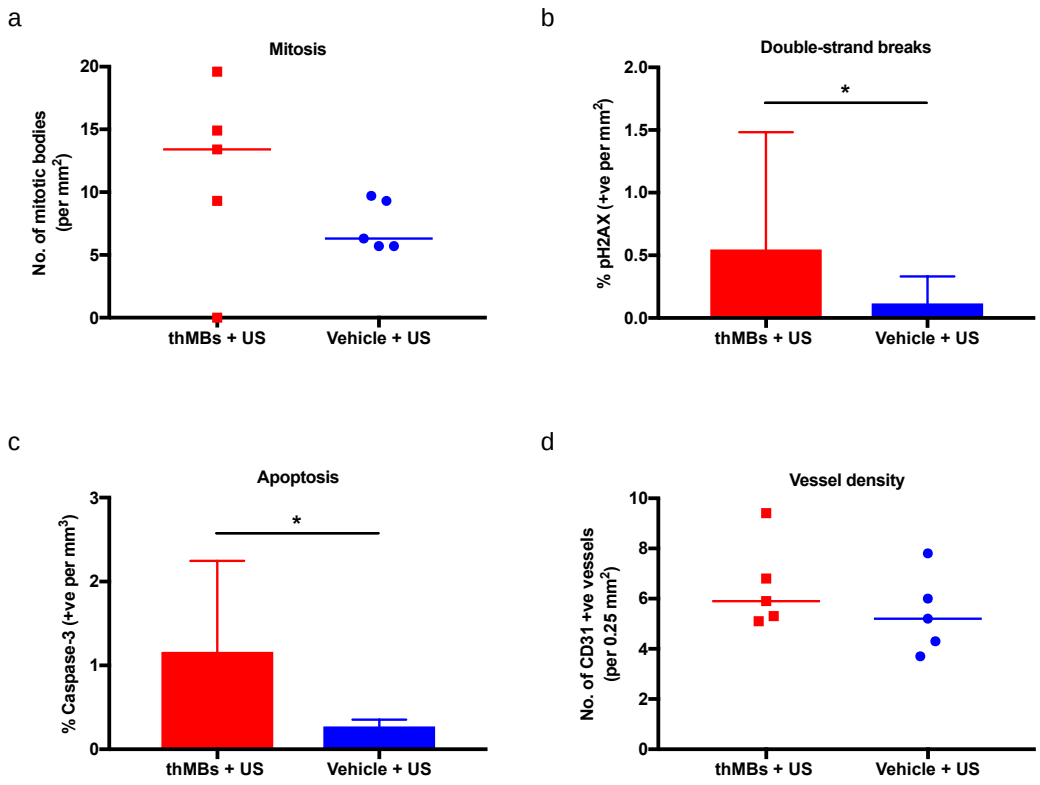

Figure 5.5 Pharmacodynamic (PD) analysis of SN38 thMB (0.4 mg/kg).

Four treatments of SN38 thMBs or vehicle, both followed by an US-trigger were used as shown in Figure **5.3** and tissue collection was 72-hour post final treatment. (a) Number of mitoses per mm^2 of tumour tissue. (b) Double-stranded DNA breaks (* p = 0.0317 Mann Whitney (one-tailed)) and (c) apoptosis per mm^2 of tumour (* p = 0.0159 Mann Whitney (two-tailed)). (d) Number of vessels per 0.25 mm^2 of tumour. The median value for each group is denoted by a bar (a - d). ThMBs were targeted to VEGFR2 and the US-trigger was a tumour localised 5-second 'tone burst' administered 4-minutes post bolus injection. ThMBs = 4x 0.4 mg/kg SN38 thMBs + US-trigger (n=5), Vehicle = 4x PBS + 10% liposome buffer + US-trigger (n=5).

5.3.3. Blood parameters associated with SN38 toxicology

Myelosuppression and neutropenia, are dose limiting side effects of SN38 chemotherapy in human clinical trials (Hamaguchi *et al.,* 2010; Norris *et al.,* 2014; Burris *et al.,* 2016; Kurzrock *et al.,* 2012). End-point blood parameters were investigated to determine any effect of SN38 thMB treatment on red blood cell, white blood cell and granulocyte counts following the treatment schedule shown in **Figure 5.3**.

Red blood cells were within the normal range for CD1 female mice for both thMB and control groups, 6.6 and 7.6 $x10^3$/µl of blood (median values), respectively (**Figure 5.6 a**). White blood cell numbers were again within the normal range for both thMB and control groups, 2.3 and 3.5 $x10^3$/µl of blood (median values), respectively (**Figure 5.6 b**). Granulocytes are a type of white blood cell of the innate immune system, specifically neutrophils, eosinophils, and basophils. The granulocyte median values were 1.0 and 1.2 $x10^3$/µl of blood for thMBs and control groups, respectively (**Figure 5.6 c**). No statistically significant differences were found between control and treated groups, indicating that SN38 thMB treatments had not been detrimental to cell numbers.

Elevated liver enzyme levels are a biomarker of liver inflammation/injury. Alanine transaminase (ALT) is a liver enzyme which is monitored clinically during chemotherapy treatment, as anti-cancer drugs are known to induce hepatotoxicity. ALT levels were analysed using the Beckman Coulter AU680 Clinical Chemistry Analyser via spectrophotometry. No statistically significant differences were found between control and treated groups, median values were 205 and 241 U/l, respectively (**Figure 5.6 d**). For mouse ALT liver enzymes, normal range is 7-46 U/l, but up to 300 U/l is not abnormal. However, values greater than 500 U/l would be indicative of liver injury (Gowda *et al.,* 2009). The control group had one anomaly, a particularly elevated value of 2135 U/l for reasons unknown. Overall the data indicate ALT levels were unaffected by SN38 thMB treatments compared to the vehicle control.

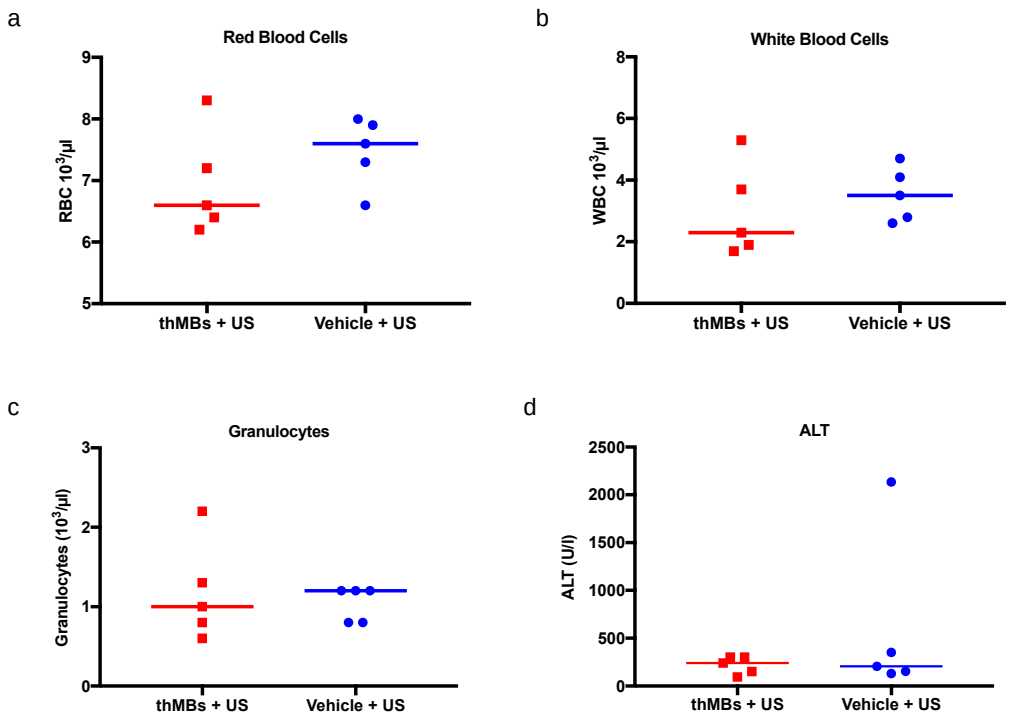

Figure 5.6 Blood parameters associated with clinical toxicity of SN38.

(a) Red blood cells, (b) white blood cells and (c) granulocytes counts were within normal range for CD1 nude mice and were not significantly different between groups. (d) ALT liver enzyme levels were within the normal range in both groups. The median value for each group is denoted by a bar. ThMBs were targeted to VEGFR2 and the US-trigger was a tumour localised 5-second 'tone burst' administered 4-minutes post bolus injection. ThMBs = 4x 0.4 mg/kg SN38 thMBs + US-trigger (n=5), Vehicle = 4x PBS + 10% liposome buffer + US-trigger (n=5).

5.3.4. Colon histology

Evaluation of any toxicity of SN38 in the colon was performed by histological analysis using H&E staining. No obvious tissue damage was observed 72-hours post final treatment with SN38 thMBs or vehicle control. The colonic mucosa showed a regular alignment of normal villi for both groups, with no inflammatory infiltrates, erosion or fibrosis evident (**Figure 5.7**). Presumably the low doses and liposome encapsulation of SN38 protected the colon from drug-related damage.

5.3.5. Lung histology

Evaluation of any toxicity and potential damage from SN38 thMBs which may collect in the lung was performed by histological analysis using H&E staining. No obvious tissue damage was observed 72-hours post final treatment with SN38 thMBs or vehicle control. The lung appeared normal with no inflammatory cell infiltrate or fibrosis (**Figure 5.8**). Presumably the doses of SN38 used were too low to have a toxic/damaging effect from thMBs potentially trapping in lung.

5.3.6. Liver histology and perivascular inflammation

Evaluation of the toxicity of SN38 in the liver was performed by histological analysis using H&E staining. No obvious tissue damage was observed 72-hours post final treatment with SN38 thMBs or vehicle control. The liver appeared normal with no inflammatory cell infiltrate or steatosis (**Figure 5.9**). Perivascular inflammation (PVI) was quantified for both groups and no statistically significant differences were found (**Figure 5.10**). The low doses and encapsulated SN38 presumably protected the liver from drug-related inflammation and steatosis.

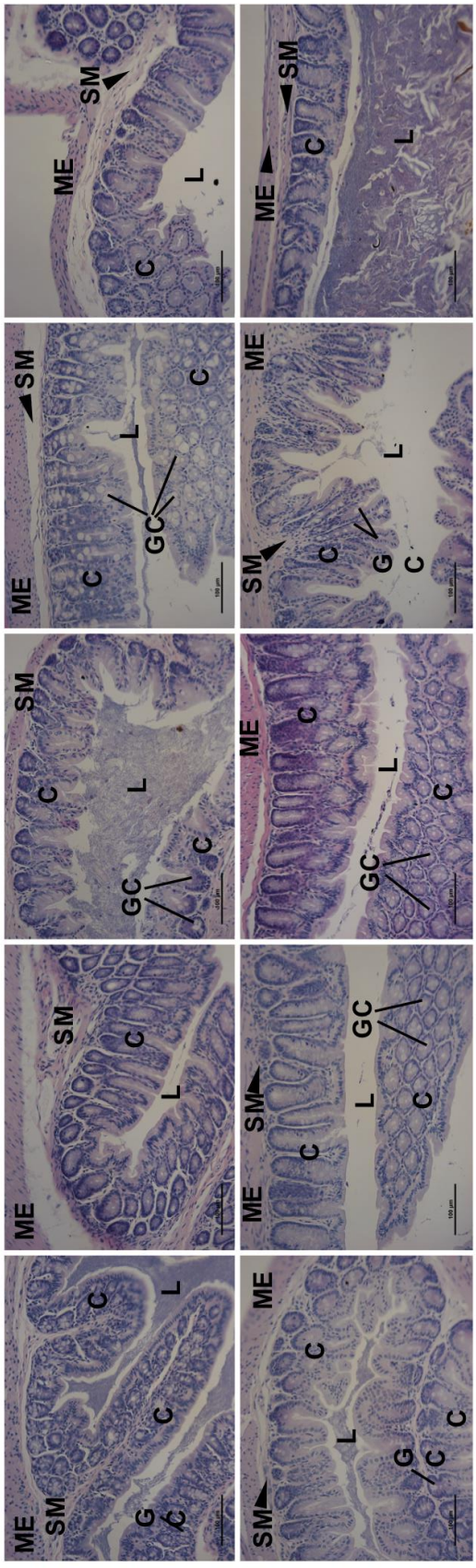

Figure 5.7 Histopathological examination of mouse colon sections stained with H&E.

Mouse colon tissue was collected 72-hour post final treatments with thMBs + US-trigger (0.4 mg/kg SN38) or vehicle + US-trigger (PBS + 10% liposome buffer). No abnormal histology was observed for either group (n=5). ME = muscularis externa, SM = submucosa, C = crypts, GC = goblet cells, L = colon lumen. Scale bar represents 100 µm.

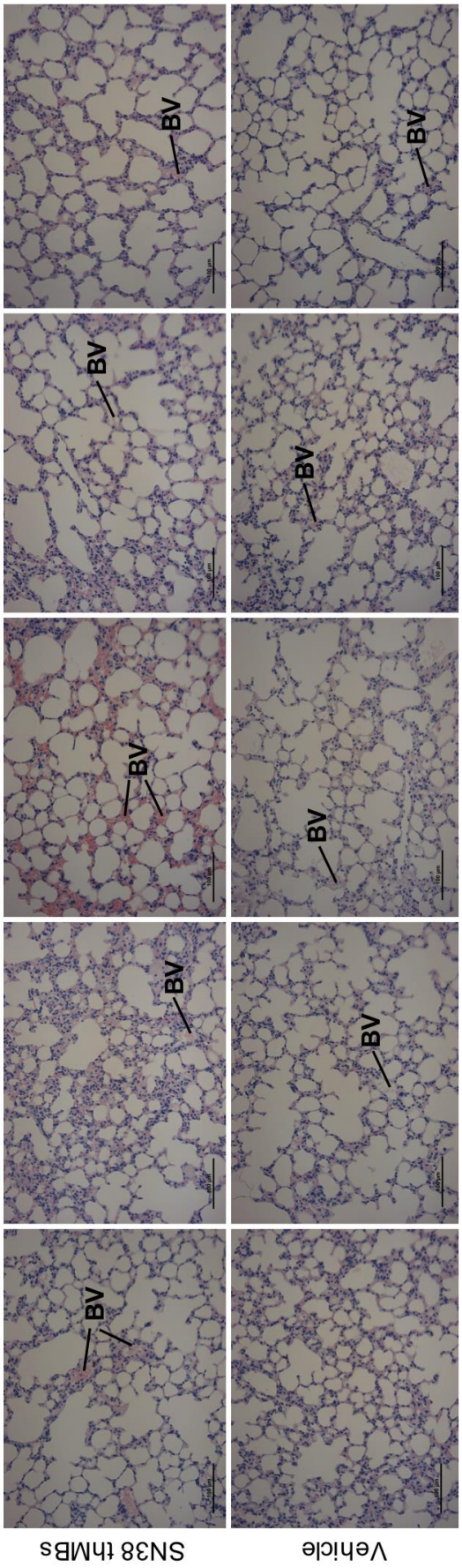

Figure 5.8 Histopathological examination of mouse lung sections stained with H&E.

Mouse lung tissue was collected 72-hour post final treatments with thMBs + US-trigger (0.4 mg/kg SN38) or vehicle + US-trigger (PBS + 10% liposome buffer). No abnormal histology was observed in either group (n=5). BV = blood vessel, air spaces are alveoli (not labelled). Scale bar represents 100 µm

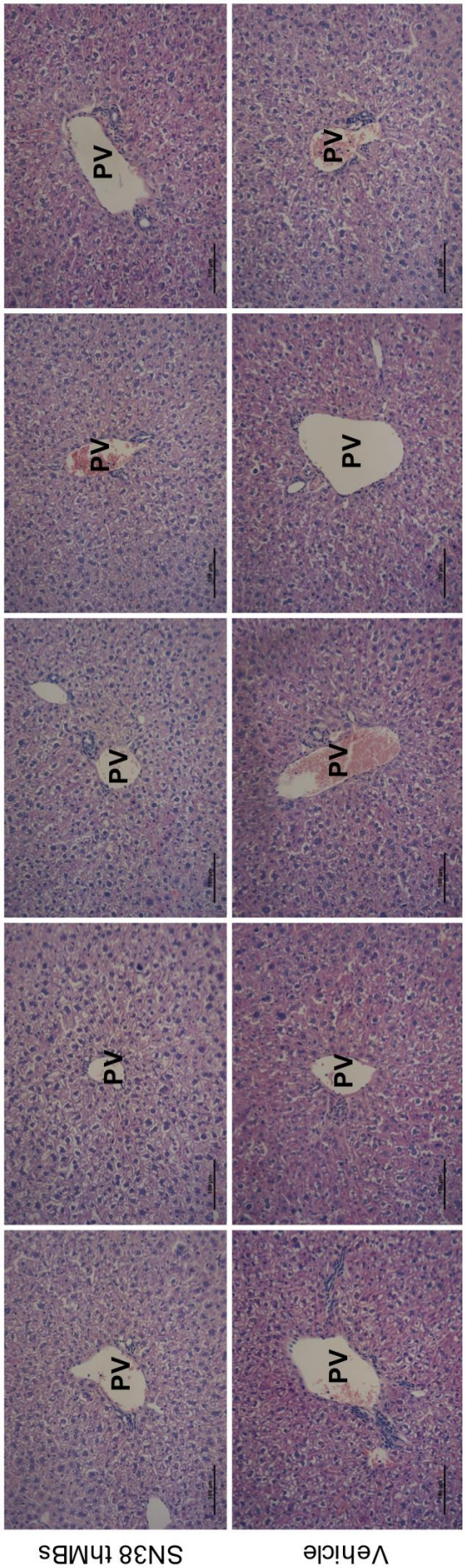

Figure 5.9 Histopathological examination of mouse liver sections stained with H&E.

Mouse liver tissue was collected 72-hour post final treatments with thMBs + US-trigger (0.4 mg/kg SN38) or vehicle + US-trigger (PBS + 10% liposome buffer). No abnormal histology was observed for either group (n=5). Portal vein (PV) surrounded by hepatocytes. Scale bar represents 100 µm

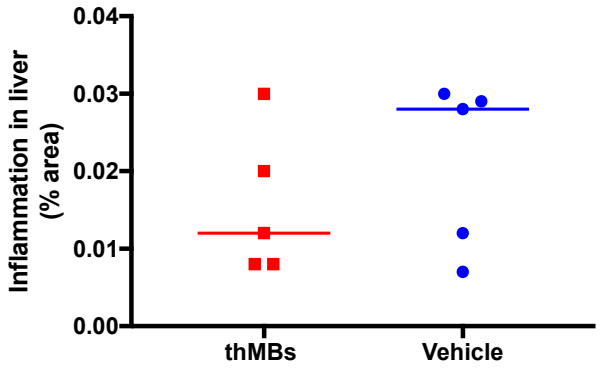

Figure 5.10 Quantification of perivascular inflammation in the liver.

Mouse liver tissue was collected 72-hour post final treatments with thMBs + US-trigger (0.4 mg/kg SN38) or vehicle + US-trigger (PBS + 10% liposome buffer). ThMBs were targeted to VEGFR2 and the US-trigger was a tumour localised 5-second 'tone burst' administered 4-minutes post bolus injection. Histopathological examination of mouse liver sections stained with H&E were scored by determining the percentage area of inflammation and was not significantly different to the control. Median value indicated by the bar. n= 5 for each group.

5.3.7. Quantification of SN38 in thMB preparations

The SN38 dose delivered by thMBs was confirmed by LC-MS/MS once the longitudinal experiment had ended. The dosage delivered was 0.4 ± 0.03 mg/kg or 7.5 ± 0.7 μg per dose, giving a total dose of 30.1 μg over 11 days (**Table 5.2**).

5.3.8. SN38 biodistribution after thMBs

Tumours were harvested at end-point, along with liver, lung, kidney, spleen, colon and plasma to determine SN38 concentrations by LC-MS/MS. As low doses (0.4 mg/kg) were delivered *in vivo*, additional steps were added to the extraction protocol in an effect to improve detection (**Section 4.4**).

Low levels of SN38 were detected in all tissues, with the exception of plasma (**Figure 5.11**). 4/4 samples had SN38 in the tumour ranging from 0.6 to 3.2 ng/g, with a median value of 1.6 ng/g at 72-hours post final treatment. One tumour had completely regressed and therefore there was not enough tissue for LC-MS/MS analysis. Lung and liver tissues had the highest concentrations of SN38, 2015 ng/g and 1173 ng/g respectively. Followed by spleen, kidney and colon 131 ng/g, 6 ng/g and 3 ng/g, respectively. SN38-G was not detected in any of the samples analysed.

Table 5.2 Quantification of SN38 thMBs (LC-MS/MS).

SN38 thMBs samples were analysed by LC-MS/MS and concentrations of SN38 quantified. Dosage was calculated using the mean mass of the thMB cohort of CD1 female mice (0.02 kg).

thMB sample	SN38 (µg/ml)	SN38 dose per 200 µl injection (µg)	Dosage (mg/kg)
1	39.4	7.9	0.39
2	41.5	8.3	0.42
3	35.6	7.1	0.36
4	34.1	6.8	0.34
Mean	37.6	7.5	0.38
SD	3.4	0.7	0.03

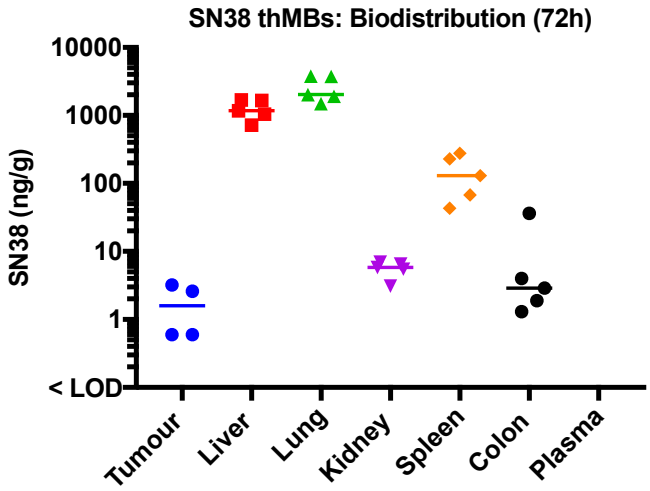

Figure 5.11 Biodistribution of SN38 thMBs by LC-MS/MS.

ThMBs with US-triggered destruction. A total of four-treatments of SN38 (0.4 mg/kg) were given over 11-days. ThMBs were targeted to VEGFR2 and the US-trigger was a tumour localised 5-second 'tone burst' administered 4-minutes post bolus injection. Samples were collected for analysis 72-hours post-final treatment. A total of 5 samples per tissue group were analysed, absent data point(s) indicates none detected (or less than the LOD) with the exception of tumour where there was only 4 samples. Median value denoted by the bar. SN38-G was not detected in any of the samples analysed.

5.4. Investigation of thMB drug delivery to human CRC xenografts using different US-sequences

ThMBs required an US-trigger for tumour drug retention and accumulation (**Chapter 3**). By analysing metabolism profiles, greater insight into early drug release and uptake may be determined. Within the tumour vasculature, thMBs are bound to endothelial cells via VEGFR2 targeting as well as free flowing. The US-trigger allows tumour targeted drug release, with MB inertial cavitation potentially driving intracellular uptake. Currently it is unknown whether inertial cavitation or stable cavitation is more favourable, in terms of *in vivo* thMB drug delivery. Previous *in vitro* MB studies suggested that a 5 MHz chirp sequence (stable cavitation) may offer superior drug uptake compared to the 2.2 MHz tone 'burst' (inertial cavitation) (McLaughlan *et al.,* 2013).

5.4.1. Tone burst US-trigger compared to chirp US sequence to aid SN38 drug delivery to tumours using thMBs

To determine whether destruction or oscillation of the thMBs was more efficient in terms of drug release and/or uptake, a tone burst US-trigger (used in previous *in vivo* experiments) was compared to a 5 MHz chirp US-trigger. The effects of the two US-triggers on drug release and metabolism were compared in human CRC xenografts, 1-hour post injection of 0.4 mg/kg SN38 thMBs. SN38-G concentrations were used as an indicator of drug release and intracellular uptake.

SN38 and SN38-G were detected in all tumours from both groups (**Figure 5.12**). However, there was significantly more SN38-G in the tone US-triggered group ($p < 0.05$ Mann Whitney (two-tailed)). SN38-G concentrations were indicative of greater intracellular SN38 metabolism, with an average of 4-times the concentrations of SN38-G than SN38, with one tumour having nearly 5-times this. This significant difference was not seen in other tissues (**Figure 5.13**), suggesting that the tone US-trigger was inducing a tumour-specific effect.

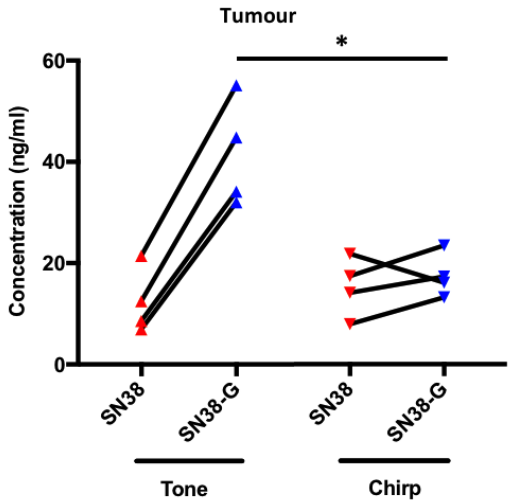

Figure 5.12 The influence of tone versus chirp US-trigger on tumour concentrations of SN38 and SN38-G following thMB drug delivery.

Concentrations of SN38 and its inactive metabolite SN38-G detected in tumours by LC-MS/MS, 1-hour post single treatment with VEGFR2 targeted SN38 thMBs (0.4 mg/kg) followed by either a 5-second 'tone burst' or chirp US-trigger localised to the tumour (n = 4 per group). SN38-G concentrations were used as an indicator of drug release and intracellular uptake, which significantly higher in the tone group (*p = 0.029, Mann-Whitney (two tailed)).

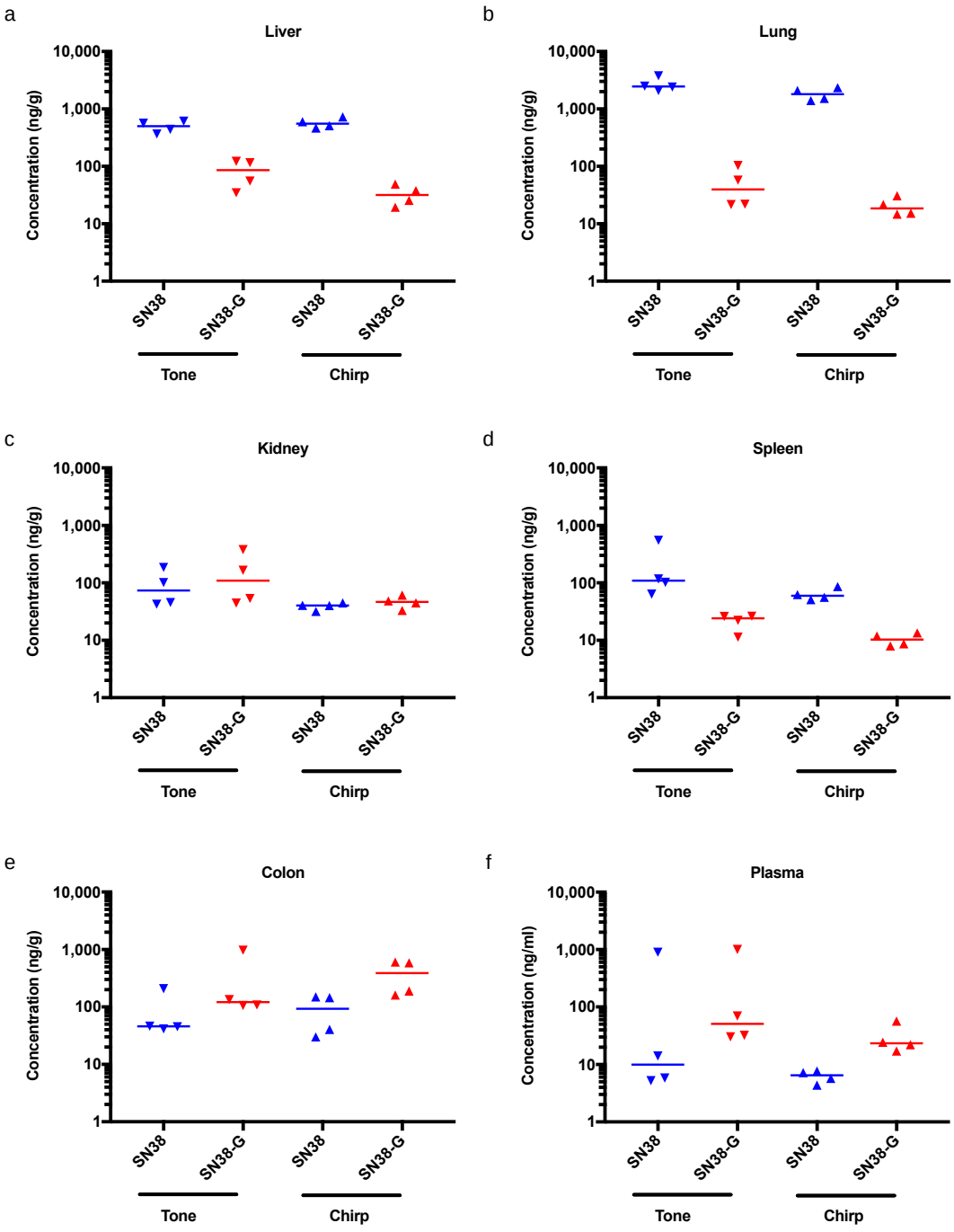

Figure 5.13 The influence of tone versus chirp US-trigger on the biodistribution of SN38 and SN38-G following thMB drug delivery.

Concentrations of SN38 and its inactive metabolite SN38-G detected in murine tissues by LC-MS/MS, 1-hour post single treatment with VEGFR2 targeted SN38 thMBs (0.4 mg/kg) followed by either a 5-second 'tone burst' or chirp US-trigger localised to the tumour (n = 4 per group). No significant differences between groups were found. Median value depicted by a bar.

5.4.2. Increasing the sonication duration of the tone burst US-trigger to improve intratumoral drug delivery

The US-trigger used in previous *in vivo* experiments had a total sonication duration of 5-seconds. It was hypothesised that a longer total sonication time may increase drug delivery to tumour tissues. A pilot study was setup to determine whether increasing the US-trigger duration from 5-second to 120-seconds would result in greater intratumoral delivery of SN38 when using thMBs. The 5 and 120-second tone burst US-triggers were compared in terms of SN38 and SN38-G concentrations in tissues, 30-minutes post administration (**Figure 5.14**). Median SN38 concentrations were 83.0 and 99.5 ng/g after the 5 and 120-second US-trigger, respectively. Median SN38-G concentrations were 104 and 97 ng/g after the 5 and 120-second US-trigger, respectively. No significant differences were found between groups and therefore the 5-second US-trigger appears to be sufficient for drug delivery, with no significant rise in intratumoral drug concentrations with the longer US-trigger. However, one tumour from the 120-second had almost twice the concentration of SN38-G than the tumours in the 5-second cohort (a marker of intratumoral SN38 delivery), suggesting further investigation is needed with larger cohort sizes.

Whole body biodistribution from the same pilot experiment is shown (**Figure 5.15**), with no significant differences determined between groups per tissue (liver, lung, kidney, spleen and colon) or in plasma.

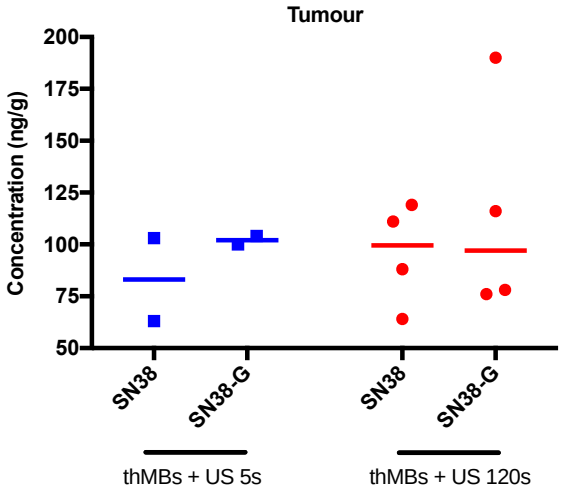

Figure 5.14 Increasing the duration of the US-trigger and effect on SN38 and SN38-G concentrations in tumours (Pilot study).

Single administration of VEGFR2 targeted SN38 thMBs (0.4 mg/kg) were followed by a tone burst US-trigger, either 5- or 120-seconds in duration. Tumour tissue was collected 30-minutes post administration and SN38/SN38-G concentration was determined by LC-MS/MS. No statistical significance differences were found between groups (although sample size low), suggesting US-trigger does not affect intratumoral drug delivery. ThMBs + US 5s = 5 second tone burst (n=2), thMBs + US 120s = 120 second tone burst (n=4). Median value depicted by the bar.

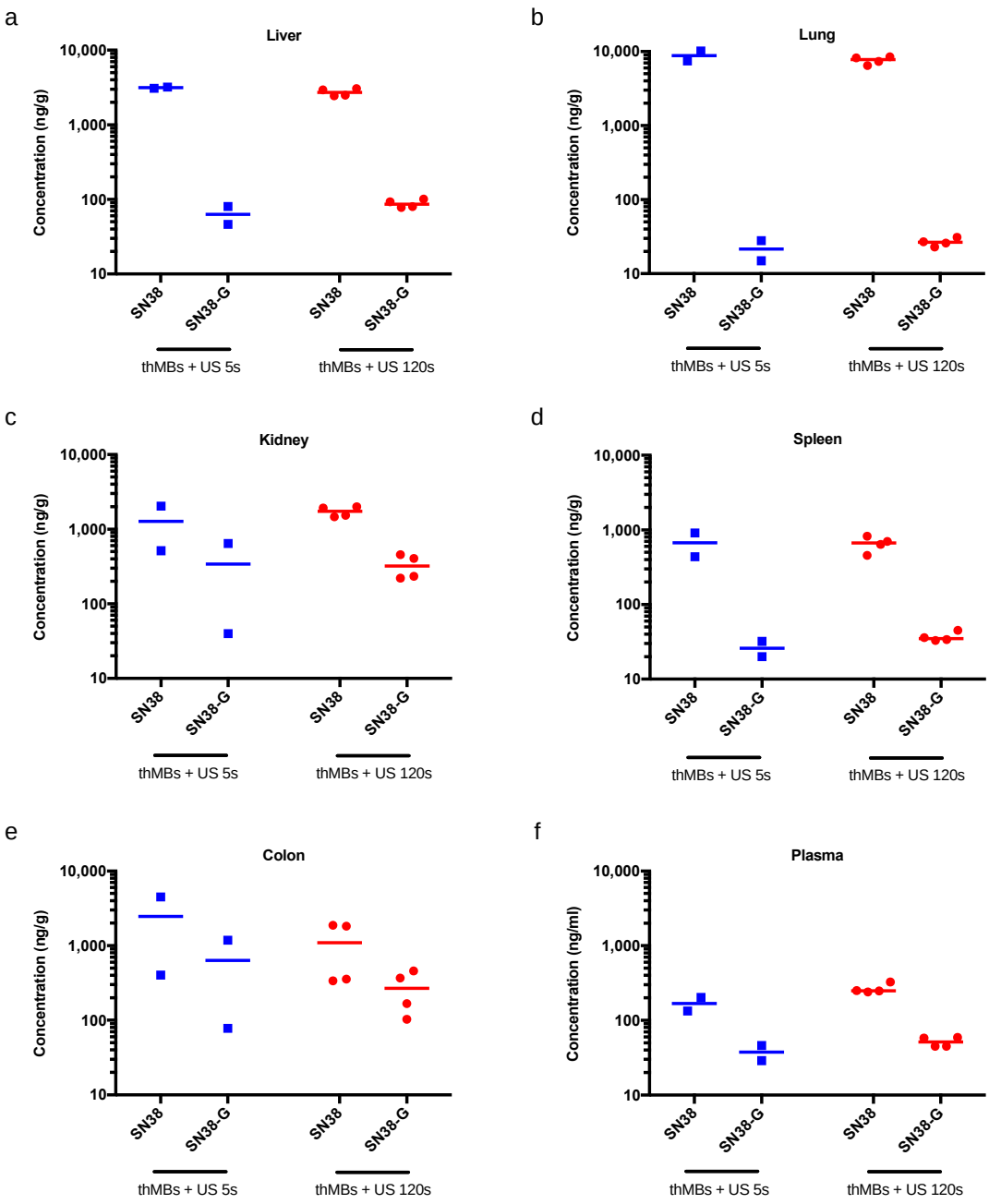

Figure 5.15 The influence of increased duration of US-trigger on the biodistribution of SN38 and SN38-G following thMB drug delivery (Pilot study).

Single administration of VEGFR2 targeted SN38 thMBs (0.4 mg/kg) were followed by a tone burst US-trigger, either 5- or 120-seconds in duration. Tissues/blood were collected 30-minutes post administration and SN38/SN38-G concentration was determined by LC-MS/MS. No significant differences between groups were found in (a) liver, (b) lung, (c) kidney, (d) spleen, (e) colon or (f) plasma, indicating the duration of US-trigger does not affect off-site drug concentrations. ThMBs + US 5s = 5 second tone burst (n=2), thMBs + US 120s = 120 second tone burst (n=4). Median value depicted by the bar.

5.5. Biodistribution of VEGFR2-targeted and non-targeted SN38 thMBs

VEGFR2 has been demonstrated to be an effective tumour target (Deshpande *et al.,* 2011; Willmann, Paulmurugan, *et al.,* 2008) for the binding of MBs within the tumour vasculature. It is this binding which may enhance intracellular drug delivery once the US-trigger is applied. A pilot study was performed to compare targeted thMBs with non-targeted thMBs in terms of intratumoral drug delivery and off-site accumulation in other tissues.

5.5.1. Intratumoral drug accumulation and metabolism using VEGFR2-targeted and non-targeted SN38 thMBs

VEGFR2-targeted and non-targeted SN38 thMBs were compared *in vivo* to determine whether targeting to a vascular receptor enhanced intracellular drug delivery to tumours. The targeted and non-targeted thMBs (followed by a 5-second tone burst US-trigger) were compared in terms of tumoural SN38 and SN38-G concentrations, 30-minutes post administration (**Figure 5.16**). The median values of SN38 (± range) were 83 (63-103) and 127 (111-132) ng/g for targeted and non-targeted, respectively. SN38 concentrations were 1.5 times higher when thMBs were untargeted, although this did not reach significance.

SN38-G was used a marker of intratumoral SN38 delivery. The median values of SN38-G (± range) were 102 (100-104) and 137 (98-137) ng/g for targeted and non-targeted, respectively. The non-targeted cohort gave a higher SN38-G concentration in 2/3 tumours compared to the VEGFR2-targeted cohort's tumour concentrations. Median values were 1.3 times higher when thMB were non-targeted, however again this did not reach statistical significance, presumably due to the low sample numbers used. This may indicate greater intratumoral drug delivery to tumour tissues in the absence of vascular targeting. Power calculations could be used to estimate cohort numbers for statistical significance for future experiments.

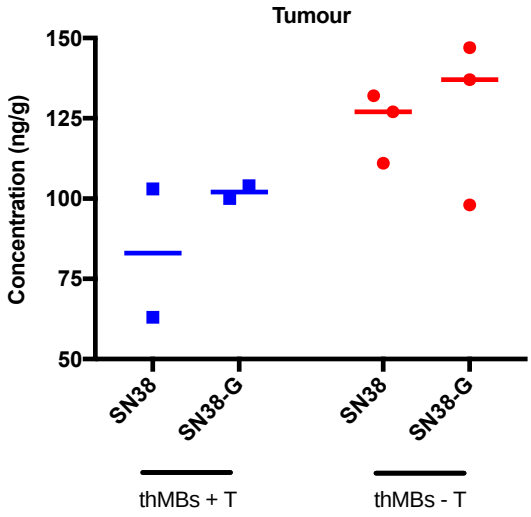

Figure 5.16 Intratumoral drug delivery using VEGFR2-targeted thMBs compared to a non-targeted control (Pilot study).

Single dose VEGFR2 targeted or non-targeted SN38 thMBs (0.4 mg/kg) were followed by a 5-second 'tone burst' US-trigger. Tumour tissue was collected 30-minutes post administration and SN38/SN38-G concentration was determined by LC-MS/MS. No statistical significance differences were found between groups (although sample size low), however the data may suggest non-targeted thMBs (thMBs – T, n=3) exhibited higher concentrations of SN38 and SN38-G in comparison to VEGFR2-targeted (thMBs + T, n=2). Median values depicted by the bar.

5.5.2. Biodistribution of VEGFR2-targeted thMBs compared to non-targeted control

VEGFR2 expression is not tumour-specific, expression in other tissues may inadvertently enhance off-site drug delivery. VEGFR2 expression has been assessed previously within the animal model used, with VEGFR2 present in the fenestrated endothelial cells of the liver sinusoids, kidney cortex and red pulp of the spleen (Dr N. Ingram, personal communication). It has been hypothesised that drug delivery to non-cancer tissues/major organs could be circumvented by focusing the US-trigger to the tumour region only.

The potential for increased off-site drug accumulation was investigated using VEGFR2-targeted SN38 thMBs with a non-targeted control. These cohorts were compared in terms of the biodistribution of SN38 and SN38-G, 30-minutes post administration. Tissues/plasma analysed determined no significant differences between VEGFR2-targeted and non-targeted groups (**Figure 5.17 b - f**), with the exception of liver (**Figure 5.17 a**). SN38 concentrations detected within the liver were 1.7 times higher in the targeted group and significantly different ($p < 0.05$ Mann Whitney (one-tailed)). Off-site VEGFR2 binding of thMBs may contribute to significantly increased drug concentrations in liver tissue or possibly the antibody loading of the thMBs increases uptake by liver Kupffer cells for more rapid clearance.

It is interesting to note that SN38-G concentrations were lower than SN38 concentrations, particularly striking in liver, lung and spleen at this early time-point. This may indicate low levels of UGT1A1 enzymes within these tissues or that SN38 was encapsulated within the thMBs/liposome construct, and therefore protected from intracellular glucuronidation.

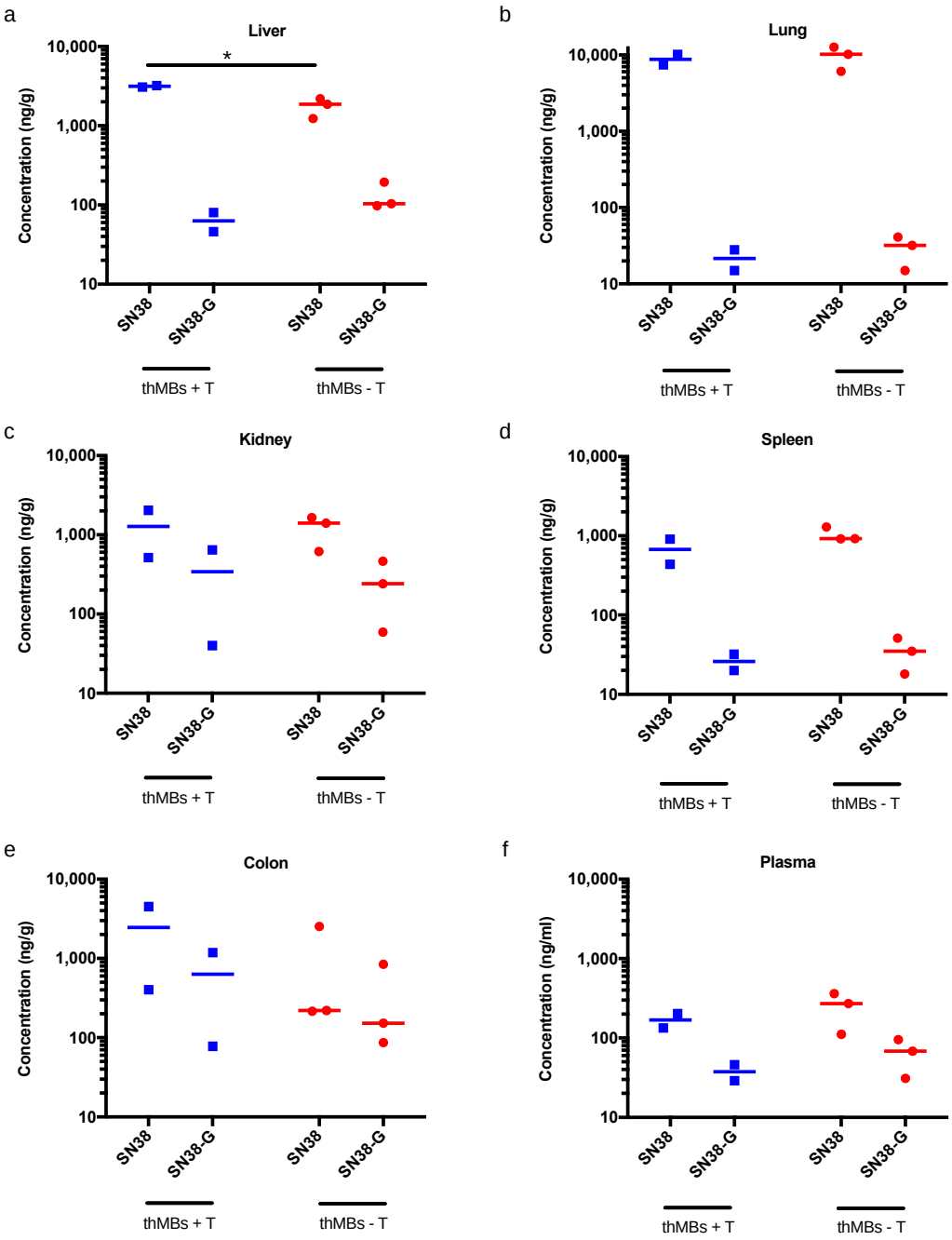

Figure 5.17 VEGFR2-targeted thMBs may enhance off-site delivery when compared to a non-targeted control (Pilot study).

Single dose VEGFR2 targeted or non-targeted SN38 thMBs (0.4 mg/kg) were followed by a 5-second 'tone burst' US-trigger. Tissues and plasma was collected 30-minutes post administration and SN38/SN38-G concentration was determined by LC-MS/MS. (a) Liver tissue; thMB + T group exhibited higher concentrations of SN38 compared to the thMB - T group (*p = 0.0286 Mann Whiney (one-tailed)). (b - f) Lung, kidney, spleen, colon and plasma; no significant differences were found between targeted (thMBs + T, n=2) and non-targeted (thMBs – T, n=3) cohorts. VEGFR2 expression in liver tissue may allow binding of thMBs and therefore enhance off-site drug delivery. Median values depicted by the bar.

5.6. UGT1A1 protein concentrations in human CRC cell lines, xenograft tumours and murine tissues

UGT1A1 is an intracellular enzyme which glucuronidates SN38 to the inactive SN38-G, for excretion. Concentrations of this protein within tumours can be used as a predictor of irinotecan efficacy in patients, as the more UGT1A1 is present the quicker SN38 is inactivated and therefore reduced time to exert its anti-cancer effect (Schulz *et al.,* 2009). Also, mutations in UGT1A1 increase likelihood of irinotecan/SN38 associated toxicity as SN38 cannot be metabolised and excreted as quickly (Takano and Sugiyama, 2017; Gagné *et al.,* 2002). UGT1A1 concentrations in other tissues may give further insight into the SN38 metabolism profiles post thMB drug delivery.

5.6.1. UGT1A1 protein concentrations in human cell lines

UGT1A1 protein concentrations were determined for four human CRC cell lines (SW480, SW620, HCT116 and HT29), and one human endothelial cell line (EA.hy926)(**Figure 5.18 a i.**). CRC cell line UGT1A1 concentrations ranged between 0.7 to 1.7 ng/mg of protein, with a median value of 1.0 ng/mg of protein. The highest concentrations were detected in SW480, followed by HT-29, SW620 and HCT116. The single endothelial cell line had the lowest concentration, with 0.4 ng/mg of protein.

5.6.2. UGT1A1 protein concentrations in human CRC xenografts

UGT1A1 protein concentrations were determined for three CRC xenografts tumours (SW480) of a similar size with a mean volume of 833 ± 65 mm^3 (**Figure 5.18 a ii.**). Tumour concentrations ranged between 0.2 to 0.9 ng/mg of protein, with a median value of 0.4 ng/mg of protein. These concentrations were over four-times less than those determined directly from SW480 cancer cells, with infiltrating mouse connective tissue and stroma presumably reducing the total UGT1A1 concentration.

5.6.3. UGT1A1 protein concentrations in murine tissues

UGT1A1 protein concentrations were determined for murine tissues and plasma (**Figure 5.18 b**). Liver had the highest concentrations with 595 ng/mg of protein, followed by kidney with 398 ng/mg of protein and lung with 70 ng/mg of protein, respectively. Colon and spleen had similar concentrations, 53 and 52 ng/mg of protein, respectively. UGT1A1 was not detected in plasma or in the mouse endothelial cell line (SVR) samples. Further experiments would be needed for reliability and to compared differences in UGT1A1 concentrations between individual mice.

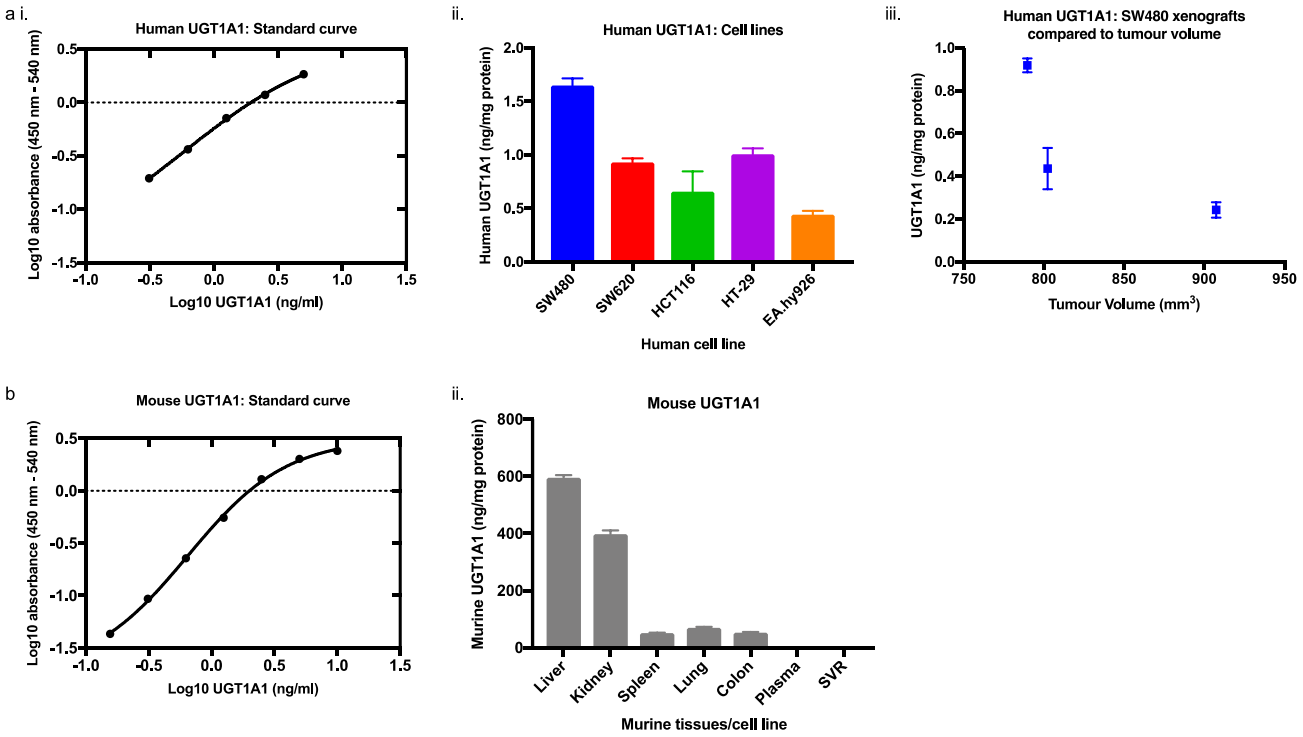

Figure 5.18 UGT1A1 protein concentration in human CRC cell lines and xenografts and murine tissues using an ELISA.

(a i.) Human UGT1A1 standard curve used to quantify (a ii.) UGT1A1 protein concentrations in human CRC cell lines (SW480, SW620, HCT116 and HT-29) and a human endothelial cell line (SVR), and (a iii.) human CRC xenograft (SW480) grown in a CD1 nude mouse. (b i) Murine UGT1A1 standard curve used to quantify (b i.) UGT1A1 protein concentrations in CD1 nude tissues (liver, lung, kidney, spleen and colon) and plasma, and mouse endothelial cell line (SVR). Data are intraexperimental duplicates from single samples, mean ± standard deviation. ELISA sensitivity was 0.156 – 10 ng/ml (human UGT1A1) and 0.078 – 5 ng/ml (murine UGT1A1). Standard curves fitted using sigmoidal four parameter logistic curve.

5.7. Discussion

This chapter presents the successful demonstration of targeted, triggered drug delivery of a higher dose of SN38 using thMBs in combination with US. SN38 was encapsulated in a liposomal formulation and characterised prior to use. This was followed by a longitudinal study involving multiple thMB treatments which confirmed tumour growth inhibition and tumour drug deposition after 72-hours. Further investigation of the US-trigger on intratumoral drug delivery confirmed high acoustic pressures were required, but a 5-second US-trigger was not significantly different when compared to a longer pulse. In a small pilot experiment, VEGFR2-targeted thMBs were not significantly different to non-targeted in terms of drug delivery to tumour but may increase off-site drug concentrations. Determination of UGT1A1 protein levels in CRC cell lines, xenografts and mouse tissues may give further insight into SN38 metabolism profiles for free and thMB drug delivery.

5.7.1. SN38 liposome characterisation

The SN38 liposomes used in the *in vivo* studies in the chapter, were characterised prior to use. The most important physiochemical factors relating to nanoparticle cellular uptake are size, shape and surface charge. Mean diameter was determined as 423 nm, 1.7-times larger than the previous batch, and hence why the liposome concentration was lower (**Section 4.3.2**). As discussed previously, the size of liposomes is an important factor for drug encapsulation as well as clearance and EPR effect (**Section 4.8.3**). Due to the increase in diameter, the concentration of SN38 was 1.7-times higher, 389 µg/ml compared to 234 µg/ml, resulting in a maximum dose of 0.4 mg/kg per 200 µl injection per mouse, 10-times the previous *in vivo* dose of SN38 (**Chapter 4**).

The zeta potential (surface charge) was determined as anionic (-50 mV), indicating these liposomes would be highly stable, with minimal aggregation and flocculation due to the strong electrostatic repulsion between particles (Labhasetwar *et al.,* 1994). In terms of surface charge on cellular uptake *in vivo*, most studies have concentrated on cationic liposomes due to positive results *in vitro* and *in vivo* for drug delivery studies (Honary and Zahir, 2013). Liposome systems have been associated with complement activation-related pseudoallergy (CARPA), an acute hypersensitivity syndrome of which anionic surface charges and increased liposome size are related factors (Szebeni and Barenholz, 2009; László *et al.,* 2014). Therefore, size and surface charge should be carefully controlled to minimise risks.

A single dose of SN38 liposomes (0.4 mg/kg) was used to determine tolerability at this higher dose and biodistribution after 24-hours. Multiple mice and more time points are needed to compare to thMB delivery, as this study used a single mice and a time-point of 24-hours. The high concentrations detected in the lung were not in line with SN38 liposomal biodistribution in the literature, which typically found SN38 in highest concentrations in the liver and spleen (Atyabi *et al.,* 2009; Li and Wang, 2016), although a recent study using targeted SN38 liposomes (< 100 nm) in a non-tumour model found a similar distribution after 6-hours (Fang *et al.,* 2018). If these liposomes had been attached to MBs it would be assumed that the lung was filtering the thMBs and therefore SN38 was trapped, as circulating MBs are trapped in the capillary beds of the lung (Butler and Hills, 1979; Bouakaz *et al.,* 1998). As the liposomes were untargeted, levels of VEGFR2 in the lungs does not account for these high levels. The size of the liposomes may be the influencing factor, as larger liposomes/nanoparticles (> 150 nm) have been shown to preferentially accumulate in lung followed by liver and spleen (Maruyama *et al.,* 1990; Abra *et al.,* 1984; Blanco *et al.,* 2015). Fang *et al*., 2018 has hypothesised that PEGylation of the liposomes may have increased circulation time and therefore increased accumulation in well perfused organs such as the lungs (Fang *et al.,* 2018).

SN38-G was not detected in any of the tissues after 24-hours, SN38 may have remained entrapped within the liposomes construct (unavailable for metabolism) and/or slowly releasing drug in low concentrations and therefore metabolite was far below the limit of detection.

5.7.2. Higher dose SN38 thMB longitudinal study

Successful targeted, triggered thMB drug delivery of SN38 has been demonstrated here and shown to reduce tumour volume and extend the therapeutic window of very low dose SN38 (0.4 mg/kg) in a model of human CRC. In preclinical trials, SN38 liposomes have been shown to be potent inhibitors of tumour growth (Pal *et al.,* 2005; Lei *et al.,* 2004; Fang *et al.,* 2016) using various doses with the lowest at 2 mg/kg (Lei *et al.,* 2004; Zhang *et al.,* 2004; Liu *et al.,* 2014; J. Wang *et al.,* 2015), which were 5-times more per treatment than those used in this study. Other groups have used nano-formulated SN38 as low as 8 mg/kg in mouse models of human CRC and demonstrated 81-91% tumour inhibition (Fang *et al.,* 2016; Zhang *et al.,* 2004; Lei *et al.,* 2004). In this study 93% tumour inhibition and tumour regression were achieved using thMB treatments 20-times less SN38 per treatment, yet with improved tumour inhibition and minimal side effects.

Treatments were well tolerated at 0.4 mg/kg, no diarrhoea or significant differences in liver enzyme levels or blood parameters (**Section 5.3**). Groups using nanoformulated SN38 at 2.5 - 40 mg/kg doses found no differences between control and treated blood counts (Sepehri *et al.,* 2014; Xu *et al.,* 2015). Encapsulation of the drug must reduce blood-related side effects such as myelosuppression and neutropenia in mice.

Body mass was significantly different to the control, with one mouse exhibiting a 4.5% loss between initial and final weights, although such loss would not be considered detrimental, a weight loss of 10-15% over a few days would be indicative of serious health complications (Foltz and Ullman-Cullere, 1999). However, the median value of the thMB group indicated no change in body mass over all (**Section 5.3.1**). Other groups using from 5-20 mg/kg dosing of SN38 nanoparticles reported minimal weight loss, with no significant differences to control groups at experimental end-points (Kim *et al.,* 2016; Fang *et al.,* 2016; Hu *et al.,* 2015; Peng *et al.,* 2011). The very low doses used in this study and the protective effect of liposomal formulation were more than likely the reason side effects were not observed and one of the benefits of this type of delivery system.

End-point tumour mass showed a trend towards significance compared to the control group ($p = 0.075$ Mann Whitney (one-tailed), and three tumours from the thMB group exhibited regression, with one of which regressed completely (**Section 5.3.1**). Analysis of PD response indicated significant differences in tumour responses in keeping with the known mechanisms of action of SN38 (**Section 5.3.2**).

Histological analysis of colon, lung and liver tissues resulted in no observable toxicity (**Sections 5.3.4 - 6**) between control and thMB treated cohorts. Presumably, it is the liposomal encapsulation which protects and spares the non-target tissues from SN38 toxicity. Another group using SN38 liposomes (10 mg/kg x3), observed no changes in histology when investigating lung, liver and kidney (Fang *et al.,* 2016). Another study using maximum tolerated doses of SN38 (30 mg/kg) in a micelle formulation, detected SN38 for several weeks post-treatment, with no observable toxicity in terms of symptoms or histology or changes in liver enzyme levels (Takahashi *et al.,* 2010). Another group showed that the colon was also better protected when SN38 was in a nanoparticle formulation when compared to irinotecan, and therefore less mucosal damage and diarrhoea (Nagano *et al.,* 2009). The nanoformulation of SN38 therefore not only allows the delivery of this hydrophobic drug but protects non-target tissues from its toxic effects.

SN38 is pH-responsive, the lactone form (active), is stable at pH less than 4.5, and exists entirely in the carboxylate form (inactive), above pH 8 (Thakur *et al.,* 2010). The instability

of the active form in physiological pH is a major problem, limiting its therapeutic capabilities. However, liposomal SN38 is protected, and the form of the drug released is therefore dependent on the pH of the microenvironment. At physiological pH 7.4, the lactone form would exist at just 15%, compared to tumour microenvironment (pH 6.8), where the lactone form would increase to 40% (Thakur *et al.,* 2010). This pH-dependent response may also act to protect non-target tissues. Kobayashi *et al.,* (1999) also investigated the pH-dependent uptake of SN38 in intestinal cells and found higher uptake rate in human CRC cell line (HT29) with decreasing pH. This may explain the gastrointestinal toxicity experienced by patients receiving irinotecan, and potentially how liposomal formulations may help to protect the intestinal tract from high levels of free SN38 (Kobayashi *et al.,* 1999).

LC-MS/MS analysis of end-point tissues, detected SN38 in all tissues (excluding plasma), after 72-hours post final treatment (**Section 5.3.8**). This was not surprising as the previous biodistribution of multiple doses of both irinotecan and SN38 thMBs (**Sections 3.4.2 and 4.6.5**) were also detectable after 72-hours post final treatment, after using a similar dosing schedule. The EPR effect may have also played a role by allowing SN38 liposomes to accumulate in the tumour over time (Maeda *et al.,* 2013). Concentrations of SN38 detected in tumour tissues were in keeping with those required to show toxic effect determined *in vitro* (**Section 4.1**), and the PD responses observed. Future experiments using higher doses or more treatments of thMBs may maintain higher SN38 levels within the tumour for increased tumour growth inhibition, as 2/5 tumours did not regress.

Highest concentrations of SN38 were detected in the lung, followed by the liver and spleen, the same biodistribution pattern observed previously with single dose liposomes (**Section 5.2**). The size of the particle directly correlates to the amount which gets entrapped by the lungs, and by the known biodistribution/excretion of MB contrast agents, as previously discussed (**Section 5.7.1**). Although no toxicity was observed in the lung after multiple doses of thMBs, this was not a favourable biodistribution profile due to the vital importance of this organ.

Nanobubbles (< 1 μm) in combination with smaller liposomes (< 150 nm) would be less likely to be filtered out by the lung capillary beds, giving a more favourable biodistribution profile and reduce any possibility of lung toxicity in future pre-clinical experiments (H. Huang *et al.,* 2013).

SN38-G was not detected at this late time point, the concentrations of SN38 detected in this study made it likely that SN38-G would be detected if SN38 was available for

metabolism, indicating that the drug remained protected by the liposome/MB lipids and/or the slow sustained release resulting in SN38-G below the limit of detection.

5.7.3. thMB drug delivery: Investigation of the US-Trigger

Two US-triggers were compared to determine whether inertial or stable cavitation of thMBs were optimal for tumour drug delivery. This study has shown significantly higher concentrations of SN38-G within tumours 1-hour post tone US-trigger compared to chirp (**Section 5.4**). No differences were determined in other tissues suggesting the those found in tumour were due to the tumour localised US-trigger. McLaughlan *et al*., has previously demonstrated the increased sonoporation efficiency of chirp *in vitro* (McLaughlan *et al.,* 2013), however in this *in vivo* study this was not the case, suggesting that MB destruction is required *in vivo,* in agreement with *in vitro* and *in vivo* studies (Lai *et al.,* 2006; Qiu *et al.,* 2010; Tinkov *et al.,* 2010). The MB jetting phenomenon from inertial cavitation may contribute to the mechanism of tumour drug uptake *in vivo* (Kooiman *et al.,* 2014).

Total sonication time of the US-trigger was increased from 5-seconds to 120-seconds in an attempt to further increase drug delivery to tumours, however, no differences were determined between the two groups in terms of SN38 or SN38-G concentrations in tumours or other tissues. The 5-second US-trigger presumably caused the whole thMB population within the tumour vasculature to inertially cavitate, and therefore any additional sonication time was futile. Another group has also demonstrated *in vitro,* that additional pulse lengths, 0.02 ms (10 cycles/pulse) up to 60 ms (30,000 cycles/pulse), did not significantly increase calcein uptake in cells (Guzman *et al.,* 2001). If inertial cavitation can occur rapidly, as shown by one group to occur after just one acoustic cycle (Flynn and Church, 1988), than the total sonication time would be made irrelevant, as shown here.

The thMB population that has accumulated within the tumour vasculature (4-minutes post i.v. injection), is presumably a mixed population of VEGFR2-bound and free flowing thMBs. Once the US-trigger is applied and the MBs have been destroyed, any free flowing thMBs from the circulation which enter the US beam are immediately destroyed and may not add to tumour drug delivery as efficiently, also shown by (Eggen *et al.,* 2014). Perhaps more time between pulses may have allowed thMBs to re-accumulation within the tumour vasculature and would have aided drug delivery more successfully. One group has demonstrated that microvascular flow rate must be estimated to accurately determine the time it takes MBs to re-fill blood vessels (Qin *et al.,* 2009). Another group has suggested that 10-seconds is enough time for MBs to re-enter between pulses, and is more successful

than continuous insonication (Miller and Quddus, 2000). By increasing the pulse repetition period shown here, from 10 μs 'on'/90 μs 'off' to incorporate 10-seconds 'off' periods (destruction replenishment method), may be more efficient than just extending the total sonication time as shown here, although it is unknown whether VEGFR2 would remain viable after MB inertial cavitation.

Even greater tumour responses may be possible by using a higher MI to target central tumour areas and multi-frequency US-triggers to enhance extravasation and penetration (Eggen *et al.,* 2014).

5.7.4. Targeting to VEGFR2

VEGFR2 targeting of thMBs did not significantly enhance drug delivery of SN38 to tumours when compared to non-targeted thMBs (**Section 5.5**). However, as the study numbers were very small, further experiments would be required to demonstrate this conclusively. Non-targeted DOX-loaded MBs in combination with US, have previously demonstrated enhanced tumour drug delivery (Tinkov *et al.,* 2010). Also, irinotecan co-delivered with non-targeted MBs in combination with US decreased tumour volume 2-fold compared to irinotecan alone (Escoffre *et al.,* 2013a). Therefore, targeting may not be necessary for MB drug delivery, but has been previously shown to be more effective than non-targeted MBs (Fan *et al.,* 2013; Chang *et al.,* 2013; Tlaxca *et al.,* 2013).

VEGFR2 is a candidate biomarker for diagnostic and therapeutic imaging in human CRC development (Smith *et al.,* 2010; Tardy *et al.,* 2010; Fischer *et al.,* 2010; Nasir *et al.,* 2016) and the VEGF family of proteins is widely targeted in antiangiogenic therapy. Previous groups have shown that VEGFR2 allows MBs to bind and accumulate within tumour vasculature (Deshpande *et al.,* 2011; Willmann, Paulmurugan, *et al.,* 2008). Therefore, by targeting to tumour blood vessels, the concentration of thMBs anchored in close proximity to the vessel walls may increase. It is this proximity which presumably aids intracellular drug delivery when the US-trigger is applied (De Cock *et al.,* 2016). Tumour-specific targeting of the thMBs via the US-trigger may have exerted enough acoustic radiation force to direct the thMBs toward the vessel wall before inertial cavitation. Previous work performed within the group had suggested that there was sufficient VEGFR2 to act as a viable tumour vascular endothelial target (Dr N Ingram, personal communication). Further studies to improve the binding and adherence of thMBs, include varying ligand linker length (Ham *et al.,* 2011), deflating MBs (Rychak *et al.,* 2006) and optimising the antibody density used for more effective targeting (Colombo *et al.,* 2016).

In terms of biodistribution of VEGFR2-targeted and non-targeted thMBs, no differences were seen in tissues or plasma, with the exception of the liver where targeted thMB had significantly more SN38 than non-targeted. Previous work performed by the group to assess potential off-target binding, detected VEGFR2 in the fenestrated endothelial cells of the liver sinusoids but not in endothelial cells of the hepatic venules, with weaker immunostaining in kidney cortex and red pulp of the spleen, and showed SMS signals *in vivo* (Dr N Ingram, personal communication). Although VEGFR2 was therefore not a tumour-specific target, drug delivery to non-tumour tissues from thMBs would potentially be avoided by localizing the US-trigger to the tumour. However, it is possible that off-site binding of thMBs to liver VEGFR2 may have resulted in the increased concentrations of SN38 detected. Another possibility is that VEGFR2 antibodies may have increased the diameter of each thMB slightly, increasing clearance rates by Kupffer cells lining the walls of the sinusoids in the liver, and would explain why a significant increase of SN38-G was not seen. Very recently, a group has demonstrated that pre-treating mice with chloroquine has been shown to improve the biodistribution profile of delivery systems by reducing accumulation of nanoparticles by the macrophage-monocyte system (Wolfram *et al.,* 2017). Perhaps Kupffer cell inhibition may improve thMB drug delivery to tumours, although so far this technique has had only modest improvements in increased tumour delivery of nanomaterials of just 2% of the total dose (Tavaresa *et al.,* 2017). Another approach to increase tumour delivery could be the reduction of antibody density applied to the thMBs, reducing the diameter slightly may reduce clearance times (Colombo *et al.,* 2016). Despite VEGFR2 being a well-studied, proven tumour target, targeting has not increased tumour drug delivery, but significantly increased drug concentrations in the liver, therefore targeting will need to be investigated further.

5.7.5. UGT1A1 protein concentrations

Low levels of UGT1A1 were detected in human colorectal cell lines and SW480 xenografts (**Section 5.6**), indicating these cells lines may be susceptible to SN38 treatment. SN38 has been shown to be metabolised most effectively by the UGT1A1 enzyme, although other isoforms of the enzyme do play a role in its metabolism (Cummings *et al.,* 2003; Gagné *et al.,* 2002). Varying levels found in xenograft tumours may explain the variation between tumour concentrations of SN38 after multiple treatments (**Section 5.3.8**). The glucuronidation activity of clinical specimens comparing normal with corresponding colon cancer biopsies has revealed stark differences not only between sample of the same patient but also up to ten-times differences of activity between patients (Cummings *et al.,*

2003). This variability between samples could have been investigated further by determining UGT1A1 levels of each xenograft after multiple treatments with SN38 thMBs to correlate concentrations of SN38-G with UGT1A1 and resulting tumour growth inhibition.

The human colorectal cell line HCT116 contained the least and may be even more susceptible to SN38 treatment. However, one study found higher levels of UGT1A1 mRNA in HCT116s compared SW620s (Landmann *et al.,* 2014), whereas this study found the opposite in terms of protein levels, although both were considered to have low concentrations. Interestingly, Landmann *et al*., (2014) also showed that human CRC cell lines had similar variations in UGT1A1 gene expression as primary human CRC samples. Therefore, these cell lines may make reliable and translatable models when investigating the UGT1A1 metabolism of SN38.

In terms of clinical tumour levels of UGT1A1, high levels may indicate SN38 resistance, as SN38 would be metabolised quickly, with less time to exert its anti-cancer effects (Landmann *et al.,* 2014). The high levels of this enzyme detected in liver, kidney and colon will rapidly glucouronidate SN38 and therefore help prevent toxicity. Similarly, lower levels found in lung and spleen may indicate potential toxic effects in these organs as saturation of the enzyme may result in delayed inactivation. UGT1A1 protein levels could be used to give further insight into the metabolism profiles of SN38.

UGT1A1 was not detected in plasma, therefore circulating SN38 would not be at risk of metabolism. Therefore, any SN38-G detected in plasma would be due to metabolism from other organs (liver/kidney/colon), having had escaped from excretion routes to re-enter circulation (enterohepatic recirculation) (Younis *et al.,* 2009).

UGT1A1 was also absent from mouse endothelial cells (SVR cell line), therefore endothelial cells may be at risk of toxicity. Tumours are actively undergoing angiogenesis, and these actively dividing endothelial cells may be subject to SN38-induced apoptosis, potentially a vascular disrupting effect. Irinotecan has been found to have vascular normalising effects in tumours, perhaps SN38 is responsible for this effect (Tong *et al.,* 2004; Vredenburgh *et al.,* 2007; Verreault *et al.,* 2011). Normalisation of the tumour vasculature would be ideal for thMB delivery systems, increasing the concentration of MB which could be delivered.

After multiple treatments, 72-hours post final treatments (**Figure 5.11**), despite high levels of SN38 and high tissues levels UGT1A1 (except plasma), SN38-G was not detected. This may be due to all available ‘free’ SN38 having been metabolised and/or excreted. The

SN38 which has been detected is therefore not bioavailable, protected from metabolism by liposome/MB construct and/or slow release and therefore below the level of detection. *In vitro* studies investigating the release rate of SN38 from liposomes and also from thMBs after US-trigger may give further insight into early and late time points described in this thesis.

UGT1A1 is located within the endoplasmic reticulum, an intracellular organelle associated with detoxification. In tumours, high levels of SN38-G were detected after tone burst US-trigger (**Section 5.4.1**), suggesting that SN38 had been delivered intracellularly at a higher concentration and/or faster rate of uptake. SN38-G levels detected in tumours must be from drug reaching the cancer cells, as neither mouse endothelial cells (SVR) or plasma had UGT1A1 at detectable levels.

5.8. Summary

This chapter has successfully investigated thMB drug delivery using SN38 for the treatment of CRC. High tumour growth inhibition and regression of xenografts, supported by PK and PD investigations has demonstrated the potential of thMB to deliver very low doses of potent drug with no observable toxic side effects in mice. The 5-second tone US-trigger proved optimal for tumour drug delivery, with VEGFR2-targeting needing further investigation. Furthermore, additional controls such as SN38 liposomes may give more credibility with the ability to better compare results to those from pre/clinical trials using the nanoformulated drug.

Chapter 6

Development of a Minimally-Invasive, Orthotopic Model of CRC Liver Metastases

Introduction

Liver metastasis is the leading cause of death for patients diagnosed with CRC. Cancer cells from the primary tumour are transported via hematogenous dissemination to secondary sites in the liver (Chambers *et al.,* 2002; Sheth and Clary, 2005). It is a multistep process and the mechanisms which drive metastasis are not fully understood. Mouse models recapitulating CRC and/or liver metastases are either genetically modified or transplantable. Genetically modified models generally take a long time to establish and have low predictability and reproducibility (Oh *et al.,* 2017; Mcintyre *et al.,* 2015). Transplantable models are much quicker but involve direct surgical implantation of cancer cells or tissues into the caecum or spleen, or injection of cells directly into the portal vein (Manzotti *et al.,* 1993; Flatmark *et al.,* 2004; Céspedes *et al.,* 2007; Thalheimer *et al.,* 2009).

The tumour microenvironment is thought to play an important role in influencing the growth of tumours cells *in vivo*. Tumours grown subcutaneously do not accurately represent the clinical tumour microenvironment which contains fibroblasts, immune cells and an extracellular matrix which have all been shown to be influencing factors for tumour establishment and growth (Wang *et al.,* 2017). Therefore, orthotopic models which mimic the clinical tumour environment would allow for more reliable and quicker translation of therapeutics to the clinic. Therefore, the generation of *in vivo* models of advanced disease in an orthotopic setting are necessary for further translation of novel therapies in order to improve treatment outcomes.

The aim of this chapter was to develop an orthotopic model of CRC liver metastases, which was minimally invasive, reproducible and enable tumour volume to be regularly monitored quickly, cheaply and safely by using HFUS. To this end, a pilot study was performed using SW620 human CRC cells in a BALB/c nude mouse. To compare the effect of the microenvironment on SW620 tumour histology, intrahepatic tumours were then compared to those grown subcutaneously.

6. Results

6.1. Non-invasive, US-guided intrahepatic injections

A total of 10 five-week old, female BALB/c nude mice(cohorts depicted in **Figure 6.1 a**) were imaged using HFUS B mode (2D) and a 40 MHz (RM-704) transducer with the VisualSonics Vevo 770 system, to determine and visualise the largest liver lobe (**Figure 6.2**

a). This lobe was then used for US-guided intrahepatic injection of $5x10^5$ SW620 CRC cells in a volume of 40 µl (with, n=5 or without matrigel, n=5) (**Figure 6.2 b**). A video showing an US guided injection performed by Laura McVeigh is included in **Appendix A**. The whole procedure from induction of anaesthesia to recovery took less than 5-minutes.

6.1.1. 3D reconstructions and tumour volumes using high-frequency US imaging (HFUS)

Mice were subsequently imaged using HFUS every week for a total of 35-days to monitor and assess tumour growth rate and volumes (**Figure 6.2 c**). Tumours were imaged in 3D mode using HFUS, as previously described (**Section 6.1**) using the minimum step size possible for the length of tumour. A video showing HFUS imaging of an intrahepatic tumour by Laura McVeigh is included in **Appendix A**.

3D reconstructions were generated post-image acquisition using Vevo 770 version 3 software (Fujifilm VisualSonics). A region of interest was outlined by hand every 5-10 frames, depending on tumour size, and tumour volume calculated by the software (**Figure 6.3**).

6.1.2. Resulting tumour morphology

Upon opening of the abdominal cavity, a large, single intrahepatic tumour was observed, 35-days post intrahepatic injection of CRC cells (**Figure 6.4 a**). Livers were dissected from the abdominal cavity and single tumours were observed at the injection site (**Figure 6.4 b**). All livers were of normal colour and texture, with no obvious tumour dissemination into the abdominal cavity.

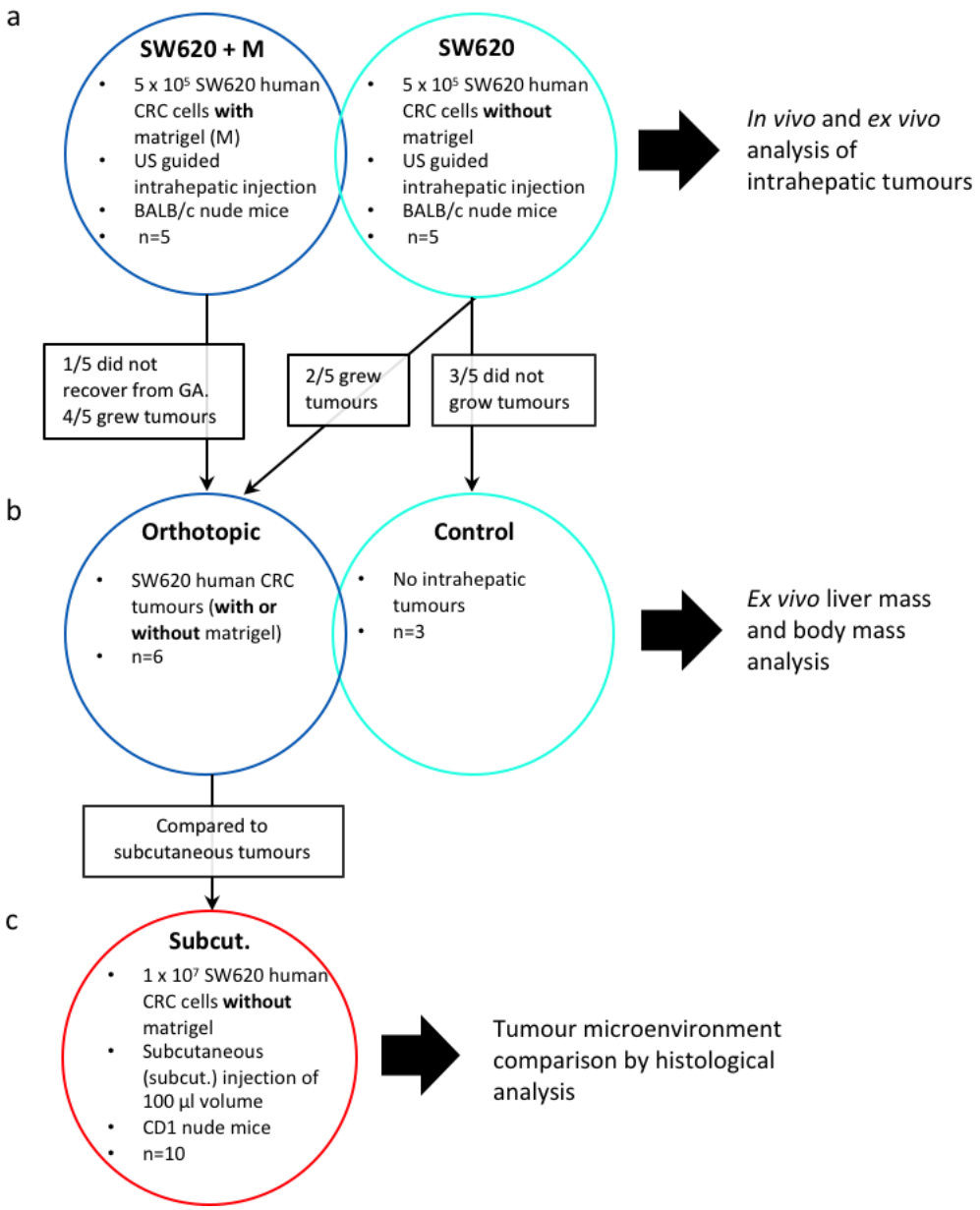

Figure 6.1 Cohorts used for human SW620 CRC liver metastases mouse model development and subsequent comparison to subcutaneously grown tumours.

Abbreviated nomenclature and treatment groups are shown with (n = number of mice per group) (a) orthotopic model development with or without matrigel and subsequent comparisons to (b) tumour free livers and (c) subcutaneous tumours.

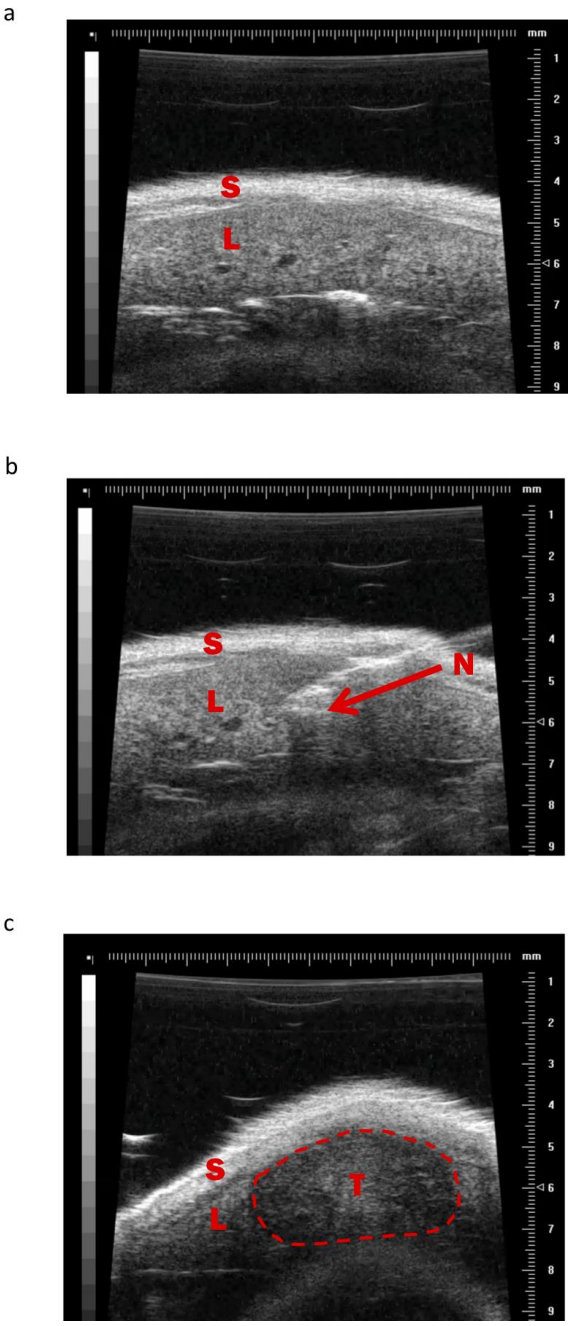

Figure 6.2 High-frequency US (HFUS) images of murine liver intrahepatic US-guided injections and subsequent tumour formation.

Representative images of US-guided intrahepatic injection and subsequent tumour growth. (a) A section of liver from the largest lobe. (b) HFUS guided intrahepatic injection of 5 x 10^5 SW620 human CRC cells in a volume of 40 µl with matrigel. Red arrow indicates direction of needle tip. (c) Subsequent CRC tumour within the liver lobe, 35-days post inoculation. Red dashed line indicates tumour region. Taken in B mode at a frequency of 25 MHz. S = skin, L = liver, N = needle, T = tumour. Scale in mm.

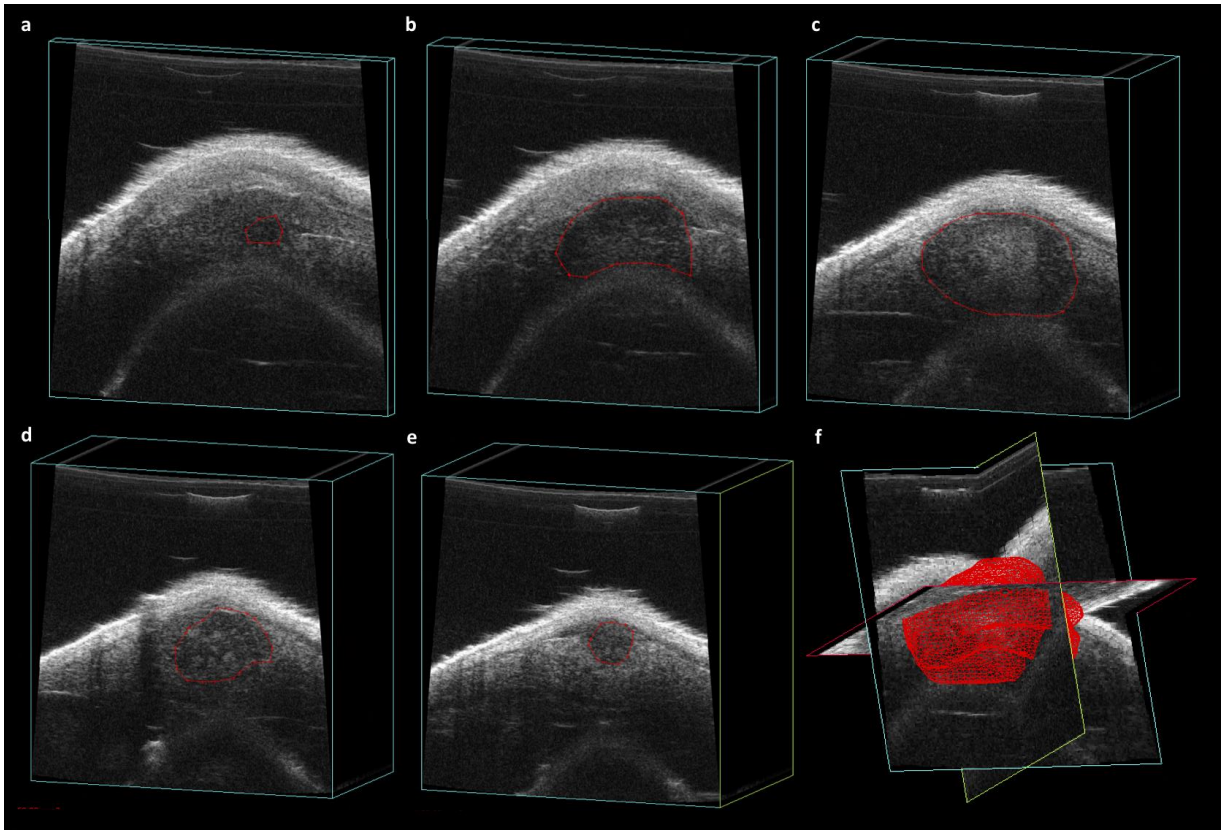

Figure 6.3 3D image of SW620 liver tumour reconstruction for volume analysis.

3D scans of tumours were performed using HFUS using a 40 MHz (RM-704) transducer on a motorised arm, with the VisualSonics Vevo 770 system. 3D reconstructions were generated post acquisition using the Vevo 770 version 3 software. Tumour volume was calculated by outlining the tumour area at regular intervals throughout scan (a-e), which generates a 3D reconstruction (f) and volume (52.9 mm3).

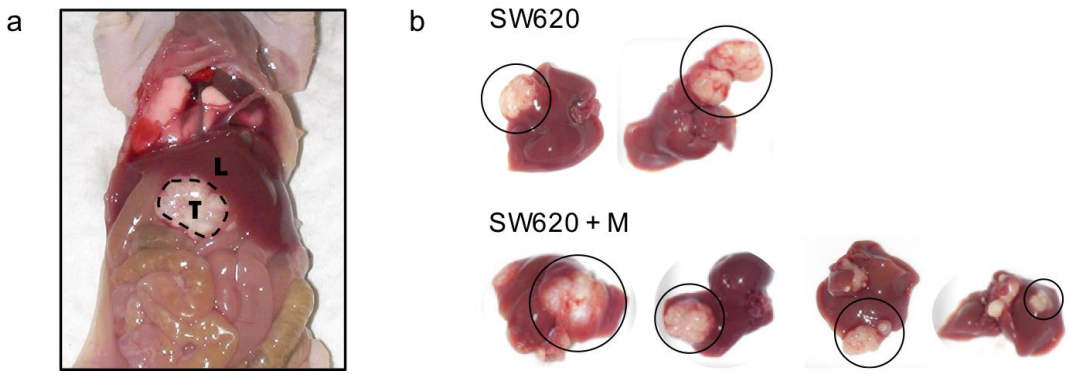

Figure 6.4 Orthotopic SW620 tumours in livers of intrahepatically injected mice.
5 x 10^5 SW620 human CRC cells were injected intrahepatically with matrigel (SW620 + M) or without (SW620). Images are shown from final-day collection (day 35). (a) Dissection revealed a clean cavity, with normal organ colour and an obvious single tumour at injection site. L = liver, T = tumour (dashed line indicates tumour region) (b) Dissected livers from all mice with tumours showed a single tumour, site circled.

Table 6.1 End-point orthotopic SW620 liver tumour volumes determined by HFUS imaging.
SW620 CRC cells (5 x10^5) were injected intrahepatically, and tumour volume was determined by *in vivo* HFUS imaging after 35-days post inoculation (end-point). 4/5 tumours grew after CRC cells were injected with matrigel. 2/5 tumours grew when the same number of cells were injected in the same way, (3/5 with no tumour). Take rate was double when matrigel was used. One mouse did not recover from general anaesthetic (non-recovery) and one tumour was positioned too low in the abdominal cavity to observe (not observed).

	Tumour volume (mm^3)	
Mouse	With Matrigel	Without Matrigel
1	93.23	81.56
2	81.39	Not Observed
3	54.08	No Tumour
4	30.32	No Tumour
5	Non-Recovery	No Tumour

6.1.3. *In vivo* and *ex vivo* analysis of intrahepatic tumour growth

Murine livers were imaged weekly using HFUS and tumour volumes were determined (**Figure 6.5 a**). End-point tumour volumes, 35-days post tumour inoculation varied between 30 – 93 mm^3 with a median volume of 81 mm^3 for both groups (**Table 6.1**). Matrigel was not necessary for tumour growth but when used in the intrahepatic injections, success rate was doubled. Matrigel may provide a more favourable environment for growth when using low cell numbers as determined by the low total volume (40 µl) that could be injected intrahepatically. When tumours grew without matrigel, there were no significant differences in size or rate of growth compared to the matrigel group. Injections of cells with matrigel resulted in 4/5 mice growing tumours in the liver. However, one mouse from the matrigel cohort did not recover post-procedure, post-mortem examination did not reveal cause of death (the portal vein may have been injected resulting in an embolism) and was therefore removed from the experiment. When matrigel was not used 2/5 grew tumours. One of these tumours grew low down in the liver lobe and was out of the imaging region. The use of matrigel may hold the cells at the injection site by the formation of a plug and prevent slippage as seen in this instance.

End-point liver mass was used to determine any significant differences between livers with tumours and those without (control group). Livers with tumours had significantly higher mass than the control group, $p > 0.05$ (Mann Whitney (two-tailed)) (**Figure 6.5 b**).

Body mass change from injection day to end-point (35 days later) were not significantly different, however mice with liver tumours increased body mass by 6% compared to the control group which gained 2% (median values), presumably due to the additional mass of the tumours (**Figure 6.5 c**). Weight-loss was not observed in any of the mice in any group at any point during the experiment, an indication of good health and well-being.

6.1.4. Histological analysis of orthotopic tumours

Livers were analysed first by H&E staining on paraffin-embedded fixed tissue and all revealed single tumours with distinct liver-tumour borders, representative images are shown (**Figure 6.6 a-b**). Immunostaining with the endothelial cell marker CD31, demonstrated how highly vascularised liver tissue was compared to tumour (**Figure 6.6 c**). The angiogenic marker VEGFR2 was detected and revealed staining of tumour endothelial cells, the fenestrated endothelial cells of the liver sinusoids but not the endothelial cells of the hepatic venules (**Figure 6.6 d**). Non-selective staining was high despite being the only recommended anti-VEGFR2 antibody for IHC analysis (Smith *et al.,* 2010).

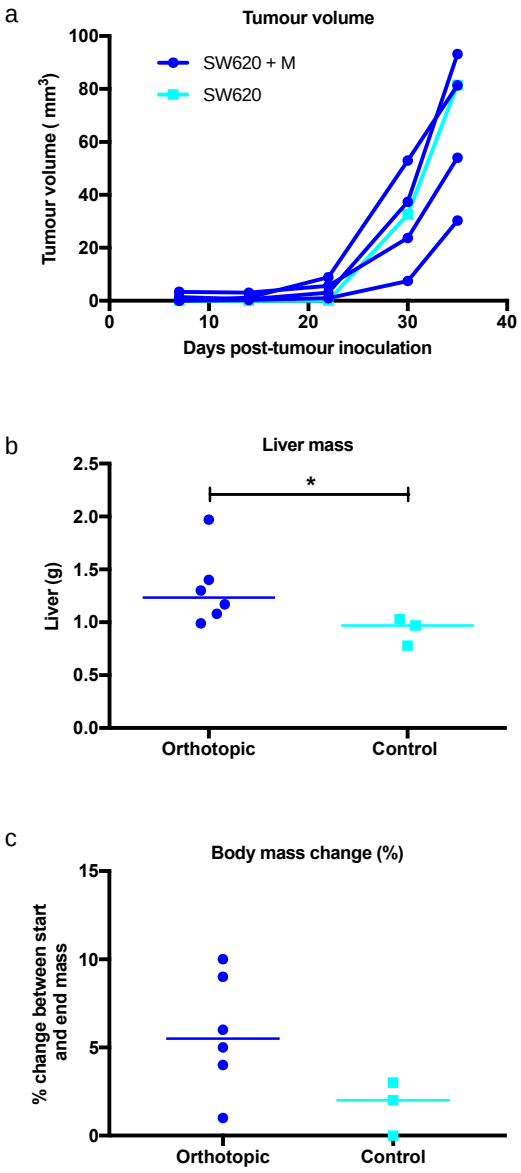

Figure 6.5 *In vivo* and *ex vivo* analysis of orthotopic SW620 liver tumour growth.

(a) Tumour volume was determined weekly by HFUS imaging. 4/4 tumours grew after SW620 CRC cells (5 x10^5) were injected intrahepatically with matrigel (SW620 + M group). 2/5 tumours grew when the same number of SW620 cells were injected in the same way, but without matrigel (SW620 group), however one tumour was positioned too low in the abdominal cavity to image. (b) End-point liver mass with tumours (Orthotopic group, n=6) was significantly higher than liver mass without tumours (Control group, n=3), *p = 0.0476 (Mann Whitney (two-tailed)). (c) Body mass change from injection day to end-point (35 days later). Both groups increased % body mass during the experiment, indicating good health throughout with no significant differences. Median indicated by the bar.

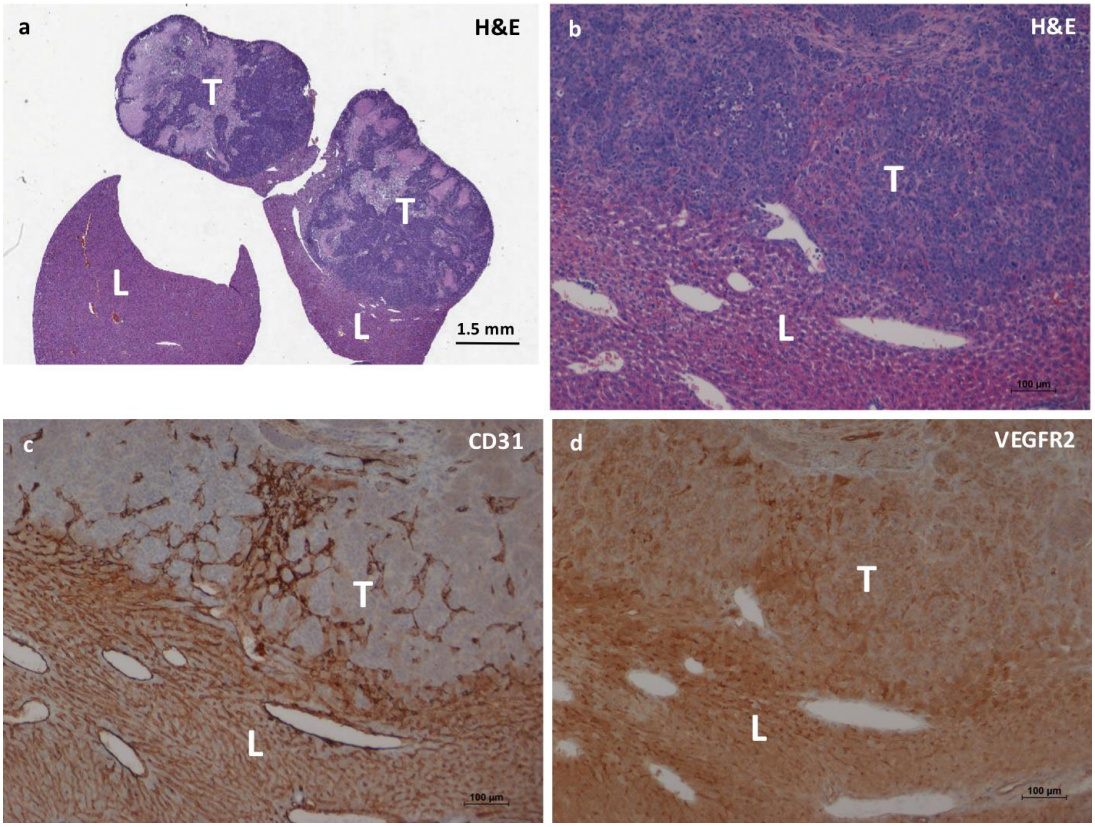

Figure 6.6 Histological analysis of orthotopic liver metastases.

(a - b) Livers with SW620 human CRC tumours were stained with H&E to reveal invasive borders between liver (L) and tumour (T). (c) The endothelial cell marker CD31 was used to immunostain blood vessels of the liver and tumour. (d) VEGFR2 staining was not tumour-specific, it was also found in the fenestrated endothelial cells of the liver sinusoids but not the endothelial cells of the hepatic venules.

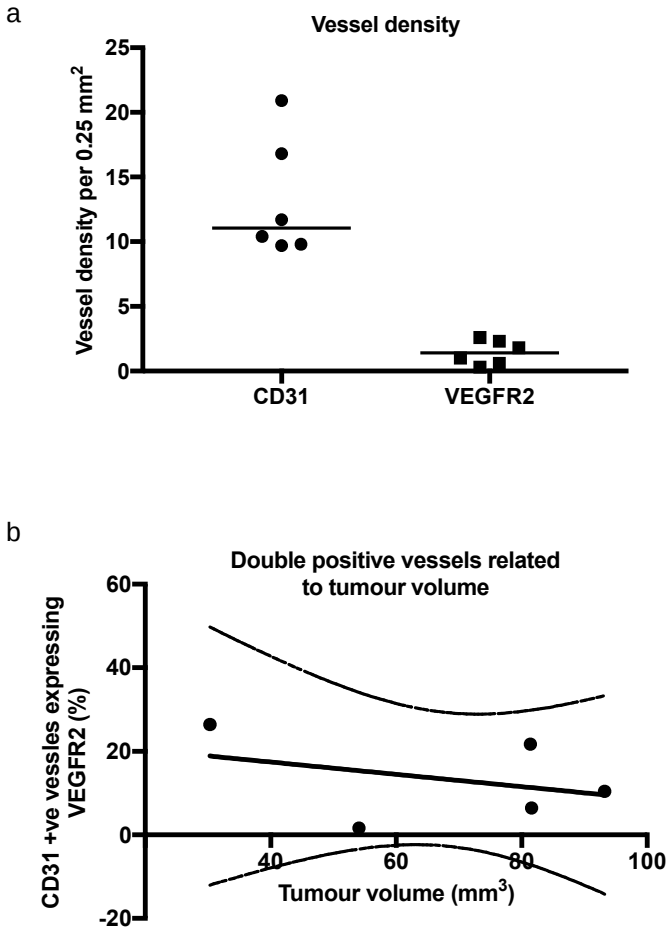

Figure 6.7 CD31 and VEGFR2 vessel density analysis of orthotopic SW620 liver tumours.

(a) Vessel density of CD31 or VEGFR2 positive vessels per 0.25 mm^2 of tumour. Median value indicated by the bar (n=6). (b) Percentage of VEGFR2/CD31 double positive blood vessels related to end-point tumour volume (95% confidence intervals shown by dashed line) Only 5/6 tumours had tumour volume determined, hence one missing data point.

To investigate whether VEGFR2 could be used as a target for future thMB drug delivery to CRC liver metastases, CD31 and VEGFR2 immunostaining was assessed semi-quantitatively to determine vessel density using each marker within the tumour region of the liver. CD31 positively stained vessels gave a vessel density of 11.1 per 0.25 mm^2 whereas VEGFR2 vessel density was 1.4 per 0.25 mm^2 (median values) (**Figure 6.7 a**). 12.6% of the CD31 positive vessels were also VEGFR2 positive. These data were plotted against end-point tumour volume to determine whether tumour size has an effect on VEGFR2 density. Tumour volume did not influence VEGFR2 density significantly (**Figure 6.7 b**), suggesting VEGFR2 could be a potential target for metastatic tumours of the liver which are too large/unsuitable for resection.

6.2. Histopathology of orthotopic and subcutaneous colorectal xenografts

The tumour microenvironment plays an important role in influencing the growth of tumours cells *in vivo*. To compare the effect of the microenvironment on SW620 tumour histology, intrahepatic tumours were compared to those grown subcutaneously. $1x10^7$ SW620 human CRC cells without matrigel were injected subcutaneously in 10 CD1 nude mice and tumours were grown for 25 days. Larger cell numbers were necessary for this type of injection, and a larger volume can be injected under the skin compared to the liver).

Tumour histology of SW620 cells grown in the liver were compared to those grown subcutaneously (**Figure 6.8**). Orthotopic tumours characteristically had necrotic islands and areas of geographic necrosis. Invasive borders into the liver parenchyma were common, with inflammatory infiltrate and blood pooling in the sinusoids of the liver (potential vascular congestion) (**Figure 6.8 a - c**). Extensive necrosis was observed in subcutaneous tumours, a necrotic core with an obvious viable rim was observed typical of subcutaneous xenografts. Islands of viable cells surrounding enlarged blood vessels were also common. No muscular invasion was observed. (**Figure 6.8 d - f)**. Both tumour microenvironments showed poor glandular differentiation and mainly formed sheets of epithelial cells, typical of SW620 tumours (Hewitt *et al.,* 2000).

Subcutaneous tumours grew rapidly in comparison to the orthotopics, this may have been due to the increased initial cell number injected (20-times more). Tumour volume was significantly higher at end-point (*p > 0.05 Mann Whiney (two-tailed)), with the median

volumes being 81 and 508 mm^3 for orthotopic and subcutaneous, respectively (**Figure 6.9 a**). Subcutaneous tumours had a much larger volume range, 19-982 mm^3 compared to 30-93 mm^3 for the orthotopics. Differences between immunocompromised mice BALB/c nude (orthotopic) and CD1 nude (subcutaneous) mice may have influenced tumour microenvironment conditions in terms of immunological influences.

Tumour necrosis is a common feature of solid tumours, where blood supply cannot keep up with rapid tumour growth. Percentage area of tumour necrosis was determined for both microenvironments (**Figure 6.9 b**). Subcutaneous tumours had over 2-times more necrosis than orthotopic tumours, which was statistically significant ($p < 0.05$ Mann Whitney (two-tailed)). Orthotopic tumours had a median value of 27% necrotic tumour area compared to subcutaneous which had 62%. This difference suggests inadequate vascularisation of the subcutaneous tumour due to rapid growth from an area that is poorly vascularised (between skin and peritoneum), therefore cells grow too fast for vascular supply to form. Necrotic area was compared to tumour volume to determine whether tumour size correlated with percentage necrotic area (**Figure 6.9 c** and **d**). The orthotopic tumour showed no correlation with tumour volume however subcutaneous tumours were significantly different to zero ($p < 0.01$, $R^2 = 0.63$) with larger tumours having high percentages of necrotic area.

Number of mitotic bodies per mm^2 of tumour was used as a marker of proliferation. The orthotopic tumour had a median of 20 mitotic bodies/mm^2, in contrast to the subcutaneous tumours with a median of 8 mitotic bodies/mm^2, which did not quite reach statistical significance ($p < 0.06$ Mann Whiney (one-tailed)) (**Figure 6.10 a**). Orthotopic tumour cells were highly proliferative in comparison to the subcutaneous cells, perhaps due to the vascular supply being able to support the growth of the orthotopic tumour, potentially due to the difference in initial cell numbers injected.

Vessel density was used to determine whether the microenvironment changes the vascularity of the tumours, however no significant differences were found between groups (**Figure 6.10 b**). Median values were 11 CD31 positively stained vessels per 0.25 mm^2 of tumour tissue for both groups, indicating that vessel density was the same irrelevant of tumour placement and despite the range in tumour volumes. This may suggest that the orthotopic tumours were not better vascularised in terms of vessel density but the vessels were better functionally.

VEGFR2 is an important marker of tumour angiogenesis. VEGFR2 blood vessel density was determined and was not found to be significantly different between groups. Subcutaneous

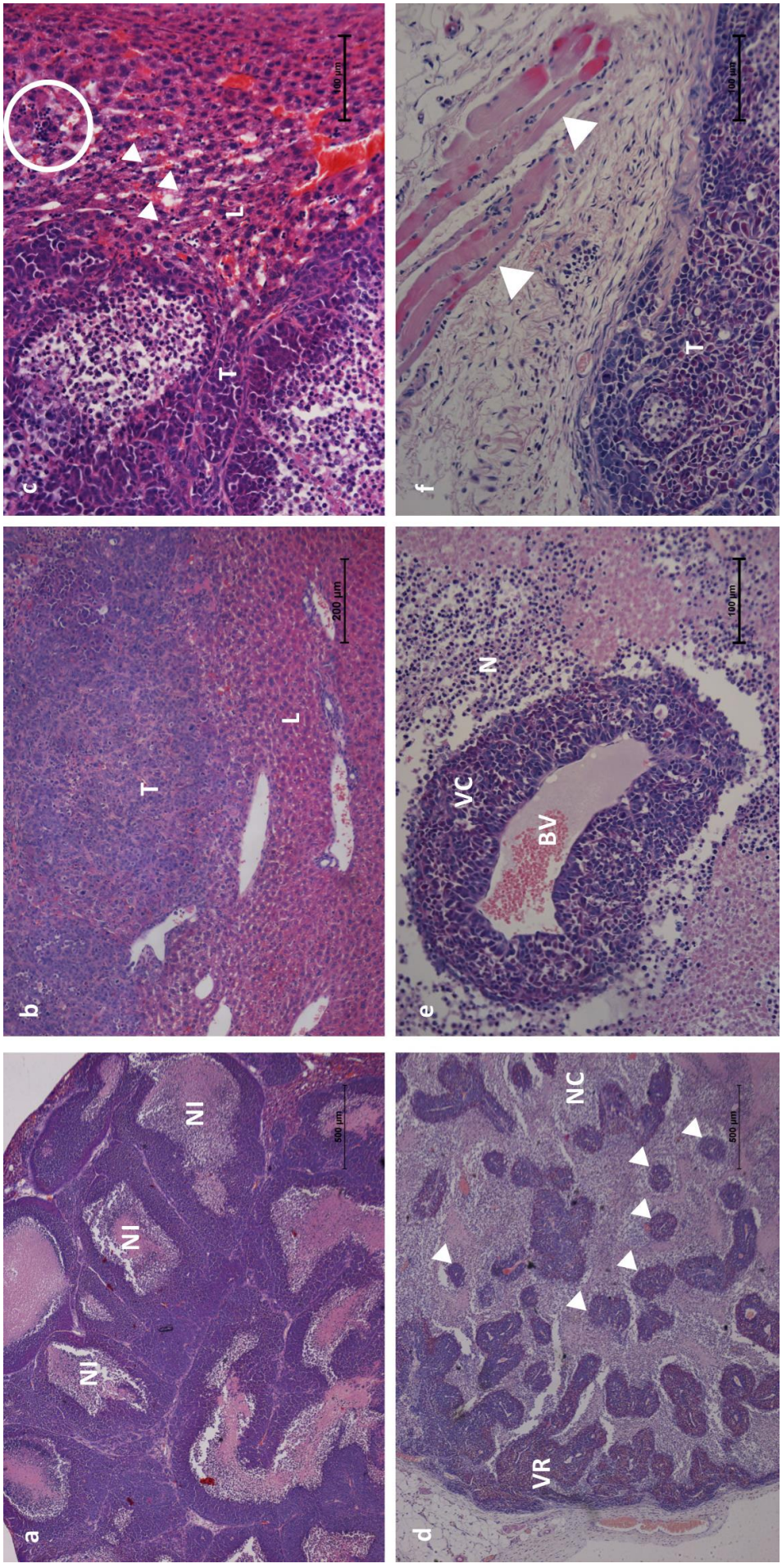
a
NI
NI
NI
500 µm
b
T
L
200 µm
c
T
L
100 µm
d
NC
VR
500 µm
e
N
VC
BV
100 µm
f
T
100 µm

Figure 6.8 A histological comparison of orthotopic liver metastases and subcutaneous human CRC xenografts (SW620).

Representative images of orthotopic tumours: (a) Necrotic islands (NI), (b) Invasive boarder between tumour (T) and liver (L), (c) Red blood cells pooling in sinusoids (arrows) with inflammatory infiltrate (circled). Representative images subcutaneous tumours: (d) Viable rim (VR) with necrotic core (NC), with islands of viable cells surrounding a blood vessel (arrows), (e) Island of viable cells (VC) encircling an enlarged blood vessel (BV) surrounded by necrosis (N), (f) Tumour (T) has not invaded skeletal muscle (arrows).Orthotopic tumours = 5 $x10^5$ intrahepatic inoculation into BALB/c nudes, Subcutaneous = 1 x 10^7 subcutaneous inoculation into right flank of CD1 nudes. For scale refer to scale bar, bottom-right for each image.

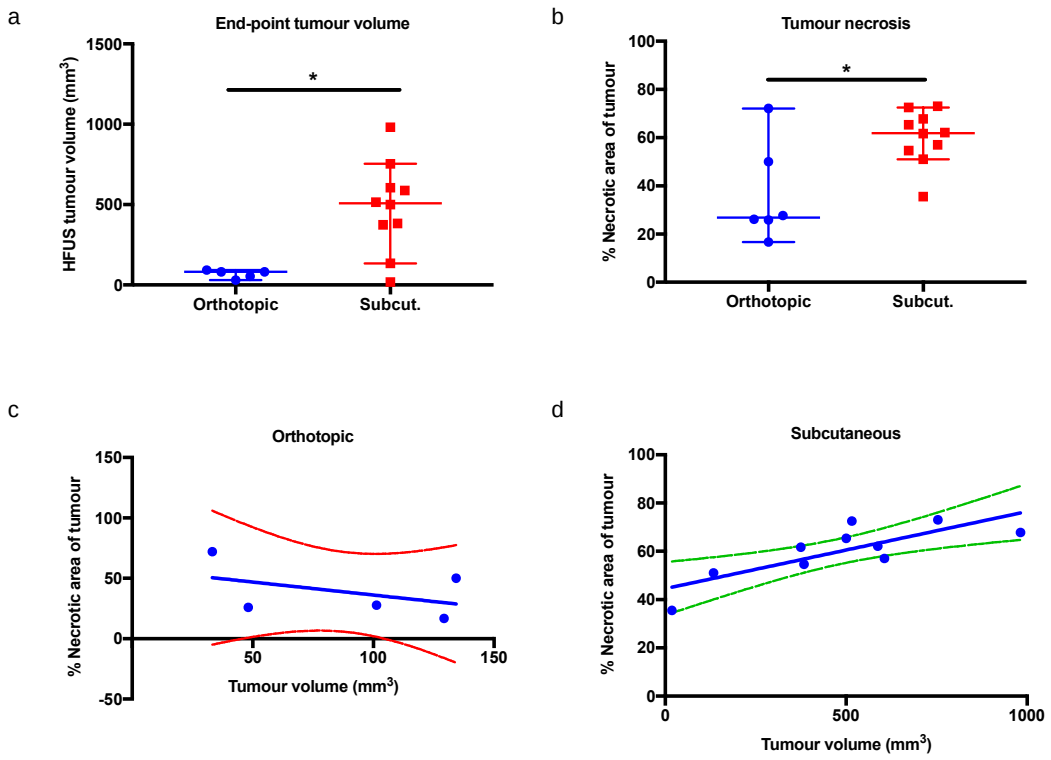

Figure 6.9 A comparison of morphology of orthotopic liver metastases and subcutaneous human CRC xenografts (SW620).

(a) End-point tumour volume determined by HFUS *p = 0.013 Mann Whitney (two-tailed). (b) Tumour necrosis *p = 0.023 Mann Whitney (two-tailed). Median (± 95% confidence interval) values indicated by bar (a-b). (c) Orthotopic tumour necrosis showed no correlation to tumour volume (deviation from zero not statistically significant). (d) Subcutaneous tumour necrosis was correlated to tumour volume (deviation from zero p = 0.006, R^2 = 0.63). Dotted lines indicate 95% confidence intervals. Orthotopic = 5 x10^5 intrahepatic inoculation into BALB/c nudes (n=6), Subcutaneous = 1 x 10^7 subcutaneous inoculation into right flank of CD1 nudes (n=10).

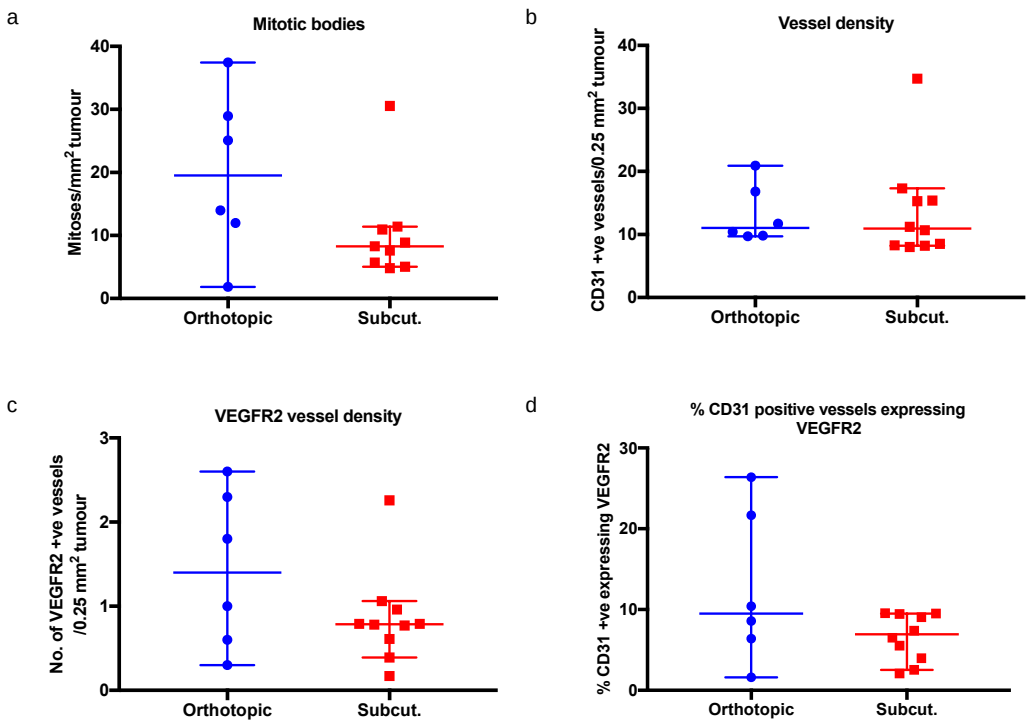

Figure 6.10 A comparison of cellular phenotypes between orthotopic liver metastases and subcutaneous CRC xenografts.

(a) Number of mitotic bodies per mm^2, neared significance p = 0.057 Mann Whitney (one-tailed), (b) CD31 positive vessel density per 0.25 mm^2, (c) VEGFR2 vessel density per 0.25 mm^2 and (d) percentage of VEGFR2/CD31 double positive blood vessels, no significant differences found between groups. Median (± 95% confidence interval) values indicated by bar. Orthotopic = 5 x 10^5 intrahepatic inoculation into BALB/c nudes (n=6), Subcutaneous = 1 x 10^7 subcutaneous inoculation into right flank of CD1 nudes (n=10). Median (± 95% confidence interval) values shown. All analyses performed on a single tumour section.

tumours had a median value of 0.8 positive vessels/0.25 mm^2, compared to orthotopic which had almost twice as many with 1.4 positive vessels/0.25 mm^2 (**Figure 6.10 c**). The percentage double positive CD31/VEGFR2 blood vessels were determined for each tumour group (**Figure 6.10 d**). The orthotopic tumours gave a median of 10% with a range of 2 – 26% double positive vessels, compared to subcutaneous which gave 7% with a range of just 2 – 9%.

6.3. Discussion

Early diagnosis of CRC (Stage I) has a 5-year survival rate of 98%, in comparison to late stage (Stage IV) where this falls to just 8% (Cancer Research UK, cancerresearchuk.org, accessed March 2018). More than 50% of those diagnosed with CRC will go on to develop liver metastases during their lifetime. Surgical resection of the metastasis is recommended (if feasible), however 70% will go on to experience recurrence (Tomlinson *et al.,* 2007). Chemotherapy used neoadjuvantly (preoperatively) may aid in reducing tumour size and therefore making a previously unresectable tumour resectable. Currently however, long term survival is poor.

The influence of the microenvironment on tumour development is well known. However, currently the use of orthotopic tumour models in translational research is far less common than subcutaneous. Murine models of CRC and metastases in their clinical environment are needed to improve and accelerate translation of future anti-cancer agents.

In this context, a murine CRC liver metastases model was developed, by intrahepatic, US-guided injection of the human CRC cell line SW620, the metastatic variant of SW480 derived from lymph node (Hewitt *et al.,* 2000). This model would be useful for investigating the effects of novel anti-cancer agents such as thMBs. Although murine liver metastasis models have previously been developed (Oh *et al.,* 2017), this is the first example of an alternative non-surgical method.

6.3.1. Minimally-invasive, US-guided intrahepatic injections

This minimally-invasive, US -guided intrahepatic injection technique for the formation of CRC liver metastases, was an alternative to the more commonly used surgical transplantation method. This technique was rapid to perform, and therefore required less time under general anaesthetic than a surgical procedure. The procedure was technically less challenging than surgery, and therefore easier to perform and minimised risks associated with surgical intervention. No loss in mouse body mass or changes to normal behaviour were noted at any point during the experiment. There was no abnormal

behaviour such as hunched posture, piloerection or isolation from the group, all indicators suggesting that the animals were in minimal discomfort after this technique. The use of a 30-gauge insulin needle to inject cells resulted in no visible wound, an advantage over surgical inoculation which requires stitches to close the abdominal cavity, therefore less inflammation and minimal healing time. Post-operative analgesics were also not necessary with such a minimally-invasive technique, with unknown effects from the use of such drugs on experimental outcomes. It has been widely suggested that pain and resulting stress can impact experimental outcomes resulting in poor reliability and reproducibility of experiments involving animals (Balcombe *et al.,* 2004).

This model is an excellent example of the National Centre for the Replacement, Refinement and Reduction of Animals in Research (NC3Rs https://www.nc3rs.org.uk/the-3rs) principles involving refinement of technique and development of techniques which minimise the 'pain, suffering, distress or lasting harm', directly improving welfare of animals in research (Prescott and Lidster, 2017). The development of a minimally invasive, non-surgical technique for the creation of a murine model of liver metastases represents a refinement of current technique.

6.3.2. Matrigel improves cell engraftment in an orthotopic model of CRC liver metastases

Matrigel is comprised of extracellular matrix proteins, collagen IV and growth factors which can be used to improve cell engraftment in difficult to grow cell lines or primary patient derived cancer cells (Gock *et al.,* 2016; Pretlow *et al.,* 1991). This orthotopic model when incorporating matrigel into the injection had a 100% success rate compared to when matrigel was absent which had only a 40% success rate. Low cell numbers (5×10^5) were used due to the small volumes that could be injected into the intrahepatic space and these may have benefited from the additional growth factors within the matrigel, providing a more favourable environment for growth. The use of matrigel may also hold the cells in the injection site by the formation of a plug (it solidifies at body temperature) and therefore prevents leakage of the cells in solution from the injection site, as seen in the group without matrigel. Although the use of matrigel was not necessary for tumour growth, it improved the take rate.

6.3.3. Intrahepatic human CRC tumours

Tumour burden consisted of an obvious single, large tumour at/near the injection site, with no dissemination into the abdominal cavity and a 100% take rate when matrigel was

used to inject the cells. Recently, a group has successfully demonstrated surgical intrahepatic inoculation of hepatocellular carcinoma cells with 100% take rates, however 50% of these also showed abdominal and pelvic tumours from leakage during intrahepatic injection or may be cell line specific (Rao *et al.,* 2016). The non-surgical transplantation of CRC cells into liver has not been done before.

The SW620 human CRC cell line was chosen for the liver metastasis model due to its relationship with the SW480 cell line used previously to model CRC subcutaneously (**Chapters 3 - 5**). SW620s were derived from a mesenteric lymph node metastasis removed from the same patient as the primary colon carcinoma of which SW480s were derived (Leibovitz *et al.,* 1976). This metastatic cell line was therefore an interesting candidate for direct intrahepatic injection to mimic metastatic colorectal liver metastasis.

The SW620s have been previously demonstrated to be a useful cell line for the formation of liver metastasis when inoculated intracaecally (after 42 days 2/10 formed liver metastases), when SW620s were compared to 11 other CRC cell lines which did not metastasise to the liver of BALB/c nude mice (Flatmark *et al.,* 2004). Other groups have also confirmed that SW620 are able to form liver metastases (Hewitt *et al.,* 2000; Zirvi *et al.,* 1991). However, a more recent paper has demonstrated that SW620s microinjected into the caecal wall of Swiss nu/nu mice, did not form liver lesions after 130 days (Céspedes *et al.,* 2007). Therefore, published literature is conflicting as to the metastatic ability of this cell line, and direct intrahepatic implantation may be a more reliable and reproducible model of liver metastases using this particular cell line.

6.3.4. HFUS allows orthotopic tumour growth to be monitored longitudinally, quickly and easily

The use of HFUS allowed the weekly determination of tumour volume and therefore is a useful technique to quantitatively assess anti-cancer therapeutics such as thMBs. HFUS is a cheap, quick and safe imaging modality as demonstrated here. Without the use of imaging, the outcome may not be known until end-point dissection and histological analysis, which would be time consuming and require many more mice to determine appropriate end-points. As shown here, end-point liver mass can be used to quantitate the degree of growth of the metastases, as livers with tumours increased in mass significantly compared to control livers. Other imaging modalities such as MRI, bioluminescence or fluorescence (Park *et al.,* 2016; Magistri *et al.,* 2017; W.Y. Lee *et al.,* 2014) may also be used for *in vivo*

tumour volume assessment but would not be as cheap, rapid or precise at measuring tumour volume.

Recently an orthotopic CRC liver metastases model (intrasplenic injection) has been used to compare imaging modalities, MRI, bioluminescence and HFUS, for the characterisation of growth of intrahepatic tumours (Ramasawmy *et al.,* 2016). MRI and US were found to be the most accurate modalities, with US more sensitive than low-field MRI (Ramasawmy *et al.,* 2016). HFUS is therefore a cheap and rapid modality for tumour volume determination.

6.3.5. A potential model for *in vivo* testing of thMBs

The liver was shown to be highly vascular, ideal for drug delivery using vascular agents such as thMBs. As the liver metastases formed close to the surface of the liver the use of an US-trigger would easily penetrate to those depths. The formation of a single tumour at the injection site allows drug efficacy to be easily monitored throughout the experiment, as opposed to multiple foci or many micro-metastases where efficacy may be more difficult to confirm without lengthy histological evaluation.

Histological analysis of SW620 tumours confirmed that VEGFR2 could be used as a target for thMB drug delivery, although not a tumour-specific marker, off-site delivery could be minimised by localising the US-trigger to the liver metastases.

SN38 nanoparticles have been tested in just two orthotopic models of human CRC, a liver metastasis model via a portal vein injection of human CRC cells (Takahashi *et al.,* 2010) and a dissemination model via intraperitoneally injected human CRC cells (Al-Kasspooles *et al.,* 2013). Therefore, further testing with a tumour model that more accurately represents the tumour microenvironment of late stage disease is required.

6.3.6. Human CRC tumour models: Subcutaneous verses orthotopic

Subcutaneous inoculation of human cancer cells is the most commonly used murine cancer model due to their ease of inoculation and palpability of subsequent tumours. However, the effect of the microenvironment on cancer cells is of obvious importance, with the influence of growth factors, angiogenesis and metastatic behaviour more like the clinical representation and therefore the use of orthotopic models may lead to more reliable translation. Comparison between SW620 human CRC cells grown in the liver parenchyma and those grown subcutaneously were found to have stark differences. Orthotopic tumours were significantly less necrotic despite having the same vessel density (CD31

positive blood vessels). Perhaps the blood supply from the liver was more nutrient rich and could support the rapid growth rate of the SW620 tumours, and hence why the cells found in the orthotopic tumours were more proliferative. Subcutaneous SW620 tumours were histologically typical of subcutaneous xenografts, displaying a necrotic core and viable rim. These tumours had extensive necrosis with islands of viable cells surrounding blood vessels, consistent with others (Hewitt *et al.,* 2000). Subcutaneous models in general have been poor predictors of drug efficacy in humans and hence the need for more predictive models of human cancers. The orthotopic model described here has one main disadvantage in that it does not mimic metastatic formation from a distant primary site and so does not model extravasation, systemic circulation and intravasation. However, the aim of this study was not to investigate the mechanisms of metastasis but rather to allow reproducible tumour growth in the appropriate microenvironment, in order to assess efficacy of anti-cancer agents as realistically as possible with the need for a minimal number of animals.

The most commonly exploited models of CRC liver metastases are injection site-dependent, either surgical inoculation of spleen or caecum involving implantation or subserosal injection (Saxena and Christofori, 2013; Heijstek *et al.,* 2005). Intrasplenic injection results in the rapid formation of liver tumours by drainage into the hepatic portal vein via the splenic vein but often involves the removal of the spleen; a vital immune organ. Caecal injections are technically more difficult and with higher risk of postsurgical complications, but with the advantage of allowing the study of invasion from the primary site. However, caecal implantation results in the slow and unreliable formation of metastases in the liver (up to four months), and with metastases also found in lung, lymph nodes and peritoneum (Céspedes *et al.,* 2007). However, this model (using matrigel) reliably resulted in relatively quick formation (4-weeks), of single tumours which could reflect late stage CRC, where large tumours in the liver would require de-bulking (i.e. obstructing portal vein), via adjuvant chemotherapy or radiation, prior to surgical resection. The formation of a single tumour allows for ease of monitoring of tumour volume via HFUS, and therefore a means of testing efficacy of novel therapeutics quickly and easily.

The technique of US-guided injection has the potential to create models of different cancers. It has been used to model cholangiocarcinoma (Imeshi Wijetunga, personal communication), using TFKLucB2 cholangiocarcinoma cells with the gallbladder as a landmark for US-guided, intrahepatic inoculation. Another example involved US-guided,

intrasplenic injections of tumour cells (Hawcroft *et al.,* 2012). In this study, all mice developed one or more liver metastases after intrasplenic injection of MC-26 mouse CRC cells (Hawcroft *et al.,* 2012). However, tumour burden consisted of either multiple, small metastases throughout the liver parenchyma or a smaller number of discrete tumours at the hilum and therefore end-point liver mass was used to determine significant differences between cohorts rather than *in vivo* tumour volume determined by HFUS.

6.4. Summary

In summary, this chapter has successfully demonstrated the development of a minimally-invasive model of CRC liver metastases, in which tumour volume was monitored throughout using HFUS. This model provides a promising experimental tool for future testing of thMBs or other anti-cancer agents for management of late stage disease.

Chapter 7

General Discussion & Future Challenges

7. General Discussion

7.1. Final summary

At the beginning of the project, a sensitive LC-MS/MS method was developed and validated to measure concentrations of irinotecan and its metabolites in murine xenograft tumours, tissues and serum/plasma samples (**Chapter 3**). The development of this method was essential to investigate the PK of thMB drug delivery as the doses of drug used were so low. The method was successfully applied throughout this project to study PK of irinotecan and/or SN38 using low dose free drug and thMBs + US-triggered delivery. It was shown that thMBs could successfully deliver irinotecan and SN38 to tumours using an *in vivo* xenografts model of human CRC (**Chapter 3 - 5**).

A PK and biodistribution study was used to demonstrate enhanced tumour-specific drug release with US-triggered thMBs, followed by a longitudinal study which confirmed preferential tumour drug deposition over other tissues after 72-hours (**Chapter 4**). An increased SN38 dose resulted in high growth inhibition and regression of xenograft tumours, with no observable toxic side effects in mice. The 5-second tone US-trigger proved optimal over 120-second chirp for intratumoral drug delivery, with VEGFR2-targeting needing further investigation (**Chapter 5**).

Finally, a minimally-invasive model of CRC liver metastases was developed (**Chapter 6**). This method was minimally invasive, whilst fast and easy to perform and was amenable to monitoring tumour growth regularly and economically via HFUS. Fewer animals were required than with traditional orthotopic models of CRC, as tumour take rates were high using matrigel and subsequent growth could be monitored non-invasively. Orthotopic tumours grow differently to the commonly used subcutaneous models and therefore the importance of using a model which takes into consideration the natural microenvironment is vital for faster and more reliable clinical translation. This model provides a promising experimental tool for future testing of thMBs or other anti-cancer agents for management of metastatic CRC as well as primary liver tumours.

7.2. Potential mechanism of thMB drug delivery

Thus far, thMBs have demonstrated increased tumour drug accumulation/retention in tumour (and other tissues) compared to free drug. Low doses of drug were used which reduced the possibility of toxic side effects, but also resulted in high tumour growth

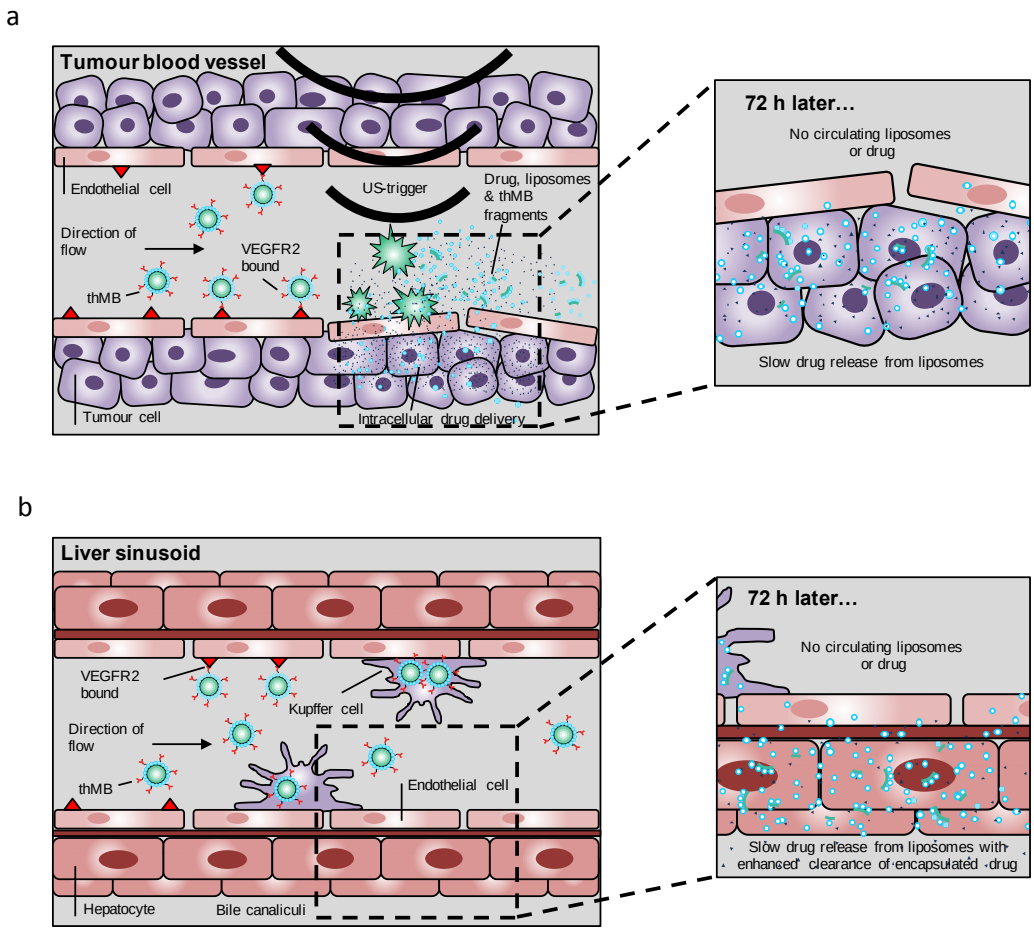

Figure 7.1 Schematic to illustrate how drug delivery using thMBs may occur.

ThMBs are injected intravenously and (a) accumulate in the tumour vasculature via endothelial cell targeting to VEGFR2. ThMBs are destroyed by a tumour localised ultrasound-trigger (US-trigger). Destruction of thMBs via inertial cavitation at the target site locally delivers a payload of chemotherapy drug and increases intracellular drug uptake via mechanisms of sonoporation such a microjetting and shockwaves. MB fragments, targeted liposomes, free drug and MB lipids are swept downstream and further diluted into systemic circulation and tissues. (b) In liver, in the absence of a direct US-trigger, intact thMBs, MB fragments and/or liposomes accumulate in liver tissue for hepatobiliary clearance. Liver macrophages (Kupffer cells) engulf thMBs, lipid fragments and/or liposomes. Drug metabolism in liver reflects that of persistently encapsulated drug preventing metabolism or release of drug thereby limiting toxicity.

inhibition. This thesis taken as a whole has demonstrated that thMB drug delivery has the potential to increase the therapeutic index of drugs delivered in this way.

US and MBs work together in two ways, delivering and destroying drug-loaded MBs in the target area, and aiding drug uptake at a cellular level. Drug-loaded MBs are injected intravenously and arrive at the tumour site, US is focused on the tumour region and the MB are destroyed as they pass through the US beam (**Figure 7.1 a**). Destruction at the target site locally delivers a payload of chemotherapy drug directly to the tumour. Sonoporation caused by shockwaves and microjetting has been proposed as the main mechanism of intracellular drug delivery. How thMBs increase drug retention over time (as demonstrated by LC-MS/MS 72-hour post final treatment, **Chapters 3-5**) is as yet unknown.

High acoustic pressures were shown to be necessary for *in vivo* drug delivery as shown by improved intratumoral drug delivery after the tone burst US-trigger compared to a chirp sequence. This implies that inertial cavitation or MB destruction improves *in vivo* drug delivery to tumours compared to stable cavitation. Lower acoustic pressures have been shown to shift uptake to endocytosis routes whereas higher acoustic pressures increase uptake mainly via the formation of pores (De Cock *et al.,* 2015). Shock waves and microjetting are MB behaviours associated with high acoustic pressures and may play a role in drug delivery/accumulation when using this thMB platform. This discovery highlights the importance of selecting the correct acoustic pressure to optimise drug delivery, and also the need for more MB behaviour-based, *in vivo* drug delivery experiments.

In terms of off-site accumulation i.e. the liver (**Figure 7.1 b**), it has been shown that MBs are rapidly engulfed by Kupffer cells, liver macrophages lining the walls of the sinusoids and part of the macrophage-monocyte system. One study using VEGFR2-targeted MBs showed Kupffer cells and splenic macrophages rapidly clear MBs from the circulation within minutes in mice (Willmann, Cheng, *et al.,* 2008). Liposomes have also been observed in higher quantities in Kupffer cells compared to the liver hepatocytes (Huang *et al.,* 1992; Litzinger *et al.,* 1994). This is consistent with the role of Kupffer cells in removing nano and micro scale particles from the blood circulation and leads to less toxicity to the hepatocytes.

7.3. Future investigations

7.3.1. Targeting to VEGFR2

In this study targeting of thMBs to VEGFR2 did not increase drug delivery to SW480 CRC xenografts compared with untargeted thMBs, however, very few animals were used precluding definitive interpretation. The success of this approach depends on the expression levels in tumour vasculature. Further studies are therefore needed to assess whether there is a benefit of using targeted versus non-targeted MBs for MB and US mediated drug delivery.

On-chip 'wash steps' are currently in development to add to the current microfluidic chip used to make MBs. This would ensure that any unbound VEGFR2 antibody would be washed away and ensure that no free antibody could bind to the receptor *in vivo* and block thMBs from binding in this way.

VEGFR2 MBs which have been dual (VEGFR2, $\alpha_v\beta_3$) and triple targeted (VEGFR2, $\alpha_v\beta_3$, P-selectin) have also been described to enhance MB accumulation in models of cancer and a similar strategy might prove useful in CRC (Warram *et al.,* 2011; Willmann, Lutz, *et al.,* 2008). Another option would be to switch from a VEGFR2 antibody to a VEGFR2 affimer. Affimer technology has been shown to be a viable alternative to using expensive humanised antibodies, are smaller in size, more stable to heat and pH changes with high affinity to target receptors (Tiede *et al.,* 2017; Martin *et al.,* 2018). Alternatively a VEGFR2 lipopeptide inserted directly into the shell of the MB would be used such as that in the Bracco BR55 MB (Willmann *et al.,* 2017; Tardy *et al.,* 2010; Pochon *et al.,* 2010).

Targeted MBs with shells that deflate to deform and increase the contact area between MBs and the endothelial wall have been shown to increase MB-endothelial wall binding (Rychak *et al.,* 2006). Studies by other groups are on-going to improve the accumulation of MBs in target regions, increasing number of targets (Warram *et al.,* 2011), and shell composition (Kooiman *et al.,* 2012).

7.3.2. Attachment strategies for loading liposomes into MBs and clinical trials

Different attachment strategies for binding drug-loaded liposomes to the MB shell may be required for use in human clinical trials i.e. neutravidin-biotin alternatives may be required before thMBs can be translated to the clinic. MBs can be targeted by attaching ligands to the outer shell. Although a simple concept, the attachment of ligands and/or drug

encapsulated nanoparticles to the MB shell has not yet been fully optimised. Coupling of the ligand to the MB or polymer is by either covalent or non-covalent bonding. Non-covalent bonds such as avidin-biotin are common for preclinical proof-of-concept experiments and can be easily exchanged for human compatible linker/covalent bonds. Avidin is a biotin binding protein derived from egg whites and multiple dosing has been shown to be immunogenic (Chinol *et al.,* 1998; Scott *et al.,* 1984; Lesch *et al.,* 2010).

Avidin doses of 20-40 µg (5-10 times more than the neutravidin used in this study) in BALB/c mice produce a much higher anti-avidin response in tested serum than PEGylated-avidin (Chinol *et al.,* 1998). Although avidin has been shown to be less immunogenic than streptavidin (bacterial origin) in mice (Marshall *et al.,* 1996; Chinol *et al.,* 1998), new attachment strategies such as maleimide-thiol conjugation are currently being developed (Yeh *et al.,* 2015), and for this reason many targeted MBs are still in the preclinical development stages.

7.3.3. Tumour drug exposure

Further PK studies to determine how long SN38 is retained in tumour tissues after thMB drug delivery may potentially allow for an alternative dosing schedule where fewer treatments are needed per week minimising stress to the animals and still ensuring anti-tumour growth efficiency. One study using a nanoliposomal formulation of irinotecan at 10 mg/kg, had detectable concentrations of irinotecan and SN38 more than 168-hours post injection (Kalra *et al.,* 2014). Another study has shown that single dose 10 mg/kg SN38 nanoparticles are detectable 72-hours later in blood and neuroblastoma xenograft tumours (Iyer *et al.,* 2015). Doxorubincin PEGylated liposomes (6 mg/kg) had detectable concentrations in plasma after 72-hours and orthotopic murine breast tumours 168-hours after injection (Charrois and Allen, 2004). Tumour drug retention and efficacy is a fine balance between the rate of tumour accumulation with the rate of drug release and metabolism. Therefore, optimising accumulation and drug release may be key to improving tumour drug exposures using nanoformulations (Charrois and Allen, 2004).

Further experimental controls using liposomal SN38 would make useful comparisons to other pre/clinical trials and possible mechanisms of thMB drug release and/or retention. In this thesis, liposomes were in limited supply as preparation relied on the kindness and availability of Dr R Abou-Saleh.

7.3.4. Tumour drug distribution

Tumour drug penetration is paramount for efficacy, with the distribution of many anti-cancer treatments to all cancer cells inadequate (Minchinton and Tannock, 2006). Tumours typically have torturous blood vessels, a result of rapid angiogenesis to feed quickly dividing cancer cells. However, it is this poor vascularisation which leads to areas of hypoxia and it makes it difficult for systemically delivered drugs to reach cancer cells. Normal drug delivery relies on crossing blood vessels to reach cancer cells, but with an abnormal blood supply not all cancer cells can be reached, or they may be exposed to only low concentrations which may contribute to tumour drug resistance (Hambley, 2009).

Matrix-assisted laser desorption/ionisation mass spectrometry imaging (MALDI MSI), is a technique which can be used to determine distribution of drugs within tissues, and also the penetration depth of drug away from blood vessels (Morosi *et al.,* 2013; Swales *et al.,* 2014). MB-mediated drug delivery has been previously shown to increase penetration depth and overall drug distribution throughout tumours (Han *et al.,* 2017). One group has shown an increased penetration depth of paclitaxel using MBs and high intensity focused US by imaging cross-sectional tumour tissues using near infrared fluorescence (Han *et al.,* 2017). It would be interesting to quantitate how far thMBs distribute drug from a tumour blood vessel and how this effects overall tumour drug distribution compared to free drug and may give further insight into the mechanisms of thMB drug delivery.

7.3.5. Could thMBs be used to overcome multidrug resistance mechanisms?

thMB drug delivery has the potential to overcome drug resistance mechanisms by the use of sonoporation rather than influx transporters to energetically deliver drug into cancer cells. An *in vitro* study using doxorubicin liposome loaded MBs and US was the first to demonstrate reversal of multidrug resistance in doxorubicin resistance human breast cancer cells (Deng *et al.,* 2014). Rapid intracellular uptake and nuclear accumulation and less efflux of the drug was found after US exposure (Deng *et al.,* 2014). Another group have replicated these finding, using 'US-detonated nano bombs', doxorubicin loaded hollow mesoporous titanium dioxide with DNA capping (Shi *et al.,* 2018). *In vitro* and *in vivo* treatment gave enhanced therapeutic effect against a doxorubicin resistance human breast cancer cell line and tumour model (Shi *et al.,* 2018).

Recently, doxorubicin-resistant hepatocellular carcinoma cells were re-sensitised using MBs and US with a combination of two therapeutic miRNAs in murine xenograft tumours

(Chowdhury *et al.,* 2016). MB delivery of small interfering RNA (siRNA) to silence ABCG2 protein which induces doxorubicin resistance in breast cancer, were shown to increase sensitivity of doxorubicin resistance xenograft tumours to doxorubicin (Bai *et al.,* 2015). Increasing the delivery of gene knockdown technology using MBs is a potential mechanism of overcoming multidrug resistance in tumours. Future experiments using drug resistant CRC cell lines may give further insight into its feasibility.

7.3.6. Therapeutic nanobubbles

The size of MBs limits them to the vasculature but nanobubbles (< 1 µm in diameter) may be able to extravasate and penetrate poorly perfused tumour areas and enhance drug distribution through the tumour tissue (Cavalli *et al.,* 2016). Nanobubbles, may also be targetable to the cancer cells themselves (H. Huang *et al.,* 2013; Cavalli *et al.,* 2016; Fan *et al.,* 2016; Peyman *et al.,* 2016).

7.3.7. Optimisation of the US-trigger used in combination with thMBs

Further optimisation of the US-trigger used in this thesis may involve increasing the total exposure time using a continuous infusion of thMBs for much longer periods than used here. Optimising the sequence of US may involve decreasing the pulse repetition frequency from 1kHz may allow thMBs to reaccumulate within the tumour vasculature and increase drug delivery more efficiently. One group has demonstrated that microvascular flow rate must be estimated to accurately determine the time it takes MBs to re-fill blood vessels (Qin *et al.,* 2009). Another group has suggested that 10-seconds is enough time for MBs to re-enter between pulses, and is more successful than continuous insonation (Miller and Quddus, 2000). The exposure duty cycle could be changed to allow for this 10-second reperfusion time, in-between US-pulses (destruction replenishment method), and may be more efficient than just extending the total sonication time as shown in **Chapter 5**.

The optimal acoustic pressure for *in vivo* drug delivery is currently under debate (as discussed in **Section 7.2**). The 5-second tone burst US-trigger used in this thesis created peak negative pressure of 250 kPa whereas other groups have used pressures ranging from 50 kPa to 3 MPa (Kooiman *et al.,* 2014; Yu *et al.,* 2015). Low pressures of 150 and 200 kPa have been shown to induce sonoporation *in vivo* using a chicken chorioallantoic membrane (Skachkov *et al.,* 2014). When using higher pressures (>200 kPa), frequency becomes less important as the MBs collapse under high acoustic pressures. The use of higher acoustic pressures has been shown to correlate with larger pore formations from inertial cavitation

(Fan *et al.,* 2012; Qiu *et al.,* 2010). It has been shown that cellular uptake of molecules increases with increasing acoustic pressures and therefore increasing the pressures used here may also increase tumour drug uptake *in vivo* (Yang *et al.,* 2008; Lentacker *et al.,* 2014). However, risk of localised mechanical damage and heat generation would also increase with increasing pressures.

The number of US cycles is also a parameter that could be further optimised, however when high pressures are used inertial cavitation occurs rapidly and longer pulse lengths may not be necessary (Lentacker *et al.,* 2014). Increasing the number of US cycles may also increase temperature locally and the FDA recommends US intensities where temperature increases are less than 1°C to avoid unwanted thermal effects (Barnett *et al.,* 2000; Mullick Chowdhury *et al.,* 2017).

Alternatively using monodispersed MBs in contrast to the polydisperse MBs used within this thesis may also increase the overall percentage of MBs that are within the resonance frequency of the US-trigger and therefore increase tumour drug delivery. Even greater tumour responses may be possible by using a higher MI to target central tumour areas and multi-frequency US-triggers to enhance extravasation and penetration (Eggen *et al.,* 2014). However, currently concentrations of monodispersed MBs are too low for pre/clinical use (Peyman *et al.,* 2012), furthermore broadband acoustic excitation signals could be used to excite polydisperse populations (McLaughlan *et al.,* 2013).

7.3.8. Efficacy of SN38 thMBs in orthotopic mouse models

The next preclinical phase of development for thMBs will involve the use of thMBs to deliver SN38 to the minimally invasive orthotopic model developed using US-guided injection (**Chapter 6**). Of the *in vivo* studies which have previously evaluated SN38 (nanoparticles) using models of CRC, only two were orthotopic models, a liver metastasis model via a portal vein injection of human CRC cells (Takahashi *et al.,* 2010), and a dissemination model via intraperitoneally injected human CRC cells (Al-Kasspooles *et al.,* 2013). This highlights the need not only for more pre-clinical testing of novel therapeutics in orthotopic models, but also the need for more robust and rapidly established models of cancer and advanced disease.

7.4. Future challenges

Future aims for SN38 thMBs are to move towards Phase I clinical trials. In order to produce thMBs of the quality needed for human standard clinical trials, several steps need to be

taken. Materials that have been produced in accord with good manufacturing practice (GMP) and processed using good laboratory practice (GLP) are necessary standards to accomplish a final human grade product. In particular, aspects such as how the liposome is attached to the MB, the way in which the thMBs are functionalised and sterility of the end product are key to clinical translation.

The Horizon MB platform is patented technology for one-step MB production developed by The University of Leeds and Epigem and may one day be used in clinic for the rapid production of drug (any) loaded MBs. This technology is being further developed to ensure that thMB preparations can be produced in the quantities needed for human scale dosing.

Kotopoulis *et al*., (2013) has for the first time demonstrated the clinical feasibility and safety of MBs co-delivered with gemcitabine in a clinical case study and later a Phase I clinical trial using patients with advanced pancreatic cancer (Kotopoulis *et al.,* 2013; Dimcevski *et al.,* 2016). Gemcitabine was delivered i.v. over 30-minutes as free drug, using the standard recommended treatment protocol for pancreatic cancer 1000 mg/m^2 (once a week for the first 7-weeks, then cycles of once weekly for 3 weeks out of 4), followed by i.v. Sonovue® US contrast MBs (Kotopoulis *et al.,* 2013; Dimcevski *et al.,* 2016). Limitations of these studies were mainly due to the use of clinical US systems where it was not possible to generate the longer duty cycles which had previously been optimised by the group *in vivo* using a custom-made single element US transducer (Kotopoulis *et al.,* 2014). The treatment area was limited to a 2D slice of the tumour, where a 3D US probe would have been able to treat a greater area. Therefore, clinical US systems which allow control over the US parameters for optimal drug delivery are necessary. Patients will present with tumours of different volumes and depths, and conditions need to be personalised for optimal efficacy.

It is clear that MBs in combination with US have the ability to enhance efficacy of chemotherapeutics. The thMBs used in this project demonstrated that very low dose irinotecan and/or SN38 can be used for enhanced drug delivery/retention in tumours resulting in anti-cancer effect with minimal side effects, but this method could be used for other cytotoxic drugs or tumour types. More preclinical trials are necessary to demonstrate feasibility, safety and efficacy using a range or combinations of cytotoxics and other types of solid tumours for quicker translation to clinical use.

References

Abbasi, E., Aval, S.F., Akbarzadeh, A., Milani, M., Nasrabadi, H.T., Joo, S.W., Hanifehpour, Y., Nejati-Koshki, K. and Pashaei-Asl, R. 2014. Dendrimers: Synthesis, applications, and properties. *Nanoscale Research Letters*. **9**(1),pp.1–10.

Abdelrahman, M.A., Marston, G., Hull, M.A., Markham, A.F., Jones, P.F., Evans, J.A. and Coletta, P.L. 2012. High-frequency ultrasound for in vivo measurement of colon wall thickness in mice. *Ultrasound in Medicine & Biology*. **38**(3),pp.432–42.

Abou-Saleh, R.H., Peyman, S.A., Johnson, B.R.G., Marston, G., Ingram, N., Bushby, R.J., Coletta, P.L., Markham, A.F. and Evans, S.D. 2016. Influence of intercalating perfluorohexane into the lipid shell on nano and microbubbles stability. *Soft Matter*. **12**,pp.7223–7230.

Abra, R.M., Hunt, C.A. and Lau, D.T. 1984. Liposome disposition in vivo VI: Delivery to the lung. *Journal of Pharmaceutical Sciences*. **73**(2),pp.203–206.

Aggarwal, C., Cohen, R.B., Yu, E., Hwang, W.T., Bauml, J.M., Alley, E., Evans, T.L. and Langer, C.J. 2018. Etirinotecan pegol (NKTR-102) in third-line treatment of patients with metastatic or recurrent non-small-cell lung cancer: Results of a phase II study. *Clinical Lung Cancer*. **19**(2),pp.157–162.

Aguado, C., García-Paredes, B., Sotelo, M.J., Sastre, J. and Díaz-Rubio, E. 2014. Should capecitabine replace 5-fluorouracil in the first-line treatment of metastatic colorectal cancer? *World Journal of Gastroenterology*. **20**(20),pp.6092–6101.

Ahmad, I. and Zhang, J.-A. 2005. Pharmaceutically active lipid based formulation of SN-38. ,p.Google Patents.

Al-Kasspooles, M.F., Williamson, S.K., Henry, D., Howell, J., Niu, F., Decedue, C.J. and Roby, K.F. 2013. Preclinical antitumor activity of a nanoparticulate SN38. *Investigational New Drugs*. **31**(4),pp.871–880.

Alamolhoda, M. and Mokhtari-Dizaji, M. 2015. Evaluation of fractionated and repeated sonodynamic therapy by using dual frequency for murine model of breast adenocarcinoma. *Journal of Therapeutic Ultrasound*. **3**(1).

Alexis, F., Pridgen, E., Molnar, L.K. and Farokhzad, O.C. 2008. Factors affecting the clearance and biodistribution of polymeric nanoparticles. *Molecular Pharmaceutics*. **5**(4),pp.505–515.

Allen, T.M. and Cullis, P.R. 2013. Liposomal drug delivery systems: From concept to clinical applications. *Advanced Drug Delivery Reviews*. **65**(1),pp.36–48.

Anderson, C.R., Hu, X., Tlaxca, J., Houghtaling, R., Sharma, K., Lawrence, M., Ferrara, K., Rychak, J.J. and Diego, S. 2011. Ultrasound molecular imaging of tumour angiogenesis with an integrin targeted microbubble contrast agent. *Investigative radiology*. **46**(4),pp.215–224.

Anderson, C.R., Rychak, J.J., Backer, M., Backer, J., Ley, K. and Klibanov, A.L. 2010. scVEGF microbubble ultrasound contrast agents: A novel probe for ultrasound molecular imaging of tumor angiogenesis. *Investigative Radiology*. **45**(10),pp.579–585.

Anselmo, A.C. and Mitragotri, S. 2016. Nanoparticles in the clinic. *Bioengineering and Translational Medicine*. **1**(1),pp.10–29.

Aoki, K. and Taketo, M.M. 2007. Adenomatous polyposis coli (APC): A multi-functional tumor suppressor gene. *Journal of Cell Science*. **120**(19),pp.3327–3335.

Arbiser, J.L., Moses, M.A., Fernandez, C.A., Ghiso, N., Cao, Y., Klauber, N., Frank, D., Brownlee, M., Flynn, E., Parangi, S., Byers, H.R. and Folkman, J. 1997. Oncogenic H-ras stimulates tumor angiogenesis by two distinct pathways. *Proceedings of the National Academy of Sciences*. **94**,pp.861–866.

Arnold, M., Sierra, M.S., Laversanne, M., Soerjomataram, I., Jemal, A. and Bray, F. 2017. Global patterns and trends in colorectal cancer incidence and mortality. *Gut*. **66**(4),pp.683–691.

Arvanitis, C.D., Bazan-Peregrino, M., Rifai, B., Seymour, L.W. and Coussios, C.C. 2011. Cavitation-enhanced extravasation for drug delivery. *Ultrasound in Medicine & Biology*. **37**(11),pp.1838–1852.

Atyabi, F., Farkhondehfai, A., Esmaeili, F., Dinarvand, R., Drug, N. and Systems, D. 2009. Preparation of pegylated nano-liposomal formulation containing SN-38: In vitro characterization and in vivo biodistribution in mice. *Acta Pharmaceutica*. **59**(2),pp.133–144.

Ayers, G.D., Mckinley, E.T., Zhao, P., Fritz, J.M., Metry, R.E., Deal, B.C., Adlerz, K.M., Coffey, R.J., Manning, H.C. and Ph, D. 2010. Volume of preclinical xenograft tumors is more accurately assessed by ultrasound imaging than manual caliper measurements. *Journal of Ultrasound in Medicine*. **29**(6),pp.891–901.

Bachawal, S. V., Jensen, K.C., Lutz, A.M., Gambhir, S.S., Tranquart, F., Tian, L. and Willmann,

J.K. 2013. Earlier detection of breast cancer with ultrasound molecular imaging in a transgenic mouse model. *Cancer Research*. **73**(6),pp.1689–1698.

Bae, Y.H. and Park, K. 2011. Targeted drug delivery to tumors: Myths, reality and possibility. *J Control Release*. **153**(3),pp.198–205.

Bahl, A. and Bakhshi, S. 2012. Metronomic chemotherapy in progressive pediatric malignancies: Old drugs in new package. *Indian Journal of Pediatrics*. **79**(12),pp.1617–1622.

Bai, M., Shen, M., Teng, Y., Sun, Y., Li, F., Zhang, X., Xu, Y., Duan, Y. and Du, L. 2015. Enhanced therapeutic effect of Adriamycin on multidrug resistant breast cancer by the ABCG2-siRNA loaded polymeric nanoparticles assisted with Ultrasound. *Oncotarget*. **6**(41).

Bala, V., Rao, S., Boyd, B.J. and Prestidge, C.A. 2013. Prodrug and nanomedicine approaches for the delivery of the camptothecin analogue SN38. *Journal of Controlled Release*. **172**(1),pp.48–61.

Balagula, Y., Garbe, C., Myskowski, P., Hauschild, A., Rapoport, B., Boers-Doets, C. and Lacouture, M. 2011. Clinical presentation and management of dermatological toxicities of epidermal growth factor receptor inhibitors. *International Journal of Dermatology*. **50**(2),pp.129–146.

Balcombe, J.P., Barnard, N.D. and Sandusky, C. 2004. Laboratory routines cause animal stress. *Contemporary Topics in Laboratory Animal Science*. **43**(6),pp.42–51.

Balducci, L. and Extermann, M. 2000. Management of cancer in the older person: A practical approach. *The Oncologist*. **5**,pp.224–237.

Barenholz, Y. 2012. Doxil® - The first FDA-approved nano-drug: Lessons learned. *Journal of Controlled Release*. **160**(2),pp.117–134.

Barken, D., Green, J. and Chambers, A. 2010. Extracellular matrix: A gatekeper in the transition from dormancy to metastatic growth. *European Journal of Cancer*. **46**(7),pp.1181–1188.

Barnett, S., Ter Haar, G., Ziskin, M., Rott, H., Duck, F. and Maeda, K. 2000. International recommendations and guidelines for the safe use of diagnostic ultrasound in medicine. *Ultrasound Med Biol.* **26**(3),pp.355–366.

Barua, A., Yellapa, A., Bahr, J.M., Machado, S.A., Bitterman, P., Basu, S., Sharma, S. and

Abramowicz, J.S. 2014. Enhancement of ovarian tumor detection with αvβ3 integrin–targeted ultrasound molecular imaging agent in laying lens. *International Journal of Gynecological Cancer*. **24**(1),pp.19–28.

Battaglin, F., Puccini, A., Intini, R., Schirripa, M., Ferro, A., Bergamo, F., Lonardi, S., Zagonel, V., Lenz, H.-J. and Loupakis, F. 2018. The role of tumor angiogenesis as a therapeutic target in colorectal cancer. *Expert Review of Anticancer Therapy*. **18**(3),pp.251–266.

Bayón, L.G., Izquierdo, M.A., Sirovich, I., Van Rooijen, N., Beelen, R.H.J. and Meijer, S. 1996. Role of Kupffer cells in arresting circulating tumor cells and controlling metastatic growth in the liver. *Hepatology*. **23**(5),pp.1224–1231.

Beijers, A.J.M., Mols, F., Van Den Hurk, C.J. and Vreugdenhil, A. 2016. Are chemotherapy-associated symptoms underestimated? A view beyond common toxicity criteria. *Acta Oncologica*. **55**(4),pp.516–518.

Berger, A. 2002. Magnetic resonance imaging. *British Medical Journal*. **324**,p.35.

Bertrand, N., Wu, J., Xu, X., Kamaly, N. and Farokhzad, O.C. 2014. Cancer nanotechnology: The impact of passive and active targeting in the era of modern cancer biology. *Advanced Drug Delivery Reviews*. **66**,pp.2–25.

Bissery, M.C., Vrignaud, P., Lavelle, F. and Chabot, G.G. 1996. Experimental antitumor activity and pharmacokinetics of the camptothecin analog irinotecan (CPT-11) in mice. *Anti-cancer drugs*. **7**(4),pp.437–60.

Blanco, E., Shen, H. and Ferrari, M. 2015. Principles of nanoparticle design for overcoming biological barriers to drug delivery. *Nature Biotechnology*. **33**(9),pp.941–951.

Bouakaz, A., de Jong, N., Cachard, C. and Jouini, K. 1998. On the effect of lung filtering and cardiac pressure on the standard properties of ultrasound contrast agent. *Ultrasonics*. **36**(1–5),pp.703–8.

Boyle, P. and Langman, J.S. 2000. ABC of colorectal cancer: Epidemiology. *BMJ: British Medical Journal*. **321**,pp.805–808.

Bozzuto, G. and Molinari, A. 2015. Liposomes as nanomedical devices. *International Journal of Nanomedicine*. **10**,pp.975–999.

Brattain, M.G., Fine, W.D., Khaled, F.M., Thompson, J. and Brattain, D.E. 1981. Heterogeneity of malignant cells from a human colonic carcinoma. *Cancer research*. **41**(5),pp.1751–6.

Bruns, C.J., Liu, W., Davis, D.W., Shaheen, R.M., McConkey, D.J., Wilson, M.R., Bucana, C.D., Hicklin, D.J. and Ellis, L.M. 2000. Vascular endothelial growth factor is an in vivo survival factor for tumor endothelium in a murine model of colorectal carcinoma liver metastases. *American Cancer Society*. **89**(3),pp.488–499.

Bujanda, L., Sarasqueta, C., Hijona, E., Hijona, L., Cosme, A., Gil, I., Elorza, J.L., Asensio, J.I., Larburu, S., Enríquez-Navascués, J.M., Jover, R., Balaguer, F., Llor, X., Bessa, X., Andreu, M., Paya, A., Castells, A. and +97 2010. Colorectal cancer prognosis twenty years later. *World Journal of Gastroenterology*. **16**(7),pp.862–867.

Burgess, D.J., Doles, J., Zender, L., Xue, W., Ma, B., McCombie, W.R., Hannon, G.J., Lowe, S.W. and Hemann, M.T. 2008. Topoisomerase levels determine chemotherapy response in vitro and in vivo. *Proceedings of the National Academy of Sciences of the United States of America*. **105**(26),pp.9053–9058.

Burke, C.W., Hsiang, Y.H.J., Alexander IV, E., Kilbanov, A.L. and Price, R.J. 2011. Covalently linking poly(lactic-co-glycolic acid) nanoparticles to microbubbles before intravenous injection improves their ultrasound-targeted delivery to skeletal muscle. *Small*. **7**(9),pp.1227–1235.

Burris, H.A., Infante, J.R., Anthony Greco, F., Thompson, D.S., Barton, J.H., Bendell, J.C., Nambu, Y., Watanabe, N. and Jones, S.F. 2016. A phase I dose escalation study of NK012, an SN-38 incorporating macromolecular polymeric micelle. *Cancer Chemotherapy and Pharmacology*. **77**(5),pp.1079–1086.

Burris, H.A., Infante, J.R., Spigel, D.R., Greco, F.A., Thompson, D.S., Matsumoto, S., Kawamura, S. and Jones, S.F. 2008. A phase I dose-escalation study of NK012. *Journal of Clinical Oncology*. **26**(15),pp.2538–2538.

Butler, B.D. and Hills, B.A. 1979. The lung as a filter for microbubbles. *Journal for Applied Physiology*. **48**(3),p.537.

Byfield, J.E. 1989. 5-fluorouracil radiation sensitization - A brief review. *Investigational New Drugs*. **7**,pp.111–116.

Bzyl, J., Lederle, W., Rix, A., Grouls, C., Tardy, I., Pochon, S., Siepmann, M., Penzkofer, T., Schneider, M., Kiessling, F. and Palmowski, M. 2011. Molecular and functional ultrasound imaging in differently aggressive breast cancer xenografts using two novel ultrasound contrast agents (BR55 and BR38). *European Radiology*. **21**(9),pp.1988–1995.

Çağdaş, M., Sezer, A.D. and Bucak, S. 2014. *Liposomes as potential drug carrier systems for drug delivery.* (A. D. Sezer, ed.). InTech.

Carpentier, A., Canney, M., Vignot, A., Reina, V., Beccaria, K., Horodyckid, C., Karachi, C., Leclercq, D., Lafon, C., Chapelon, J.-Y., Capelle, L., Cornu, P., Sanson, M., Hoang-Xuan, K., Delattre, J.-Y. and Idbaih, A. 2016. Clinical trial of blood-brain barrier disruption by pulsed ultrasound. *Science Translational Medicine*. **8**(343),p.343re2–343re2.

Carrato, A. 2008. Adjuvant treatment of colorectal cancer. *Gastrointestinal Cancer Research*. **2**(4),pp.S42–S46.

Cavalieri, F., Zhou, M. and Ashokkumar, M. 2010. The design of multifunctional microbubbles for ultrasound image-guided cancer therapy. *Current topics in medicinal chemistry*. **10**(12),pp.1198–210.

Cavalli, R., Soster, M. and Argenziano, M. 2016. Nanobubbles: a promicing efficient tool for therapeutic delivery. *Therapeutic Delivery*. **6**,pp.1239–1241.

Céspedes, M.V., Espina, C., García-Cabezas, M.A., Trias, M., Boluda, A., Gómez del Pulgar, M.T., Sancho, F.J., Nistal, M., Lacal, J.C. and Mangues, R. 2007. Orthotopic microinjection of human colon cancer cells in nude mice induces tumor foci in all clinically relevant metastatic sites. *The American Journal of Pathology*. **170**(3),pp.1077–85.

Chabot, G.G. 1997. Clinical pharmacokinetics of irinotecan. *Clinical Pharmacokinetics*. **33**(4),pp.245–259.

Chambers, A., Groom, A. and MacDonald, I. 2002. Dissemination and growth of cancer cells in metastatic sites. *Nature Reviews Cancer*. **2**,pp.563–572.

Chambers, A.F., MacDonald, I.C., Schmidt, E.E., Koop, S., Morris, V.L., Khokha, R. and Groom, A.C. 1995. Steps in tumor metastasis: New concepts from intravital videomicroscopy. *Cancer and Metastasis Reviews*. **14**,pp.279–301.

Chang, S., Guo, J., Sun, J., Zhu, S., Yan, Y., Zhu, Y., Li, M., Wang, Z. and Xu, R.X. 2013. Targeted microbubbles for ultrasound mediated gene transfection and apoptosis induction in ovarian cancer cells. *Ultrasonics Sonochemistry*. **20**,pp.171–179.

Charrois, G.J.R. and Allen, T.M. 2004. Drug release rate influences the pharmacokinetics, biodistribution, therapeutic activity, and toxicity of pegylated liposomal doxorubicin formulations in murine breast cancer. *Biochimica et Biophysica Acta - Biomembranes*. **1663**(1–2),pp.167–177.

Chen, H. and Hwang, J. 2013. Ultrasound-targeted microbubble destruction for chemotherapeutic drug delivery to solid tumors. *Journal of Therapeutic Ultrasound*. **1**(10).

Chen, S., Yueh, M.-F., Bigo, C., Barbier, O., Wang, K., Karin, M., Nguyen, N. and Tukey, R.H. 2013. Intestinal glucuronidation protects against chemotherapy-induced toxicity by irinotecan (CPT-11). *Proceedings of the National Academy of Sciences*. **110**(47),pp.19143–19148.

Chen, X., Peer, C.J., Alfaro, R., Tian, T., Spencer, S.D. and Figg, W.D. 2012. Quantification of irinotecan, SN38, and SN38G in human and porcine plasma by ultra high-performance liquid chromatography-tandem mass spectrometry and its application to hepatic chemoembolization. *Journal of pharmaceutical and biomedical analysis*. **62**,pp.140–8.

Cheng, Y., Zhao, L., Li, Y. and Xu, T. 2011. Design of biocompatible dendrimers for cancer diagnosis and therapy: Current status and future perspectives. *Chemical Society Reviews*. **40**(5),pp.2673–2703.

Chertok, B. and Langer, R. 2018. Circulating magnetic microbubbles for localized real-time control of drug delivery by ultrasonography-guided magnetic targeting and ultrasound. *Theranostics*. **8**(2),pp.341–357.

Chinol, M., Casalini, P., Maggiolo, M., Canevari, S., Omodeo, E.S., Caliceti, P., Veronese, F.M., Cremonesi, M., Chiolerio, F., Nardone, E., Siccardi, A.G. and Paganelli, G. 1998. Biochemical modifications of avidin improve pharmacokinetics and biodistribution, and reduce immunogenicity. *British Journal of Cancer*. **78**(2),pp.189–197.

Choijamts, B., Naganuma, Y., Nakajima, K., Kawarabayashi, T., Miyamoto, S., Tachibana, K. and Emoto, M. 2011. Metronomic irinotecan chemotherapy combined with ultrasound irradiation for a human uterine sarcoma xenograft. *Cancer Science*. **102**(2),pp.452–459.

Chowdhury, F.U., Shah, N., Scarsbrook, A.F. and Bradley, K.M. 2010. [18F]FDG PET/CT imaging of colorectal cancer: A pictorial review. *Postgraduate Medical Journal*. **86**(1013),pp.174–182.

Chowdhury, S.M., Wang, T.Y., Bachawal, S., Devulapally, R., Choe, J.W., Abou Elkacem, L., Yakub, B.K., Wang, D.S., Tian, L., Paulmurugan, R. and Willmann, J.K. 2016. Ultrasound-guided therapeutic modulation of hepatocellular carcinoma using complementary microRNAs. *Journal of Controlled Release*. **238**,pp.272–280.

Christman, C.L., Carmichael, A.J., Mossoba, M.M. and Riesz, P. 1987. Evidence for free radicals produced in aqueous solutions by diagnostic ultrasound. *Ultrasonics*. **25**(1),pp.31–34.

Church, C.C. 2005. Frequency, pulse length, and the mechanical index. *Acoustics Research Letters Online*. **6**(3),p.162.

Churchman, A.H., Mico, V., de Pablo, J.G., Peyman, S.A., Freear, S. and Evans, S.D. 2018. Combined flow-focus and self-assembly routes for the formation of lipid stabilized oil-shelled microbubbles. *Microsystems & Nanoengineering*. **4**(17087).

Clark, C.R. and Starr, T.K. 2016. Mouse models for the discovery of colorectal cancer driver genes. *World Journal of Gastroenterology*. **22**(2),pp.815–822.

Cochran, M.C., Eisenbrey, J., Ouma, R.O., Soulen, M. and Wheatley, M.A. 2011. Doxorubicin and paclitaxel loaded microbubbles for ultrasound triggered drug delivery. *International Journal of Pharmaceutics*. **414**(1–2),pp.161–170.

De Cock, I., Lajoinie, G., Versluis, M., De Smedt, S.C. and Lentacker, I. 2016. Sonoprinting and the importance of microbubble loading for the ultrasound mediated cellular delivery of nanoparticles. *Biomaterials*. **83**,pp.294–307.

De Cock, I., Zagato, E., Braeckmans, K., Luan, Y., de Jong, N., De Smedt, S.C. and Lentacker, I. 2015. Ultrasound and microbubble mediated drug delivery: Acoustic pressure as determinant for uptake via membrane pores or endocytosis. *Journal of Controlled Release*. **197**,pp.20–28.

Colnot, S., Niwa-Kawakita, M., Hamard, G., Godard, C., Le Plenier, S., Houbron, C., Romagnolo, B., Berrebi, D., Giovannini, M. and Perret, C. 2004. Colorectal cancers in a new mouse model of familial adenomatous polyposis: Influence of genetic and environmental modifiers. *Laboratory Investigation*. **84**(12),pp.1619–1630.

Colombo, M., Fiandra, L., Alessio, G., Mazzucchelli, S., Nebuloni, M., Palma, C. De, Kantner, K., Pelaz, B., Rotem, R., Corsi, F., Parak, W.J. and Prosperi, D. 2016. Tumour homing and therapeutic effect of colloidal nanoparticles depend on the number of attached antibodies. *Nature Communications*. **7**(23818).

Colorectal Cancer Collaborative Group 2001. Adjuvant radiotherapy for rectal cancer: A systematic overview of 8,507 patients from 22 randomised trials. *The Lancet*. **358**,pp.1291–1304.

Cool, S.K., Breyne, K., Meyer, E., De Smedt, S.C. and Sanders, N.N. 2013. Comparison of in

vivo optical systems for bioluminescence and fluorescence imaging. *Journal of Fluorescence*. **23**(5),pp.909–920.

Cool, S.K., Geers, B., Roels, S., Stremersch, S., Vanderperren, K., Saunders, J.H., De Smedt, S.C., Demeester, J. and Sanders, N.N. 2013. Coupling of drug containing liposomes to microbubbles improves ultrasound triggered drug delivery in mice. *Journal of Controlled Release*. **172**(3),pp.885–893.

Corbett, T.H., Griswold, D.P., Roberts, B.J., Peckham, J.C. and Schabel, F.M. 1975. Tumor induction relationships in development of transplantable cancers of the colon in mice for chemotherapy assays, with a note on carcinogen structure. *Cancer Research*. **35**(9),pp.2434–2439.

Correas, J.M., Meuter, A.R., Singlas, E., Kessler, D.R., Worah, D. and Quay, S.C. 2001. Human pharmacokinetics of a perfluorocarbon ultrasound contrast agent evaluated with gas chromatography. *Ultrasound in Medicine and Biology*. **27**(4),pp.565–570.

Cosgrove, D. 1996. Why do we need contrast agents for ultrasound? *Clinical Radiology*. **51**(1),pp.1–4.

Costley, D., Mc Ewan, C., Fowley, C., McHale, A.P., Atchison, J., Nomikou, N. and Callan, J.F. 2015. Treating cancer with sonodynamic therapy: A review. *International Journal of Hyperthermia*. **31**(2),pp.107–117.

Crommelin, D.J. a and Florence, A.T. 2013. Towards more effective advanced drug delivery systems. *International Journal of Pharmaceutics*. **454**(1),pp.496–511.

Cummings, J., Ethell, B.T., Jardine, L., Boyd, G., Macpherson, J.S., Burchell, B., Smyth, J.F. and Jodrell, D.I. 2003. Glucuronidation as a mechanism of intrinsic drug resistance in human colon cancer: reversal of resistance by food additives. *Cancer Research*. **63**,pp.8443–8450.

Danks, M.K., Morton, C.L., Krull, E.J., Cheshire, P.J., Richmond, L.B., Naeve, C.W., Pawlik, C. a, Houghton, P.J. and Potter, P.M. 1999. Comparison of activation of CPT-11 by rabbit and human carboxylesterases for use in enzyme / prodrug therapy. *Clinical Cancer Research*. **5**,pp.917–924.

Deng, Z., Yan, F., Jin, Q., Li, F., Wu, J., Liu, X. and Zheng, H. 2014. Reversal of multidrug resistance phenotype in human breast cancer cells using doxorubicin-liposome-microbubble complexes assisted by ultrasound. *Journal of Controlled Release*. **174**(1),pp.109–116.

Denlinger, C. and Barsevick, A. 2009. The callenges of colorectal cancer survivorship. *Journal of the National Comprehensive Cancer Network*. **7**(8),pp.883–894.

Deshpande, N., Ren, Y., Foygel, K., Rosenberg, J. and Willmann, J.K. 2011. Tumor angiogenic marker expression levels during tumor growth: longitudinal assessment with molecularly targeted microbubles and US imaging. *Radiology*. **258**(3),pp.804–811.

Diasio, R.B. and Harris, B.E. 1989. Clinical pharmacology of 5-Fluorouracil. *Clinical Pharmacokinetics*. **16**(4),pp.215–237.

Dienstmann, R., Vermeulen, L., Guinney, J., Kopetz, S., Tejpar, S. and Tabernero, J. 2017. Consensus molecular subtypes and the evolution of precision medicine in colorectal cancer. *Nature Reviews Cancer*. **17**(2),pp.79–92.

Dimcevski, G., Kotopoulis, S., Bjanes, T., Hoem, D., Schjott, J., Gjertsen, B.T., Biermann, M., Molven, A., Sorbye, H., McCormack, E., Postema, M. and Gilja, O.H. 2016. A human clinical trial using ultrasound and microbubbles to enhance gemcitabine treatment of inoperable pancreatic cancer. *Journal of Controlled Release*. **243**,pp.172–181.

Dinarvand, M., Kiani, M., Mirzazadeh, F., Esmaeili, A., Mirzaie, Z., Soleimani, M., Dinarvand, R. and Atyabi, F. 2015. Oral delivery of nanoparticles containing anticancer SN38 and hSET1 antisense for dual therapy of colon cancer. *International Journal of Biological Macromolecules*. **78**,pp.112–121.

Donigan, M., Norcross, L.S., Aversa, J., Colon, J., Smith, J., Madero-Visbal, R., Li, S., McCollum, N., Ferrara, A., Gallagher, J.T. and Baker, C.H. 2009. Novel murine model for colon cancer: Non-operative trans-anal rectal injection. *Journal of Surgical Research*. **154**(2),pp.299–303.

Edelmann, W., Yang, K., Kuraguchi, M., Heyer, J., Lia, M., Kneitz, B., Fan, K., Brown, A.M.C., Lipkin, M. and Kucherlapati, R. 1999. Tumorigenesis in Mlh1 and Mlh1 / Apc1638N Mutant Mice. *Cancer Research*. **59**,pp.1301–1307.

Eggen, S., Fagerland, S.M., Mørch, Ý., Hansen, R., Søvik, K., Berg, S., Furu, H., Bøhn, A.D., Lilledahl, M.B., Angelsen, A., Angelsen, B. and De Lange Davies, C. 2014. Ultrasound-enhanced drug delivery in prostate cancer xenografts by nanoparticles stabilizing microbubbles. *Journal of Controlled Release*. **187**,pp.39–49.

Ellegala, D.B., Leong-Poi, H., Carpenter, J.E., Klibanov, A.L., Kaul, S., Shaffrey, M.E., Sklenar, J. and Lindner, J.R. 2003. Imaging tumor angiogenesis with contrast ultrasound and

microbubbles targeted to αvβ3. *Circulation*. **108**(3),pp.336–341.

Ellis, L.M., Y, T., W, L. and Shaheen, R. 2000. Vascular endothelial growth factor in human colon cancer: biology and therapeutic implications. *The Oncologist*. **5**,pp.11–15.

Escoffre, Novell, A., Serrière, S., Lecomte, T. and Bouakaz, A. 2013a. Irinotecan delivery by microbubble-assisted ultrasound: In vitro validation and a pilot preclinical study. *Molecular Pharmaceutics*. **10**(7),pp.2667–75.

Escoffre, Novell, A., Serrière, S., Lecomte, T. and Bouakaz, A. 2013b. Irinotecan delivery by microbubble-assisted ultrasound - A pilot preclinical study. *Molecular Pharmaceutics*. **10**(7),pp.2667–2675.

Eshghifar, N., Farrokhi, N., Naji, T. and Mohammadreza Zali 2017. Tumor suppressor genes in familial adenomatous polyposis. *Gastroenterology and Hepatology From Bed to Bench*. **10**(1),pp.3–13.

Ewing, J. 1928. *Neoplastic Diseases* 3rd ed.

Fan, C.H., Ting, C.Y., Liu, H.L., Huang, C.Y., Hsieh, H.Y., Yen, T.C., Wei, K.C. and Yeh, C.K. 2013. Antiangiogenic-targeting drug-loaded microbubbles combined with focused ultrasound for glioma treatment. *Biomaterials*. **34**(8),pp.2142–2155.

Fan, X., Wang, L., Guo, Y., Xiong, X., Zhu, L. and Fang, K. 2016. Inhibition of prostate cancer growth using doxorubicin assisted by ultrasound-targeted nanobubble destruction. *International Journal of Nanomedicine*. **11**,pp.3585–3596.

Fan, Z., Kumon, R.E. and Deng, C.X. 2014. Mechanisms of microbubble-facilitated sonoporation for drug and gene delivery. *Therapeutic Delivery*. **5**(4),pp.467–486.

Fan, Z., Liu, H., Mayer, M. and Deng, C. 2012. Spatiotemporally controlled single cell sonoporation. *Proc. Natl. Acad. Sci. U.S.A.* **109**,pp.16486–16491.

Fang, T., Dong, Y., Zhang, X., Xie, K., Lin, L. and Wang, H. 2016. Integrating a novel SN38 prodrug into the PEGylated liposomal system as a robust platform for efficient cancer therapy in solid tumors. *International Journal of Pharmaceutics*. **512**(1),pp.39–48.

Fang, Y.-P., Chuang, C.-H., Wu, Y.-J., Lin, H.-C. and Lu, Y.-C. 2018. SN38-loaded <100 nm targeted liposomes for improving poor solubility and minimizing burst release and toxicity: in vitro and in vivo study. *International Journal of Nanomedicine*. **Volume 13**,pp.2789–2802.

FDA 2001. *Guidance for Industry: Bioanalytical Method Validation*.

Fearon, E. and Vogelstein, B. 1990. A genetic model for colorectal tumorigenesis. *Cell*. **61**,pp.759–767.

Ferraioli, G. and Meloni, M.F. 2018. Contrast-enhanced ultrasonography of the liver using SonoVue. *Ultrasonography*. **37**,pp.25–35.

Ferrara, K.W. 2008. Driving delivery vehicles with ultrasound. *Advanced Drug Delivery Reviews*. **60**(10),pp.1097–1102.

Fidler, I.J. 1970. Metastasis: Quantitative analysis of distribution and fate of tumour emboli labeled with 125I-5-iodo-2'-deoxyuridine. *The Journal of the National Cancer Institute*. **45**,pp.773–782.

Fidler, I.J. 2003. The pathogenesis of cancer metastasis: The 'seed and soil' hypothesis revisited. *Nature Reviews Cancer*. **3**(6),pp.453–458.

Filipe, V., Hawe, A. and Jiskoot, W. 2010. Critical evaluation of nanoparticle tracking analysis (NTA) by NanoSight for the measurement of nanoparticles and protein aggregates. *Pharmaceutical Research*. **27**(5),pp.796–810.

Fischer, T., Thomas, A., Tardy, I., Schneider, M., Hünigen, H., Custodis, P., Beyersdorff, D., Plendl, J., Schnorr, J., Diekmann, F. and Gemeinhardt, O. 2010. Vascular endothelial growth factor receptor 2-specific microbubbles for molecular ultrasound detection of prostate cancer in a rat model. *Investigative Radiology*. **45**(10),pp.675–684.

Flatmark, K., Mælandsmo, G.M., Martinsen, M., Rasmussen, H. and Fodstad, Ø. 2004. Twelve colorectal cancer cell lines exhibit highly variable growth and metastatic capacities in an orthotopic model in nude mice. *European Journal of Cancer*. **40**(10),pp.1593–1598.

Fleeman, N., Abdulla, A., Bagust, A., Beale, S., Richardson, M., Stainthorpe, A., Boland, A., Kotas, E., McEntee, J. and Palmer, D. 2017. Pegylated liposomal irinotecan hydrochloride trihydrate for treating pancreatic cancer after gemcitabine: An evidence review group perspective of a NICE single technology appraisal. *PharmacoEconomics*. **36**(3),pp.289–299.

Flynn, H.G. and Church, C.C. 1988. Transient pulsations of small gas bubbles in water. *The Journal of the Acoustical Society of America*. **84**(3),pp.1863–1876.

Fodde, R., Edelmann, W., Yang, K., van Leeuwen, C., Carlson, C., Renault, B., Breukel, C., Alt, E., Lipkin, M., Khan, P.M. and Kucherlapati, R. 1994. A targeted chain-termination mutation in the mouse Apc gene results in multiple intestinal tumors. *Proceedings of*

the National Academy of Sciences of the United States of America. **91**(19),pp.8969–73.

Folkman, J. 2006. Angiogenesis. *Annual Review of Medicine*. **57**,pp.1–18.

Folkman, J. 1971. Tumour angiogenesis: Therapeutic implications. *The New England Journal of Medicine*. **285**(21),pp.1182–6.

Foltz, C.J. and Ullman-Cullere, M. 1999. Guidelines for assessing the health and condition of mice. *Lab Animal*. **28**(4),pp.28–32.

Foygel, K., Wang, H., MacHtaler, S., Lutz, A.M., Chen, R., Pysz, M., Lowe, A.W., Tian, L., Carrigan, T., Brentnall, T.A. and Willmann, J.K. 2013. Detection of pancreatic ductal adenocarcinoma in mice by ultrasound imaging of thymocyte differentiation antigen 1. *Gastroenterology*. **145**(4),pp.885–894.

Freear, S., Cowell, D.M.J. and Smith, P.R. 2014. Ultrasound generation. ,p.WO 2014096789 A2.

Frinking, P.J.A., Tardy, I., Theraulaz, M., Arditi, M., Powers, J., Pochon, S. and Tranquart, F. 2012. Effects of acoustic radiation force on the binding efficiency of BR55, a VEGFR2-specific ultrasound contrast agent. *Ultrasound in Medicine and Biology*. **38**(8),pp.1460–1469.

Gabizon, A. and Papahadjopoulos, D. 1988. Liposome formulations with prolonged circulation time in blood and enhanced uptake by tumors. *Proceedings of the National Academy of Sciences of the United States of America*. **85**,pp.6949–6953.

Gagné, J., Montminy, V., Belanger, P., Journault, K., Gaucher, G. and Guillemette, C. 2002. Common human UGT1A polymorphisms and the altered metabolism of irinotecan active metabolite 7-ethyl-10-hydroxycamptothecin (SN-38). *Molecular pharmacology*. **62**(3),pp.608–17.

Gao, X., Zhang, M., Tang, Y. and Liang, X. 2017. Cancer cell dormancy: Mechanisms and implications of cancer recurrence and metastasis. *OncoTargets and Therapy*. **10**,pp.5219–5228.

Garrett, C.R., Bekaii-saab, T.S., Ryan, T., Fisher, G.A., Clive, S., Kavan, P., Shacham-Shmueli, E., Buchbinder, A. and Goldberg, R.M. 2013. Randomized phase 2 study of pegylated SN-38 (EZN-2208) or irinotecan plus cetuximab in patients with advanced colorectal cancer. *Cancer*. **119**(24),pp.4223–4230.

Geers, B., De Wever, O., Demeester, J., Bracke, M., De Smedt, S.C. and Lentacker, I. 2013. Targeted liposome-loaded microbubbles for cell-specific ultrasound-triggered drug delivery. *Small*. **9**(23),pp.4027–4035.

van der Geest, L.G.M., Lam-Boer, J., Koopman, M., Verhoef, C., Elferink, M.A.G. and de Wilt, J.H.W. 2015. Nationwide trends in incidence, treatment and survival of colorectal cancer patients with synchronous metastases. *Clinical & Experimental Metastasis*. **32**,pp.457–465.

Gill, B.P.S., Espina, B.M., Muggia, F., Cabriales, S., Tulpule, A., Esplin, J.A., Liebman, H.A., Forssen, E., Ross, M.E. and Levine, A.M. 1995. Phase I / II clinical and pharmacokinetic evaluation of liposomal daunorubicin. *Journal of Clinical Oncology*. **13**(4),pp.996–1003.

Gock, M., Kühn, F., Mullins, C.S., Krohn, M., Prall, F., Klar, E. and Linnebacher, M. 2016. Tumor take rate optimization for colorectal carcinoma patient-derived xenograft models. *BioMed Research International*. **2016**.

Goldwasser, F., Bae, I., Valenti, M., Goldwasser, F., Torres, K. and Pommier, Y. 1995. Topoisomerase I-related parameters and camptothecin activity in the colon carcinoma cell lines from the national cancer Institute anticancer screen. *Cancer research*. **55**,pp.2116–2121.

Goldwirt, L., Lemaitre, F., Zahr, N., Farinotti, R. and Fernandez, C. 2012. A new UPLC-MS/MS method for the determination of irinotecan and 7-ethyl-10-hydroxycamptothecin (SN-38) in mice: Application to plasma and brain pharmacokinetics. *Journal of Pharmaceutical and Biomedical Analysis*. **66**,pp.325–333.

Gowda, S., Desai, P.B., Hull, V. V, Math, A. a K., Vernekar, S.N. and Kulkarni, S.S. 2009. A review on laboratory liver function tests. *The Pan African Medical Journal*. **3**.

Graham, S.M., Carlisle, R., Choi, J.J., Stevenson, M., Shah, A.R., Myers, R.S., Fisher, K., Peregrino, M.-B., Seymour, L. and Coussios, C.C. 2014. Inertial cavitation to non-invasively trigger and monitor intratumoral release of drug from intravenously delivered liposomes. *Journal of Controlled Release*. **178**,pp.101–7.

Gramiak, R. and Shah, P.M. 1968. Echocardiography of the aortic root. *Investigative Radiology*. **3**,pp.356–366.

Greish, K. 2012. Enhanced permeability and retention effect for selective targeting of

anticancer nanomedicine : are we there yet ? *Drug Discovery Today: Technologies*. **9**(2),pp.e161–e166.

Guichard, S., Terret, C., Hennebelle, I., Lochon, I., Chevreau, P., Frétigny, E., Selves, J., Chatelut, E., Bugat, R. and Canal, P. 1999. CPT-11 converting carboxylesterase and topoisomerase activities in tumour and normal colon and liver tissues. *British Journal of Cancer*. **80**(3/4),pp.364–370.

Guinney, J., Dienstmann, R., Wang, X., Reyniès, A. De, Schlicker, A., Soneson, C., Marisa, L., Roepman, P., Nyamundanda, G., Angelino, P., Bot, B.M., Morris, J.S., Simon, I.M., Gerster, S., Fessler, E., Melo, F.D.S.E., Missiaglia, E., Ramay, H., Barras, D., Homicsko, K., Maru, D., Manyam, G.C., Broom, B., Boige, V., Perez-villamil, B., Laderas, T., Salazar, R., Gray, J.W., Hanahan, D., Tabernero, J., Bernards, R., Friend, S.H. and Laurent-puig, P. 2015. The consensus molecular subtypes of colorectal cancer. *Nature Medicine*. **21**(11),pp.1350–1356.

Gupta, E., Safa, A.R., Wang, X. and Ratain, M.J. 1996. Pharmacokinetic modulation of irinotecan and metabolites by cyclosporin A. *Cancer Research*. **56**(6),pp.1309–1314.

Gupta, E., Wang, X., Ramirez, J. and Ratain, M.J. 1997. Modulation of glucuronidation of SN-38, the active metabolite of irinotecan, by valproic acid and phenobarbital. *Cancer Chemotherapy and Pharmacology*. **39**(5),pp.440–444.

Guzman, H.R., Nguyen, D.X., Khan, S. and Prausnitz, M.R. 2001. Ultrasound-mediated disruption of cell membranes. I. Quantification of molecular uptake and cell viability. *The Journal of the Acoustical Society of America*. **110**(1),pp.588–596.

Hackl, C., Man, S., Francia, G., Milsom, C., Xu, P. and Kerbel, R.S. 2013. Metronomic oral topotecan prolongs survival and reduces liver metastasis in improved preclinical orthotopic and adjuvant therapy colon cancer models. *Gut*. **62**(2),pp.259–271.

Haggar, F.A. and Boushey, R.P. 2009. Colorectal cancer epidemiology: Incidence, mortality, survival, and risk factors. *Clinics in Colon and Rectal Surgery*. **22**(4),pp.191–197.

Ham, A.S.W., Klibanov, A.L. and Lawrence, M.B. 2011. Action at a distance: Lengthening adhesion bonds with poly(ethylene glycol) spacers enhances mechanically stressed affinity for improved vascular targeting of microparticles. *Langmuir*. **25**(17),pp.10038–10044.

Hamaguchi, T., Doi, T., Eguchi-Nakajima, T., Kato, K., Yamada, Y., Shimada, Y., Fuse, N., Ohtsu, A., Matsumoto, S.I., Takanashi, M. and Matsumura, Y. 2010. Phase I study of

NK012, a novel SN-38-incorporating micellar nanoparticle, in adult patients with solid tumors. *Clinical Cancer Research*. **16**(20),pp.5058–5066.

Hambley, T.W. 2009. Is anticancer drug development heading in the right direction? *Cancer Research*. **69**(4),pp.1259–1263.

Hammond, W.A., Swaika, A. and Mody, K. 2016. Pharmacologic resistance in colorectal cancer: A review. *Therapeutic Advances in Medical Oncology*. **8**(1),pp.57–84.

Han, H., Lee, H., Kim, K. and Kim, H. 2017. Effect of high intensity focused ultrasound (HIFU) in conjunction with a nanomedicines-microbubble complex for enhanced drug delivery. *Journal of Controlled Release*. **266**,pp.75–86.

Hanahan, D. and Weinberg, R.A. 2000. The Hallmarks of Cancer. *Cell*. **100**,pp.57–70.

Hatakeyama, H., Akita, H., Kogure, K., Oishi, M., Nagasaki, Y., Kihira, Y., Ueno, M. and Kobayashi, H. 2007. Development of a novel systemic gene delivery system for cancer therapy with a tumor-specific cleavable PEG-lipid. *Gene Therapy*. **14**,pp.68–77.

Hawcroft, G., Volpato, M., Marston, G., Ingram, N., Perry, S.L., Cockbain, A.J., Race, A.D., Munarini, A., Belluzzi, A., Loadman, P.M., Coletta, P.L. and Hull, M.A. 2012. The omega-3 polyunsaturated fatty acid eicosapentaenoic acid inhibits mouse MC-26 colorectal cancer cell liver metastasis via inhibition of PGE 2-dependent cell motility. *British Journal of Pharmacology*. **166**(5),pp.1724–1737.

Heijstek, M.W., Kranenburg, O., Borel Rinkes, I.H.M., Kranenburg, M.W.H.O., Rinkes, I.H.M.B., Heijstek, M.W., Kranenburg, O. and Borel Rinkes, I.H.M. 2005. Mouse Models of Colorectal Cancer and Liver Metastases. *Digestive surgery*. **22**(1–2),pp.16–25.

Heldin, C.H., Rubin, K., Pietras, K. and Östman, A. 2004. High interstitial fluid pressure - An obstacle in cancer therapy. *Nature Reviews Cancer*. **4**(10),pp.806–813.

Hernot, S. and Klibanov, A.L. 2008. Microbubbles in ultrasound-triggered drug and gene delivery. *Advanced Drug Delivery Reviews*. **60**(10),pp.1153–1166.

Hewitt, R.E., McMarlin, A., Kleiner, D., Wersto, R., Martin, P., Tsokos, M., Stamp, G.W., Stetler-Stevenson, W.G. and Tsoskas, M. 2000. Validation of a model of colon cancer progression. *The Journal of Pathology*. **192**(4),pp.446–54.

Hirose, K., Kozu, C., Yamashita, K., Maruo, E. and Kitamura, M. 2012. Correlation between plasma concentration ratios of SN-38 glucuronide and SN-38 and neutropenia

induction in patients with colorectal cancer and wild-type UGT1A1 gene. *Oncology Letters*. **3**,pp.694–698.

Hofheinz, R.D., Heinemann, V., Von Weikersthal, L.F., Laubender, R.P., Gencer, D., Burkholder, I., Hochhaus, A. and Stintzing, S. 2012. Capecitabine-Associated handfootskin reaction is an independent clinical predictor of improved survival in patients with colorectal cancer. *British Journal of Cancer*. **107**(10),pp.1678–1683.

Honary, S. and Zahir, F. 2013. Effect of zeta potential on the properties of nano-drug delivery systems - A review (Part 1). *Tropical Journal of Pharmaceutical Research*. **12**(2),pp.255–264.

Hrvoje, L. and Greenstaff, M.W. 2014. X-ray computed tomography contrast agents. *Chemical Reviews*. **113**(3),pp.1641–1666.

Hsiang, Y.-H., Hertzberg, R., Hecht, S. and Liu, L.F. 1985. Camptothecin induces protein-linked DNA breaks via mammalian DNA topoisomerase I. *The Journal of Biological Chemistry*. **260**(27),pp.1487–14878.

Hsiang, Y., Lihou, M.G. and Liu, L.F. 1989. Arrest of replication forks by drug-stabilized topoisomerase I-DNA cleavable complexes as a mechanism of cell killing by camptothecin. *Cancer Research*. **49**,pp.5077–5082.

Hu, S., Lee, E., Wang, C., Wang, J., Zhou, Z., Li, Y., Li, X., Tang, J., Lee, D.H., Liu, X., Shen, Y., Haeng, D., Liu, X., Shen, Y., Lee, D.H., Liu, X. and Shen, Y. 2015. Amphiphilic drugs as surfactants to fabricate excipient-free stable nanodispersions of hydrophobic drugs for cancer chemotherapy. *Journal of Controlled Release*. **220**,pp.175–179.

Huang, H., Hu, S., Hung, S., Chiang, C., Liu, H. and Chiu, T. 2013. SPIO nanoparticle-stabilized PAA-F127 thermosensitive nanobubbles with MR / US dual-modality imaging and HIFU-triggered drug release for magnetically guided in vivo tumor therapy. *Journal of Controlled Release*. **172**(1),pp.118–127.

Huang, P., You, X., Pan, M., Li, S., Zhang, Y., Zhao, Y., Wang, M., Hong, Y., Pu, Z., Chen, L., Yang, G. and Guo, Y. 2013. A novel therapeutic strategy using ultrasound mediated microbubbles destruction to treat colon cancer in a mouse model. *Cancer Letters*. **335**(1),pp.183–190.

Huang, S.K., Mayhew, E., Gilani, S., Lasic, D.D., Martin, F.J. and Papahadjopoulos, D. 1992. Pharmacokinetics and therapeutics of sterically stabilized liposomes in mice bearing C-26 colon carcinoma. *Cancer Research*. **52**,pp.6774–6781.

Huang, Y., Cole, S., Cai, T. and Cai, Y. 2016. Applications of nanoparticle drug delivery systems for the reversal of multidrug resistance in cancer (Review). *Oncology Letters*. **12**,pp.11–15.

Humerickhouse, R., Lohrbach, K., Li, L., Bosron, W.F. and Dolan, M.E. 2000. Characterization of CPT-11 hydrolysis by human liver carboxylesterase isoforms hCE-1 and hCE-2. *Cancer Research*. **60**,pp.1189–1192.

Husseini, G. and Pitt, W. 2008. Micelles and nanoparticles for ultrasonic drug and gene delivery. *Advanced Drug Delivery Reviews*. **60**(10),pp.1137–1152.

Ibsen, S., Benchimol, M., Simberg, D., Schutt, C., Steiner, J. and Esener, S. 2011. A novel nested liposome drug delivery vehicle capable of ultrasound triggered release of its payload. *Journal of Controlled Release*. **155**(3),pp.358–366.

Ignee, A., Atkinson, N.S.S., Schuessler, G. and Dietrich, C.F. 2016. Ultrasound contrast agents. *Endoscopic Ultrasound*. **5**(6),pp.355–362.

Ihnatsenka, B. and Boezaart, A. 2010. Ultrasound: Basic understanding and learning the language. *International Journal of Shoulder Surgery*. **4**(3),pp.55–62.

Ilyas, M., Tomlinson, I.P., Rowan, A., Pignatelli, M. and Bodmer, W.F. 1997. Beta-catenin mutations in cell lines established from human colorectal cancers. *Proceedings of the National Academy of Sciences of the United States of America*. **94**(19),pp.10330–4.

Ingram, N., Macnab, S.A., Marston, G., Scott, N., Carr, I.M., Markham, A.F., Whitehouse, A. and Coletta, P.L. 2013. The use of high-frequency ultrasound imaging and biofluorescence for in vivo evaluation of gene therapy vectors. *BMC Medical Imaging*. **13**(35).

Iwamoto, T. 2013. Clinical application of drug delivery systems in cancer chemotherapy: Review of the efficacy and side effects of approved drugs. *Biological and Pharmaceutical Bulletin*. **36**(5),pp.715–718.

Iyer, L., King, C.D., Whitington, P.F., Green, M.D., Roy, S.K., Tephly, T.R., Coffman, B.L. and Ratain, M.J. 1998. Genetic predisposition to the metabolism of irinotecan (CPT-11): Role of uridine diphosphate glucuronosyltransferase isoform 1A1 in the glucuronidation of its active metabolite (SN-38) in human liver microsomes. *Journal of Clinical Investigation*. **101**(4),pp.847–854.

Iyer, R., Croucher, J.L., Chorny, M., Mangino, J.L., Alferiev, I.S., Levy, R.J., Kolla, V., Brodeur, G.M., Ivan, S., Levy, R.J., Kolla, V. and Brodeur, G.M. 2015. Nanoparticle delivery of an

SN38 conjugate is more effective than irinotecan in a mouse model of neuroblastoma. *Cancer Letters*. **360**(2),pp.205–212.

Jackson-Thompson, J., Ahmed, F., German, R.R., Lai, S.-M. and Friedman, C. 2006. Descriptive epidemiology of colorectal cancer in the United States, 1998–2001. *Cancer*. **107**(S5),pp.1103–1111.

Jang, H.-J., Yu, H. and Kim, T.K. 2009. Contrast-enhanced ultrasound in the detection and characterization of liver tumors. *Cancer imaging*. **9**,pp.96–103.

Janib, S., Moses, A. and MacKay, J. 2010. Imaging and drug delivery using theranostic nanoparticles. *Advanced Drug Delivery Reviews*. **62**(11),pp.1051–1063.

Jansen, S., Andries, M., Vekemans, K., Vanbilloen, H., Verbruggen, A. and Bollen, M. 2009. Rapid clearance of the circulating metastatic factor autotaxin by the scavenger receptors of liver sinusoidal endothelial cells. *Cancer Letters*. **284**(2),pp.216–221.

Jansen, W.J.M., Zwart, B., Hulscher, S.T.M., Giaccone, G., Pinedo, H.M. and Boven, E. 1997. CPT-11 in human colon-cancer cell lines and xenografts: characterization of cellular sensitivity determinants. *International Journal of Cancer*. **70**,pp.335–340.

Janssen, K.P., Alberici, P., Fsihi, H., Gaspar, C., Breukel, C., Franken, P., Rosty, C., Abal, M., El Marjou, F., Smits, R., Louvard, D., Fodde, R. and Robine, S. 2006. APC and oncogenic KRAS are synergistic in enhancing Wnt signaling in intestinal tumor formation and progression. *Gastroenterology*. **131**(4),pp.1096–1109.

Järvinen, H.J., Aarnio, M., Mustonen, H., Aktan-Collan, K., Aaltonen, L.A., Peltomäki, P., De La Chapelle, A. and Mecklin, J.P. 2000. Controlled 15-year trial on screening for colorectal cancer in families with hereditary nonpolyposis colorectal cancer. *Gastroenterology*. **118**(5),pp.829–834.

Jensen, N.F., Agama, K., Roy, A., Smith, D.H., Pfister, T.D., Romer, M.U., Zhang, H.L., Doroshow, J.H., Knudsen, B.R., Stenvang, J., Brunner, N. and Pommier, Y. 2016. Characterization of DNA topoisomerase I in three SN-38 resistant human colon cancer cell lines reveals a new pair of resistance-associated mutations. *Journal of Experimental and Clinical Cancer Research*. **35**(56).

Jeong, W., Park, S.R., Rapisarda, A., Fer, N., Kinders, R.J., Chen, A., Melillo, G., Turkbey, B., Steinberg, S.M., Choyke, P., Doroshow, J.H. and Kummar, S. 2014. Weekly EZN-2208 (PEGylated SN-38) in combination with bevacizumab in patients with refractory solid tumors. *Investigational New Drugs*. **32**(2),pp.340–346.

Jevševar, S., Kunstelj, M. and Porekar, V.G. 2010. PEGylation of therapeutic proteins. *Biotechnology Journal*. **5**,pp.113–128.

Jha, S., Sharma, P.K. and Malviya, R. 2016. Hyperthermia: Role and risk factor for cancer treatment. *Achievements in the Life Sciences*. **10**,pp.161–167.

Johnson, J.I., Decker, S., Zaharevitz, D., Rubinstein, L. V., Venditti, J.M., Schepartz, S., Kalyandrug, S., Christian, M., Arbuck, S., Hollingshead, M. and Sausville, E.A. 2001. Relationships between drug activity in NCI preclinical in vitro and in vivo models and early clinical trials. *British Journal of Cancer*. **84**(10),pp.1424–1431.

Johnson, R.L. and Fleet, J.C. 2013. Animal models of colorectal cancer. *Cancer and Metastasis Reviews*. **32**(0),pp.39–61.

Jokerst, J. V, Lobovkina, T., Zare, R.N. and Gambhir, S.S. 2011. Nanoparticle PEGylation for imaging and therapy. *Nanomedicine*. **6**(4),pp.715–728.

Jones, J.A., Lutz, S.T., Chow, E. and Johnstone, P.A. 2014. Palliative radiotherapy at the end of life: A critical review. *CA: A Cancer Journal for Clinicians*. **64**(5),pp.296–310.

Jones, R.P. and Poston, G.J. 2017. Resection of liver metastases in colorectal cancer in the era of expanding systemic therapy. *Annual Review of Medicine*. **68**(1),pp.183–196.

De Jong, A.E., Morreau, H., Nagengast, F.M., Mathus-Vliegen, E.M.H., Kleibeuker, J.H., Griffioen, G., Cats, A. and Vasen, H.F.A. 2005. Prevalence of adenomas among young individuals at average risk for colorectal cancer. *American Journal of Gastroenterology*. **100**(1),pp.139–143.

Joralemon, M.J., McRae, S. and Emrick, T. 2010. PEGylated polymers for medicine: From conjugation to self-assembled systems. *Chemical Communications*. **46**,pp.1377–1393.

Jun, H.Y., Park, S.H., Kim, H.S. and Yoon, K.H. 2010. Long residence time of ultrasound microbubbles targeted to integrin in murine tumor model. *Academic Radiology*. **17**,pp.54–60.

Kalra, A. V, Kim, J., Klinz, S.G., Paz, N., Cain, J., Drummond, D.C., Nielsen, U.B. and Fitzgerald, J.B. 2014. Preclinical activity of nanoliposomal irinotecan is governed by tumor deposition and intratumor pro-drug conversion. *Cancer research*. **74**(23),pp.7003–7013.

Kawato, Y., Aonuma, M., Hirota, Y., Kuga, H. and Sato, K. 1991. Intracellular roles of SN-38, a metabolite of the camptothecin derivative CPT-11, in the antitumor effect of CPT-

11. *Cancer Research*. **51**(16),pp.4187–4191.

Kekelidze, M., D'Errico, L., Pansini, M., Tyndall, A. and Hohmann, J. 2013. Colorectal cancer: Current imaging methods and future perspectives for the diagnosis, staging and therapeutic response evaluation. *World Journal of Gastroenterology*. **19**(46),pp.8502–8514.

Kenmotsu, H., Yasunaga, M., Goto, K., Nagano, T., Kuroda, J.I., Koga, Y., Takahashi, A., Nishiwaki, Y. and Matsumura, Y. 2010. The antitumor activity of NK012, an SN-38-incorporating micelle, in combination with bevacizumab against lung cancer xenografts. *Cancer*. **116**(19),pp.4597–4604.

Khan, S., Ahmad, A., Guo, W., Wang, Y.F., Abu-Qare, A. and Ahmad, I. 2005. A simple and sensitive LC/MS/MS assay for 7-ethyl-10-hydroxycamptothecin (SN-38) in mouse plasma and tissues: Application to pharmacokinetic study of liposome entrapped SN-38. *Journal of Pharmaceutical and Biomedical Analysis*. **37**(1),pp.135–142.

Khatib, A.M., Knotogiannea, M., Fallavollita, L., Jamison, B., Meterissian, S. and Brodt, P. 1999. Rapid induction of cytokine and E- selectin expression in the liver in response to metastatic tumor cells. *Cancer Research*. **59**(6),pp.1356–1361.

Kheirolomoom, A., Dayton, P.A., Lum, A.F.H., Little, E., Paoli, E.E., Zheng, H. and Ferrara, K.W. 2007. Acoustically-active microbubbles conjugated to liposomes: Characterization of a proposed drug delivery vehicle. *Journal of Controlled Release*. **118**(3),pp.275–284.

Kim, H., Lee, Y., Kang, S., Choi, M., Lee, S., Kim, S., Gujrati, V., Kim, J. and Jon, S. 2016. Self-assembled nanoparticles comprising aptide–SN38 conjugates for use in targeted cancer therapy. *Nanotechnology*. **27**(48).

Knickelbein, K. and Zhang, L. 2015. Mutant KRAS as a critical determinant of the therapeutic responce of colorectal cancer. *Genes & Diseases*. **2**(1),pp.4–12.

Kobayashi, K., Bouscarel, B., Matsuzaki, Y., Ceryak, S., Kudoh, S. and Fromm, H. 1999. pH-dependent uptake of irinotecan and its active metabolite, SN38, by intestinal cells. *International Journal of Cancer*. **83**,pp.491–496.

Koizumi, F., Kitagawa, M., Negishi, T., Onda, T., Matsumoto, S.I., Hamaguchi, T. and Matsumura, Y. 2006. Novel SN-38-incorporating polymeric micelles, NK012, eradicate vascular endothelial growth factor-secreting bulky tumors. *Cancer Research*. **66**(20),pp.10048–10056.

Kooiman, K., Kokhuis, T.J.A., Skachkov, I., Bosch, J.G., Van Der Steen, A.F.W., Van Cappellen, W.A. and De Jong, N. 2012. Surface contact of bound targeted microbubbles. *IEEE International Ultrasonics Symposium Proceeding*.,pp.2161–2163.

Kooiman, K., Vos, H.J., Versluis, M. and De Jong, N. 2014. Acoustic behavior of microbubbles and implications for drug delivery. *Advanced Drug Delivery Reviews*. **72**,pp.28–48.

Korpanty, G., Carbon, J.G., Grayburn, P.A., Fleming, J.B. and Brekken, R.A. 2007. Monitoring response to anticancer therapy by targeting microbubbles to tumor vasculature. *Clinical Cancer Research*. **13**(1),pp.323–330.

Kotoh, S., Naito, S., Yokomizo, A., Bladder, H.C., Cells, C. and Frac, A.B. 1994. Increased expression of DNA topoisomerase I gene and collateral sensitivity to camptothecin in human cisplatin-resistant bladder cancer cells. *Cancer Research*. **54**,pp.3248–3252.

Kotopoulis, S., Delalande, A., Popa, M., Mamaeva, V., Dimcevski, G., Gilja, O.H., Postema, M., Gjertsen, B.T. and McCormack, E. 2014. Sonoporation-enhanced chemotherapy significantly reduces primary tumour burden in an orthotopic pancreatic cancer xenograft. *Molecular Imaging and Biology*. **16**(1),pp.53–62.

Kotopoulis, S., Dimcevski, G., Gilja, O.H., Hoem, D. and Postema, M. 2013. Treatment of human pancreatic cancer using combined ultrasound, microbubbles, and gemcitabine: A clinical case study. *The International Journal of Medical Physics Research and Practice*. **40**(7).

Kozuka, S., Nogaki, M., Ozeki, T. and Masumori, S. 1975. Premalignancy of the mucosal polyp in the large intestine: II. Estimation of the periods required for malignant transformation of mucosal polyps. *Diseases of the Colon & Rectum*. **18**(6),pp.483–493.

Kraut, E.H., Fishman, M.N., Lorusso, P.M., Gordon, M.S., Rubin, E.H., Haas, A., Fetterly, G.J., Cullinan, P., Dul, J.L. and Steinberg, J.L. 2017. Final results of a phase I study of liposome encapsulated SN-38 (LE-SN38): Safety, pharmacogenomics, pharmacokinetics, and tumor response. *Journal of Clinical Oncology*. **23**(16).

Kraut, E.H., Fishman, M.N., Lorusso, P.M., Steinberg, J.L., Nieves, J.A., Fetterly, G.J., Darling, I.M., Wanaski, S.P., Dul, J.L. and Sherman, J.W. 2004. Pharmacogenomic and pharmacokinetic assessment of liposome encapsulated SN-38 (LE-SN38) in advanced cancer patients. *Journal of Clinical Oncology*. **22**(14),pp.2501–2501.

Kudo, N., Okada, K. and Yamamoto, K. 2009. Sonoporation by single-shot pulsed ultrasound with microbubbles adjacent to cells. *Biophysical Journal*. **96**(12),pp.4866–4876.

Kuipers, E.J., Grady, W.M., Lieberman, D., Seufferlein, T., Sung, J.J., Boelens, P.G., van de Velde, C.J.H. and Watanabe, T. 2015. Colorectal cancer. *Nature Reviews Disease Primers*. **1**.

Kuroda, J.I., Kuratsu, J.I., Yasunaga, M., Koga, Y., Kenmotsu, H., Sugino, T. and Matsumura, Y. 2010. Antitumor effect of NK012, a 7-ethyl-10-hydroxycamptothecin-incorporating polymeric micelle, on U87MG orthotopic glioblastoma in mice compared with irinotecan hydrochloride in combination with bevacizumab. *Clinical Cancer Research*. **16**(2),pp.521–529.

Kurzrock, R., Goel, S., Wheler, J., Hong, D., Fu, S., Rezai, K., Morgan-Linnell, S.K., Urien, S., Mani, S., Chaudhary, I., Ghalib, M.H., Buchbinder, A., Lokiec, F. and Mulcahy, M. 2012. Safety, pharmacokinetics, and activity of EZN-2208, a novel conjugate of polyethylene glycol and SN38, in patients with advanced malignancies. *Cancer*. **118**(24),pp.6144–6151.

Kweekel, D.M., Gelderblom, H. and Guchelaar, H.J. 2005. Pharmacology of oxaliplatin and the use of pharmacogenomics to individualize therapy. *Cancer Treatment Reviews*. **31**(2),pp.90–105.

Labhasetwar, V., Mohan, M.S. and Dorle, A.K. 1994. A study on zeta potential and dielectric constant of liposomes. *Journal of Microencapsulation*. **11**(6),pp.663–668.

Lai, C.-Y., Wu, C.-H., Chen, C.-C. and Li, P.-C. 2006. Quantitative relations of acoustic inertial cavitation with sonoporation and cell viability. *Ultrasound in Medicine & Biology*. **32**(12),pp.1931–1941.

Lammers, T., Aime, S., Hennink, W.E., Storm, G. and Kiessling, F. 2011. Theranostic nanomedicine. *Accounts of Chemical Research*. **44**(10),pp.1029–1038.

Landmann, H., Proia, D.A., He, S., Ogawa, L.S., Kramer, F., Beibarth, T., Grade, M., Gaedcke, J., Ghadimi, M., Moll, U., M., D., Landmann, H., Proia, D.A., He, S., Ogawa, L.S., Kramer, F., Beissbarth, T., Grade, M., Gaedcke, J., Ghadimi, M., Moll, U. and Dobbelstein, M. 2014. UDP glucuronosyltransferase 1A expression levels determine the response of colorectal cancer cells to the heat shock protein 90 inhibitor ganetespib. *Cell Death and Disease*. **5**(e1411).

Langers, I., Renoux, V.M., Thiry, M., Delvenne, P. and Jacobs, N. 2012. Natural killer cells: Role in local tumor growth and metastasis. *Biologics: Targets & Therapy*. **6**,pp.73–82.

Langley, R.R. and Fidler, I.J. 2011. The seed and soil hypothesis revisited - The role of tumor-stroma interactions in metastasis to different organs. *International Journal of Cancer*. **128**(11),pp.2527–2535.

László, D., Fülöpa, T., Mészárosa, T. and Szénási, G. 2014. Features of complement activation-related pseudoallergy to liposomes with different surface charge and PEGylation: Comparison of the porcine and rat responsese. *Journal of Controlled Release*. **195**,pp.2–10.

Lavilla-Alonso, S., Abo-Ramadan, U., Halavaara, J., Escutenaire, S., Tatlisumak, T., Saksela, K., Kanerva, A., Hemminki, A. and Pesonen, S. 2011. Optimized mouse model for the imaging of tumor metastasis upon experimental therapy. *PLoS ONE*. **6**(11).

Lecomte, T., Ferraz, J.-M., Zinzindohoué, F., Loriot, M.-A., Tregouet, D.-A., Landi, B., Berger, A., Cugnenc, P.-H., Jian, R., Beaune, P. and Laurent-Puig, P. 2004. Thymidylate synthase gene polymorphism predicts toxicity in colorectal cancer patients receiving 5-fluorouracil-based chemotherapy. *Clinical Cancer Research*. **10**(17),pp.5880–5888.

Lee, C.S., Ryan, E.J. and Doherty, G.A. 2014. Gastro-intestinal toxicity of chemotherapeutics in colorectal cancer: The role of inflammation. *World Journal of Gastroenterology*. **20**(14),pp.3751–3761.

Lee, D.J., Lyshchik, A. and Huamani, J. 2008. Relationship between retention of a vascular endothelial growth factor and the level of VEGFR2 expression in an In vivo breast cancer model. *Journal of Ultrasound in Medicine*. **27**,pp.855–866.

Lee, N.K., Kim, S., Lee, J.W., Lee, S.H., Kang, D.H., Kim, G.H. and Seo, H. Il 2009. Biliary MR Imaging with Gd-EOB-DTPA and Its Clinical Applications. *RadioGraphics*. **29**(6),pp.1707–1724.

Lee, W.Y., Hong, H.K., Ham, S.K., Kim, C.I. and Cho, Y.B. 2014. Comparison of colorectal cancer in differentially established liver metastasis models. *Anticancer Research*. **34**(7),pp.3321–3328.

Leen, E., Angerson, W.J., Wotherspoon, H., Moule, B., Cook, T.G. and McArdle, C.S. 1995. Detection of colorectal liver metastases: Comparison of laparotomy, CT, US, and Doppler perfusion index and evaluation of postoperative follow-up results. *Radiology*. **195**(1),pp.113–116.

De Leeuw, A., Brouwer, A. and Knook, D. 1990. Sinusoidal endothelial cells of the liver: fine structure and function in relation to age. *Journal of Electron Microscopy Technique*. **14**(3),pp.218–36.

Leguerney, I., Scoazec, J.-Y., Gadot, N., Robin, N., Pénault-Llorca, F., Victorin, S. and Lassau, N. 2015. Molecular ultrasound imaging using contrast agents targeting endoglin, vascular endothelial growth factor receptor 2 and integrin. *Ultrasound in Medicine & Biology*. **41**(1),pp.197–207.

Lei, S., Chien, P.-Y., Sheikh, S., Zhang, A., Ali, S. and Ahmad, I. 2004. Enhanced therapeutic efficacy of a novel liposome-based formulation of SN-38 against human tumor models in SCID mice. *Anti-cancer drugs*. **15**(8),pp.773–8.

Leibovitz, A., Stinson, J.C., McCombs, William B., I., McCoy, C.E., Mazur, K.C. and Mabry, N.D. 1976. Classification of human colorectal adenocarcinoma cell lines. *Cancer Research*. **36**(12),pp.4562–4569.

Leighton, T.G. 2007. What is ultrasound? *Progress in Biophysics and Molecular Biology*. **93**,pp.3–83.

Lentacker, I., De Cock, I., Deckers, R., De Smedt, S.C. and Moonen, C.T.W. 2014. Understanding ultrasound induced sonoporation: Definitions and underlying mechanisms. *Advanced Drug Delivery Reviews*. **72**,pp.49–64.

Lentacker, I., De Geest, B.G., Vandenbroucke, R.E., Peeters, L., Demeester, J., De Smedt, S.C. and Sanders, N.N. 2006. Ultrasound-responsive polymer-coated microbubbles that bind and protect DNA. *Langmuir*. **22**(17),pp.7273–7278.

Leong-Poi, H., Christiansen, J., Klibanov, A.L., Kaul, S. and Lindner, J.R. 2003. Noninvasive assessment of angiogenesis by ultrasound and microbubbles targeted to αv-integrins. *Circulation*. **107**,pp.455–460.

Lesch, H.P., Kaikkonen, M.U., Pikkarainen, J.T. and Ylä-Herttuala, S. 2010. Avidin-biotin technology in targeted therapy. *Expert Opinion on Drug Delivery*. **7**(5),pp.551–564.

Li, K. and Wang, S. 2016. Preparation, pharmacokinetic profile, and tissue distribution studies of a liposome-based formulation of SN-38 using an UPLC-MS/MS method. *AAPS PharmSciTech*. **17**(6),pp.1450–1456.

Li, P., Zheng, Y., Ran, H., Tan, J., Lin, Y., Zhang, Q., Ren, J. and Wang, Z. 2012. Ultrasound triggered drug release from 10-hydroxycamptothecin-loaded phospholipid microbubbles for targeted tumor therapy in mice. *Journal of Controlled Release*.

162(2),pp.349–354.

Li, S.-D. and Huang, L. 2011. Stealth nanoparticles: High density but sheddable PEG is a key for tumor targeting. *Journal of Controlled Release*. **145**(3),pp.178–181.

Lian, J., Nelson, R. and Lehner, R. 2018. Carboxylesterases in lipid metabolism: from mouse to human. *Protein & Cell*. **9**(2),pp.178–195.

Liang, Z. and Richards, R. 2010. Virtual colonoscopy vs optical colonoscopy. *Expert Opinion on Medical Diagnostics*. **4**(2),pp.159–169.

Lin, C.-Y., Huang, Y.-L., Li, J.-R., Chang, F.-H. and Lin, W.-L. 2010. Effects of focused ultrasound and microbubbles on the vascular permeability of nanoparticles delivered into mouse tumors. *Ultrasound in Medicine & Biology*. **36**(9),pp.1460–1469.

Lindner, J.R. 2004. Microbubbles in medical imaging: current applications and future directions. *Nature Reviews Drug Discovery*. **3**(6),pp.527–533.

Litzinger, D.C., Buiting, A.M.J., van Rooijen, N. and Huang, L. 1994. Effect of liposome size on the circulation time and intraorgan distribution of amphipathic poly(ethylene glycol)-containing liposomes. *Biochimica et Biophysica Acta - Biomembranes*. **1190**(1),pp.99–107.

Liu, H., Lu, H., Liao, L., Zhang, X., Gong, T. and Zhang, Z. 2014. Lipid nanoparticles loaded with 7-ethyl-10-hydroxycamptothecin-phospholipid complex: in vitro and in vivo studies. *Drug Delivery*. **22**(6),pp.701–709.

Liu, Y., Wang, W., Yang, J., Zhou, C. and Sun, J. 2013. pH-sensitive polymeric micelles triggered drug release for extracellular and intracellular drug targeting delivery. *Asian Journal of Pharmaceutical Sciences*. **8**(3),pp.159–167.

Longley, D.B. and Johnston, P.G. 2005. Molecular mechanisms of drug resistance. *Journal of Pathology*. **205**(2),pp.275–292.

Longmire, M., Choyke, P.L. and Kobayashi, H. 2008. Clearance properties of nano-sized particles and molecules as imagin agents: consideration and caveats. *Nanomedicine*. **3**(5),pp.703–717.

Lu, L., Zhou, J., Shi, J., Peng, X.J., Qi, X.X., Wang, Y., Li, F., Zhou, F.Y., Liu, L. and Liu, Z.Q. 2015. Drug-metabolizing activity, protein and gene expression of UDP-glucuronosyltransferases are significantly altered in hepatocellular carcinoma patients. *PLoS ONE*. **10**(5).

Lv, Y., Hao, L., Hu, W., Ran, Y., Bai, Y. and Zhang, L. 2016. Novel multifunctional pH-sensitive nanoparticles loaded into microbubbles as drug delivery vehicles for enhanced tumor targeting. *Scientific Reports*. **6**(29321).

Lynch, H.T. and Lynch, J.F. 2000. Hereditary nonpolyposis colorectal cancer. *Seminars in Surgical Oncology*. **18**(4),pp.305–13.

Lyu, Z. and Peng, L. 2017. Potent drugless dendrimers. *Nature Biomedical Engineering*. **1**(9),pp.686–688.

Madaan, K., Kumar, S., Poonia, N., Lather, V. and Pandita, D. 2014. Dendrimers in drug delivery and targeting: Drug-dendrimer interactions and toxicity issues. *Journal of Pharmacy and Bioallied Sciences*. **6**(3),pp.139–150.

Maeda, H. 2015. Toward a full understanding of the EPR effect in primary and metastatic tumors as well as issues related to its heterogeneity. *Advanced Drug Delivery Reviews*. **91**,pp.3–6.

Maeda, H., Nakamura, H. and Fang, J. 2013. The EPR effect for macromolecular drug delivery to solid tumors: Improvement of tumor uptake, lowering of systemic toxicity, and distinct tumor imaging in vivo. *Advanced Drug Delivery Reviews*. **65**(1),pp.71–79.

Magistri, P., Battistelli, C., Toietta, G., Strippoli, R., Sagnotta, A., Forgione, A., Di Benedetto, F., Uccini, S., Vittorioso, P., D'Angelo, F., Aurello, P., Ramacciato, G. and Nigri, G. 2017. In vivo bioluminescence-based monitoring of liver metastases from colorectal cancer: An experimental model. *Journal of Microscopy and Ultrastructure*. **(in press)**.

Maiti, R. 2014. Metronomic chemotherapy. *Journal of Pharmacology and Pharmacotherapeutics*. **5**(3),pp.186–192.

Manzotti, C., Audisio, R.A. and Pratesi, G. 1993. Importance of orthotopic implantation for human tumors as model systems: Relevance to metastasis and invasion. *Clinical & Experimental Metastasis*. **11**(1),pp.5–14.

El Marjou, F., Janssen, K.P., Chang, B.H.J., Li, M., Hindie, V., Chan, L., Louvard, D., Chambon, P., Metzger, D. and Robine, S. 2004. Tissue-specific and inducible Cre-mediated recombination in the gut epithelium. *Genesis*. **39**(3),pp.186–193.

Markman, B., Javier Ramos, F., Capdevila, J. and Tabernero, J. 2010. EGFR and KRAS in colorectal cancer. *Advances in Clinical Chemistry*. **51**,pp.71–119.

Marley, A.R. and Nan, H. 2016. Molecular epidemiology of colorectal cancer. *International*

Journal of Molecular Epidemiology and Genetics. **7**(3),pp.105–114.

Marosi, C. and Köller, M. 2016. Challenge of cancer in the elderly. *ESMO Open*. **1**(3).

Marsh, S. and Hoskins, J.M. 2011. Irinotecan pharmacogenomics. *Pharmacogenomics*. **11**(7),pp.1003–1010.

Marshall, D., Pedley, R.B., Boden, J. a, Boden, R., Melton, R.G. and Begent, R.H. 1996. Polyethylene glycol modification of a galactosylated streptavidin clearing agent: Effects on immunogenicity and clearance of a biotinylated anti-tumour antibody. *British Journal of Cancer*. **73**,pp.565–72.

Martin, H.L., Bedford, R., Heseltine, S.J., Tang, A.A., Haza, K.Z., Rao, A., McPherson, M.J. and Tomlinson, D.C. 2018. Non-immunoglobulin scaffold proteins: Precision tools for studying protein-protein interactions in cancer. *New Biotechnology*. **S1871**-**6784**(17).

Maruyama, K., Holmberg, E., Kennel, S.J., Klibanov, A., Torchilin, V.P. and Huang, L. 1990. Characterization of in vivo immunoliposome targeting to pulmonary endothelium. *American Pharaceutical Association*. **79**(11),pp.978–984.

Mathijssen, R.H., van Alphen, R.J., Verweij, J., Loos, W.J., Nooter, K., Stoter, G. and Sparreboom, A. 2001. Clinical pharmacokinetics and metabolism of irinotecan (CPT-11). *Clinical Cancer Research*. **7**(8),pp.2182–2194.

Matsumura, Y. 2008. Polymeric micellar delivery systems in oncology. *Japanese Journal of Clinical Oncology*. **38**(12),pp.793–802.

Matsusaka, S. and Lenz, H.-J. 2015. Pharmacogenomics of fluorouracil-based chemotherapy toxicity. *Expert Opinion on Drug Metabolism & Toxicology*. **11**(5),pp.811–821.

Matthaios, D., Foukas, P.G., Kefala, M., Hountis, P., Trypsianis, G., Panayiotides, I.G., Chatzaki, E., Pantelidaki, E., Bouros, D., Karakitsos, P. and Kakolyris, S. 2012. γ-H2AX expression detected by immunohistochemistry correlates with prognosis in early operable non-small cell lung cancer. *OncoTargets and Therapy*. **5**,pp.309–314.

Mayer, C.R., Geis, N.A., Katus, H.A. and Bekeredjian, R. 2008. Ultrasound targeted microbubble destruction for drug and gene delivery. *Expert Opinion on Drug Delivery*. **5**(10),pp.1121–1138.

Mcintyre, R.E., Buczacki, S.J.A., Arends, M.J. and Adams, D.J. 2015. Mouse models of colorectal cancer as preclinical models. *BioEssays*. **37**(8),pp.909–920.

McLafferty, F.W. 1981. Tandem mass spectrometry. *Science*. **214**(4518),pp.280–287.

McLaughlan, J., Ingram, N., Smith, P.R., Harput, S., Coletta, P.L., Evans, S. and Freear, S. 2013. Increasing the sonoporation efficiency of targeted polydisperse microbubble populations using chirp excitation. *IEEE Transactions on Ultrasonics, Ferroelectrics, and Frequency Control*. **60**(12),pp.2511–2520.

McLaughlan, J.R., Harput, S., Abou-Saleh, R.H., Peyman, S.A., Evans, S. and Freear, S. 2016. Characterisation of liposome-loaded microbubble populations for subharmonic imaging. *Ultrasound in Medicine & Biology*. **43**(1),pp.346–356.

Meijering, B.D.M., Juffermans, L.J.M., Wamel, A. Van, Henning, R.H., Zuhorn, I.S., Emmer, M., Versteilen, A.M.G., Paulus, W.J., Gilst, W.H. Van, Kooiman, K., Jong, N. De, Musters, R.J.P., Deelman, L.E. and Kamp, O. 2009. Ultrasound and microbubbles targeted delivery of macromolecules is regulated bu induction of endocytosis and pore formation. *Integrative Physiology*. **104**(5),pp.679–687.

Messerer, C.L., Ramsay, E.C., Waterhouse, D., Ng, R., Simms, E.M., Harasym, N., Tardi, P., Mayer, L.D. and Bally, M.B. 2004. Liposomal irinotecan: Formulation development and therapeutic assessment in murine xenograft models of colorectal cancer. *Clinical Cancer Research*. **10**(19),pp.6638–6649.

Mico, V., Charalambous, A., Peyman, S.A., Abou-Saleh, R.H., Markham, A.F., Coletta, P.L. and Evans, S.D. 2017. Evaluation of lipid-stabilised tripropionin nanodroplets as a delivery route for combretastatin A4. *International Journal of Pharmaceutics*. **526**(1–2),pp.547–555.

Miller, D.L. and Quddus, J. 2000. Diagnostic ultrasound activation of contrast agent gas bodies induces capillary rupture in mice. *Proceedings of National Academy of Sciences of the United States of America*. **97**(18),pp.10179–10184.

Mina, L.A. and Sledge, G.W. 2011. Rethinking the metastatic cascade as a therapeutic target. *Nature Reviews Clinical Oncology*. **8**,pp.325–332.

Minchinton, A.I. and Tannock, I.F. 2006. Drug penetration in solid tumours. *Nature reviews. Cancer*. **6**(8),pp.583–592.

Misra, R., Acharya, S. and Sahoo, S.K. 2010. Cancer nanotechnology: Application of nanotechnology in cancer therapy. *Drug Discovery Today*. **15**(19–20),pp.842–850.

Momen-Heravi, F., Balaj, L., Alian, S., Tigges, J., Toxavidis, V., Ericsson, M., Distel, R.J., Ivanov, A.R., Skog, J. and Kuo, W.P. 2012. Alternative methods for characterization of

extracellular vesicles. *Frontiers in Physiology*. **3**(354),pp.1–8.

Mook, O.R.F., Van Marie, J., Jonges, R., Vreeling-Sindelarova, H., Frederiks, W.M. and Van Noorden, C.J.F. 2008. Interactions between colon cancer cells and hepatocytes in rat in relation to metastasis. *Journal of Cellular and Molecular Medicine*. **12**(5B),pp.2052–2061.

Moriarity, A., O'Sullivan, J., Kennedy, J., Mehigan, B. and McCormick, P. 2016. Current targeted therapies in the treatment of advanced colorectal cancer: A review. *Therapeutic Advances in Medical Oncology*. **8**(4),pp.276–293.

Morosi, L., Spinelli, P., Zucchetti, M., Pretto, F., Carrà, A., D'Incalci, M., Giavazzi, R. and Davoli, E. 2013. Determination of Paclitaxel Distribution in Solid Tumors by Nano-Particle Assisted Laser Desorption Ionization Mass Spectrometry Imaging. *PLoS ONE*. **8**(8),pp.1–9.

Morris, K. AL and Haboubi, N.Y. 2015. Pelvic radiation therapy: Between delight and disaster. *World Journal of Gastrointestinal Surgery*. **7**(11),pp.279–288.

Mosallaei, N., Mahmoudi, A., Ghandehari, H., Yellepeddi, V.K., Jaafari, M.R. and Malaekeh-Nikouei, B. 2016. Solid lipid nanoparticles containing 7-ethyl-10-hydroxycamptothecin (SN38): Preparation, characterization, in vitro, and in vivo evaluations. *European Journal of Pharmaceutics and Biopharmaceutics*. **104**,pp.42–50.

Moser, A., Pitot, H.C. and Dove, W.F. 1990. A dominant mutation that predisposes to multiple intestinal neoplasia in the mouse. *Science*. **247**(4940),pp.322–324.

Mosmann, T. 1983. Rapid colorimetric assay for cellular growth and survival: Application to proliferation and cytotoxicity assays. *Journal of Immunological Methods*. **65**(1–2),pp.55–63.

Mullick Chowdhury, S., Lee, T. and Willmann, J.K. 2017. Ultrasound-guided drug delivery in cancer. *Ultrasonography*. **36**(3),pp.171–184.

Muthukkaruppan, V.R., Kubai, L. and Auerbach, R. 1982. Tumor-induced neovascularization in the mouse eye. *Journal of the National Cancer Institute*. **69**(3),pp.699–708.

Nagano, T., Yasunaga, M., Goto, K., Kenmotsu, H., Koga, Y., Kuroda, J.I., Nishimura, Y., Sugino, T., Nishiwaki, Y. and Matsumura, Y. 2009. Antitumor activity of NK012 combined with cisplatin against small cell lung cancer and intestinal mucosal changes in tumor-bearing mouse after treatment. *Clinical Cancer Research*. **15**(13),pp.4348–4355.

Nagano, T., Yasunaga, M., Goto, K., Kenmotsu, H., Koga, Y., Kuroda, J.I., Nishimura, Y., Sugino, T., Nishiwaki, Y. and Matsumura, Y. 2010. Synergistic antitumor activity of the SN-38-incorporating polymeric micelles NK012 with S-1 in a mouse model of non-small cell lung cancer. *International Journal of Cancer*. **127**(11),pp.2699–2706.

Nakajima, T.E., Yanagihara, K., Takigahira, M., Yasunaga, M., Kato, K., Hamaguchi, T., Yamada, Y., Shimada, Y., Mihara, K., Ochiya, T. and Matsumura, Y. 2008. Antitumor effect of SN-38-releasing polymeric micelles, NK012, on spontaneous peritoneal metastases from orthotopic gastric cancer in mice compared with irinotecan. *Cancer Research*. **68**(22),pp.9318–9322.

Nasir, A., Reising, L.O. neill, Nedderman, D.M., Fulford, A.D., Uhlik, M.T., Benjamin, L.E., Schade, A.E. and Holzer, T.R. 2016. Heterogeneity of vascular endothelial growth factor receptors 1, 2, 3 in primary human colorectal carcinoma. *Anticancer Research*. **36**(6),pp.2683–2696.

Naumov, G.N., Akslen, L.A. and Folkman, J. 2006. Role of angiogenesis in human tumor dormancy: Animal models of the angiogenic switch. *Cell Cycle*. **5**(16),pp.1779–1787.

Norris, R.E., Shusterman, S., Gore, L., Muscal, J.A., Macy, M.E., Fox, E., Berkowitz, N., Buchbinder, A., Bogatell, R. and Bagatell, R. 2014. Phase 1 Evaluation of EZN-2208, a Polyethylene Glycol Conjugate of SN38, in Children Adolescents and Young Adults With Relapsed or Refractory Solid Tumors. *Pediatr Blood Cancer*. **61**,pp.1792–1797.

O'Connor, O.J., McDermott, S., Slattery, J., Sahani, D. and Blake, M.A. 2011. The use of PET-CT in the assessment of patients with colorectal carcinoma. *International Journal of Surgical Oncology*. **2011**(846512).

O'Farrell, A.C., Shnyder, S.D., Marston, G., Coletta, P.L. and Gill, J.H. 2013. Non-invasive molecular imaging for preclinical cancer therapeutic development. *British Journal of Pharmacology*. **169**(4),pp.719–735.

O'Neill, B.E., Vo, H., Angstadt, M., Li, K.P.C., Quinn, T. and Frenkel, V. 2009. Pulsed high intensity focused ultrasound mediated nanoparticle delivery: mechanisms and efficacy in murine muscle. *Ultrasound in Medicine and Biology*. **35**(3),pp.416–424.

Ocean, A.J., Niedzwiecki, D., Atkins, J.N., Parker, B., O'Neil, B.H., Lee, J.W., Wadler, S. and Goldberg, R.M. 2008. LE-SN38 for metastatic colorectal cancer after progression on oxaliplatin: Results of CALGB 80402. *Journal of Clinical Oncology*. **26**(90150),pp.4109–4109.

Oei, A.L., Vriend, L.E.M., Krawczyk, P.M., Horsman, M.R., Franken, N.A.P. and Crezee, J. 2017. Targeting therapy-resistant cancer stem cells by hyperthermia. *International Journal of Hyperthermia*. **33**(4),pp.419–427.

Oerlemans, C., Bult, W., Bos, M., Storm, G., Nijsen, J.F.W. and Hennink, W.E. 2010. Polymeric micelles in anticancer therapy: Targeting, imaging and triggered release. *Pharmaceutical Research*. **27**,pp.2569–2589.

Oh, B.Y., Hong, H.K., Lee, W.Y. and Cho, Y.B. 2017. Animal models of colorectal cancer with liver metastasis. *Cancer Letters*. **387**,pp.114–120.

Ojima, E., Inoue, Y., Watanabe, H., Hiro, J., Toiyama, Y., Miki, C. and Kusunoki, M. 2006. The optimal schedule for 5-fluorouracil radiosensitization in colon cancer cell lines. *Oncology Reports*. **16**(5),pp.1085–1091.

Osborne, C.R.C., O'Shaughnessy, J., Holmes, F.A., Kim, H.S., Kocs, D.M., Steinberg, M.S., Richards, P.D., Vukelja, S.J., Berkowitz, N.C. and Buchbinder, A. 2012. Final analysis of phase II study of EZN-2208 (PEG-SN38) in metastatic breast cancer (MBC). *Journal of Clinical Oncology*. **30**(15).

Oshima, M., Oshima, H., Kitagawa, K., Kobayashi, M., Itakura, C. and Taketo, M. 1995. Loss of Apc heterozygosity and abnormal tissue building in nascent intestinal polyps in mice carrying a truncated Apc gene. *Proceedings of the National Academy of Sciences of the United States of America*. **92**(10),pp.4482–6.

Owen, J., Rademeyer, P., Chung, D., Cheng, Q., Holroyd, D., Coussios, C., Friend, P., Pankhurst, Q.A. and Stride, E. 2015. Magnetic targeting of microbubbles against physiologically relevant flow conditions. *Interface focus*. **5**.

Pachman, D.R., Qin, R., Seisler, D.K., Smith, E.M.L., Beutler, A.S., Ta, L.E., Lafky, J.M., Wagner-Johnston, N.D., Ruddy, K.J., Dakhil, S., Staff, N.P., Grothey, A. and Loprinzi, C.L. 2015. Clinical course of oxaliplatin-induced neuropathy: Results from the randomized phase III trial N08CB (Alliance). *Journal of Clinical Oncology*. **33**(30),pp.3416–3422.

Paefgen, V., Doleschel, D. and Kiessling, F. 2015. Evolution of contrast agents for ultrasound imaging and ultrasound-mediated drug delivery. *Frontiers in Pharmacology*. **6**(SEP),pp.1–16.

Paget, S. 1889. The distribution of secondary growths in cancer of the breast. *Cancer Microenvironment*. **8**,pp.98–101.

Pal, A., Khan, S., Wang, Y.F., Kamath, N., Sarkar, A.K., Ahmad, A., Sheikh, S., Ali, S., Carbonaro, D., Zhang, A. and Ahmad, I. 2005. Preclinical safety, pharmacokinetics and antitumor efficacy profile of liposome-entrapped SN-38 formulation. *Anticancer Research*. **25**,pp.331–342.

Palakurthi, S. 2015. Challenges in SN38 drug delivery: Current success and future directions. *Expert Opinion on Drug Delivery*. **12**(12),pp.1911–1921.

Pancione, M., Remo, A. and Colantuoni, V. 2012. Genetic and epigenetic events generate multiple pathways in colorectal cancer progression. *Pathology Research International*. **2012**.

Panis, Y., Ribeiro, J., Chrétien, Y. and Nordlinger, B. 1992. Dormant liver metastases: An experimental study. *British Journal of Surgery*. **79**(3),pp.221–223.

Park, D.J., Won, J.H., Cho, A.R., Yun, H.J., Heo, J.H., Hwhang, T.H., Lee, D.H. and Kim, W.M. 2014. Determination of irinotecan and its metabolite SN-38 in rabbit plasma and tumors using a validated method of tandem mass spectrometry coupled with liquid chromatography. *Journal of Chromatography B*. **962**,pp.147–152.

Park, J., Fan, Z. and Deng, C.X. 2011. Effects of shear stress cultivation on cell membrane disruption and intracellular calcium concentration in sonoporation of endothelial cells. . **44**(1),pp.164–169.

Park, J.Y., Murakami, T., Lee, J.Y., Zhang, Y., Hoffman, R.M. and Bouvet, M. 2016. Fluorescent-antibody targeting of insulin-like growth factor-1 receptor visualizes metastatic human colon cancer in orthotopic mouse models. *PLOS One*. **11**(1).

Paschos, K.A., Majeed, A.W. and Bird, N.C. 2014. Natural history of hepatic metastases from colorectal cancer - pathobiological pathways with clinical significance. *World Journal of Gastroenterology*. **20**(14),pp.3719–3737.

Passero, F.C., Grapsa, D., Syrigos, K.N. and Saif, M.W. 2016. The safety and efficacy of Onivyde (irinotecan liposome injection) for the treatment of metastatic pancreatic cancer following gemcitabine-based therapy. *Expert Review of Anticancer Therapy*. **16**(7),pp.697–703.

Patnaik, A., Papadopoulos, K.P., Tolcher, A.W., Beeram, M., Urien, S., Schaaf, L.J., Tahiri, S., Bekaii-Saab, T., Lokiec, F.M., Rezaï, K. and Buchbinder, A. 2013. Phase I dose-escalation study of EZN-2208 (PEG-SN38), a novel conjugate of poly(ethylene) glycol and SN38, administered weekly in patients with advanced cancer. *Cancer*

Chemotherapy and Pharmacology. **71**(6),pp.1499–1506.

Peng, C.-L., Tsai, H.-M., Yang, S.-J., Luo, T.-Y., Lin, C.-F., Lin, W.-J. and Shieh, M.-J. 2011. Development of thermosensitive poly(n-isopropylacrylamide-co-((2-dimethylamino) ethyl methacrylate))-based nanoparticles for controlled drug release. *Nanotechnology*. **22**(26),p.265608.

Perego, P., Capranico, G., Supino, R. and Zunino, F. 1994. Topoisomerase I gene expression and cell sensitivity to camptothecin in human cell lines of different tumor types. *Anti-cancer drugs*. **5**(6),pp.645–649.

Petrovic, M. and Barceló, D. 2013. Liquid chromatography-tandem mass spectrometry. *Analytical and Bioanalytical Chemistry*. **405**(18),pp.5857–5858.

Peyman, S.A., Abou-Saleh, R.H., McLaughlan, J.R., Ingram, N., Johnson, B.R.G., Critchley, K., Freear, S., Evans, J.A., Markham, A.F., Coletta, P.L. and Evans, S.D. 2012. Expanding 3D geometry for enhanced on-chip microbubble production and single step formation of liposome modified microbubbles. *Lab on a Chip*. **12**,pp.4544–4552.

Peyman, S.A., McLaughlan, J.R., Abou-Saleh, R.H., Marston, G., Johnson, B.R.G., Freear, S., Coletta, P.L., Markham, A.F. and Evans, S.D. 2016. On-chip preparation of nanoscale contrast agents towards high-resolution ultrasound imaging. *Lab on a Chip*. **16**,pp.679–687.

Pfister, T.D., Hollingshead, M., Kinders, R.J., Zhang, Y., Evrard, Y.A., Ji, J., Khin, S.A., Borgel, S., Stotler, H., Carter, J., Divelbiss, R., Kummar, S., Pommier, Y., Parchment, R.E., Tomaszewski, J.E. and Doroshow, J.H. 2012. Development and validation of an immunoassay for quantification of topoisomerase I in solid tumor tissues. *PLOS One*. **7**(12).

Pfister, T.D., Reinhold, W.C., Agama, K., Gupta, S., Khin, S.A., Kinders, R.J., Parchment, R.E., Tomaszewski, J.E., Doroshow, J.H. and Pommier, Y. 2009. Topoisomerase I levels in the NCI-60 cancer cell line panel determined by validated ELISA and microarray analysis and correlation with indenoisoquinoline sensitivity. *Molecular Cancer Therapeutics*. **8**(7),pp.1878–84.

Piscaglia, F., Bolondi, L., Aiani, L., Luigi Angeli, M., Arienti, V., Barozzi, L., Basilico, R., Bertolotto, M., Biasini, E., Busilacchi, P., Calliada, F., Caremani, M., Caturelli, E., Celli, N., Colecchia, A. and +29 2006. The safety of Sonovue® in abdominal applications: Retrospective analysis of 23188 investigations. *Ultrasound in Medicine and Biology*.

32(9),pp.1369–1375.

Pitt, W.G., Husseini, G.A. and Staples, B.J. 2004. Ultrasonic drug delivery - A general review. *Expert opinion on drug delivery*. **1**(1),pp.37–56.

Pochon, S., Tardy, I., Bussat, P., Bettinger, T., Brochot, J., von Wronski, M., Passantino, L. and Schneider, M. 2010. BR55: A lipopeptide-based VEGFR2-targeted ultrasound contrast agent for molecular imaging of angiogenesis. *Investigative Radiology*. **45**(2),pp.89–95.

Prabhakar, U., Maeda, H., K. Jain, R., Sevick-Muraca, E.M., Zamboni, W., Farokhzad, O.C., Barry, S.T., Gabizon, A., Grodzinski, P. and Blakey, D.C. 2013. Challenges and key considerations of the enhanced permeability and retention effect for nanomedicine drug delivery in oncology. *Cancer Research*. **73**(8),pp.2412–2417.

Prescott, M.J. and Lidster, K. 2017. Improving quality of science through better animal welfare: The NC3Rs strategy. *Lab Animal*. **46**(4),pp.152–156.

Pretlow, T.G., Delmoro, C.M., Dilley, G.G., Spadafora, C.G. and Pretlow, T.P. 1991. Transplantation of human prostatic carcinoma into nude mice in matrigel. *Cancer Research*. **51**(14),pp.3814–3817.

Przybylo, M., Glogocka, D., Dobrucki, J.W., Fraczkowska, K., Podbielska, H., Kopaczynska, M., Borowik, T. and Langner, M. 2016. The cellular internalization of liposome encapsulated protoporphyrin IX by HeLa cells. *European Journal of Pharmaceutical Sciences*. **85**,pp.39–46.

Pullicino, R. and Das, K. 2017. Is it safe to use galolinium-based contrast agents in MRI? *The Journal of the Royal College of Physicians of Edinburgh*. **47**(3),pp.243–246.

Pysz, M.A., Foygel, K., Rosenberg, J., Gambhir, S.S., Schneider, M., Willmann, J.K. and 1 2010. Antiangiogenic cancer therapy: monitoring with molecular US and a clinically translatable contrast agent (BR55). *Radiology*. **256**,pp.519–527.

Pysz, M.A., Guracar, I., Tian, L. and Willmann, J.K. 2012. Fast microbubble dwell-time based ultrasonic molecular imaging approach for quantification and monitoring of angiogenesis in cancer. *Quantitative Imaging in Medicine and Surgery*. **2**(2),pp.68–80.

Pysz, M.A., Machtaler, S.B., Seeley, E.S., Lee, J.J., Brentnall, T.A., Rosenberg, J., Tranquart, F. and Willmann, J.K. 2015. Vascular endothelial growth factor receptor type 2–targeted contrast-enhanced US of pancreatic cancer neovasculature in a genetically engineered mouse model: Potential for earlier detection. *Radiology*. **274**(3),pp.790–

799.

Qin, S., Caskey, C. and Ferrara, K. 2009. Ultrasound contrast microbubbles in imaging and therapy: physical principles and engineering. *Physics in medicine and biology*. **54**(6),pp.1–42.

Qiu, Y., Luo, Y., Zhang, Y., Cui, W., Zhang, D., Wu, J., Zhang, J. and Tu, J. 2010. The correlation between acoustic cavitation and sonoporation involved in ultrasound-mediated DNA transfection with polyethylenimine (PEI) in vitro. *Journal of Controlled Release*. **145**(1),pp.40–48.

Quinto, C., Mohindra, P., Tong, S. and Bao, G. 2015. Multifunctional superparamagnetic iron oxide nanoparticles for combined chemotherapy and hyperthermia cancer treatment. *Nanoscale*. **7**(29),pp.12728–12736.

Raefsky, E., Spigel, D.R., Infante, J.R., Bendell, J.C., Jones, S.F., Lipman, A.J., Trent, D., Kawamura, S., Greco, F.A., Hainsworth, J.D. and Burris, H.A. 2011. Phase II study of NK012 in relapsed small cell lung cancer. *Journal of Clinical Oncology*. **29**(15),pp.7079–7079.

Ramasawmy, R., Johnson, S.P., Roberts, T.A., Stuckey, D.J., David, A.L., Pedley, R.B., Lythgoe, M.F., Siow, B. and Walker-Samuel, S. 2016. Monitoring the growth of an orthotopic tumour xenograft model: Multi-modal imaging assessment with benchtop MRI (1T), high-field MRI (9.4T), ultrasound and bioluminescence. *PLOS One*. **11**(5).

Rao, Q., You, A., Guo, Z., Zuo, B., Gao, X., Zhang, T., Du, Z., Wu, C. and Yin, H.F. 2016. Intrahepatic tissue implantation represents a favorable approach for establishing orthotopic transplantation hepatocellular carcinoma mouse models. *PLOS One*. **11**(1).

Ratna, A. and Mandrekar, P. 2017. Alcohol and cancer: Mechanisms and therapies. *Biomolecules*. **7**(61),pp.1–20.

Reitmair, A.H., Redston, M., Cai, J.C., Chuang, T.C.Y., Bjerknes, M., Cheng, H., Hay, K., Gallinger, S., Bapat, B. and Mak, T.W. 1996. Spontaneous intestinal carcinomas and skin neoplasms in Msh2-deficient mice. *Cancer Research*. **56**,pp.3842–3849.

Riihimaki, M., Hemminki, A., Sundquist, J. and Hemminki, K. 2016. Patterns of metastasis in colon and rectal cancer. *Scientific Reports*. **6**,pp.1–9.

Rivory, L.P. 2002. New drugs for colorectal cancer - mechanisms of action. *Australian Prescriber*. **25**,pp.108–110.

Robert, J. and Rivory, L. 1998. Pharmacology of irinotecan. *Drugs Today*. **34**,pp.777–803.

Rychak, J.J., Lindner, J.R., Ley, K. and Klibanov, A.L. 2006. Deformable gas-filled microbubbles targeted to P-selectin. *Journal of Controlled Release*. **114**,pp.288–299.

Sadzuka, Y., Hirotsu, S. and Hirota, S. 1998. Effect of liposomalization on the antitumor activity, side-effects and tissue distribution of CPT-11. *Cancer Letters*. **127**(1–2),pp.99–106.

Sadzuka, Y., Nakai, S., Miyagishima, A., Nozawa, Y. and Hirota, S. 1997. Effects of administered route on tissue distribution and antitumor activity of polyethyleneglycol-coated liposomes containing adriamycin. *Cancer Letters*. **111**,pp.77–86.

Sahani, D. V., Kalva, S.P., Tanabe, K.K., Hayat, S.M., O'Neill, M.J., Halpern, E.F., Saini, S. and Mueller, P.R. 2004. Intraoperative US in patients undergoing surgery for liver neoplasms: Comparison with MR imaging. *Radiology*. **232**(3),pp.810–814.

Saini, R. and Hoyt, K. 2014. Recent developments in dynamic contrast-enhanced ultrasound imaging of tumor angiogenesis. *Imaging in Medicine*. **6**(1),pp.41–52.

Sapra, P., Zhao, H., Mehlig, M., Malaby, J., Kraft, P., Longley, C., Greenberger, L.M. and Horak, I.D. 2008. Novel delivery of SN38 markedly inhibits tumor growth in xenografts, including a camptothecin-11-refractory model. *Clinical Cancer Research*. **14**(6),pp.1888–1896.

Sargent, D., Niedzwiecki, D., O'Connell, M. and Schilsky, R. 2011. Recommendation for caution with irinotecan, fluorouracil, and leucovorin for colrectal cancer. *The New England Journal of Medicine*. **345**(2),pp.144–151.

Saxena, M. and Christofori, G. 2013. Rebuilding cancer metastasis in the mouse. *Molecular Oncology*. **7**,pp.283–296.

Sayari, E., Dinarvand, M., Amini, M., Azhdarzadeh, M., Mollarazi, E., Ghasemi, Z. and Atyabi, F. 2014. MUC1 aptamer conjugated to chitosan nanoparticles, an efficient targeted carrier designed for anticancer SN38 delivery. *International Journal of Pharmaceutics*. **473**(1–2),pp.304–315.

Schinkel, A.F.L., Kaspar, M. and Staub, D. 2016. Contrast-enhanced ultrasound: Clinical applications in patients with atherosclerosis. *International Journal of Cardiovascular Imaging*. **32**,pp.35–48.

Schulz, C., Boeck, S., Heinemann, V. and Stemmler, H. 2009. UGT1A1 genotyping: A predictor of irinotecan-associated side effects and drug efficacy? *Anti-Cancer Drugs*. **20**,pp.867–879.

Scott, D., Nitecki, D.E., Kindler, H. and Goodman, J.W. 1984. Immunogenicity of biotinylated hapten-avidin complexes. *Molecular Immunology*. **21**(11),pp.1055–1060.

Sebaugh, J.L. 2011. Guidelines for accurate EC50/IC50 estimation. *Pharmaceutical Statistics*. **10**,pp.128–134.

Sennoga, C.A., Kanbar, E., Auboire, L., Dujardin, P., Fouan, D., Escoffre, J. and Bouakaz, A. 2017. Microbubble-mediated ultrasound drug-delivery and therapeutic monitoring. *Expert Opinion on Drug Delivery*. **14**(9),pp.1031–1043.

Senter, P.D., Beam, K.S., Mixan, B. and Wahl, A.F. 2001. Identification and activities of human carboxylesterases for the activation of CPT-11, a clinically approved anticancer drug. *Bioconjugate Chemistry*. **12**(6),pp.1074–1080.

Seo, J. and Kim, Y. 2017. Ultrasound imaging and beyond: Recent advances in medical ultrasound. *Biomedical Engineering Letters*. **7**(2),pp.57–58.

Sepehri, N., Rouhani, H., Tavassolian, F., Montazeri, H., Khoshayand, M.R., Ghahremani, M.H., Ostad, S.N., Atyabi, F. and Dinarvand, R. 2014. SN38 polymeric nanoparticles: In vitro cytotoxicity and in vivo antitumor efficacy in xenograft balb/c model with breast cancer versus irinotecan. *International Journal of Pharmaceutics*. **471**(1–2),pp.485–497.

Sercombe, L., Veerati, T., Moheimani, F., Wu, S.Y., Sood, A.K. and Hua, S. 2015. Advances and challenges of liposome assisted drug delivery. *Frontiers in Pharmacology*. **6**,pp.1–13.

Shafi, M.A. and Bresalier, R.S. 2010. The gastrointestinal complications of oncologic therapy. *Gastroenterology Clinics of North America*. **39**(3),pp.629–647.

Shankar, H. and Pagel, P.S. 2011. Potential adverse ultrasound-related biological effects. *Anesthesiology*. **115**(5),pp.1109–1124.

Sharpless, N.E. and DePinho, R.A. 2006. The mighty mouse: Genetically engineered mouse models in cancer drug development. *Nature Reviews Drug Discovery*. **5**(9),pp.741–754.

Sheng, Y., Beguin, E., Nesbitt, H., Kamila, S., Owen, J., Barnsley, L.C., Callan, B., O'Kane, C.,

Nomikou, N., Hamoudi, R., Taylor, M.A., Love, M., Kelly, P., O'Rourke, D., Stride, E., McHale, A.P. and Callan, J.F. 2017. Magnetically responsive microbubbles as delivery vehicles for targeted sonodynamic and antimetabolite therapy of pancreatic cancer. *Journal of Controlled Release*. **262**,pp.192–200.

Sheth, K.R. and Clary, B.M. 2005. Management of hepatic metastases from colorectal cancer. *Clinincs in Colon and Rectal Surgery*. **18**(3),pp.215–223.

Shi, J., Kantoff, P.W., Wooster, R. and Farokhzad, O.C. 2016. Cancer nanomedicine: Progress, challenges and opportunities. *Nature Reviews Cancer*. **17**(1),pp.20–37.

Shi, J., Liu, W., Fu, Y., Yin, N., Zhang, H., Chang, J. and Zhang, Z. 2018. "US-detonated nano bombs" facilitate targeting treatment of resistant breast cancer. *Journal of Controlled Release*. **274**,pp.9–23.

Shimada, X., Yoshino, M., Wakui, A., Nakao, I., Futatsuki, K., Sakata, Y., Kambe, M., Taguchi, T. and Ogawa, N. 1993. Phase II study of CPT-11, a new camptothecin derivative, in metastatic colorectal cancer. CPT-11 gastrointestinal cancer study group. *Journal of Clinical Oncology*. **11**(5),pp.909–913.

Shimizu, S., Yamada, N., Sawada, T., Ikeda, K., Nakatani, K., Seki, S., Kaneda, K. and Hirakawa, K. 2000. Ultrastructure of early phase hepatic metastasis of human colon carcinoma cells with special reference to desmosomal junctions with hepatocytes. *Pathology International*. **50**(12),pp.953–959.

Shoemaker, R.H. 2006. The NCI60 human tumour cell line anticancer drug screen. *Nature reviews. Cancer*. **6**(10),pp.813–23.

Siegel, R.L., Miller, K.D., Fedewa, S.A., Ahnen, D.J., Meester, R.G.S., Barzi, A. and Jemal, A. 2017. Colorectal Cancer Statistics, 2017. *CA: A Cancer Journal for Clinicians*. **67**(3),pp.177–193.

Singh, A.D. and Parmar, S. 2015. Ramucirumab (Cyramza): A Breakthrough Treatment for Gastric Cancer. *Pharmacy and Therapeutics*. **40**(7),pp.430–68.

Skachkov, I., Luan, Y., Van Der Steen, A.F.W., De Jong, N. and Kooiman, K. 2014. Targeted microbubble mediated sonoporation of endothelial cells in vivo. *IEEE Transactions on Ultrasonics, Ferroelectrics, and Frequency Control*. **61**(10),pp.1661–1667.

Smagowska, B. and Pawlaczyk-Łuszczyńska, M. 2013. Effects of ultrasonic noise on the human body - A bibliographic review. *International Journal of Occupational Safety and Ergonomics*. **19**(2),pp.195–202.

Smith, N.R., Baker, D., James, N.H., Ratcliffe, K., Jenkins, M., Ashton, S.E., Sproat, G., Swann, R., Gray, N., Ryan, A., Jürgensmeier, J.M. and Womack, C. 2010. Vascular endothelial growth factor receptors VEGFR-2 and VEGFR-3 are localized primarily to the vasculature in human primary solid cancers. *Clinical Cancer Research*. **16**(14),pp.3548–3561.

Smith, P.R., Mclaughlan, J.R., Ingram, N., Cowell, D.M.J., Coletta, L. and Freear, S. n.d. Composite high frequency, low frequency system for pre-clinical microbubble sonoporation.

Sorace, A.G., Saini, R., Mahoney, M. and Hoyt, K. 2012. Molecular ultrasound imaging using a targeted contrast agent for assessing early tumor response to antiangiogenic therapy. *Journal of Ultrasound in Medicine*. **31**(10),pp.1543–1550.

De Souza, R., Zahedi, P., Badame, R.M., Allen, C. and Piquette-Miller, M. 2011. Chemotherapy dosing schedule influences drug resistance development in ovarian cancer. *Molecular Cancer Therapeutics*. **10**(7),pp.1289–1299.

Souza, V., Dong, Y. Bin, Zhou, H.S., Zacharias, W. and McMasters, K.M. 2005. SW-620 cells treated with topoisomerase I inhibitor SN-38: gene expression profiling. *Journal of translational medicine*. **3**,p.44.

Stein, A., Voigt, W. and Jordan, K. 2010. Chemotherapy-induced diarrhea: Pathophysiology, frequency and guideline-based management. *Therapeutic Advances in Medicial Oncology*. **2**(1),pp.51–63.

Stintzing, S., Fischer Von Weikersthal, L., Vehling-Kaiser, U., Stauch, M., Hass, H.G., Dietzfelbinger, H., Oruzio, D., Klein, S., Zellmann, K., Decker, T., Schulze, M., Abenhardt, W., Puchtler, G., Kappauf, H., Mittermüller, J., Haberl, C., Giessen, C., Moosmann, N. and Heinemann, V. 2011. Correlation of capecitabine-induced skin toxicity with treatment efficacy in patients with metastatic colorectal cancer: Results from the German AIO KRK-0104 trial. *British Journal of Cancer*. **105**(2),pp.206–211.

Stride, E. and Saffari, N. 2003. Microbubble ultrasound contrast agents: A review. *Journal of Engineering in Medicine*. **217**(6),pp.429–47.

Subhawong, T.K., Fishman, E.K., Swart, J.E., Carrino, J.A., Attar, S. and Fayad, L.M. 2010. Soft-tissue masses and masslike conditions: What does CT add to diagnosis and management? *American Journal of Roentgenology*. **194**(6),pp.1559–1567.

Sugimoto, Y., Tsukahara, S., Oh-hara, T., Isoe, T. and Tsuruo, T. 1990. Decreased expression

of DNA topoisomerase I in camptothecin-resistant tumor cell lines as determined by a monoclonal antibody. *Cancer research*. **50**(21),pp.6925–6930.

Sun, W., Hu, Q., Ji, W., Wright, G. and Gu, Z. 2017. Leveraging Physiology for Precision Drug Delivery. *Physiological Reviews*. **97**(1),pp.189–225.

Susan, M. 2015. Intratumoural drug metabolism and the disposition of anticancer agents: implications for clinical treatment. *Cancer World*. **65**,pp.43–47.

Swales, J.G., Tucker, J.W., Strittmatter, N., Nilsson, A., Cobice, D., Clench, M.R., Mackay, C.L., Andren, P.E., Takáts, Z., Webborn, P.J.H. and Goodwin, R.J.A. 2014. Mass spectrometry imaging of cassette-dosed drugs for higher throughput pharmacokinetic and biodistribution analysis. *Analytical Chemistry*. **86**(16),pp.8473–8480.

Szebeni, J. and Barenholz, Y.C. 2009. *Adverse immune effects of liposomes: Complement activation, immunogenicity and immune suppression. Harnessing biomaterials for nanomedicine: Preparation, toxicity and applications.* Pan Standford Publishing Pte Ltd.

Tabernero, J., Yoshino, T., Cohn, A.L., Obermannova, R., Bodoky, G., Garcia-Carbonero, R., Ciuleanu, T.E., Portnoy, D.C., Van Cutsem, E., Grothey, A., Prausová, J., Garcia-Alfonso, P., Yamazaki, K., Clingan, P.R., Lonardi, S., Kim, T.W., Simms, L., Chang, S.C. and Nasroulah, F. 2015. Ramucirumab versus placebo in combination with second-line FOLFIRI in patients with metastatic colorectal carcinoma that progressed during or after first-line therapy with bevacizumab, oxaliplatin, and a fluoropyrimidine (RAISE): A randomised, double-blind, multicentre, phase 3 study. *The Lancet Oncology*. **16**(5),pp.499–508.

Tachibana, K., Uchida, T., Ogawa, K., Yamashita, N. and Tamura, K. 1999. Induction of cell-membrane porosity by ultrasound. *The Lancet*. **353**,p.1409.

Takahashi, A., Ohkohchi, N., Yasunaga, M., Kuroda, J.I., Koga, Y., Kenmotsu, H., Kinoshita, T. and Matsumura, Y. 2010. Detailed distribution of NK012, an SN-38-incorporating micelle, in the liver and its potent antitumor effects in mice bearing liver metastases. *Clinical Cancer Research*. **16**(19),pp.4822–4831.

Takakura, A., Kurita, A., Asahara, T. and Yokoba, M. 2012. Rapid deconjugation of SN-38 glucuronide and adsorption of released free SN-38 by intestinal microorganisms in rat. *Oncology Letters*. **3**,pp.520–524.

Takano, M. and Sugiyama, T. 2017. UGT1A1 polymorphisms in cancer: Impact on irinotecan treatment. *Pharmacogenomic and Personalized Medicine*. **10**,pp.61–68.

Tardy, I., Pochon, S., Theraulaz, M., Emmel, P., Passantino, L., Tranquart, F. and Schneider, M. 2010. Ultrasound molecular imaging of VEGFR2 in a rat prostate tumor model using BR55. *Investigative Radiology*. **45**(10),pp.573–578.

Tariq, K. and Ghias, K. 2016. Colorectal cancer carcinogenesis: A review of mechanisms. *Cancer Biology & Medicine*. **13**(1),pp.120–35.

Tavaresa, A.J., Poona, W., Zhanga, Y.-N., Daia, Q., Beslac, R., Dinga, D., Ouyanga, B., Lic, A., Chene, J., Zhenge, G., Robbinsc, C. and Chan, W.C.W. 2017. Effect of removing Kupffer cells on nanoparticle tumor delivery. *Proceedings of the National Academy of Sciences of the United States of America*. **114**(51).

Taylor, S.L., Rahim, A.A., Bush, N.L., Bamber, J.C. and Porter, C.D. 2007. Targeted retroviral gene delivery using ultrasound. *The Journal of Gene Medicine*. **9**,pp.77–87.

Tenant, S.C. and Gutteridge, C.M. 2016. The clinical use of contrast-enhanced ultrasound in the kidney. *Ultrasound*. **24**(2),pp.94–103.

Thakur, R., Sivakumar, B. and Savva, M. 2010. Thermodynamic studies and loading of 7-ethyl-10-hydroxycamptothecin into mesoporous silica particles MCM-41 in strongly acidic solutions. *Journal of Physical Chemistry B*. **114**,pp.5903–5911.

Thalheimer, A., Otto, C., Bueter, M., Illert, B., Gattenlohner, S., Gasser, M., Fein, M., Germer, C.T. and Waaga-Gasser, A.M. 2009. The intraportal injection model: A preclinical animal model for hepatic metastases and tumor dissemination in human colon cancer. *European Surgical Research*. **42**(3),pp.195–200.

Tiede, C., Bedford, R., Heseltine, S.J., Smith, G., Wijetunga, I., Ross, R., Alqallaf, D., Roberts, A.P.E. and +38 2017. Affimer proteins are versatile and renewable affinity reagents. *eLife*. **6**,pp.1–35.

Timmers, M., Vekemans, K., Vermijlen, D., Asosingh, K., Kuppen, P., Bouwens, L., Wisse, E. and Braet, F. 2004. Interactions between rat colon carcinoma cells and kupffer cells during the onset of hepatic metastasis. *International Journal of Cancer*. **112**(5),pp.793–802.

Ting, C.-Y., Fan, C.-H., Liu, H.-L., Huang, C.-Y., Hsieh, H.-Y., Yen, T.-C., Wei, K.-C. and Yeh, C.-K. 2012. Concurrent blood–brain barrier opening and local drug delivery using drug-carrying microbubbles and focused ultrasound for brain glioma treatment.

Biomaterials. **33**(2),pp.704–712.

Tinkov, S., Coester, C., Serba, S., Geis, N.A., Katus, H.A., Winter, G. and Bekeredjian, R. 2010. New doxorubicin-loaded phospholipid microbubbles for targeted tumor therapy: In-vivo characterization. *Journal of Controlled Release*. **148**(3),pp.368–372.

Tlaxca, J.L., Rychak, J.J., Ernst, P.B., Konkalmatt, P.R., Shevchenko, T.I., Pizzaro, T.T., Rivera-Nieves, J., Klibanov, A.L. and Lawrence, M.B. 2013. Ultrasound-based molecular imaging and specific gene delivery to mesenteric vasculature by endothelial adhesion molecule targeted microbubbles in a mouse model of Crohn's disease. *Journal of Controlled Release*. **165**(3),pp.216–225.

Tobin, P., Clarke, S., Seale, J.P., Lee, S., Solomon, M., Aulds, S., Crawford, M., Gallagher, J., Eyers, T. and Rivory, L. 2006. The in vitro metabolism of irinotecan (CPT-11) by carboxylesterase and beta-glucuronidase in human colorectal tumours. *British Journal of Clinical Pharmacology*. **62**(1),pp.122–129.

Toffoli, G., De Mattia, E., Cecchin, E., Biason, P., Masier, S. and Corona, G. 2007. Pharmacology of epidermal growth factor inhibitors. *The International journal of Biological Markers*. **22**(1 (Suppl 4)),pp.S24–S39.

Tomayko, M.M. and Reynolds, C.P. 1989. Determination of subcutaneous tumor size in athymic (nude) mice. *Cancer Chemotherapy and Pharmacology*. **24**(3),pp.148–154.

Tomlinson, J.S., Jarnagin, W.R., DeMatteo, R.P., Fong, Y., Kornprat, P., Gonen, M., Kemeny, N., Brennan, M.F., Blumgart, L.H. and D'Angelica, M. 2007. Actual 10-year survival after resection of colorectal liver metastases defines cure. *Journal of Clinical Oncology*. **25**(29),pp.4575–4580.

Twelves, C., Cortés, J., O'Shaughnessy, J., Awada, A., Perez, E.A., Im, S. –A, Gómez-Pardo, P., Schwartzberg, L.S., Diéras, V., Yardley, D.A., Potter, D.A., Mailliez, A., Moreno-Aspitia, A., Ahn, J.S., Zhao, C., Hoch, U., Tagliaferri, M., Hannah, A.L. and Rugo, H.S. 2017. Health-related quality of life in patients with locally recurrent or metastatic breast cancer treated with etirinotecan pegol versus treatment of physician's choice: Results from the randomised phase III BEACON trial. *European Journal of Cancer*. **76**,pp.205–215.

Twelves, C., Scheithauer, W., Mckendrick, J., Seitz, J.F., Van Hazel, G., Wong, A., Díaz-Rubio, E., Gilberg, F. and Cassidy, J. 2012. Capecitabine versus 5-fluorouracil/folinic acid as adjuvant therapy for stage III colon cancer: Final results from the X-ACT trial with

analysis by age and preliminary evidence of a pharmacodynamic marker of efficacy. *Annals of Oncology*. **23**(5),pp.1190–1197.

Umemura, S. ichiro, Yumita, N., Umemura, K. and Nishigaki, R. 1999. Sonodynamically induced effect of rose bengal on isolated sarcoma 180 cells. *Cancer Chemotherapy and Pharmacology*. **43**(5),pp.389–393.

Unger, E.C., McCreery, T., Sweitzer, R., Robert, H., Caldwell, V.E. and Wu, Y. 1998. Acoustically active lipospheres containing paclitaxel: A new therapeutic ultrasound contrast agent. *Investigative Radiology*. **33**(12),pp.886–892.

Unger, E.C., McCreery, T., Sweitzer, R., Vielhauer, G., Wu, G., Shen, D. and Yellowhair, D. 1998. MRX 501: A novel ultrasound contrast agent with therapeutic properties. *Academic Radiology*. **5**,pp.247–249.

Vladimir, T. 2009. Multifunctional and stimuli-sensitive pharmaceutical nanocarriers. *European Journal of Pharmaceutics and Biopharmaceutics*. **71**(3),pp.431–444.

Voskoglou-Nomikos, T., Pater, J.L. and Seymour, L. 2003. Clinical predictive value of the in vitro cell line, human xenograft, and mouse allograft preclinical cancer models. *Clinical Cancer Research*. **9**,pp.4227–4239.

Wagner, A., Arnold, D., Grothey, A., Haerting, J. and Unverzagt, S. 2009. Anti-angiogenic therapies for metastatic colorectal cancer. *Cochrane Database of Systematic Reviews*. (3).

Wall, M.E., Wani, M.C., Cook, C.E., Palmer, K.H., Mcphail, A.T. and Sim, G.A. 1996. Plant antitumor agents. I. the isolation and structure of camptothecin, a novel alkaloidal leukemia and tumor inhibitor from camptotheca acuminata. *Journal of the American Chemical Society*. **88**(16),pp.3888–3890.

Wan, G.-Y., Liu, Y., Chen, B.-W., Liu, Y.-Y., Wang, Y.-S., Zhang, N., Wan, G.-Y., Liu, Y., Chen, B.-W., Liu, Y.-Y., Wang, Y.-S. and Zhang, N. 2016. Recent advances of sonodynamic therapy in cancer treatment. *Cancer Biology & Medicine*. **13**(3),pp.325–338.

Wang, H., Kaneko, O.F., Tian, L., Hristov, D. and Willmann, J.K. 2015. Three-dimensional ultrasound molecular imaging of angiogenesis in colon cancer using a clinical matrix array ultrasound transducer. *Investigative radiology*. **50**(5),pp.322–329.

Wang, J., Mao, W., Lock, L.L., Tang, J., Sui, M., Sun, W., Cui, H., Xu, D. and Shen, Y. 2015. The role of micelle size in tumor accumulation, penetration, and treatment. *ACS Nano*. **9**(7),pp.7195–7206.

Wang, M., Zhao, J., Zhang, L., Wei, F., Lian, Y., Wu, Y. and Gong, Z. 2017. Role of tumor microenvironment in tumorigenesis. *Journal of Cancer*. **8**,pp.761–773.

Wang, S., Hossack, J.A. and Klibanov, A.L. 2018. Targeting of microbubbles: Contrast agents for ultrasound molecular imaging. *Journal of Drug Targeting*. **26**(5–6),pp.420–434.

Warram, J.M., Sorace, A.G., Saini, R., Umphrey, H.R., Zinn, K.R. and Hoyt, K. 2011. A triple-targeted ultrasound contrast agent provides improved localization to tumor vasculature. *Journal of Ultrasound in Medicine*. **30**(7),pp.921–31.

Wei, S., Fu, N., Sun, Y., Yang, Z., Lei, L., Huang, P. and Yang, B. 2014. Targeted contrast-enhanced ultrasound imaging of angiogenesis in an orthotopic mouse tumor model of renal carcinoma. *Ultrasound in Medicine and Biology*. **40**(6),pp.1250–1259.

Weisenberg, E. 2018. TNM staging of colorectal carcinoma (AJCC 8th edition). *PathologyOutlines.com website.* [Online]. [Accessed 18 May 2018]. Available from: http://www.pathologyoutlines.com/topic/colontumorstaging8ed.html. .

West, N.P., Sutton, K.M., Ingeholm, P., Hagemann-Madsen, R.H., Hohenberger, W. and Quirke, P. 2010. Improving the quality of colon cancer surgery through a surgical education program. *Diseases of the Colon and Rectum*. **53**(12),pp.1594–1603.

Wildiers, H., Ahmed, B., Guetens, G., De Boeck, G., De Bruijn, E.A., Landuyt, W. and Van Oosterom, A.T. 2004. Combretastatin A-4 phosphate enhances CPT-11 activity independently of the administration sequence. *European Journal of Cancer*. **40**(2),pp.284–290.

Wilke, H., Glynne-Jones, R., Thaler, J., Adenis, A., Preusser, P., Aguilar, E.A., Aapro, M.S., Esser, R., Loos, A.H. and Siena, S. 2008. Cetuximab plus irinotecan in heavily pretreated metastatic colorectal cancer progressing on irinotecan: MABEL study. *Journal of Clinical Oncology*. **26**(33),pp.5335–5343.

Willmann, J.K., Bonomo, L., Testa, A.C., Rinaldi, P., Rindi, G., Valluru, K.S., Petrone, G., Martini, M., Lutz, A.M. and Gambhir, S.S. 2017. Ultrasound molecular imaging with BR55 in patients with breast & ovarian lesions: First-in-human results. *Journal of Clinical Oncology*. **35**(19),pp.2133–2140.

Willmann, J.K., Cheng, Z., Davis, C., Lutz, A.M., Nielsen, C.H. and Gambhir, S.S. 2008. Targeted microbubbles for imaging tumor angiogenesis: Assessment of whole-body biodistribution with dynamic micro-PET in mice. *Radiology*. **249**(1),pp.212–219.

Willmann, J.K., Kimura, R.H., Deshpande, N., Lutz, A.M., Cochran, J.R. and Gambhir, S.S.

2010. Targeted contrast-enhanced ultrasound imaging of tumor angiogenesis with contrast microbubbles conjugated to integrin-binding knottin peptides. *Journal of Nuclear Medicine*. **51**,pp.433–440.

Willmann, J.K., Lutz, A.M., Paulmurugan, R., Patel, M.R., Chu, P., Rosenberg, J. and Gambhir, S.S. 2008. Dual-targeted contrast agent for US assessment of tumor angiogenesis in vivo. *Radiology*. **248**(3),pp.936–944.

Willmann, J.K., Paulmurugan, R., Chen, K., Gheysens, O., Rodriguez-Porcel, M., Lutz, A.M., Chen, I.Y., Chen, X. and Gambhir, S.S. 2008. US imaging of tumor angiogenesis with microbubbles targeted to vascular endothelial growth factor receptor type 2 in mice. *Radiology*. **246**(2),pp.508–518.

Wilson, S.R. and Burns, P.N. 2010. Microbubble-enhanced US in body imaging: What role? *Radiology*. **257**(1),pp.24–39.

Wolfram, J., Nizzero, S., Liu, H., Li, F., Zhang, G. and Li, Z. 2017. A chloroquine-induced macrophage-preconditioning strategy for improved nanodelivery. *Scientific Reports*. **7**(1).

Wood, A.K.W. and Sehgal, C.M. 2015. A review of low-intensity ultrasound for cancer therapy. *Ultrasound in Medicine and Biology*. **41**(4),pp.905–928.

Wright, A.I., Grabsch, H.I. and Treanor, D.E. 2015. RandomSpot: A web-based tool for systematic random sampling of virtual slides. *Journal of Pathology Informatics*. **6**(8),pp.41–45.

Wu, J., Yin, M., Hapke, G., Tóth, K. and Rustum, Y.M. 2002. Induction of biphasic DNA double strand breaks and activation of multiple repair protein complexes by DNA topoisomerase I drug 7-ethyl-10-hydroxy-camptothecin. *Molecular pharmacology*. **61**(4),pp.742–8.

Xu, G., Shi, C., Guo, D., Wang, L., Ling, Y., Han, X. and Luo, J. 2015. Functional-segregated coumarin-containing telodendrimer nanocarriers for efficient delivery of SN-38 for colon cancer treatment. *Acta Biomaterialia*. **21**,pp.85–98.

Xu, G., Zhang, W., Ma, M.K. and McLeod, H.L. 2002. Human carboxylesterase 2 is commonly expressed in tumor tissue and is correlated with activation of irinotecan. *Clinical Cancer Research*. **8**,pp.2605–2611.

Yang, F., Gu, N., Chen, D., Xi, X., Zhang, D., Li, Y. and Wu, J. 2008. Experimental study on cell self-sealing during sonoporation. *Journal of Controlled Release*. **131**,pp.205–210.

Yeh, J.-S.M., Sennoga, C.A., McConnell, E., Eckersley, R., Tang, M.X., Nourshargh, S., Seddon, J.M., Haskard, D.O. and Nihoyannopoulos, P. 2015. A targeting microbubble for ultrasound molecular imaging. *PLOS One*. **10**(7),pp.1–23.

Yona, S. and Gordon, S. 2015. From the reticuloendothelial to mononuclear phagocyte system - The unaccounted years. *Frontiers in Immunology*. **6**.

Young, M., Ordonez, L. and Clarke, A.R. 2013. What are the best routes to effectively model human colorectal cancer? *Molecular Oncology*. **7**(2),pp.178–189.

Younis, I.R., Malone, S., Friedman, H.S., Schaaf, L.J. and Petros, W.P. 2009. Enterohepatic recirculation model of irinotecan (CPT-11) and metabolite pharmacokinetics in patients with glioma. *Cancer Chemotherapy and Pharmacology*. **63**(3),pp.517–524.

Yu, H., Lin, Z., Xu, L., Liu, D. and Shen, Y. 2015. Theoretical study of microbubble dynamics in sonoporation. *Ultrasonics*. **61**,pp.136–144.

Yu, M.H., Lee, J.Y., Kim, H.R., Kim, B.R., Park, E., Kim, H.S., Han, J.K. and Choi, B.I. 2016. Therapeutic effects of microbubbles added to combined high-intensity focused ultrasound and chemotherapy in a pancreatic cancer xenograft model. *Korean Journal of Radiology*. **17**(5),pp.779–788.

Zamboni, C., Stewart, F., Cheshire, J., Richmond, L.B., Hanna, S.K., Mcgovren, J.P., Houghton, J.A. and Houghton, P.J. 1998. Human colon efficacy tumor and pharmacology of irinotecan against xenograft models. *Clinical Cancer Research*. **4**(28),pp.743–753.

Zauber, A., Winawer, S., O'Brien, M., Lansdorp-Vogelaar, I. and van Ballegooijen, M. 2012. Colonoscopic polypectomy and long-term prevention of colorectal-cancer deaths. *The New England Journal of Medicine*. **366**(8),pp.687–696.

Zhang, H. 2016. Onivyde for the therapy of multiple solid tumors. *OncoTargets and Therapy*. **9**,pp.3001–3007.

Zhang, H., Tam, S., Ingham, E.S., Mahakian, L.M., Lai, C.Y., Tumbale, S.K., Teesalu, T., Hubbard, N.E., Borowsky, A.D. and Ferrara, K.W. 2015. Ultrasound molecular imaging of tumor angiogenesis with a neuropilin-1-targeted microbubble. *Biomaterials*. **56**,pp.104–113.

Zhang, H., Wang, J., Mao, W., Huang, J., Wu, X., Shen, Y. and Sui, M. 2013. Novel SN38 conjugate-forming nanoparticles as anticancer prodrug: In vitro and in vivo studies. *Journal of Controlled Release*. **166**(2),pp.147–158.

Zhang, J.A., Xuan, T., Parmar, M., Ma, L., Ugwu, S., Ali, S. and Ahmad, I. 2004. Development and characterization of a novel liposome-based formulation of SN-38. *International Journal of Pharmaceutics*. **270**(1–2),pp.93–107.

Zhao, X., Li, L., Starr, T. and Subramanian, S. 2017. Tumor location impacts immune response in mouse models of colon cancer. *Oncotarget*. **8**(33),pp.54775–54787.

Zhou, Z., Nimeiri, H.S. and Benson, A.B. 2013. Preoperative chemotherapy for locally advanced resectable colon cancer - a new treatment paradigm in colon cancer? *Annals of translational medicine*. **1**(2),pp.11–16.

Ziemba, B., Janaszewska, A., Ciepluch, K., Krotewicz, M., Fogel, W.A., Appelhans, D., Voit, B., Bryszewska, M. and Klajnert, B. 2011. In vivo toxicity of poly(propyleneimine) dendrimers. *Journal of Biomedical Materials Research Part A*. **99**(2),pp.261–268.

Zirvi, K.A., Keogh, J.P., Slomiany, A. and Slomiany, B.L. 1991. Transglutaminase activity in human colorectal carcinomas of differing metastatic potential. *Cancer Letters*. **60**(1),pp.85–92.

Zisman, A.L., Nickolov, A., Brand, R.E., Gorchow, A. and Roy, H.K. 2006. Associations between the age at diagnosis and location of colorectal cancer and the use of alcohol and tobacco: Implications for screening. *Archives of Internal Medicine*. **166**(6),pp.629–634.

Appendix A

Supplementary information for Chapter 6

Video 1: Intrahepatic injection of CRC cells

HFUS guided intrahepatic injection of 5 x 10^5 SW620 human CRC cells. A needle tip can be seen penetrating the skin and liver, cells injected and needle removed. Taken in B-mode using a 40 MHz transducer. Video in real-time.

Video 2: Intrahepatic CRC tumour

HFUS video of an intrahepatic human CRC tumour (SW620), 20-days post injection. Taken in B-mode using a 40 MHz transducer. Video in real-time.